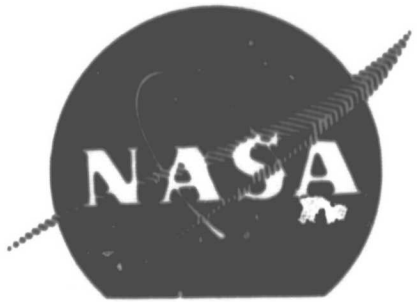


General Disclaimer

One or more of the Following Statements may affect this Document

- This document has been reproduced from the best copy furnished by the organizational source. It is being released in the interest of making available as much information as possible.
- This document may contain data, which exceeds the sheet parameters. It was furnished in this condition by the organizational source and is the best copy available.
- This document may contain tone-on-tone or color graphs, charts and/or pictures, which have been reproduced in black and white.
- This document is paginated as submitted by the original source.
- Portions of this document are not fully legible due to the historical nature of some of the material. However, it is the best reproduction available from the original submission.



NASA CR-120935
R-8973-1

(NASA-CR-120935) SPACE STORABLE PROPELLANT
PERFORMANCE GAS/LIQUID LIKE-DOUBLET
INJECTOR CHARACTERIZATION A.Y. Falk
(Rocketdyne) Oct. 1972 211 p CSCL 21I

N72-33730

Unclass
44253

G3/27

SPACE STORABLE PROPELLANT PERFORMANCE GAS/LIQUID
LIKE-DOUBLET INJECTOR CHARACTERIZATION

by
A. Y. Falk



ROCKETDYNE
A DIVISION OF NORTH AMERICAN ROCKWELL CORPORATION
6633 CANOGA AVENUE, CANOGA PARK, CALIFORNIA

prepared for
NATIONAL AERONAUTICS AND SPACE ADMINISTRATION

NASA-Lewis Research Center
NAS3-12051
Larry H. Gordon, Project Manager

FOREWORD

The work described herein was conducted for the NASA-Lewis Research Center, Cleveland, Ohio, by the Advanced Programs Department of Rocketdyne, a division of North American Rockwell Corporation. The study was conducted in accordance with Contract NAS3-12051, Rocketdyne G.O. 09222. This report (R-8973-1), which covers primarily the like-doublet injector characterization portion of the contract work, is one of three reports emerging from the subject contract. Separate reports describing the coaxial injector characterization portion of the contract work (R-8973-2) and a design manual summarizing injector-thrust chamber design criteria for both injector types (R-8973-3) are being published.

Mr. L. H. Gordon of the NASA-Lewis Research Center served as NASA Technical Project Manager. The Rocketdyne Program Manager was Mr. H. G. Diem. Technical guidance of the program was provided by Mr. S. D. Clapp and Dr. D. T. Campbell.

Important contributions to the conduct of the program were made by the following Rocketdyne personnel: R. J. Burick, J. T. Sabol, and R. R. Doubleday.

CONTENTS

Foreword	ii
Abstract	v
1.0 Introduction	1
2.0 Summary	5
3.0 Analytical Parametric Combustion Analysis	9
3.1 Propellant Vaporization	9
3.2 Propellant Distribution/Mixing	20
3.3 Summary of Analytical Model Studies	27
4.0 Experimental Hardware	29
4.1 Injectors	29
4.2 Thrust Chambers	51
5.0 Experimental Results and Discussion	59
5.1 Injector Models	59
5.2 Full-Scale Performance and Chamber Compatible Injectors	89
5.3 Optimized Injector Configuration	104
5.4 Data Correlations	114
6.0 Concluding Remarks	117
6.1 Like-Doublet Performance and Chamber Heat Transfer Characteristics	117
6.2 Cold-Flow Injector Modeling Techniques	118
6.3 Application of Results to Other Propellant Systems	118
6.4 Recommendations for Future Work	120
<u>Appendix A</u>	
K-Prime Combustion Model	A-1
<u>Appendix B</u>	
Pressurized Cold-Flow Mixing Facility	B-1
<u>Appendix C</u>	
Pressurized Cold-Flow Atomization Facility	C-1
<u>Appendix D</u>	
Hot-Fire Facilities and Procedures	D-1
<u>Appendix E</u>	
Calculation of Corrected c^* Efficiency	E-1
<u>Appendix F</u>	
Heat Transfer Data Reduction Technique	F-1
<u>Appendix G</u>	
Physical Property and Theoretical Performance Summary	G-1
<u>Appendix H</u>	
Performance Data Measurement Error Analysis	H-1
<u>Appendix I</u>	
Random Walk Measurement Analysis Program	I-1
<u>Appendix J</u>	
References	J-1
<u>Appendix K</u>	
Distribution List (Contract NAS2-12051)	K-1

PRECEDING PAGE BLANK NOT FILMED

ABSTRACT

A 30-month applied research program encompassing an analytical, design, and experimental effort to relate injector design parameters to simultaneous attainment of high performance and component (injector/thrust chamber) compatibility for gas/liquid space storable propellants was conducted. The gas/liquid propellant combination selected for study was FLOX (82.6% F_2)/ ambient temperature gaseous methane. The injector pattern characterized was the like (self)-impinging doublet. Program effort was apportioned into four basic technical tasks: Task I--Injector and Thrust Chamber Design, Task II--Injector and Thrust Chamber Fabrication, Task III--Performance Evaluation Testing, and Task IV--Data Evaluation and Reporting. Analytical parametric combustion analyses and cold-flow distribution and atomization experiments were conducted with injector segment models to support design of injector/thrust chamber combinations for hot-fire evaluation. Hot-fire tests were conducted to: (1) optimize performance of the injector "core" elements, and (2) provide design criteria for the outer zone elements so that injector/thrust chamber compatibility could be achieved with only minimal performance losses.

The performance of the optimized injector configuration was 97 to 98 percent of the shifting equilibrium value in the reference chamber ($L^* = 40$ in.; $\epsilon_c = 3$) at nominal design conditions ($P_c = 500$ psia; $MR = 5.25$; sea level thrust = 3000 lbf) with excellent injector/thrust chamber compatibility.

Results of this study provide concise and specific criteria for attenuation of chamber heat loads which previously have impeded actual predevelopment for FLOX/light hydrocarbon propulsion systems. This was made possible by data from the cold-flow modeling tests which provided a clear physical description of both the injected gas and liquid flow patterns. One of the most important achievements of the entire program has been the development of the cold-flow modeling experimental apparatus and techniques. These methods have now been advanced so that flow distribution and propellant mixing measurements for gas/liquid injectors can now be made on a par with those developed earlier for characterization of liquid/liquid injectors. These techniques and many of the parametric data are applicable to any gas/liquid propellant combination, not only to FLOX/methane (g), but also, for example, to LOX/GH₂ or LOX/propane (g).

PRECEDING PAGE BLANK NOT FILMED

PRECEDING PAGE BLANK NOT FILMED
ILLUSTRATIONS

1. Logic Flow Diagram for Injector-Chamber Optimization Process	3
2. Effect of Propellant Drop Size and Chamber Geometry on c^* Efficiency (Due to Vaporization) for FLOX/CH ₄ (g)	13
3. Simplified Schematics of Thrust Chamber Geometries Considered for Combustion Model Analysis	14
4. Effects of Initial Propellant Drop Size and Chamber Contraction Ratio on c^* Efficiency (Due to Vaporization) for FLOX/CH ₄ (g) at Several Chamber Pressures	16
5. Effects of Mixture Ratio and Initial Propellant Drop Size on c^* Efficiency (Due to Vaporization) for FLOX/CH ₄ (g)	17
6. Effect of Mixture Ratio on c^* Efficiency (Due to Vaporization), Fraction of Injected Propellants Burned, and the Burned-to-Injected Mixture Ratio	18
7. Predicted Effect of Propellant Mixing on Performance for FLOX/CH ₄ (g) and FLOX/B ₂ H ₆	22
8. Effect of Peripheral Zone Mass and Mixture Ratio on Characteristic Velocity Efficiency (Due to Distribution) for FLOX/CH ₄ and FLOX/B ₂ H ₆ . .	24
9. Comparison of Distribution c^* Efficiency for FLOX/CH ₄ and FLOX/B ₂ H ₆ as a Function of Peripheral Zone Gas Temperature for Several Peripheral Mass Fractions	26
10. Schematic Representation of Like-Doublet Element Showing Geometric Factors Affecting Propellant Mixing/Atomization	31
11. Face Pattern of 1/4-Segment Model of Injector A	32
12. Predicted Oxidizer Drop Size (Eq. 8) as a Function of Relative Velocity Difference Between Combustion Gas and Liquid Jet for Several Orifice Diameters and Injection Velocities	35
13. Schematic Representation of Injector A Assembly	37
14. Schematic Representation of Face Pattern of Injector A	39
15. Schematic Representation of Face Pattern of Chamber Compatible C Injector	41
16. Schematic of Optimized Like-Doublet Dual Manifold Injector	44
17. Illustration of Face Pattern and Element Fan Alignment for Optimized Like-Doublet Injector	45
18. Front View Photograph of Five Plates Which Were Diffusion Bonded Together for "Optimized" Like-Doublet Injector Configuration	48
19. Back View Photograph of Five Plates Which Were Diffusion Bonded Together for "Optimized" Like-Doublet Injector Configuration	49
20. Photograph of Optimized Injector Configuration	50
21. Schematic Representation of Reference ($L^* = 40$ -Inches; $\epsilon_c = 3$) Chamber Assembly Showing Segmented Design and Dimensions	54
22. Schematic of Chamber Heat Flux Transducer	56
23. Photograph of Hardware on Test Stand Willie at Propulsion Research Area	57
24. Schematics of Conical Diffuser and Base Bleed Injector Gas Recirculation Suppression Devices Used for Single-Element Cold-Flow Mixing Experiments	63
25. Distribution c^* /Mixing Efficiency as a Function of Fan Inclination Angle (α) and Propellant Momentum Ratio (o/f) for Zero Fan Spacing Single-Element Gas/Liquid Like-Doublet Elements	64

26. Effect of Fan Inclination Angle (α) on Local Propellant Mass Flux Distribution for Zero Fan Spacing Single-Element Gas/Liquid Like-Doublet Element	65
27. Effect of Propellant Momentum Ratio (σ/f) on Local Propellant Mass Flux Distribution for Zero Fan Spacing Single-Element Gas/Liquid Like-Doublet Elements	66
28. Effect of Fan Inclination Angle (α) on Mixing for Candidate D Injector Core Elements	70
29. Effect of Momentum Ratio on Mixing for D Injector Core Single-Element	71
30. Effect of Element Density on Mixing for Injector A Type (Fan Spacing = 0) Like-Doublet Elements	74
31. Effect of Gas Injection on Drop Size for Gas/Liquid Like-Doublet Element	77
32. Effect of Chamber Pressure and Gaseous Fuel Injection on Drop Size for D Injector Core Element	79
33. Effect of Fan Spacing and Inclination Angle on the Mixing Index E_M for Chamber Compatible Single-Element Gas/Liquid Like-Doublet Elements	82
34. Effect of Oxidizer to Fuel Momentum Ratio on E_M for Single-Element Chamber Compatible Gas/Liquid Like-Doublet Elements	83
35. Effect of Fan Spacing and Inclination Angle on the Mixing Index, E_M , for Single-Element Gas/Liquid Like-Doublet Elements	84
36. Fuel and Oxidizer Mass Flux Data for Momentum Ratio (σ/f) = 0.775, α = 15 degrees, S = 0.125 Inch Test	86
37. Fuel and Oxidizer Mass Flux Data for Momentum Ratio (σ/f) = 0.755, α = 15 degrees, S = 0.250 Inch Test	87
38. Fuel and Oxidizer Mass Flux Data for Momentum Ratio (σ/f) = 0.34, α = 0 degrees; S = 0.250 Inch Test	88
39. Effect of Chamber L^* and Chamber Pressure on Performance for Like-Doublet Injector A-1	91
40. Predicted Effect of Chamber L^* on Vaporization c^* Efficiency for FLOX/ $\text{CH}_4(\text{g})$	93
41. Effect of Momentum Ratio and Orifice Diameter Ratio on Performance for A Injector Configurations	94
42. Comparison of Corrected c^* Efficiencies Based on Measurement of Chamber Pressure and Thrust	96
43. Comparison of Hot-Fire Performance Characteristics of A and C Configuration Like-Doublet Injectors	97
44. Effect of Injector Design and Chamber Pressure on Thrust Chamber Heat Transfer Characteristics	99
45. Effect of Mixture Ratio on Thrust Chamber Heat Transfer for Chamber Compatible C Injector	100
46. Comparison of Cold-Flow Predicted and Actual Hot-Fire Performance for A and C Like-Doublet Injectors	103
47. Normalized Mass Flux Profile for Cold-Flow Mixing Test Conducted With Full D Injector	107
48. Performance Characteristics of D Injector Core	108
49. Effect on Peripheral Zone Mixture Ratio on Performance for Optimized Like-Doublet Injector Configuration	110
50. Effect of Peripheral Zone Mixture Ratio on Chamber Heat Flux for Optimized Like-Doublet Injector Configuration	111

51. Effect of Peripheral Zone Mixture Ratio on Chamber Heat Transfer Characteristics for Optimized Like-Doublet Injector	112
52. Effect of Percent Mass Flow to Peripheral Zone on Chamber Heat Transfer for Optimized Like-Doublet Injector	113
53. Comparison of Cold-Flow Predicted and Actual Hot-Fire Performance for A, C, and D Like-Doublet Injectors	115
54. Effect of Element Density on Mixing for Zero Fan Spacing Optimized Like-Doublet Injector	116
55. Effect of Peripheral Zone Element Design, Mixture Ratio, and Percent Mass Flow on Average Cylindrical Chamber Heat Flux for FLOX/CH ₄ (g) Like-Doublet Injector	119

PRECEDING PAGE BLANK NOT FILMED
TABLES

I. Summary of Cold-Flow Test Conditions and Results for Initial Series of Single-Element Mixing Experiments to Define Element Design Criteria for Injector A	61
II. Quantitative Index to Grid Densities in Fig. 26 and 27	67
III. Summary of Cold-Flow Mixing Test Conditions and Results for Single-Element Experiments Conducted to Verify Injector D Core Element Design	69
IV. Summary of Cold-Flow Data Used to Define Element Density Effects on Mixing for Performance Optimized Like-Doublt Elements	73
V. Summary of Drop Size Experimental Test Conditions and Results for Injector A Type Single Element	75
VI. Summary of Atomization Experiment Test Conditions and Results for D Injector Core Element	78
VII. Summary of Cold-Flow Mixing Test Conditions and Results for Single-Element Experiments Conducted to Define Element Design Criteria for Chamber Compatible (Fan Spacing ≠ 0) Elements	81
VIII. Summary of Cold-Flow Mixing Test Conditions and Data for Full-Scale Injectors A-3 and C	102
IX. Summary of Cold-Flow Test Conditions and Data for Optimized Like-Doublt Injector	105

PRECEDING PAGE BLANK NOT FILMED

1.0 INTRODUCTION

The class of propellants known as "space-storable" have received considerable attention in recent years. These propellant combinations, although loosely defined, are characterized by high specific impulse values, high bulk density, hypergolic ignition, overlapping liquid ranges of fuel and oxidizer, and semicryogenic storage temperatures. FLOX or OF₂ as oxidizers with light hydrocarbon fuels are typical examples of such propellant combinations. These propellants are attractive for missions requiring long-term space storage of propellants and high specific impulse. In addition, they may also have application for uprating of existing earth-storable propellant stages wherein higher specific impulse and comparable bulk density are important.

In previous technology programs undertaken with these propellants (FLOX/light hydrocarbons), primary emphasis has been placed on either evaluation of their cooling capabilities (e.g., Ref. 1 and 2) or definition of high-performance injector design criteria (e.g., Ref. 3 and 4). In general, technology studies directed toward systematic simultaneous definition of high performance and injector-chamber compatibility design criteria are lacking for the FLOX/light hydrocarbon propellant combinations.

The work presented herein is the result of a 30-month program of analysis, design, and experiment conducted to relate injector/thrust chamber design parameters to simultaneous attainment of high performance and component compatibility for a FLOX/gaseous methane propulsion system. The performance goal was 99 percent of the theoretical shifting characteristic exhaust velocity at a mixture ratio of 5.25. Design criteria were to be established in such a manner as to allow for subsequent extrapolation of the program results to other advanced gas/liquid propellant combinations and operating conditions.

This work was a follow-on effort to the FLOX/LPG work conducted on contract NAS-11199 (Ref. 3). The effort of the subject program involved the study of two injector types, like-doublet and coaxial. Results of the coaxial injector study, which was an add-on effort to the like-double work, are presented in a separate volume (Ref. 5). This volume describes the portion of the program directed toward evaluation of the like-doublet injector type. It should be noted that the subject work represents the first time that the like-doublet injector pattern has been employed for gas/liquid propellant systems. Propellants were FLOX (82.6% F₂) and ambient temperature gaseous methane. Design conditions were for a sea level thrust of 3000 lbf at a chamber pressure of 500 psia. Passively cooled thrust chamber assemblies, based on currently available technology, were employed throughout the experimental portion of the program.

To accomplish the program objectives, the program effort was apportioned into four basic technical tasks: Task I--Injector and Thrust Chamber Design, Task II--Injector and Thrust Chamber Fabrication, Task III--Performance Evaluation Testing, and Task IV--Data Evaluation and Reporting.

The initial program effort (Task I) was directed toward conducting analytical parametric combustion analyses and cold-flow distribution and atomization experiments with injector element and segment models to support design of injector-thrust

chamber combinations for hot-fire evaluation during Task III. A logic flow diagram for the injector-chamber optimization process is presented in Fig. 1. Initially, an analytical combustion study (Task IA--Parametric Combustion Analysis) was conducted to define the effects of propellant atomization and distribution on performance as a function of chamber geometry/operating conditions for FLOX (82.6% F₂)/CH₄(g). Results from this study, in conjunction with cold-flow distribution and atomization experiments conducted with injector models (Task IB), were used to support design of the hot-fire injectors and thrust chambers (Tasks IC and ID). Prime consideration was directed toward conducting experiments designed to achieve injector chamber compatibility with minimal distribution losses during the Task III experimental effort. To this end, the approach selected was to develop a two-zoned injector with a core region of very high performing elements and a peripheral (or outer) zone of elements which biased mass flux and/or mixture ratio to enhance injector/chamber compatibility. The initial full-scale injector (injector A) was used to optimize performance for the "core" of the "optimized (or two-zoned) injector" (injector D) configuration. Injector concepts B/C were used to provide design criteria for subsequent application to the outer zone elements of injector D so that injector-thrust chamber compatibility could be achieved with only minimal performance losses. The effects of peripheral zone mass and mixture ratio distribution on performance and chamber heat transfer characteristics were studied with the optimized injector configuration (D injector).

Previous programs at Rocketdyne have employed an analogous approach (i.e., use of cold-flow techniques to supplement hot-fire testing) to establish design criteria for both liquid/liquid (Ref. 3 and 6) and gas/liquid (Ref. 7) propellant systems. Thus, this effort was a logical extension of these cold-flow/hot-fire techniques to establish design criteria for the subject program.

Technology developed on this program also represents an extension of the Contract NAS3-11199 (FLOX/LPG) study work to higher pressures (500 instead of 100 psia) and to bi-phase propellant combinations. More importantly, however, results of this program were intended to provide concise and specific criteria for attenuation of chamber heat load which previously has impeded actual predevelopment for FLOX/light hydrocarbon propulsion systems.

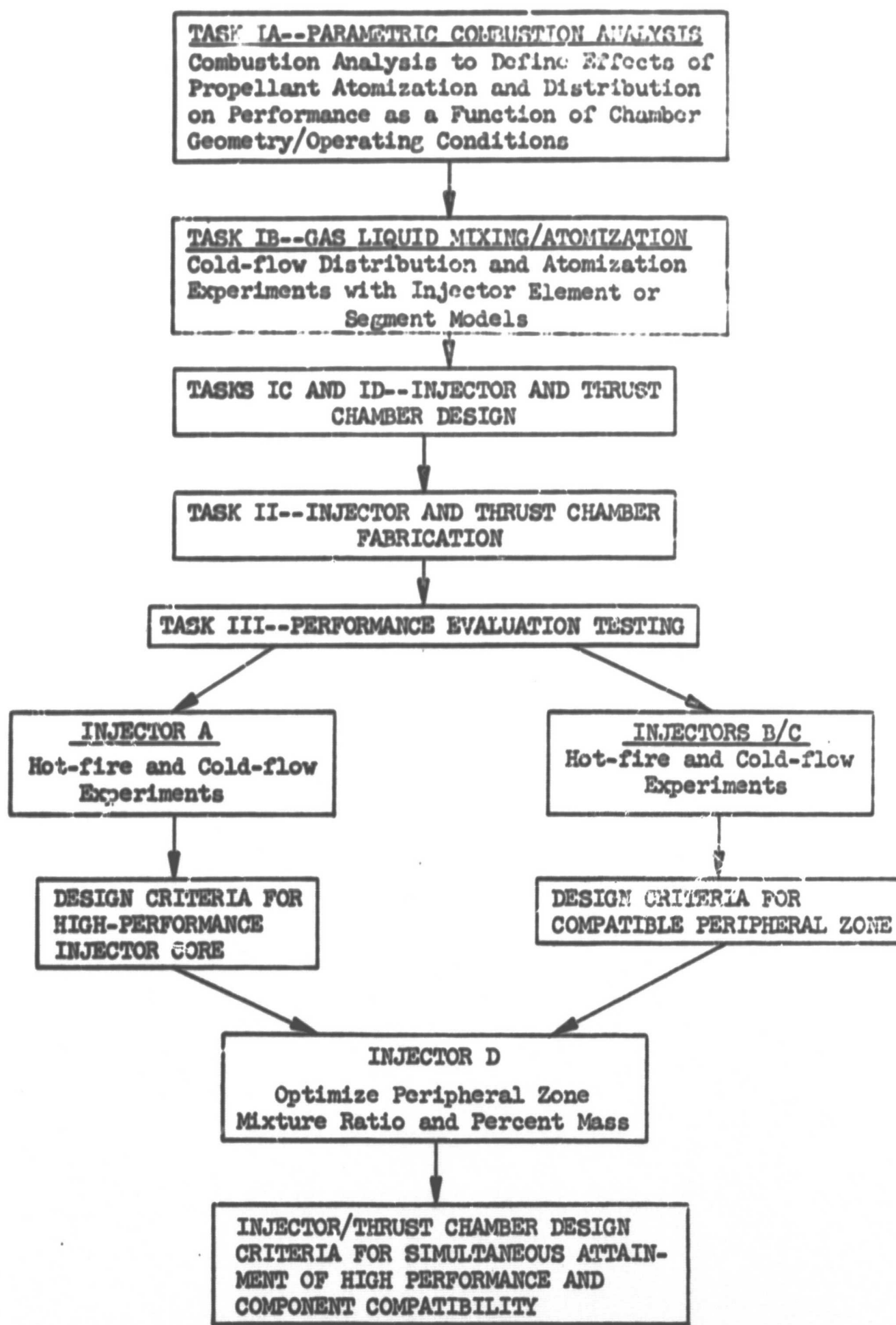


Figure 1. Logic Flow Diagram for Injector-Chamber Optimization Process

PRECEDING PAGE BLANK NOT FILMED

2.0 SUMMARY

This report presents the results of an analytical, design, and experimental program to develop injector-thrust chamber design criteria for simultaneous attainment of high-performance and component compatibility for gas/liquid space storable propellants. The propellant system selected for study was FLOX (82.6% F_2)/ambient temperature gaseous methane. Design conditions were for sea level thrust of 3000 lbf at a chamber pressure of 500 psia. The gas/liquid injector pattern employed (characterized) was the like (self)-impinging doublet. Design criteria were to be established in such a manner as to allow for subsequent extrapolation of the program results to other advanced space storable gas/liquid propellant combinations and operating conditions. The basic premises on which attainment of this program objective was based are the fundamental arguments that: (1) the injector-induced effects of propellant atomization and mixing will predominantly determine the ultimate c^* efficiency, and (2) peripheral zone mass fraction and combustion gas temperature are of primary importance for chamber compatibility for most contemporary space-storable propellants.

This work was a follow-on effort to the FLOX/LPG work conducted on contract NAS3-11199 (Ref. 3). The effort of the subject program involved the study of two injector types, like-doublet and coaxial. Results of the coaxial injector study, which was an add-on effort to the like-doublet work, are presented in separate volume (Ref. 5). The subject work represents the first time that the like-doublet injector pattern has been employed for gas/liquid propellant systems.

The initial program effort was directed toward conducting analytical parametric combustion analyses and cold-flow (mixing/atomization) experiments to support design of injector-thrust chamber combinations for hot-fire evaluation. A Rocketdyne-developed combustion model computer program was used to analytically define performance losses due to incomplete vaporization as a function of the variables affecting vaporization c^* efficiency. The effects of propellant (oxidizer) drop size and chamber geometry (L^* and ϵ_c) were analyzed, as were the secondary effects of chamber pressure and mixture ratio. The effects of propellant mixing/distribution on performance (c^* efficiency) also were evaluated on an analytical basis using simplified stream tube analysis techniques. Results of these analytical studies permitted definition of required atomization, mixing, and distribution characteristics for the hot-fire injectors. Cold-flow mixing and atomization experiments conducted with single-element injector and segment models provided element design criteria for separate "high-performance" and "chamber compatible" hot-fire injector designs (injectors A and C, respectively).

Three full-scale injectors were designed, fabricated, and hot-fire tested during this program. The first (injector A) was designed primarily for high performance in terms of having specific element features that promote efficient mixing and atomization. The second (injector C) was designed to provide design criteria for element orientation so that injector-thrust chamber compatibility could be achieved with only minimal performance losses. The final design, an "optimized configuration," contained separately manifolded high-performance core and chamber-compatible peripheral zones. Design of the high-performance core region was based on cold-flow and hot-fire experiments conducted with the A injector configuration. The

peripheral zone design, which was intended to provide injector-chamber compatibility with minimal performance losses, was based on cold-flow and hot-fire data generated from the C injector. All of the injector designs were based on current design principles supported by cold-flow distribution and atomization experiments conducted using injector segment models. All of the full-scale hot-fire injectors were fabricated employing recently developed diffusion bonding technology. This fabrication technique was employed because it permitted placement of significantly more like-doublet elements in the fixed injector face area than conventional radial-fed or ring-type injectors.

Element design and/or operating parameters (fan inclination angle, propellant momentum ratio, etc.) for the A (high-performance, zero fan spacing element) injector were optimized in terms of mixing uniformity by use of cold-flow mixing experiments conducted employing single elements. Cold-flow mixing tests conducted with a single element, the A injector, and a 1/4-segment model injector with an element density 1-1/2 times that of the A injector were used to define element density effects on overall injector mixing uniformity. Information from these experiments were employed to design the core of the final optimized injector configuration. Hot-fire testing of both the A and D injectors confirmed the cold-flow mixing results upon which their designs were based.

Cold-flow mixing experiments also were conducted with single-element injector models to define element design/operating parameters for the C injector. The fuel and oxidizer fans for these elements were intentionally displaced (i.e., fan spacing $\neq 0$) to provide a fuel-rich region adjacent to the wall for injector-chamber compatibility. Element design/operating parameters optimized (in terms of mixing/chamber wall mixture ratio bias) were fan spacing, fan inclination angle, and propellant momentum ratio. Hot-fire testing of the C injector confirmed the cold-flow results in that performance and heat transfer characteristics of the C injector elements were adequate for its designed application (i.e., to provide design criteria for the elements in the peripheral zone of the D injector).

Hot-fire tests were conducted with the optimized injector configuration to define its performance and chamber heat transfer characteristics as a function of peripheral zone mixture ratio and mass function. Peripheral zone mixture ratio was varied from 3 to 5.5 with 30-percent mass flow to the periphery. In addition, the peripheral zone mass flow was varied from 15 to 40 percent at a peripheral zone mixture ratio of approximately 3.75. The overall mixture ratio and chamber pressure were held constant at 5.25 and 500 psia for all of these tests. The performance in the reference chamber ($L^* = 40$ in.; $\epsilon_c = 3$) at nominal design conditions ($P_c = 500$ psia; $MR = 5.25$, sea level thrust = 3000 lbf) was 97 to 98 percent of the shifting equilibrium value with injector/thrust chamber compatibility. A stability rating test conducted with the D injector indicated that it is marginally unstable; however, it appears that the injector could be made stable with minimal effort. Results of this study provide concise and specific criteria for attenuation of chamber heat load which previously have impeded actual predevelopment for FLOX/light hydrocarbon propulsion systems.

The overall success of the program was made possible by data from the cold-flow modeling tests which provided a clear physical description of both the injected

gas and liquid flow patterns. One of the most important achievements of the program has been the development of the cold-flow modeling experimental apparatus and techniques. These methods have now been advanced so that flow distribution and propellant mixing measurements for gas/liquid injectors can now be made on a par with those developed earlier for characterization of liquid/liquid injectors. These techniques and many of the parametric data are applicable to any gas/liquid propellant combination, not only to FLOX/CH₄(g) but, also, for example, to LOX/GH₂ or LOX/propane (g).

PRECEDING PAGE BLANK NOT FILMED

3.0 ANALYTICAL PARAMETRIC COMBUSTION ANALYSIS

Rational design of rocket engine components using fundamental engineering principles requires a basic understanding of combustion and its relationship to the physical processes which control it. For most liquid/liquid or gas/liquid bipropellant systems, of which FLOX (82.6% F₂)/gaseous methane is typical, c* efficiency (performance) is affected by both propellant vaporization and mixing. In general, these two processes can be considered independently (Ref. 3, 6, and 7) in their effects on c* efficiency. A close approximation of overall c* efficiency can be obtained from:

$$\eta_{c^*} = \eta_{c^*, \text{vap}} \times \eta_{c^*, \text{mix}} \quad (1)$$

where

η_{c^*} = the overall c* efficiency

$\eta_{c^*, \text{vap}}$ = the c* efficiency which would be obtained if propellant mixing were completely uniform, and the only losses were caused by incomplete propellant vaporization

$\eta_{c^*, \text{mix}}$ = the c* efficiency which would be obtained if propellant vaporization were entirely complete, and the only losses were caused by nonuniform propellant mixing

Analysis of the parameters which affect c* efficiency is, therefore, logically divided into considerations of $\eta_{c^*, \text{vap}}$ and $\eta_{c^*, \text{mix}}$.

An analytical parametric combustion study was conducted to support definition of injector and thrust chamber design requirements for FLOX (82.6% F₂)/CH₄(g). Performance calculations were made using the vaporization rate-limited and distribution-limited computer programs employed during Contract NAS3-11199 (Ref. 3). The basic objectives of this study were to determine the effect of propellant atomization and mixing/distribution on performance as a function of chamber geometry and operating conditions. The propellant mixing analysis included definition of peripheral mass and mixture ratio distribution zoning on performance.

3.1 PROPELLANT VAPORIZATION

The effects of incomplete propellant vaporization on c* efficiency can be quantitatively studied by means of an analytical propellant combustion model developed at Rocketdyne several years ago by Lambiris, Combs, and Levine (Ref. 8). This combustion model exists in the form of a Fortran IV Computer Program written for the IBM-360 computer. To determine the degree of propellant vaporization, the combustion model takes into consideration:

1. Compressible combustion gas flow with mass and energy addition
2. Droplet drag in the accelerating combustion gas flow
3. Droplet vaporization with convective heat transfer from the hot combustion gas

These factors result in an analytical description of the "bootstrap" combustion processes typical of rocket engines. The model calculates axial profiles of chamber pressure, combustion gas velocity, vaporization from a range of droplet sizes corresponding to the droplet size distribution produced by the injector, droplet velocities, and the overall percentage of fuel and/or oxidizer vaporized.

The combustion model takes into account the compressible flow of combustion gases by the normal gas-dynamic equations; taking into account the effects of mass and energy addition from the vaporizing and reacting propellant(s).

Droplet drag, for the distribution of droplet sizes produced by the injector, is accounted for by the scalar equation shown below:

$$\frac{dV_D}{dt} = \frac{3}{4} \times \frac{C_D \rho_g (V_g - V_D)^2}{\rho_L D} \quad (2)$$

where

V_D = droplet velocity, ft/sec

t = time, seconds

C_D = drag coefficient (a function of droplet Reynolds number)

ρ_g = combustion gas density, lb/ft³

ρ_L = droplet liquid density, lb/ft³

V_g = combustion gas velocity, ft/sec

D = droplet diameter, feet

Droplet vaporization is accounted for by an equation similar to:

$$\frac{d(D^2)}{dt} = k' = \frac{144 \times 8\lambda_g}{\rho_L C_p V} \ln \left[1 + \frac{C_p V}{\Delta H_v} (T_g - T_v) \right] \left(1 + 0.6 \Pr^{1/3} \Re^{1/2} \right) \quad (3)$$

where

k' = droplet vaporization constant, in.²/sec

D = droplet diameter

λ_g = combustion gas thermal conductivity

ρ_L = liquid density

C_{p_v} = vaporized propellant heat capacity
 ΔH_v = liquid propellant heat of vaporization
 T_g = combustion gas temperature
 T_L = liquid propellant boiling temperature
 Pr = Prandtl Number for the combustion gas
 ρ_g = combustion gas density
 Re = Reynolds Number for combustion gas

For computer solution of Eq. 3, the application is more complex. The simplified expression presented above shows the effects of various physical parameters on droplet vaporization rate. The last bracketed term on the right-hand side of Eq. 3 represents the effects of forced convection on droplet vaporization, and the remainder of the terms represent the effects of propellant physical properties and combustion gas properties on droplet vaporization rate.

For the FLOX/CH₄(g) propellant combination, incomplete propellant vaporization (at an injected mixture ratio equal to that at the theoretical optimum c^* value) can degrade c^* performance in two ways: (1) it reduces the total amount of combustion gas produced, and (2) it can make the burned gas mixture ratio different from the injected mixture ratio, thereby affecting the temperature, molecular weight, etc., of the burned gas. Both of these effects have been included by Priem (Ref. 9) in the following equation which allows the determination of $\eta_{c^*,vap}$ from parameters calculated by the combustion model computer program:

$$\eta_{c^*,vap} = \left(\frac{\dot{w}_B}{\dot{w}_I} \right) \left(\frac{c^* B}{c^* I} \right) \quad (4)$$

where

\dot{w}_B = flowrate of burned gas at the geometric throat
 \dot{w}_I = injection flowrate of fuel plus oxidizer
 $c^* B$ = theoretical c^* corresponding to the composition of the burned gas at the geometric throat
 $c^* I$ = theoretical c^* corresponding to the injection mixture ratio

This computerized combustion model, the general nature of which is described in very brief form by Eq. 1 through 4, was used to parametrically investigate the effects of design and operating variables on $\eta_{c^*,vap}$ for the FLOX (82.6% F₂)/CH₄(g) propellant combination.

3.1.1 Propellant Drop Size and Chamber Geometry Effects

The two most important variables affecting the vaporization c^* efficiency, $\eta_{c^*, \text{vap}}$, are propellant drop size distribution and combustion chamber geometry.

A like-doublet (Ref. 6) drop size distribution was employed for the combustion model analysis. From Eq. 3, it can be seen that the residence time required to completely vaporize a droplet is proportional to the square of the droplet diameter. Equally important, the geometry of the combustion chamber dictates the total residence time during which the droplets must vaporize. If this residence time is too short, the droplets will not be completely vaporized.

The effect of the mean propellant drop size and chamber geometry on characteristic velocity efficiency due to vaporization, $\eta_{c^*, \text{vap}}$, is shown parametrically in Fig. 2 for FLOX (82.6% F_2)/CH₄(g). Curves of $\eta_{c^*, \text{vap}}$ versus initial propellant mean drop size are shown for conventionally shaped thrust chambers (see Fig. 3) having characteristic lengths of 15, 30, and 60 inches. The solid lines ($A_c/A_t = 2$) and dashed lines ($A_c/A_t = 4$) define the effect of chamber contraction ratio at any given L^* value. These calculations are for a chamber pressure of 500 psia (the design value) and 5.75 mixture ratio.

Figure 2 shows that when propellant mean drop size is small, the effects of chamber geometry are generally attenuated. Conversely, when initial propellant drop sizes are large, chamber geometry effects become pronounced and c^* efficiency becomes much more sensitive to specific geometric features such as chamber length and contraction ratio. For a given initial drop size and chamber L^* , increase in vaporization efficiency can be effected by reduction of the contraction area ratio (corresponding to an increase of physical chamber length). This (contraction ratio) effect is negligible at the high-performance level ($\eta_{c^*, \text{vap}} \geq 95$); however, it becomes significant when $\eta_{c^*, \text{vap}}$ drops below 95.

Equation 3 is an implicit expression showing that propellant vaporization efficiency is governed by droplet acceleration and heating by the high-temperature combustion gas. For thrust chambers having contraction area ratios greater than about 2, combustion gas flow can be considered incompressible; therefore, chamber L^* is a good index of combustion gas residence time. From continuity, combustion gas velocity for the 2:1 chamber will always be higher than that for the 4:1 chamber. Higher combustion gas velocities will generally be accompanied by an increased velocity lag between combustion gas and propellant droplets. The increased velocity lag between combustion gas and droplet for the smaller contraction area ratio chambers will tend to result in longer residence time for the droplets. The higher relative velocity between the combustion gas and propellant droplets also will tend to enhance convective heating and resultant droplet vaporization.

The combustion model results presented in Fig. 2 indicate that if propellant drop sizes similar to those obtained during the Contract NAS3-11199 FLOX/LPG (Ref. 3) study (i.e., ~75 microns) are induced during the current program, the program performance goal (99-percent c^* efficiency at optimum mixture ratio) could be attained in either a 2 or 4:1 contraction ratio chamber of approximately 30 in. in L^* . Two important facts should be kept in mind when using Fig. 2 to estimate performance

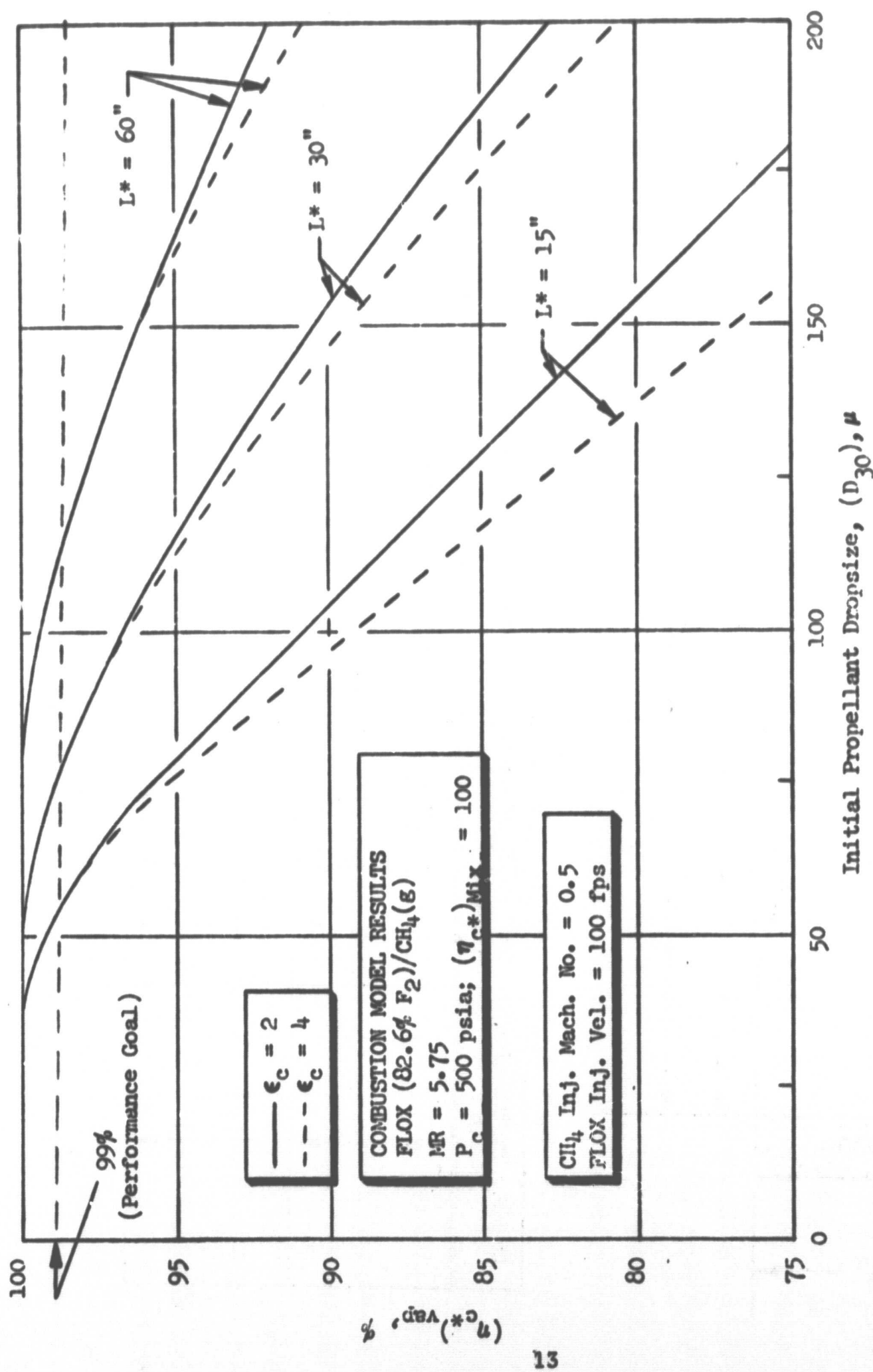
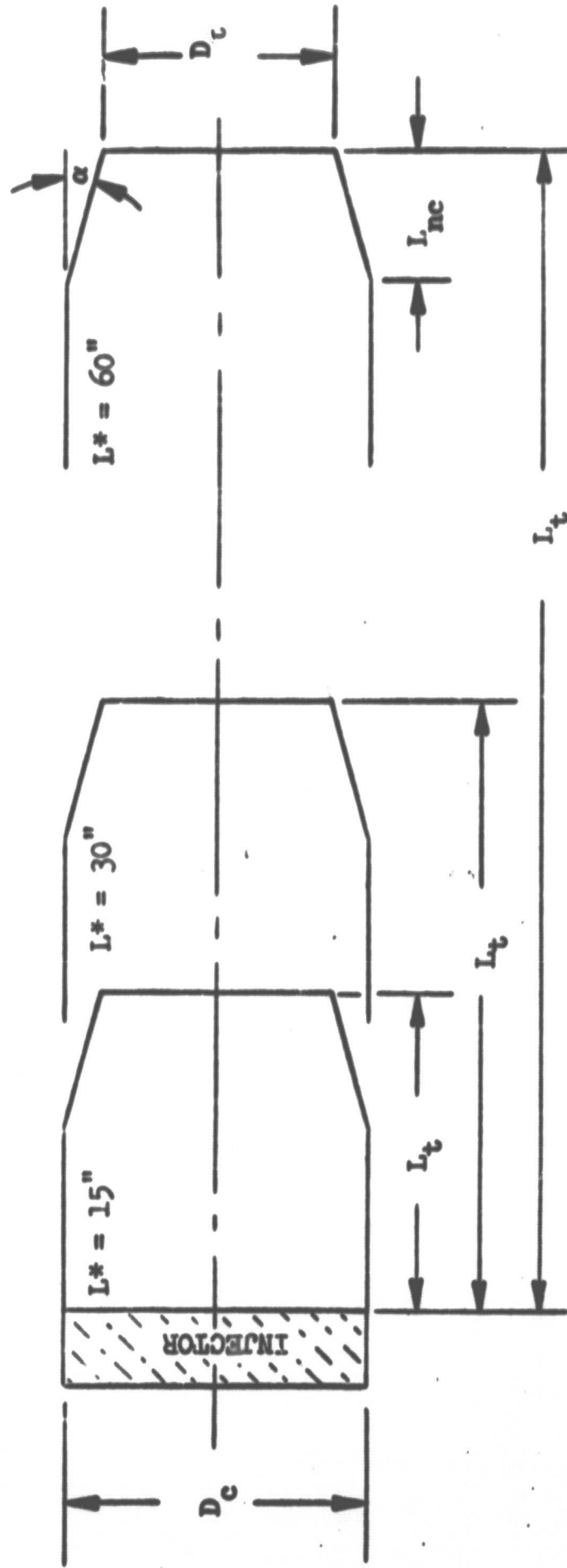


Figure 2. Effect of Propellant Drop Size and Chamber Geometry on η_c^* Efficiency (Due to Vaporization) for FLOX/CH₄ (g)



Chamber Contraction Ratio	L_c^* inches	D_c , Inches	D_t , Inches	L_t , Inches	L_{nc} , Inches	α , Degrees
2	15	3.175	2.245	7.87	1.41	18.3
	30			15.37		
	60			30.37		
4	15	4.490		4.815	2.55	23.8
	30			8.565		
	60			16.065		

Figure 3. Simplified Schematics of Thrust Chamber Geometries Considered for Combustion Model Analysis (Chamber Geometries are Similar to Those Considered for Hot-Fire Portion of Program)

(c^* efficiency). First, the mixing-limited c^* efficiency is assumed to be 100. Second, as was noted during the previous contract (Contract NAS3-1199), for given injection conditions (orifice diameter and injection velocity, etc.) mean propellant drop sizes may be larger in a 4:1 contraction ratio chamber than in a 2:1 contraction ratio chamber because of combustion gas velocity effects of secondary atomization. The results shown in Fig. 2 do not explicitly account for these phenomena.

3.1.2 Chamber Pressure Effects

The effect of chamber pressure on c^* efficiency as influenced by vaporization is shown in Fig. 4. The curves are for a common mixture ratio (MR = 5.75) and chamber characteristic length, L^* , of 30 in. Curves of $\eta_{c^*,vap}$ versus drop size are shown for chamber pressures of 250, 500, and 750 psia. The solid lines ($A_c/A_t = 2$) and dashed lines ($A_c/A_t = 4$) define the effect of contraction ratio at the three chamber pressure values. The effect of chamber pressure on $\eta_{c^*,vap}$ is attenuated when propellant drop size is small, while both pressure and geometry effects become more pronounced with larger drop sizes. Improved vaporization c^* efficiency with increasing chamber pressure is primarily due to increased combustion gas density*. Chamber pressure primarily effects combustion gas density with only secondary effects on combustion temperature, etc. Increased combustion gas density (Eq. 3) results in an increase in convective heating of the droplets, but also tends to accelerate the droplets because of a corresponding increase in drag force on the droplets. The net effect, however, is toward improved vaporization efficiency for a given mean drop size, particularly when drop sizes are initially large and lag effects become more pronounced.

3.1.3 Mixture Ratio Effects

The effect of mixture ratio on c^* efficiency (due to vaporization) for FLOX/CH₄(g) is shown in Fig. 5. $\eta_{c^*,vap}$ is shown plotted as a function of mixture ratio for several drop sizes in this figure. The curves are for the design chamber pressure of 500 psia and a constant thrust chamber geometry ($L^* = 30$ in.; $\epsilon_c = 2$). The effect of mixture ratio is small when initial propellant drop size is small (≤ 100 microns) and, conversely, becomes more pronounced when initial drop sizes are large. Minimum vaporization c^* efficiency occurs near the theoretical optimum c^* mixture ratio of 5.75. Oxidizer drop sizes of between 50 and 100 microns are expected; therefore, mixture ratio effects on vaporization efficiency for the given spray drop size distribution were expected to be small during the experimental portion of the program. Again, it should be noted that this analysis precludes the possible influence of mixture ratio upon the spray drop sizes.

An explanation of mixture ratio effects on $\eta_{c^*,vap}$ can be aided by reference to Fig. 6 in which $(\eta_{c^*})_{vap}$ is shown plotted as a function of mixture ratio for a nominal drop size of 150 microns. The contributing product terms, which allow for calculation of $(\eta_{c^*})_{vap}$ from the combustion model output, are shown as dashed lines in this figure. The contributing terms are defined in Eq. 4. $(\eta_{c^*})_{vap}$

*It should be noted that these parametric curves do not reflect the influences of chamber pressure on the spray drop sizes.

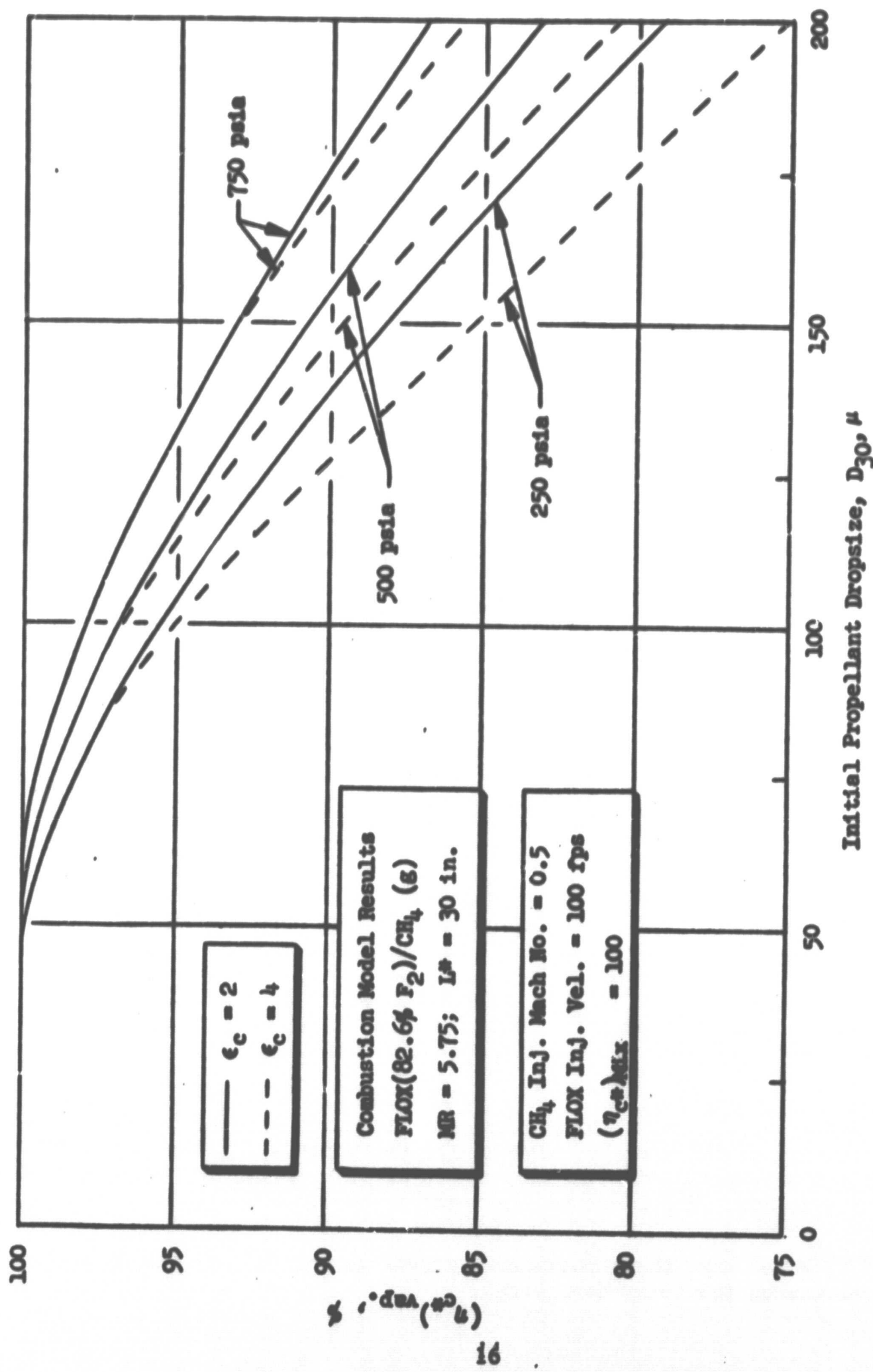


Figure 4. Effects of Initial Propellant Drop Size and Chamber Contraction Ratio on c^* Efficiency (Due to Vaporization) for FLOR/CH₄ (g) at Several Chamber Pressures

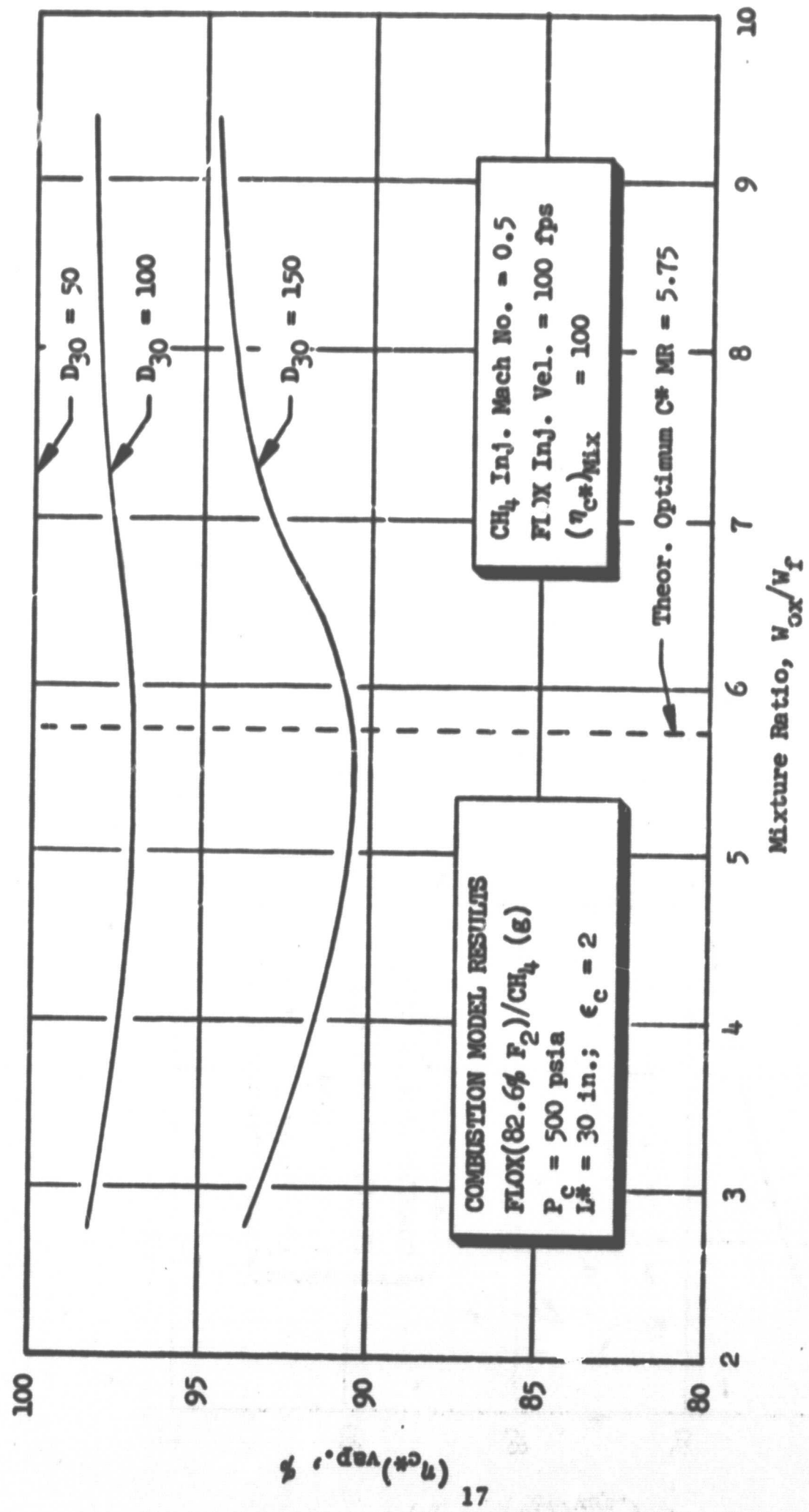


Figure 5. Effects of Mixture Ratio and Initial Propellant Drop Size on c^* Efficiency (Due to Vaporization) for FLOX/CH₄ (g)

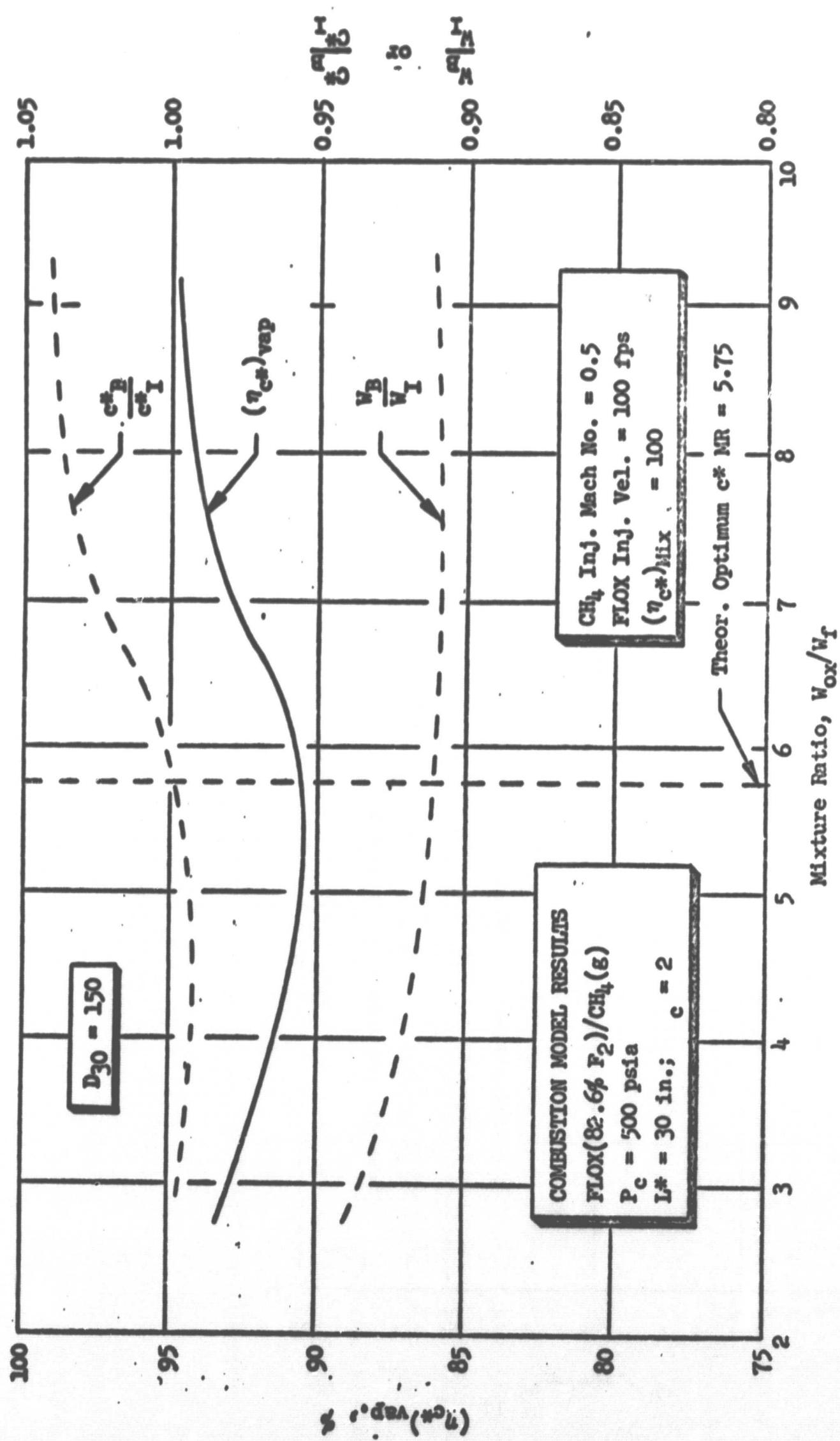


Figure 6. Effect of Mixture Ratio on c^* Efficiency (Due to Vaporization), Fraction of Injected Propellants Burned, and the Burned-to-Injected Mixture Ratio

increases with both increasing and decreasing mixture ratio relative to the theoretical optimum c^* value of 5.75. $(\eta_{c^*})_{vap}$ increases with decreasing mixture ratio primarily because the fraction of propellant burned, (\dot{w}_B/\dot{w}_I) increases while (c^*B/c^*_I) remains essentially constant. Vaporization c^* efficiency increases with increasing mixture ratio because (c^*B/c^*_I) increases while the fraction of propellant burned remains nearly constant.

3.1.4 Other Variables

The effect of other potentially significant variables were examined to assess their effect on vaporization efficiency for FLOX/CH₄(g). Specific areas investigated included the effect of initial droplet injection velocity, initial vaporization conditions, and specific input variables in the combustion model itself.

The initial droplet injection velocity was perturbed by a factor of 3 to determine its effect on the resultant propellant vaporization when all other factors (including drop size) are held constant. Generally, propellant vaporization is increased at lower initial injection velocities. This results from a longer residence time and in an increased convective heat transfer rate as the drops are gradually accelerated by the combustion gases. Although lower initial droplet velocity generally gives increased vaporization c^* efficiency, low initial droplet velocity and efficient atomization are contradictory in nature for the like-doublet element under study. High propellant injection velocities are required for efficient atomization (i.e., lower mean drop size) and this effect will usually far outweigh the potential benefits of reduced initial droplet velocity for fixed values of mean drop size.

An assumption made in the one-dimensional combustion model program input is the amount of combustion which occurs within the initial injection region. This is required to arrive at a nearly one-dimensional region and eliminate calculations in the grossly nonuniform injection region (Ref. 10) immediately adjacent to the injector face. It is usually assumed that 10 percent of the propellants have vaporized and reacted within 1 in. of the injector face. This initial condition has proved adequate and permits good correlation with observed experimental results (e.g., Ref. 3, 6, and 7). To assess the effect of variations in this assumption, combustion model calculations were conducted assuming that 5, 10, and 20 percent, respectively, of the FLOX was vaporized at the start of the analysis. These variations were found to have an insignificant influence on calculated performance. Performance variation due to assumption of 5 or 20 percent initial propellants vaporized instead of 10 percent was $< \pm 0.5$ percent in the range of drop size ($D_{30} \leq 200$) and L^* (15 in. to 60 in.) considered. Effects of injection velocity and percent of propellants initially reacted were only significant when the propellant drop size is very large or when geometric restrictions favored lower performance.

Other parameters investigated were the effect of drop size distribution about the median value, physical properties variation with temperature and pressure, inclusion or exclusion of propellant sensitive heat capacity, and variations of gas and film properties. Again, these variables were of secondary importance and significant only when conditions favored a generally reduced vaporization efficiency (i.e., larger initial drop size and small chamber L^* geometry). This

analysis disclosed that chamber geometry and initial propellant drop size were of primary importance, and that the other variables were of secondary significance.

3.2 PROPELLANT DISTRIBUTION/MIXING

The effect of propellant mass and mixture ratio distribution on performance is considered to be of equal importance to the vaporization process. In general, regardless of the injector type or propellant combination, uniform mixing is a prerequisite for high combustion/c* efficiency. In the absence of uniform mass and mixture ratio distribution, local striated fuel and oxidizer-rich regions will persist throughout the rocket chamber. Because of the short axial dimensions associated with rocket chambers, turbulent mixing and diffusion are relatively ineffective in equilibration of propellant concentration (Ref. 10 through 14). Consequently, the c* potential will be largely dependent on the initial distribution of fuel and oxidizer at the injector end of the chamber. Hence, if by cold-flow techniques the mass and mixture ratio can be determined for local regions within the chamber, the mixing efficiency can be determined by application of a simple streamtube model.

The general features of the streamtube mixing model permit analytical consideration of an idealized rocket engine composed of N imaginary rocket chambers forming individual, isolated, streamtubes within the main chamber. Each streamtube at its own mass and mixture ratio is allowed to expand isentropically through the chamber and nozzle without heat or mass transfer to adjacent streamtubes. Complete vaporization and combustion of the propellants is assumed. The resulting overall c* efficiency as limited by mixing ($\eta_{c^*,\text{mix}}$) is determined by summation of individual mass weighted c* contributions of each individual streamtube and comparing the total to that theoretically attainable at the injected mixture ratio.

Correction factors for changes in specific heat ratio as a function of mixture ratio may be applied. In general, however, the effect of γ variation on the sonic point for each individual station can be neglected (Ref. 6) and the mixing c* efficiency can be expressed simply as:

$$\eta_{c^*,\text{mix}} = \frac{\sum_i^n M F_i c^*_i}{c^*_{\text{theo}}} \quad (5)$$

where

$M F_i$ = the mass fraction in the individual stream being considered

c^*_i = theoretical c* corresponding to the mixture ratio of the local stream

c^*_{theo} = theoretical c* corresponding to the overall mixture ratio

As shown by the above equation, $(\eta_{c^*})_{\text{mix}}$ is simply the sum of the mass weighted c* contributions of each individual stream tube divided by the c* theoretically attainable at the overall injected mixture ratio.

The mixing quality can be expressed by an index, E_m , which defines the mass weighted deviation of local mixture ratio from initially injected overall mixture ratio. The index, E_m , was developed by Rupe (Ref. 15) and is defined below:

$$E_m = \left[1 - \left(\sum_i^N MF_i \frac{(R - r_i)}{R} + \sum_i^N MF_i \frac{(R - \bar{r}_i)}{R - 1} \right) \right] 100 \quad (6)$$

where

E_m = mixing index

MF_i = mass fraction in the stream tube

R = ratio of total oxidizer mass to total oxidizer and fuel mass

r_i = ratio of oxidizer mass to total oxidizer and fuel mass in an individual stream tube for $r_i < R$

\bar{r}_i = ratio of oxidizer mass to total oxidizer and fuel mass in an individual stream tube for $r_i > R$

The foregoing expression for the distribution index is not universal because it is also functionally related to the injected mixture ratio. The c^* efficiency due to propellant distribution, $\eta_{c^*, mix}$, is a function of both the distribution index, E_m , and the initially injected mixture ratio.

3.2.1 Propellant Mixing Effects

The actual relationship between E_m , MR, and the resultant mixing c^* efficiency is shown in Fig. 7 for the FLOX/CH₄(g) propellant combination considered in this study. Mixing-limited c^* efficiency is shown plotted as a function of E_m for various values of mixture ratio. It should be noted that the basis of constant mixture ratio would be more correctly expressed as bands because, even at a constant mixture ratio, $\eta_{c^*, mix}$ is not uniquely related to the E_m index. Analysis and verification experiments indicate, however, that the band width is normally narrow for most injector-produced spray distribution and the actual error introduced by use of single curves is negligible. The curves illustrated in the referenced figure can be used directly to assess the mixing-limited c^* efficiency of a given injector for which E_m is known. In practice, however, it is more accurate and often easier to derive an expression for $\eta_{c^*, mix}$ directly from cold-flow experimental data by utilization of the basic $\eta_{c, mix}$ expression of Eq. 5. The index, E_m , is useful, however, in that it permits a more generalized approach to performance analysis because it permits $\eta_{c^*, mix}$ estimation for any injector in which the same propellants are used. In practical use, the figure permits specific estimation of the required injector distribution index E_m for a given target level of mixing efficiency, $\eta_{c^*, mix}$, at any desired operating mixture ratio.

In general, performance losses due to nonuniform propellant mass and mixture ratio distribution are substantially larger for FLOX/light hydrocarbon systems than for

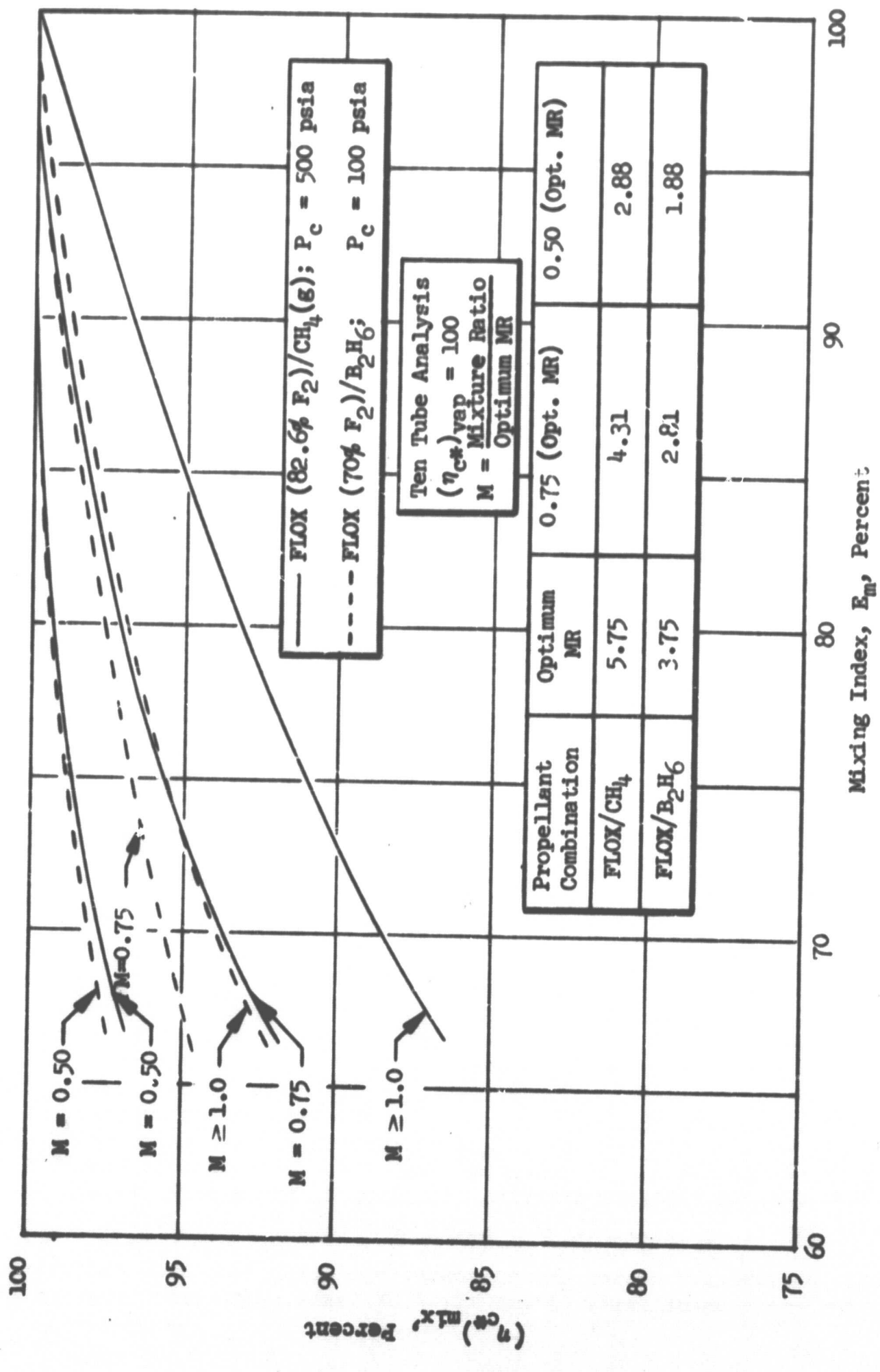


Figure 7. Predicted Effect of Propellant Mixing on Performance for FLOX/CH₄ (g) and FLOX/B₂H₆ (Analytical Results)

most propellant combinations. This is caused by the relatively rapid decrease in theoretical characteristic exhaust velocity with increasing or decreasing mixture ratio around the optimum value for FLOX/light hydrocarbon systems as compared to other propellant combinations. Consequently, to attain high performance with FLOX/CH₄(g), careful consideration must be given to injector design variables that influence propellant distribution.

A cursory analysis was conducted to define performance losses due to distribution for another space-storable propellant combination (FLOX/B₂H₆) and to compare these losses with those for FLOX/CH₄. Results of this analysis are also presented in Fig. 7. (FLOX/B₂H₆ was chosen for comparison because of the extensive work that has been conducted with this propellant combination by JPL.) Note that performance losses at optimum mixture ratio (and given E_m) are substantially greater for FLOX/CH₄ than for FLOX/B₂H₆. These characteristics are related to the general shape of the theoretical c* curves as a function of mixture ratio.

Figure 7 permits determination of the required injector produced distribution index (E_m) for a given level of (η_{c*})_{dist}, at any desired operating mixture ratio. As indicated, an E_m value of approximately 96 (assuming vaporization c* efficiency = 100) will be required to meet the performance objectives of this program (99-percent c* efficiency at optimum mixture ratio). Uniform mixture ratio distribution is essential for high c* efficiency at optimum mixture ratio.

3.2.2 Mixture Ratio Zoning Effects

The above suggests that performance losses due to propellant mass and mixture ratio zoning for injector-chamber compatibility will be substantially greater for FLOX/CH₄ than for most propellant combinations. A cursory analysis was conducted to define performance losses (due to distribution) as a function of peripheral conditions for FLOX/CH₄, and to compare these losses with those for another space-storable propellant combination (FLOX/B₂H₆).

Mixing-limited c* efficiency is shown plotted as a function of percent mass in the peripheral zone for several peripheral mixture ratios in Fig. 8. Curves are presented for both FLOX/CH₄ and FLOX/B₂H₆. The efficiency shown was calculated as follows:

$$(\eta_{c*})_{\text{mix}} = \frac{c^*}{c^*_{\text{optimum}}} \quad (7)$$

where

$$c^* = (MF)_p (c^*)_p + (MF)_c (c^*)_c$$

$$c^*_{\text{optimum}} = \text{theoretical } c^* \text{ at optimum mixture ratio (optimum mixture ratio = mixture ratio at maximum theoretical } c^*)$$

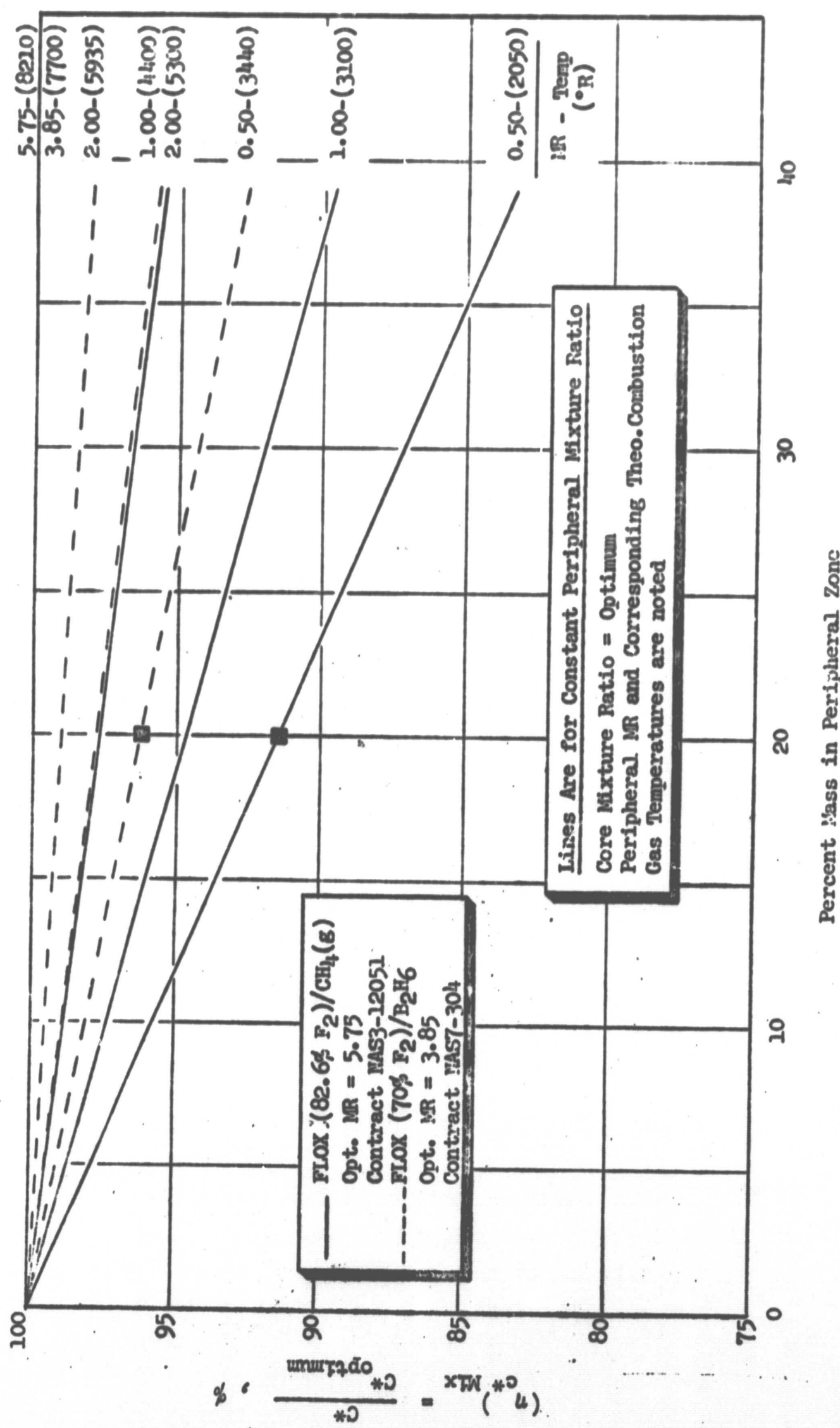


Figure 8. Effect of Peripheral Zone Mass and Mixture Ratio on Characteristic Velocity Efficiency (Due to Distribution) for FLOX/CH₄ and FLOX/B₂H₆ (Analytical Results)

and

MF = mass fraction of propellant

Subscripts

p = peripheral zone

c = core region

As is noted in Eq. 7, the chamber was divided into two sections (the core region and peripheral zone) for this analysis. Values of (η_{c*}) shown in Fig. 8 are for the case of a constant core mixture ratio equal to the optimum value. Use of this core mixture ratio will result in the maximum delivered c^* (neglecting vaporization effects). Solid lines are for FLOX/CH₄; dashed lines are for FLOX/B₂H₆. Peripheral mixture ratio and corresponding theoretical combustion gas temperature (R) are noted.

In general, performance decreases linearly (at constant peripheral mixture ratio) with increasing mass fraction in the periphery for both propellant combinations. The performance decrement at constant mass fraction increases with decreasing peripheral mixture ratio (increasing propellant maldistribution). For a given peripheral mass fraction and mixture ratio, distribution losses are substantially greater for FLOX/CH₄ than for FLOX/B₂H₆. For example, at a peripheral percent mass and mixture ratio of 20 and 0.5, respectively, $(\eta_{c*})_{\text{mix}}$ is 96.2 for FLOX/B₂H₆ and 91.5 for FLOX/CH₄. Performance losses are 4.7 percent greater for FLOX/CH₄.

The above method of comparing distribution losses between propellant combinations for given peripheral conditions is somewhat misleading. A more reasonable comparison of performance losses for "equivalent peripheral conditions" would be to compare performance losses at equal peripheral mass fractions and gas temperatures. A cross plot of the curves in Fig. 8 is presented in Fig. 9 for this purpose. (η_{c*}) is plotted versus the peripheral zone gas temperature for several peripheral mass fractions in this figure. Figure 9 reveals that, to match the critical chamber wall conditions (MF = 20; gas temperature = 3440 R) of FLOX/B₂H₆ considered in the above example, with FLOX/CH₄ only a 0.9 percent greater performance loss, $(\eta_{c*})_{\text{mix}} = 95.3$ is realized. A peripheral mixture ratio of ~1.1 (FLOX/CH₄) would be required as compared to 0.5 (FLOX/B₂H₆). In general, it appears that performance losses for equivalent peripheral mass fractions and gas temperatures for FLOX/CH₄ are not substantially greater than for FLOX/B₂H₆.

It should be pointed out that the preceding cursory analysis does not consider differences in chemical species in the peripheral zone. The analysis is based on the premise that peripheral mass fraction and gas temperature are of primary importance for chamber compatibility.

Careful examination of Fig. 7 and 9 revealed that attainment of the performance goal (99-percent c^* efficiency at optimum mixture ratio), while attaining injector-chamber compatibility, would require careful design of the injector. It was expected that sufficiently good atomization could be achieved so that vaporization losses would be minimal, but design criteria to limit distribution losses to

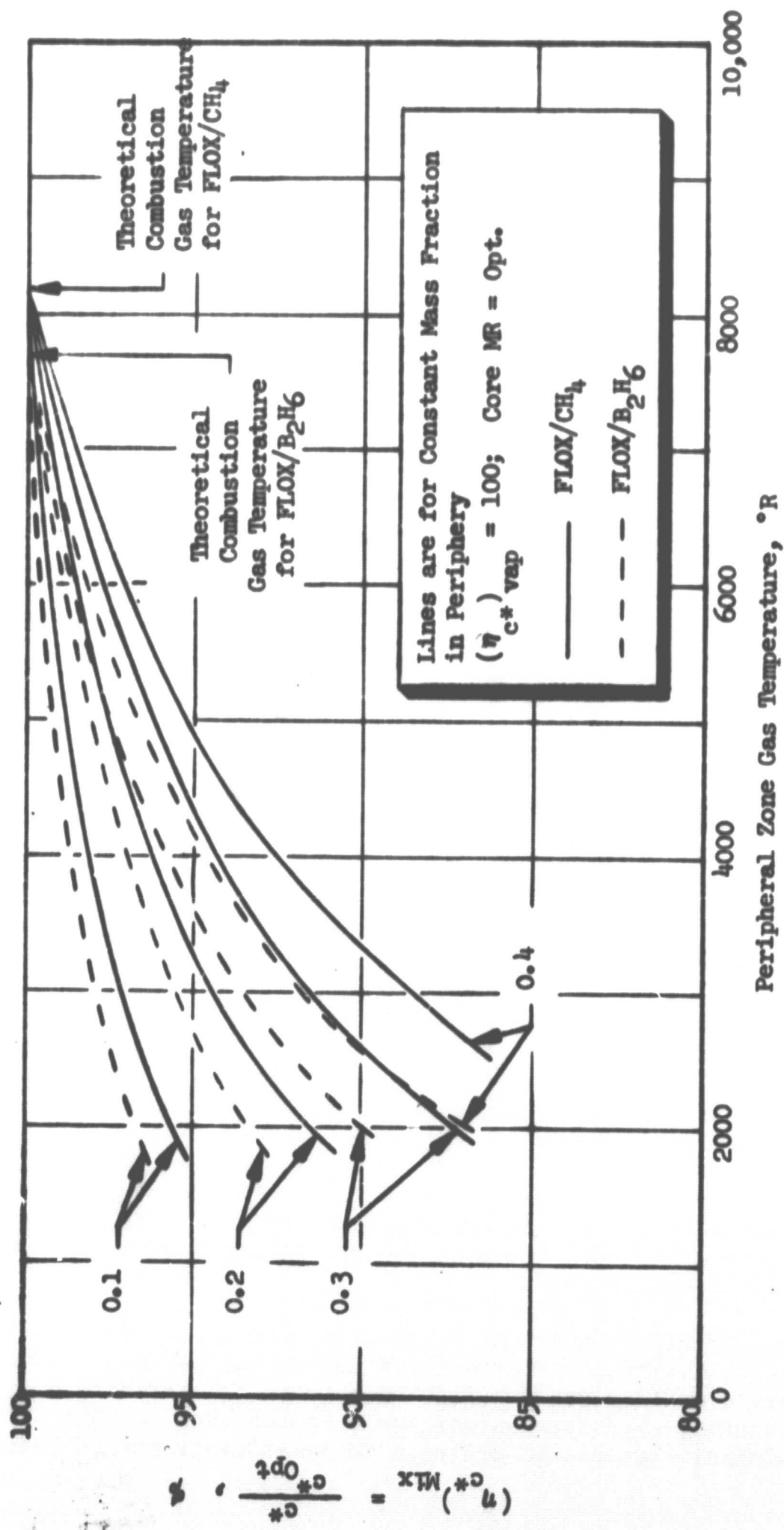


Figure 9. Comparison of Distribution c^* Efficiency for FLOX/CH₄ and FLOX/B₂H₆ as a Function of Peripheral Zone Gas Temperature for Several Peripheral Mass Fractions (Analytical Results)

1 percent while attaining a reasonable temperature (~ 3000 R) in the peripheral zone were expected to be more difficult.

3.3 SUMMARY OF ANALYTICAL MODEL STUDIES

In summary, the combustion model analysis disclosed that propellant drop size and chamber geometry were the two most sensitive and important variables affecting propellant vaporization. For a fixed drop size distribution, chamber pressure was found to have a secondary effect and only becomes important when propellant drop size or chamber geometry favor reduced vaporization efficiency. Similarly, for given drop sizes, mixture ratio effects were found to be of secondary importance. Other input parameters were found to be of minor consequence. The most singularly important finding was that mean propellant drop sizes of 75 microns or less would be required to attain sufficient vaporization for 99-percent c^* efficiency in a nominal 30-in. L* thrust chamber.

Analysis of propellant mixing effects indicated that a very uniform mixture ratio distribution was essential for high c^* efficiency. Further, it was shown that the effect of propellant distribution on c^* efficiency due to mixing was sensitive to the operating mixture ratio of the injector. The mixing analysis indicates that performance using light hydrocarbon fuels (specifically CH_4 but, generally, for others also) is more sensitive to mixing than with other fuels such as B_2H_6 (and also amine fuels). For FLOX/ CH_4 (g) at the nominal optimum mixture ratio of 5.75, it was found that a mixing uniformity index of approximately 96 would be required for eventual attainment of 99-percent c^* efficiency. Attainment of this performance goal with injector-chamber compatibility requires a high-performance core with careful control of the peripheral zone condition.

PRECEDING PAGE BLANK NOT FILMED

4.0 EXPERIMENTAL HARDWARE

The primary objective of this program was to relate injector design parameters to simultaneous attainment of high performance and component (injector-thrust chamber) compatibility for a 3000 lbf (sea level) thrust FLOX (82.6% F₂)/CH₄(g) engine operating at a nominal chamber pressure of 500 psia. Applicable injector and chamber design principles, the basis for selection of the chosen designs (i.e., the design approach), and specific design details are presented herein for the injectors and thrust chambers employed during the experimental portion of the program. The injector type selected for study was a like (self)-impinging doublet. Passively cooled thrust chamber assemblies of a graphite material (ATJ graphite) were employed throughout the hot-fire experimental portion of the program.

4.1 INJECTORS

A properly designed injector should result in attainment of an optimum combination of performance and engine life. Definition of injector design criteria for both high performance and control of injector/chamber erosion caused by excessive heat fluxes and/or thermochemical reactions was a prime objective of this program.

The gas/liquid injector pattern selected for study was a like-doublet (like-doublet element = pair of oxidizer and fuel doublets). This pattern was selected for study (Ref. 16) primarily because of its proved amenability to optimization of performance and chamber compatibility characteristics in related technology programs (Ref. 3, 17, and 18). A review of previous programs in which like-impinging stream injector patterns were employed indicated that a like-doublet pattern can be predictably optimized to produce high performance (Ref. 3, 17, and 18). In addition to attaining efficient combustion through proper injector design, this pattern is quite adaptable to design variations that can affect thrust chamber compatibility concerning heat fluxes and/or thermochemical reactions. Like-doublet injectors (of relatively simple design), which result in high-performance efficiencies, are durable, and exhibit desirable chamber compatibility characteristics, have been developed at Rocketdyne for a number of fluorinated oxidizers and various fuels (Ref. 3, 17, and 18). These results provided confidence of successful use of the like-doublet pattern for attainment of the program goals. It should be emphasized, however, that this program represents the first time that the subject injector pattern has been employed for a gas/liquid propellant system. In general, injector patterns that specifically employ the gas to atomize the liquid (e.g., coaxial, triplet, etc.) have been used for gas/liquid propellant combinations.

Three full-scale injectors were designed and fabricated during this program. The first (injector A) was designed primarily for high performance in terms of having specific element features that promote efficient mixing and atomization. The second (injector C) was designed to provide design criteria for element orientation so that injector-thrust chamber compatibility could be achieved with only minimal performance losses. The final design (injector D), an "optimized configuration," contained a high-performance core region based on design criteria derived from evaluation of the A injector and a chamber-compatible peripheral zone based on the C injector studies. All of the injector designs were based on current design principles supported by cold-flow distribution and atomization experiments

conducted using injector models. The cold-flow injector models are described below. This is followed by descriptions of the specific designs for the full-scale hot-fire injectors.

4.1.1 Cold-Flow Injector Models

Single-Elements. Cold-flow mixing and atomization experiments were conducted with single-element injectors to support design of the full-scale injectors. A schematic representation of a like-doublet injector element (the element is defined to include a matched pair of fuel and oxidizer doublets) is presented in Fig. 10. The geometric factors affecting propellant distribution (mixing)/atomization for this element type are illustrated in this figure.

Single-element injectors with fan inclination angles (α) of 0, 15, 30, and 45 degrees were designed and fabricated for use in defining element design criteria for the full-scale A and C injectors. Each of these elements was designed to permit testing at fan spacing (S) of 0, 0.125, or 0.250 in. All elements had an intra-element spacing (γ) of 0.20 in. and a fan impingement angle (β) of 0 degrees. The liquid orifice diameter for all elements was 0.052 in. Gas doublet orifice diameters of 0.055, 0.082, and 0.140 were employed with the fixed liquid orifice diameter. A jet impingement angle (included angle) of 60 degrees was used for all gas/liquid doublets, and free stream and orifice L/D ratios of approximately 4 and 10, respectively, were employed on all of the like-doublet elements during this program.

Three additional single-element injectors were designed/fabricated for use in supporting design of the high performance core of the D injector. Each of these elements had a fan spacing(s) of 0, fan impingement angle (β) of 0, intra-element spacing (γ) of 0.15 in., and liquid and gas orifice diameters of 0.037 and 0.043 in., respectively. The design variable was fan inclination angle (α), values of which were 0, 15, and 30 degrees.

Reasons for selection of the values/ranges of element design variables employed is discussed under the specific full-scale injector headings.

Injector Segment. A 1/4-segment model of the A injector also was fabricated and cold-flow tested (mixing tests only). The purpose of this segment model was to allow cold-flow measurement of the influence of interelement mixing and, by comparison with results of cold-flow tests with various single-element and full-scale injectors, to provide a definitive correlation between mixing efficiency and element density. The 1/4-segment model (see face pattern in Fig. 11) of the A injector was a replica of a 1/4-segment of the full-scale injector with the exception that its design had been "photographically" reduced to fit into a 3.2-in.-diameter chamber rather than a 3.9-in.-diameter chamber. As a result, the element density of the injector model was approximately 1-1/2 times that of the A injector. Element design parameters were: $S = 0$, $\beta = 0$, $\gamma = 0.15$ in.; $\alpha = 15$ degrees; $d_L = 0.037$ in., and $d_g = 0.043$ in.

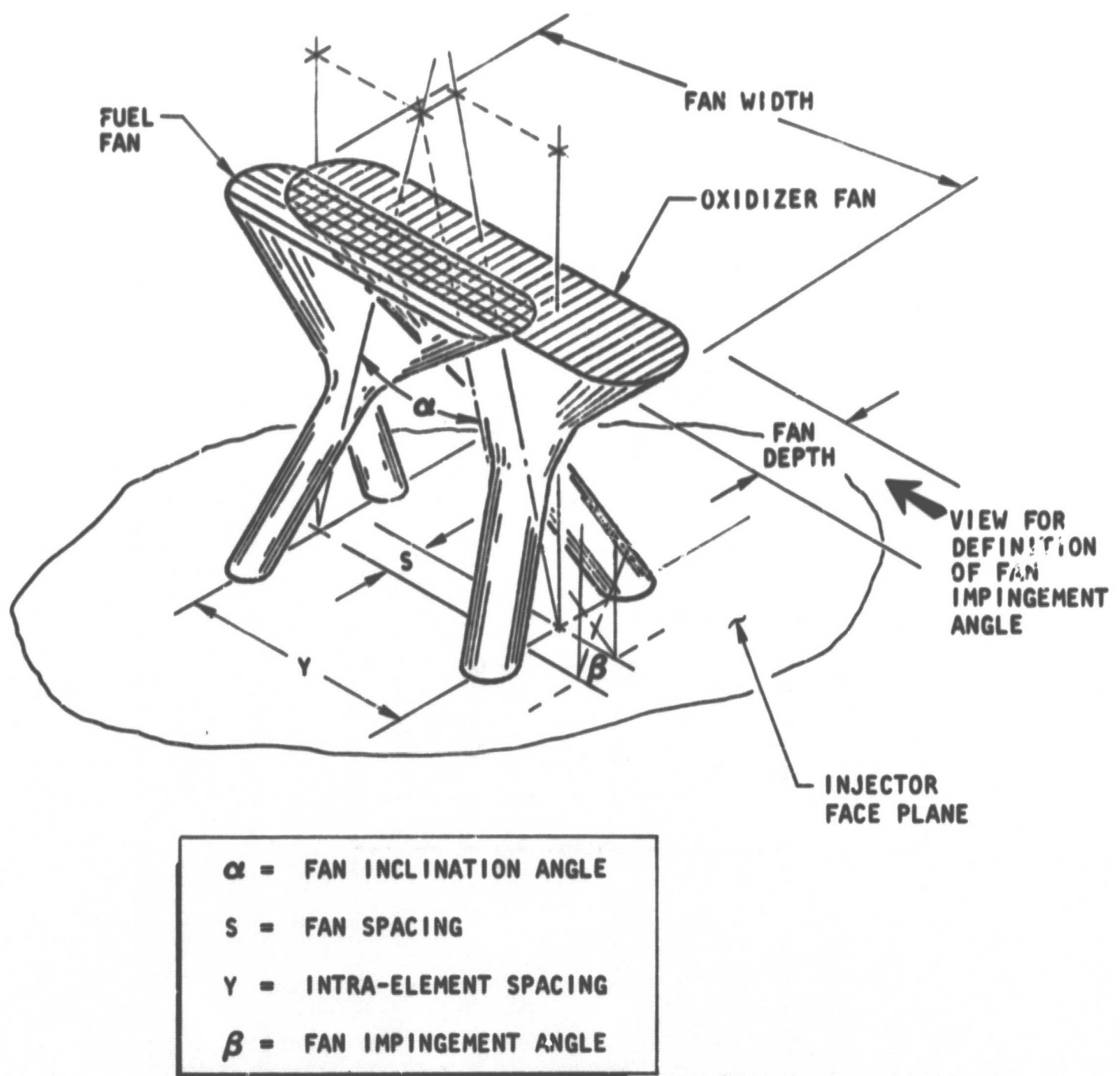


Figure 10. Schematic Representation of Like-Doublet Element Showing Geometric Factors Affecting Propellant Mixing/Atomization (Element = Pair of Fuel and Oxidizer Doublets)

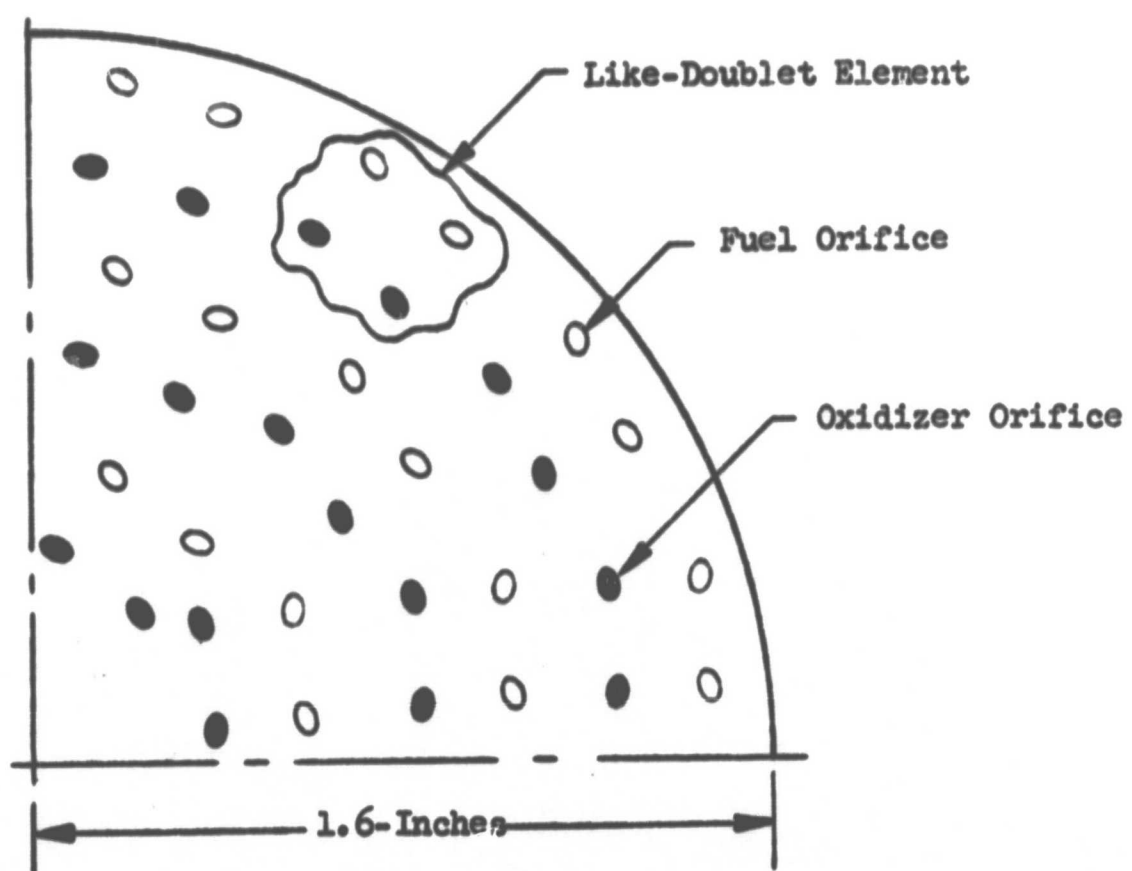


Figure 11. Face Pattern of 1/4-Segment Model of Injector A

4.1 2 Full-Scale Hot-Fire Injectors

Performance Injector (Injector A). This injector was designed primarily for high performance in terms of having specific design features that promote efficient atomization and mixing.

As was noted in Fig. 2 from the previous section of the report, it was expected that hot-fire propellant (oxidizer) mean drop sizes (D_{30}) \leq approximately 75 microns would be required to achieve the program performance goal (99-percent c^* efficiency at optimum mixture ratio) in a 30-in. L^* chamber. Since a reference chamber L^* of about 30 in. was desired (this was the reference chamber L^* for the FLOX/LPG study, Ref. 3) for this program, oxidizer drop sizes of \leq 75 microns would be required to make performance losses due to incomplete propellant vaporization negligible in the reference chamber. Prime consideration could then be directed toward experiments designed to assess the effects of propellant distribution on performance and chamber compatibility.

Performance losses at optimum (the design) mixture ratio due to nonuniform propellant mass and mixture ratio distribution are substantially greater for FLOX/light hydrocarbon systems than for most propellant combinations. Consequently, careful consideration must be given to injector design variables (individual element design, element density, etc.) that influence propellant distribution in order to obtain high performance with FLOX/ $\text{CH}_4(g)$.

Cold-flow distribution and atomization experiments were conducted using the injector segment models to support design of the A injector. Results of these experiments are presented in subsequent sections of this report. Associated drop size calculations and related experience are presented below.

In the recent program described in Ref. 3, liquid/liquid like-doublet injectors were evaluated for requirements very similar to those of the present program. The principal difference in the subject program is that the LPG fuel is replaced by gaseous methane. Qualitatively then, it may be expected that the presence of the adjacent gas injection can only enhance the liquid oxidizer atomization, if it affects it at all. In the referenced program, drop sizes were calculated using the following equation:

$$D_{30} = \frac{25,400}{2.64 \sqrt{\frac{V_j}{D_j}} + K \left(\frac{\rho_{\text{actual}}}{\rho_{\text{ref}}} \right)^{1/4} |(\Delta V)|} \quad (8)$$

where

D_{30} = volume-mean-diameter of resulting droplets, microns
 D_j = liquid orifice diameter, in.
 V_j = liquid injection velocity, ft/sec
 K = $0.97 \times \left[\left(\frac{\mu\sigma}{\rho} \right) \text{n-heptane} / \left(\frac{\mu\sigma}{\rho} \right) \text{FLOX} \right]^{1/4}$

$$\left(\frac{\rho_{\text{actual}}}{\rho_{\text{ref}}} \right)$$

= ratio of actual to reference gas density

$$\Delta V = (V_g - V_j) = \text{relative velocity difference between combustion gas and liquid jet, ft/sec}$$

Hot-fire mean drop sizes for the FLOX/LPG propellant system were successfully predicted during the referenced program using Eq. 8. Oxidizer mean drop sizes calculated using Eq. 8 will not reflect the effects of injection of the fuel as a gas on the resulting drop size. Consequently, drop sizes from Eq. 8 were expected to represent an upper limit on those anticipated with injector A. Drop size experiments were conducted during this program to define the effects of gas injection on the resulting liquid drop size.

Oxidizer drop sizes calculated from Eq. 8 are shown plotted as a function of ΔV for several orifice diameters and injection velocities in Fig. 12. The range of orifice diameter (~0.030 to 0.090 in.) and injection velocity (50 to 200 ft/sec) shown cover the practical range for the subject program.

Drop sizes at a liquid injection velocity of 100 ft/sec (corresponding to an injector ΔP of ~150 psi) are shown plotted as a function of ΔV in Fig. 12A for several orifice diameters. Examination of this figure reveals that for orifice diameters in the range of interest, the resulting drop size is fairly independent of orifice diameter for relative velocity differences greater than ~200 ft/sec. The effect of liquid injection velocity on drop size is shown in Fig. 12B. Drop size is plotted as a function of ΔV for liquid injection velocities of 50, 100, and 200 ft/sec in this figure. These injection velocities correspond to injector pressure drops of approximately 38, 150, and 600 psi, respectively. Results are for an orifice diameter of 0.0469 in. (the liquid orifice diameter in the initial A injector). As is noted in this figure, oxidizer drop size also is relatively independent of the injection velocity for values of ΔV greater than ~200 ft/sec.

This analysis indicates that for given injection conditions (i.e., D_j and V_j), drop size is a strong function of ΔV for relative velocity differences ≤ 200 ft/sec. Since V_g is essentially proportional to the chamber contraction ratio (Ref. 3), smaller drop sizes are associated with the use of low contraction ratio chambers. ΔV varied from approximately 60 to 260 in the Ref. 3 study ($\epsilon_c = 2$ and 4). Based on these data, an effective ΔV for the subject program ($\epsilon_c = 3$) would be expected to be within this range.

An effective combustion gas velocity of ~320 ft/sec ($\Delta V = 220$ ft/sec) was estimated for FLOX/CH₄(g) at the design operating conditions. This value was estimated on the basis of results from the recently completed FLOX/LPG program (Ref. 3) in combination with combustion model analysis. As is noted in Fig. 12, an oxidizer drop size of ~50 microns is predicted at the injector A design conditions based on this value of V_g . This drop size would result in negligible performance losses due to incomplete propellant vaporization in a 30-in. L* chamber (Fig. 2).

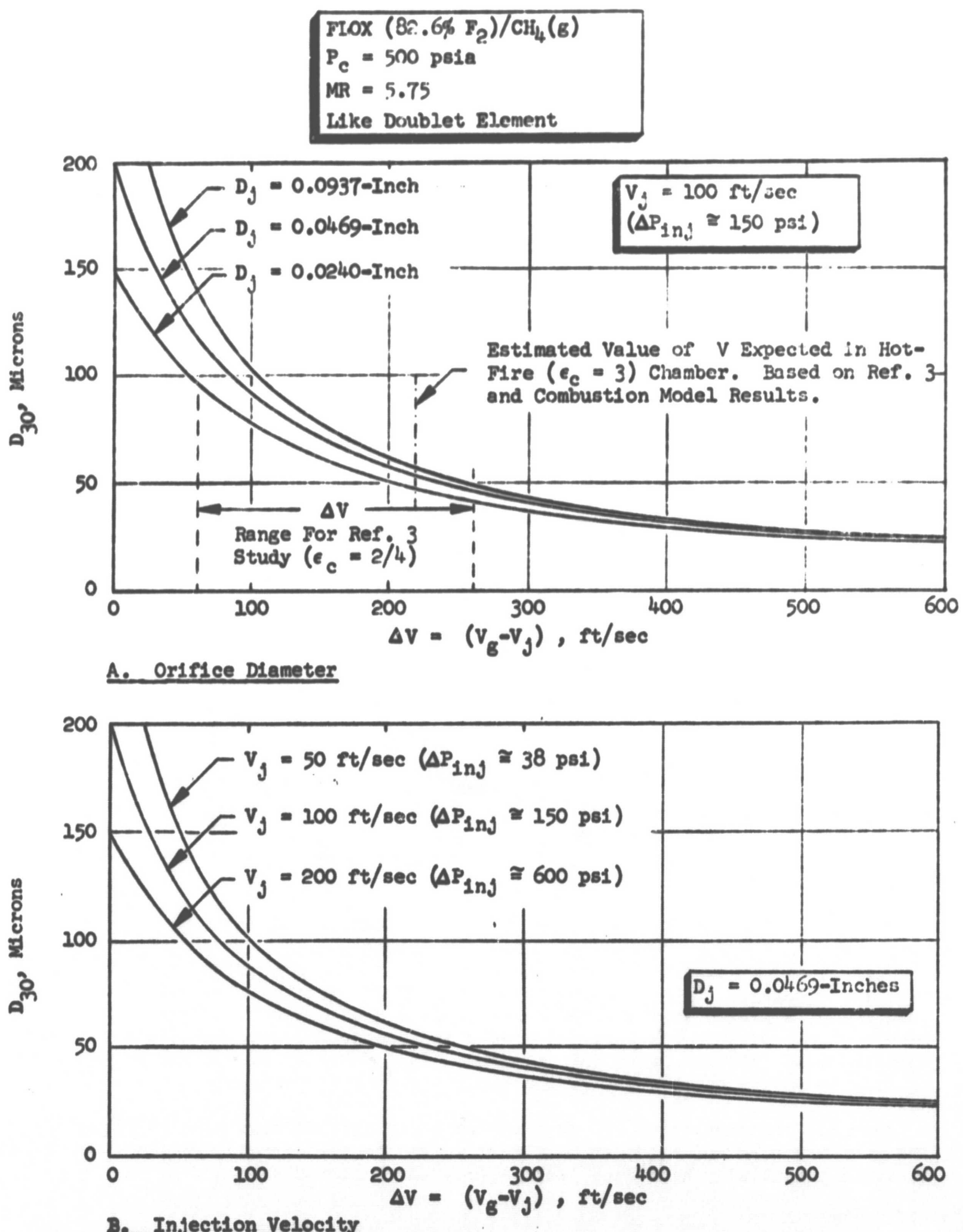


Figure 12. Predicted Oxidizer Drop Size (Eq. 8) as a Function of Relative Velocity Difference Between Combustion Gas and Liquid Jet for Several Orifice Diameters and Injection Velocities

Propellant mixing is primarily a function of spray fan orientation for the like-doublet pattern. Geometric factors affecting propellant distribution for a like-doublet element were shown in Fig. 10. For a fixed geometry, mixing is primarily a function of the propellant momentum ratio.

Previous experience with liquid/liquid propellant systems employing like-doublet element injectors and specific injector design constraints for this program were used to help select a practical test matrix to support definition of element design criteria for the A injector. Preselection of a zero fan spacing (S) and impingement angle (β) as optimum was predicated on previous studies with liquid/liquid propellant systems. Design considerations for the full-scale injectors (number of elements required for simultaneous attainment of high performance and control of injector-chamber compatibility, available injector face area, orifice diameters required for good atomization/reasonable injector pressure drops, etc.) limited the range of usable intra-element spacing (~0.15 to 0.30 in.) and orifice diameters (~0.03 to 0.09 in.). Intra-element spacings of 0.20 and 0.15 in. were employed for these experiments. Selection of these values was based on previous experience with liquid/liquid propellant systems. Although these studies have shown that optimization of the spacing and fan inclination angle are interrelated, intra-element spacing effects had been negligible in the range of practical interest for injector A. Fan inclination angle (α) and propellant momentum ratio were selected as the primary test variables associated with individual element design. Previous experience with liquid/liquid like-doublet elements indicate that both of these variables influence mixing and lend themselves to optimization. The other major experimental variable was element density which influences the degree of interelement mixing. Element density, of course, varies directly with the number of elements per injector, and inversely with thrust per element.

Based on the above related experience and results of the single-element cold-flow mixing and atomization studies (discussed later), the following design parameters were initially selected for the A injector elements: fan spacing, $S = 0$, fan impingement angle, $\beta = 0$; intra-element spacing, $Y = 0.20$ in.; fan inclination angle, $\alpha = 15$ degrees; momentum ratio (o/f) = 0.75 at nominal chamber pressure and mixture ratio; liquid (oxidizer) orifice diameter, $d_L = 0.0469$ in.; and gas (fuel) orifice diameter, $d_g = 0.055$ in.

Based on liquid/liquid propellant system experience, an injector with 30 to 40 elements was selected. Design of a conventional radial-fed or ring-type injector with near-uniform propellant mass distribution and the desired number of elements was not feasible. Both of these injector concepts limited the number of elements that could be placed in the fixed injector face area below that desired. Element feeding problems were encountered. For this reason, diffusion-bonded injectors were selected for use during this program. This fabrication concept provided flexibility in design not offered by the other two injector concepts.

A schematic representation of the A injector assembly is presented in Fig. 13. The fuel manifold and oxidizer dome were welded to the diffusion-bonded body assembly to avoid potentially hazardous leakage from the dome/manifold.

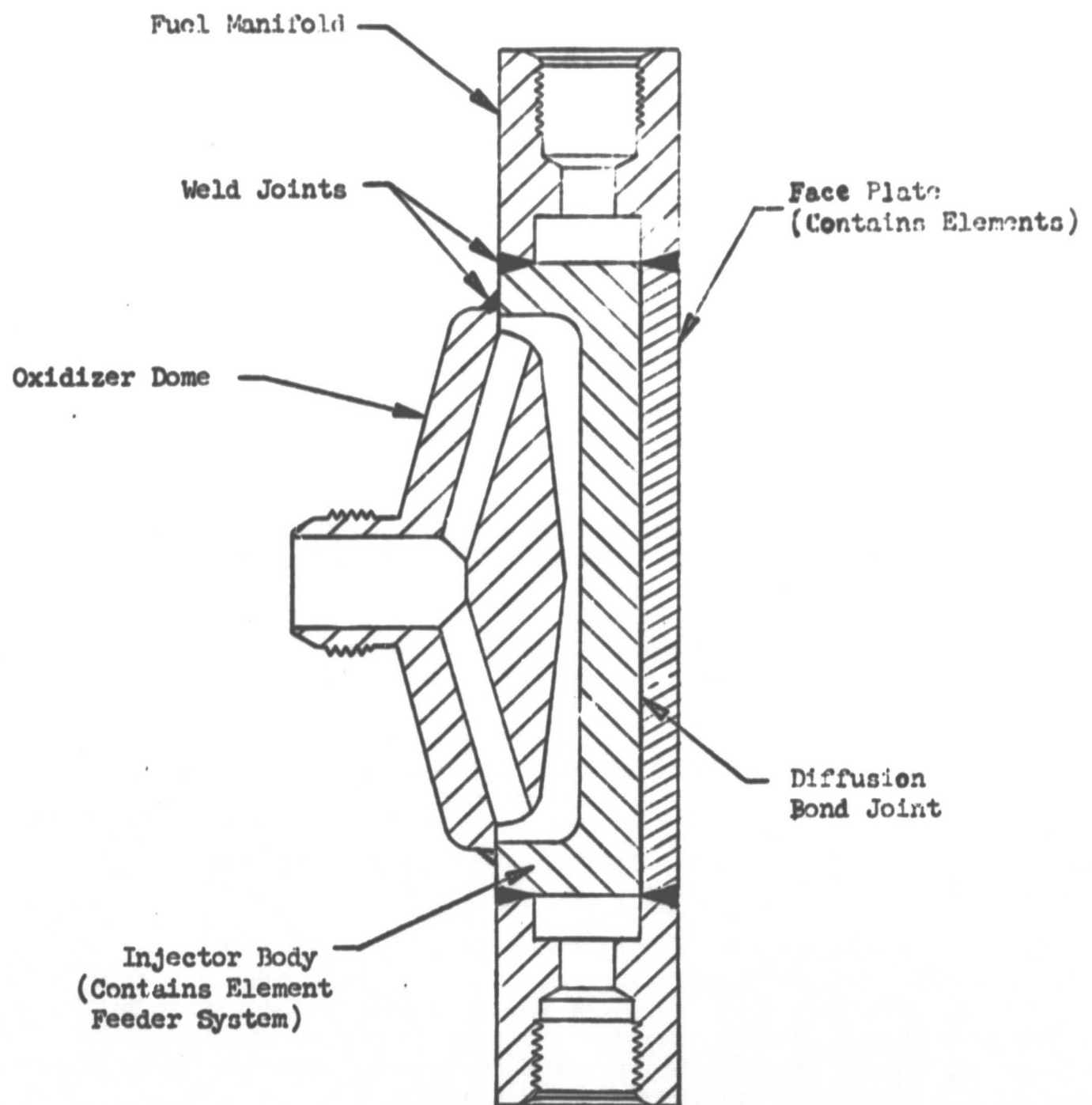


Figure 13. Schematic Representation of Injector A Assembly

The injector contained 37 elements arranged in four rings (Fig. 14). The fuel doublet is on the outside (chamber wall side) of the element. Some of the elements are turned slightly (i.e., the doublet fans are not exactly perpendicular to the chamber wall) to permit placement of more elements in a given ring.

Important design details of the injector are summarized below.

1. Element placement on the face of the injector was such as to provide essentially uniform propellant mass flux distribution.
2. Oxidizer manifold/feeder passages were sized so that velocities were less than 10 ft/sec at the design operating conditions and passage entrances were chamfered or rounded as much as possible to avoid sharp edges. Fuel manifold/feeder velocities were ~80 ft/sec at the design operating conditions.
3. Oxidizer orifice L/D's were ~10. Fuel orifice L/D's were approximately 8. Free stream L/D's for both oxidizer and fuel were between 3 and 5.
4. The impingement point of the like stream was 0.20 in. from the injector face (The included impingement angle of all liquid/gas doublet streams was 60 degrees.)

The injector was designed for an oxidizer ΔP of 150 psi (injection velocity = 100 ft/sec) and a fuel injection Mach number of 0.5 at the design operating conditions.

The face plate and body material were Nickel 270. The body contained the manifolding (feed system) for the elements in the face plate. The body assembly (i.e., the bonded face plate and body) was finish machined after the face plate had been diffusion bonded to the body.

The fuel (gaseous methane) was fed into the annular manifold surrounding the body assembly. The oxidizer (FLOX) was fed through the dome. The manifold and dome material was 321 stainless steel. Photocons to monitor combustion stability and thermocouples to measure manifold propellant temperatures were installed in both the dome and manifold.

The injector face plates for all of the full-scale injectors were water-flow checked for proper stream impingement prior to and after being bonded. In addition, after the injectors had been bonded and the manifold and dome welded onto the body, it was pressure checked for leakage (from the manifold/dome and between the fuel and oxidizer manifolds) prior to being hot-fire tested. Special fixtures were fabricated to make the above injector checks possible.

A second A injector was fabricated and hot-fire tested. This was necessary because of a FLOX incident that damaged the initial injector. This injector was identical to the initial injector except that the fuel and orifice diameters were 0.0469 and 0.041 in., respectively. To complete the experimental portion of the program, which included definition of the effects of propellant momentum ratio on distribution/performance, the fuel/oxidizer orifices were eventually enlarged. This injector was hot-fire tested with the following orifice diameters; $d_f = 0.041$ in., $d_o = 0.0469$ in.; $d_f = 0.052$ in., $d_o = 0.0469$ in.; $d_f = 0.052$ in.; $d_o = 0.055$ in. These injector configurations were termed A-1, A-2, and A-3, respectively.

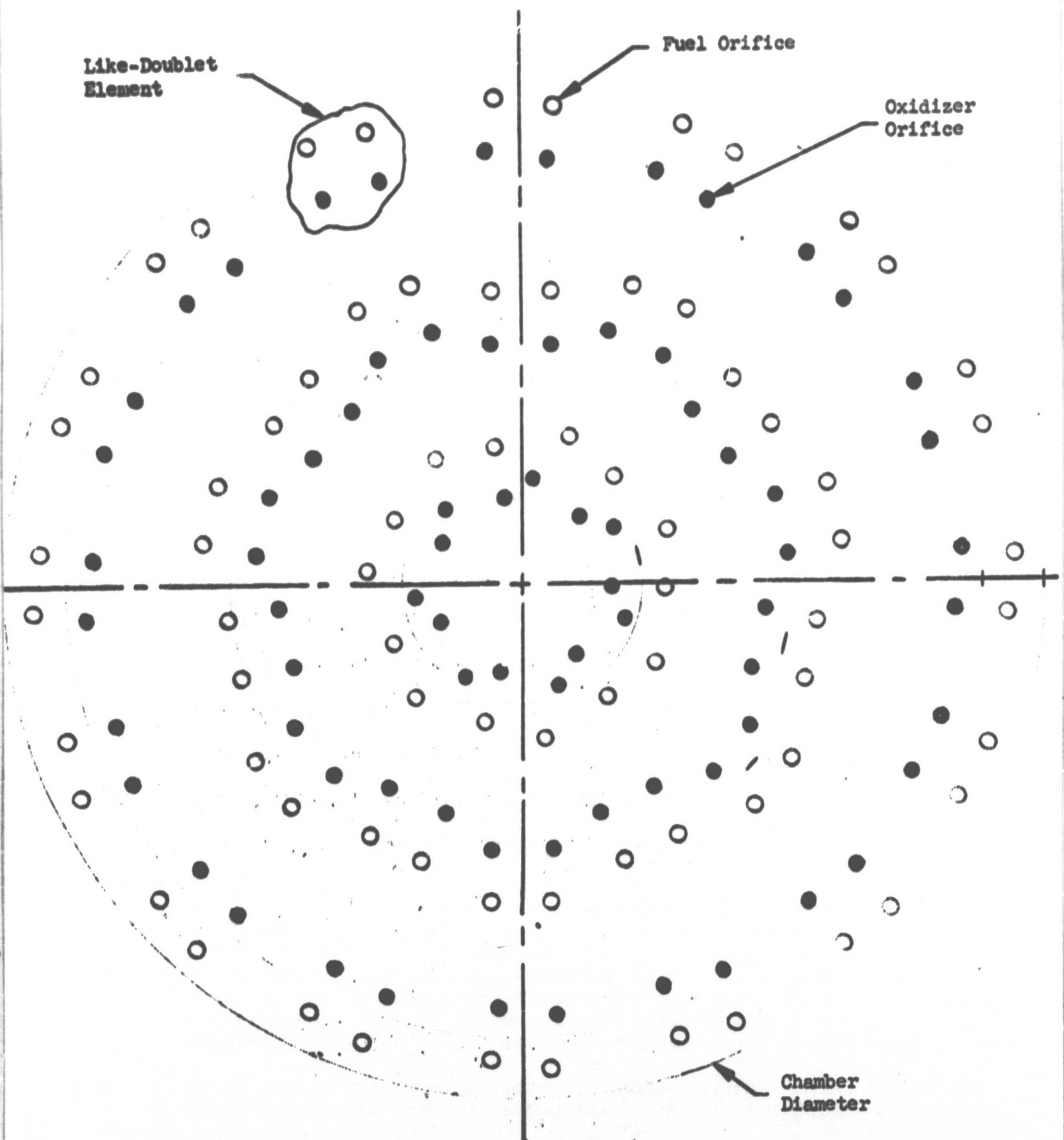


Figure 14. Schematic Representation of Face Pattern of Injector A

Chamber Compatible Injectors (Injectors B/C). These injectors were designed to provide design information for the peripheral zone elements in the "optimized injector configuration" so that injector-thrust chamber compatibility could be achieved with only minimal performance losses.

The subject injectors were designed to provide a fuel-rich zone adjacent to the chamber wall for injector-chamber compatibility. The fuel and oxidizer fans in the like-doublet elements were intentionally misaligned (i.e., fan spacing $\neq 0$) to provide this fuel-rich zone near the chamber wall. This approach is similar to that employed in related advanced technology programs (Ref. 3 and 17), where improved injector-thrust chamber compatibility was required with liquid/liquid like-doublet injectors.

Cold-flow distribution experiments were conducted, using the injector segment models described earlier, to provide design criteria with respect to element configuration and operating conditions. The primary test variables were fan spacing(s), fan inclination angle (α), and propellant momentum ratio. Two injector design concepts (B and C) were selected based primarily on the results of these experiments, which are presented in a subsequent section of this report.

Based on the single-element cold-flow experimental data, the following element design parameters were selected for the B configuration injector: fan spacing $S = 0.125$ in.; fan impingement angle, $\beta = 0$ degrees; intra-element spacing, $Y = 0.20$ in.; fan inclination angle, $\alpha = 15$ degrees. Design parameters for the C configuration injector were fan spacing, $S = 0.250$ in.; fan impingement angle, $\beta = 0$, intra-element spacing, $Y = 0.20$ in.; fan inclination angle, $\alpha = 0$ degrees. The liquid and gas orifice diameters selected for both configurations were 0.0469 and 0.055 in., respectively.

Basically, the C design concept represented the configuration indicated by cold-flow data to offer the best chamber compatibility, though at some cost in performance. The B concept resulted from a compromise between mixture ratio control and performance potential in which performance should remain relatively high, but wall protection was still provided. Only one of the configurations, the C configuration, was fabricated and hot-fire tested.

Basic construction of the C injector was quite similar to the A injector, with the exception of the element design parameters. The C injector contained 35 elements arranged in three rings (Fig. 15). The fuel doublet is on the outside (chamber wall side) of the element (Fig. 15). Based on the cold-flow data, the elements were turned slightly (i.e., the doublet fans are not exactly parallel to the chamber wall) to provide the lowest possible mixture ratio adjacent to the wall. All elements in the C injector were of the same type to make more sensitive measurement of the performance losses due to use of the nonzero fan spacing elements.

Additional design details (element placement on the injector face, feeder passage velocities, orifice L/D's, etc.) are similar to those for the A injector.

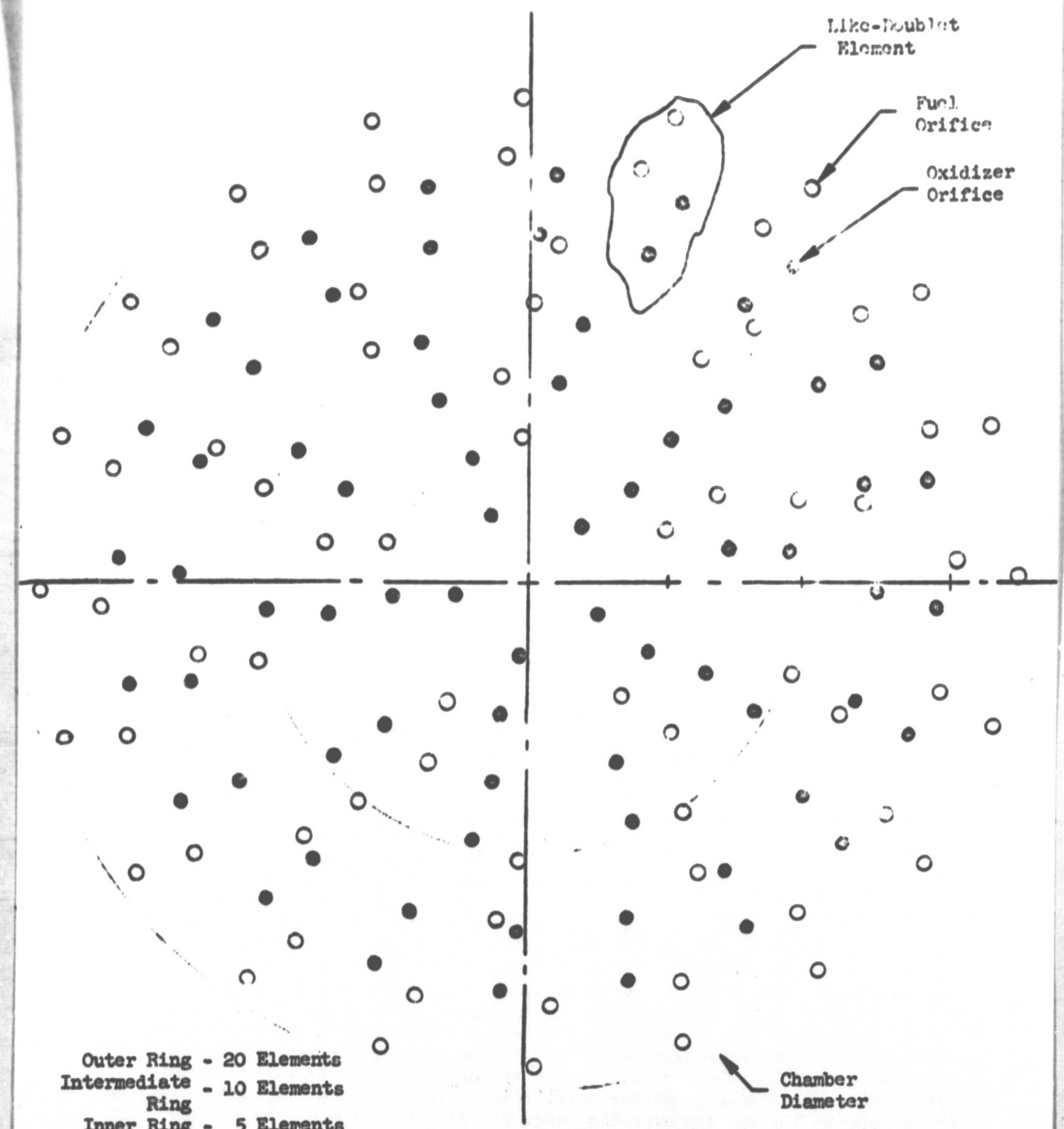


Figure 15. Schematic Representation of Face Pattern of Chamber Compatible C Injector

Optimum Configuration (Injector D). The optimized injector configuration (Injector D) had separately manifolded "high-performance" core and "chamber-compatible" peripheral zones. Design of the high-performance core region was based on cold-flow and hot-fire experiments conducted with the A injector configurations. The peripheral zone design, which was intended to provide injector-chamber compatibility with minimal performance losses, was based on cold-flow and hot-fire data generated from the B/C injector studies. The separately manifolded core and peripheral zone design concept was employed in the D injector to permit optimization of the injector-thrust chamber combination. Experiments were conducted with the D injector to define the effects of operating conditions (i.e., mass fraction of propellants and mixture ratio in the peripheral zone) on performance and chamber heat transfer characteristics. The dual (separate) manifolding of the core and peripheral regions permitted independent variation of core and peripheral operating conditions and, thereby, made possible further optimization of the like-doublet injector pattern with this single piece of hardware.

Several important conclusions from the A and C injector hot-fire testing significantly affected the D injector design. First, the A injector design pattern tested was not adequate for the high-performance core of the D injector ($n_{c^*} < 99$ percent in the design mixture ratio range for the core; $5.25 < MR < 6.5$). Second, performance (n_{c^*}) of the C injector in the mixture ratio range of interest (~ 3 to 4 for the peripheral zone elements) appeared to be adequate for its desired application. The C injector pattern also exhibited very favorable chamber heat transfer characteristics. Performance losses for the A injector were attributable primarily to nonuniform propellant mixing. Since individual element design parameters for the A injector had been optimized in terms of mixing, further increase in mixing uniformity could only be obtained by increasing inter-element mixing (element density).

To achieve the performance goal, element density in the core region of the D injector was increased by a factor of 2 over that in the A injector. Selection of this element density (~ 6 elements/in.² of injector face area) was based on injector model cold-flow results and design considerations. Analysis of cold-flow mixing data from injector A and its segment and single-element models indicated that the desired performance goal could be attained in the core of the injector with this element density level using previously defined optimized element design and operating parameters. A substantially greater element density was not feasible from a design standpoint, as this would introduce element feeding problems.

Selection of a 15-degree fan inclination angle for the core elements was based on the slightly higher mixing at the fan inclination angle and injector design considerations. Design considerations indicated that use of the 15-degree fan inclination angle also permitted incorporation of a higher element density (elements/in.² of injector area) than would 0- or 30-degree inclination angles. The high element density for the core of the D injector (6 elements/in.²) was achieved by making the elements 3/4-scale reductions of the elements in the A injector. Fuel and oxidizer orifice diameter sizes were selected so as to keep the momentum ratio (o/f) between 0.6 and 1, oxidizer injection $\Delta P < 150$ psi, and fuel injection Mach number between 0.3 and 0.6 over the range of test conditions. This element density, and these design and operating conditions, should ensure attainment of the highest possible performance from the injector core.

Performance and heat transfer characteristics of the C injector elements were such that their use in the periphery of the D injector could be recommended without change. Design considerations (element density and percent mass in the core, separate manifolding of the core and periphery, control of injector-thrust chamber compatibility, etc.) dictated that the elements in the periphery should be 3/4-scale reductions of the C injector element. Fuel and oxidizer orifice sizes were selected so as to keep the momentum ratio (o/f) between 0.3 and 0.6, oxidizer injection $\Delta P < 150$ psi, and fuel injector Mach number between 0.5 and 0.9 over the range of test conditions. The element design was expected to provide reasonable performance/chamber heat transfer characteristics.

Based on the reasoning discussed above, an injector with 60 to 70 elements was designed. As was noted previously, design of a conventional, radial-fed or ring-type injector with near-uniform propellant mass distribution, the desired number of elements, and separate core and periphery manifolding was not feasible. Both of these injector fabrication concepts limit the number of elements that can be placed in the fixed injector face area below that desired. Element feeding problems would be encountered. For this reason, a diffusion-bonded injector design was again selected. This fabrication concept provided flexibility in design not offered by the other methods.

The D (optimized) injector has several complexities not present in the A and C injectors. The element density on the face of the injector was approximately doubled and the outer ring of elements separately manifolded from the core elements. Three candidate designs (the original with multiple diffusion-bond joints, an alternate with a single diffusion-bond joint, and a three-piece design with brazed construction) were considered for the like-doublet dual manifold "optimized" injector configuration. All designs had a common injector element face pattern. Primary differences were in the manifolding of the propellants and the method of construction. After a thorough review, the original design was chosen as the most appropriate.

Selection of the original design over the alternate designs was based primarily on fabrication feasibility and cost. Diffusion bonding of the single-joint, diffusion-bonded injector was considered too risky by the NAR Los Angeles Division diffusion-bonding group. This design incorporated several thin (0.060 to 0.090 in.) tall (1/2 in.) webs between propellants that would have been high risk areas for diffusion-bond failure. The three-piece brazed construction design was rejected primarily because its cost and fabrication time were approximately twice those of the original design. This injector design also featured extremely long feeder passages (L/D's up to 70) and could have resulted in FLOX heating and/or methane cooling problems within the injector, i.e., excessive interpropellant heat exchange.

A schematic representation of the D injector configuration is presented in Fig. 16. The injector contains 63 elements arranged in four rings (Fig. 17). The inner three rings (42 elements) constituted the core region and the outer ring (21 elements) was the peripheral zone. Details of the individual elements in the core are noted below.

FLOX / METHANE
OVERALL $MR = 5.25$
 $F = 3000 \text{ LBF. (Sea Level)}$

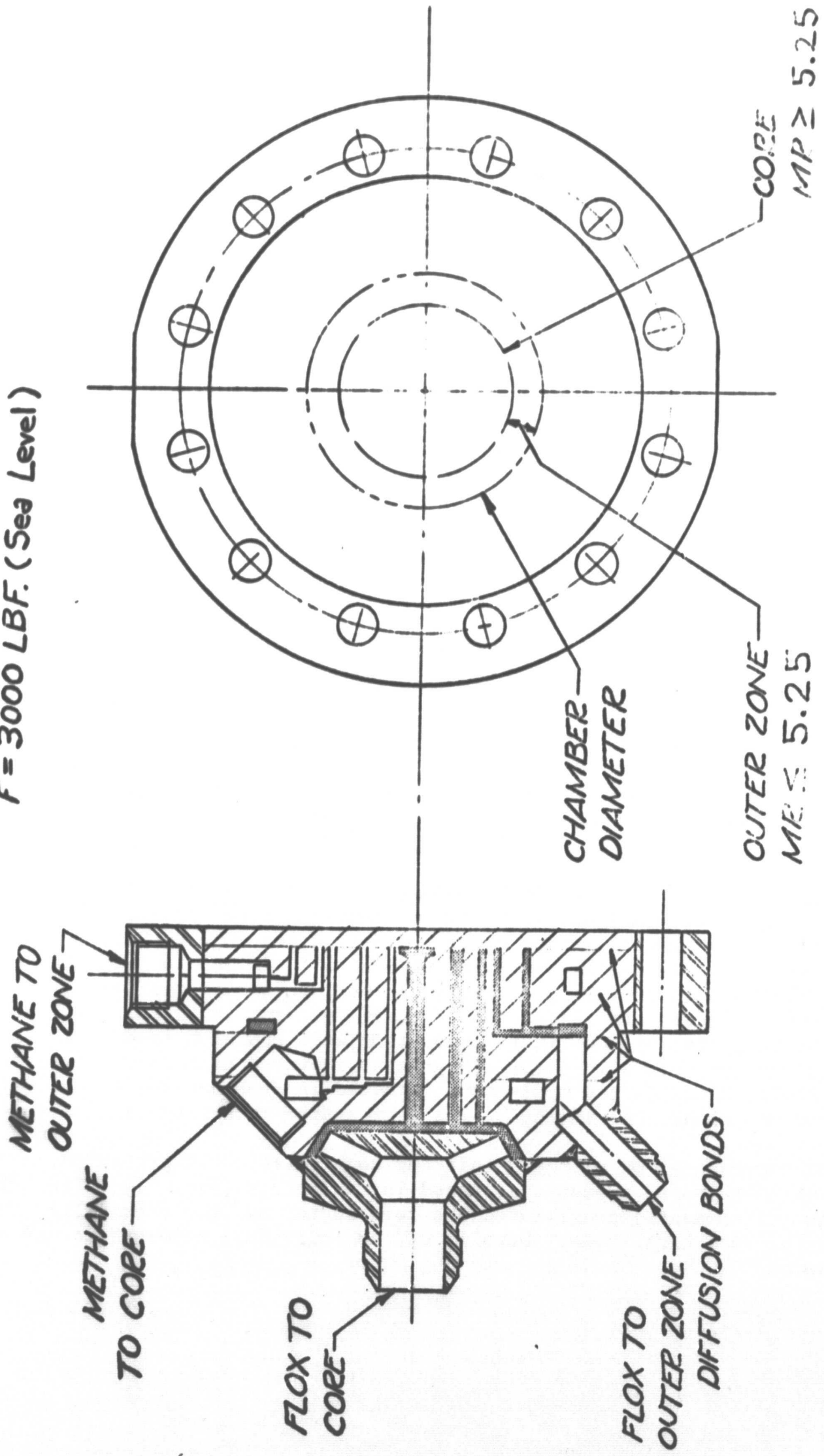


Figure 16. Schematic of Optimized Like-Doublét Dual Manifold Injector

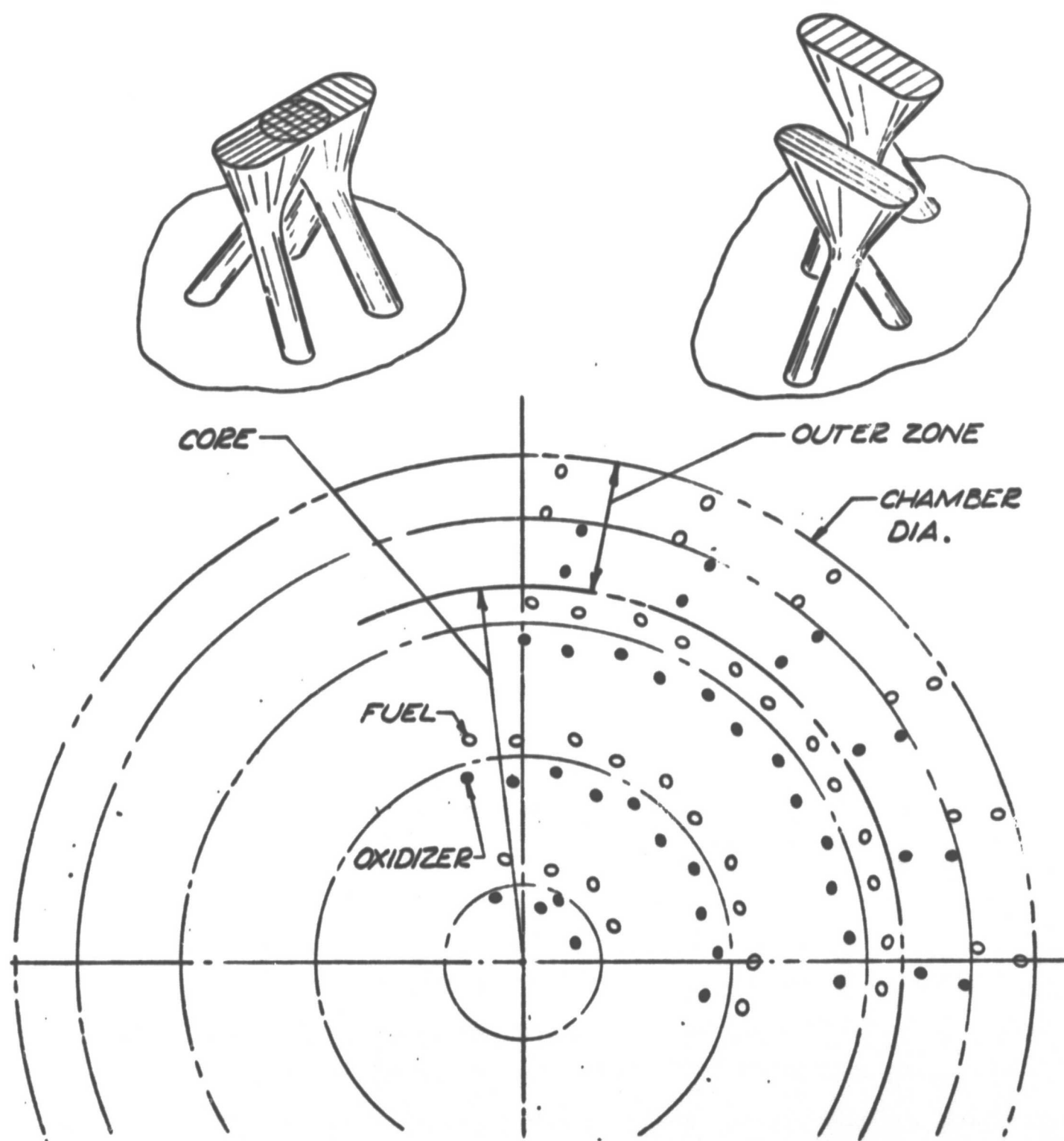


Figure 17. Illustration of Face Pattern and Element Fan Alignment for Optimized Like-Doublet Injector

d_1 = liquid (oxidizer) orifice diameter = 0.037 in.
 d_g = gas (fuel) orifice diameter = 0.043 in.
 s = fan spacing = 0.0 in.
 β = fan impingement angle = 0 degrees
 α = fan inclination angle = 15 degrees
 γ = intra-element spacing = 0.15 in.

The injector face pattern and element fan alignment for the D injector are shown schematically in Fig. 17. Note that the fuel doublet is on the outside (chamber wall side) of the element. Fuel and oxidizer fans are aligned edge-on-edge (fan spacing = 0) and nearly perpendicular to the chamber wall in the core region. The elements were turned slightly (i.e., the doublet fans are not exactly perpendicular to the chamber wall) to permit placement of more elements in the fixed injector face area. Details of the individual elements in the peripheral zone are noted below:

d_1 = 0.037 in.
 d_g = 0.043 in.
 s = 3/16 in.
 β = 0 degree
 α = 0 degree
 γ = 0.15 in.

Note that the fuel doublet is on the outside (chamber wall side) of the element and that the elements are turned slightly (i.e., the doublet fans are not exactly parallel to the chamber wall) to provide the lowest possible mixture ratio region adjacent to the wall. Peripheral elements have a fan spacing of 3/16 in. and are oriented nearly parallel to the chamber wall. The fuel fan is positioned nearest to the chamber wall.

Additional design details (element placement on the injector face, feeder passage velocities, orifice L/D's, etc.) are similar to those for the A and C injectors.

The injector was designed for an oxidizer ΔP of ~ 150 psi (injection velocity ≈ 100 ft/sec) and a fuel injection Mach number of 0.5 at the design operating conditions.

The face plate and body (i.e., the four other plates that were diffusion bonded) material was Nickel 270. The body contained the manifolding (feed system) for the elements in the face plate. The peripheral zone fuel manifold was made of Inconel 625 and electron-beam welded to the Nickel 270 body. The oxidizer core dome and peripheral zone oxidizer inlet fittings were welded to the diffusion-bonded assembly to avoid potentially hazardous leakage from the dome/manifold. These parts were made from 321 stainless steel.

The injector face plate was water-flow checked for proper stream impingement prior to and after being bonded to the body. After the injector had been bonded and welded together, it was pressure checked for leakage (from and between the manifolds) prior to being hot fired. Special fixtures were fabricated to make possible the above injector checks.

Front and back view photographs (pre-bond) of the five plates that were bonded together to form the D injector body are presented in Fig. 18 and 19, respectively.

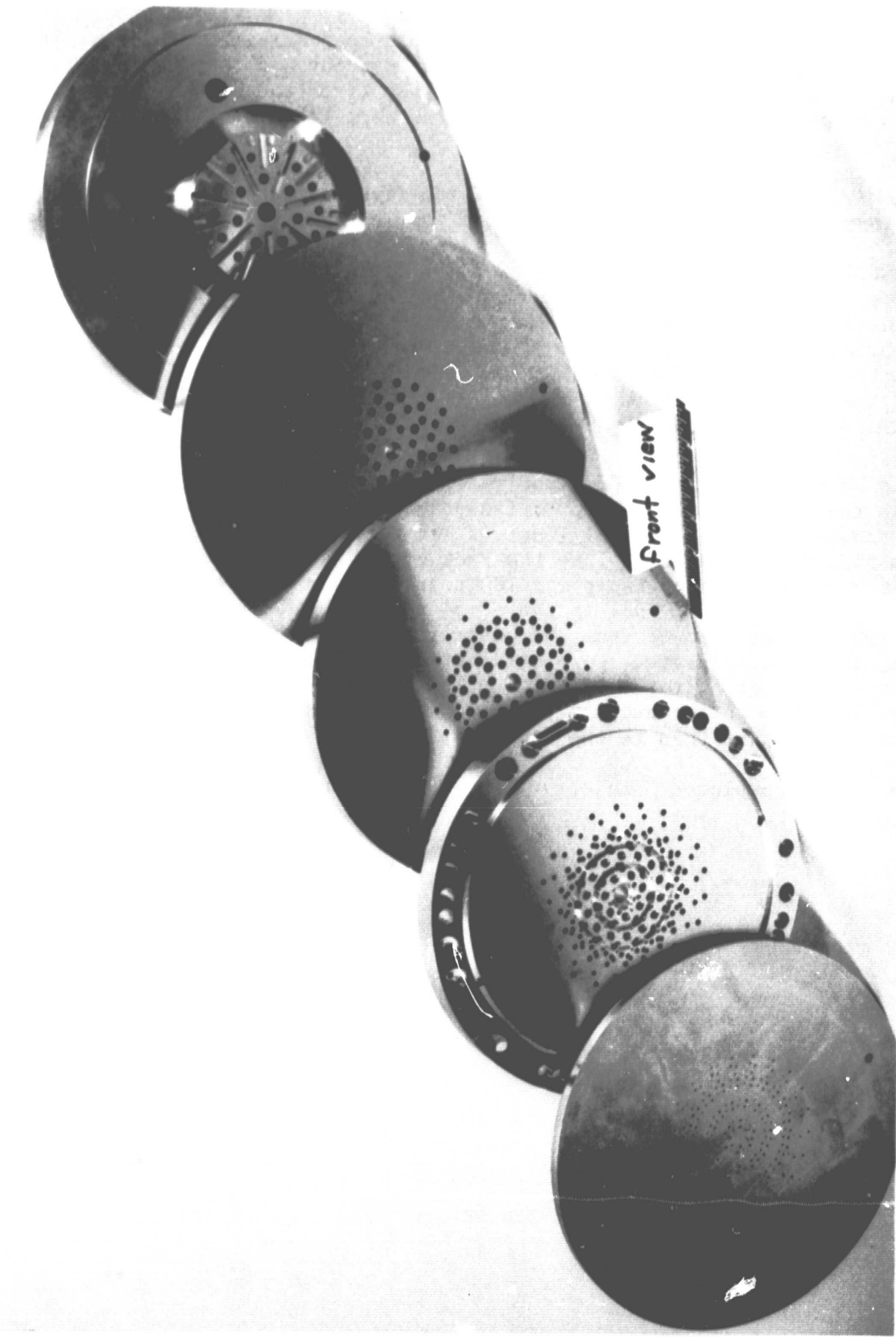
Various geometric configurations typical of those employed in the diffusion-bonded injectors were machined into the periphery of the No. 2 plate (i.e., the second plate from the front in Fig. 18). This was done so that the sample configurations could be analyzed to yield information on the diffusion bonds within the injector. The outer portion of the bonded assembly (outside the circumferential groove in the periphery of the front view of plate No. 2) was removed prior to welding the propellant manifold and inlet ports onto the injector.

The schematic of the dual-manifolded "optimized" injector assembly presented in Fig. 16 shows the location of the four diffusion-bond joints and the propellant manifolding scheme. Outer zone fuel (CH_4) is fed through two ports 180 degrees apart to a manifold ring machined into the back of the No. 2 plate. Outer zone oxidizer (FLOX) is fed through two ports 180 degrees apart to a manifold ring in the back of the No. 3 plate. Fuel to the core is fed through two ports 180 degrees apart (90 degrees removed from the outer zone oxidizer ports) to a manifold in the front of the No. 5 plate. Core oxidizer is fed through a single port in the back of the injector. It should be noted that the relative complexity of this design is attributable to the necessity for separate manifolding of the core and peripheral regions rather than to the "two-zone" injector concept.

A photograph of the completed D injector is presented in Fig. 20.

1XX41-4/7/71-S1L

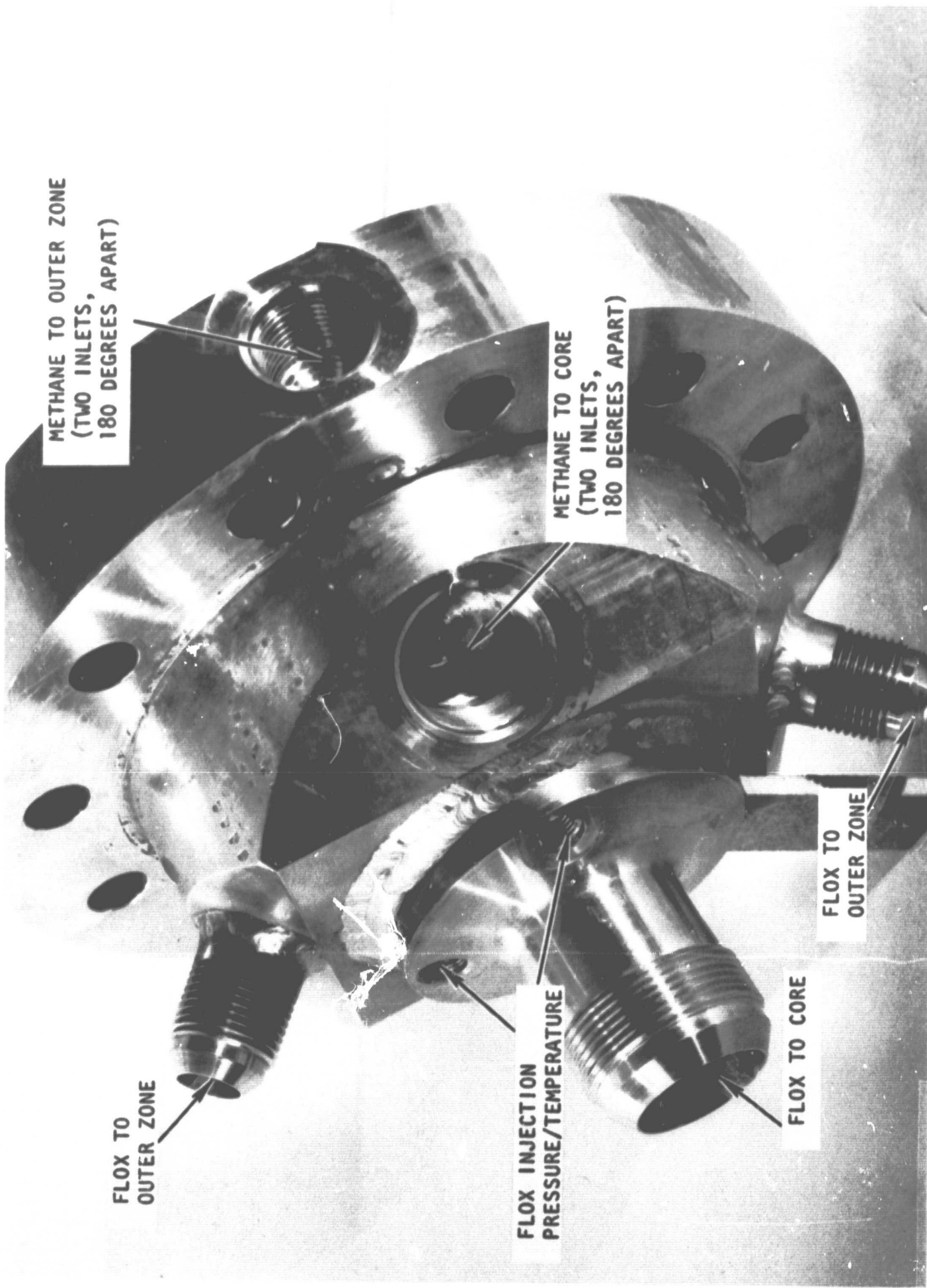
Figure 18. Front View Photograph of Five Plates Which Were Diffusion Bonded Together for "Optimized" Like-Doublet Injector Configuration (Pre-bond)



1XX41-4/7/71-S1K

Figure 19. Back View Photograph of Five Plates Which Were Diffusion Bonded Together for "Optimized" Like-Doublet Injector Configuration (Pre-bond)





SAA34-6/4/71-S1B

Figure 20. Photograph of Optimized Injector Configuration (Injector D)

4.2 THRUST CHAMBERS

The basic (reference) thrust chamber assembly consisted of multiple cylindrical chamber sections with an attached conventional (convergent-divergent) nozzle. This design fixture was selected to permit maximum use of available hardware while studying the effects of chamber L^*/length on performance. Since primary program emphasis was on the development of injector design criteria and not thrust chamber design, possibly cooled thrust chamber assemblies of a graphite material (ATJ graphite) were employed throughout the hot-fire experimental portion of the program. This approach minimized thrust chamber cost while still providing a means for determination of chamber heat flux levels. Provisions were made for measurement of transient circumferential and axial chamber and nozzle heat flux profiles.

4.2.1 Basic Configuration

Dimensions of the basic thrust chamber assemblies were established with the aid of results from the analytical parametric combustion study, certain injector design considerations, and the following system requirements:

Propellants: FLOX (82.6% F_2)/ CH_4 (g)
Design Operating Conditions: $P_c = 500$ psia
Mixture ratio - 5.25
Sea level thrust = 3000 lbf with an optimum sea level expansion nozzle
Performance target: 99-percent c^* efficiency (shifting equilibrium)

System requirements were specified in the program statement of work (Ref. 19). These requirements were used to define pertinent dimensions (throat diameter, expansion ratio, etc.) of the thrust chamber assembly. The results of the analytical performance study and injector design considerations were used to aid in defining the chamber contraction ratio and characteristic chamber lengths to be employed. Nozzle design details such as convergence angle, radius of curvature of the throat-to-throat radius ratio, etc., are similar to those commonly used on similar research programs (Ref. 3 and 17).

The selected chamber/nozzle parameters are listed below for the thrust chamber assemblies:

Nozzle throat area, in. ²	= 3.96
Nozzle throat diameter, in.	= 2.245
Nozzle expansion ratio	= 5.55 = optimum sea level expansion at $P_c = 500$ psia
Nozzle convergence angle, degrees	= 30
Exit nozzle (cone), degrees	= 15

$$\frac{R_c}{R_t} = \frac{\text{radius of curvature of nozzle throat}}{\text{throat radius}} = 2.0$$

$$\text{Contraction ratio} = \frac{A_c}{A_t} = \frac{\text{chamber cross-sectional area}}{\text{throat area}} = 3.0$$

Chamber diameter, in. = 3.888

Chamber L*, in. = 10, 20, 30, and 40

Detailed descriptions of the individual thrust chamber assembly components are given in subsequent paragraphs. Prior to this, however, the analytical performance study results and injector design considerations which were used to support selection of the chamber contraction ratio and characteristic chamber lengths are reviewed. The analytical performance study results were presented, in detail, in the preceding section of this report.

In the analytical study, performance calculations were made using the vaporization rate- and mixing-limited computer programs. Since mixing-limited c^* efficiency is not a direct function of chamber geometry, only the vaporization c^* efficiency portion of the analytical performance study is reviewed herein. Distribution considerations could influence selection of the chamber diameter (and, thereby, chamber contraction ratio) if the available injector area restricts the number of elements below that necessary for good mixing/controllable injector-chamber compatibility.

The two most important variables affecting the vaporization-limited c^* efficiency are propellant drop size and combustion chamber geometry. The effect of these two variables on $(\eta_{c^*})_{\text{vap}}$ was shown parametrically in Fig. 2 for FLOX (82.6% F_2)/ $\text{CH}_4(\text{g})$. Curves of $(\eta_{c^*})_{\text{vap}}$ as a function of initial propellant drop size are shown for conventionally shaped chambers having characteristic chamber lengths of 15, 30, and 60 in. Simplified schematics of the thrust chamber geometries considered for the combustion model analysis were shown in Fig. 3. The solid lines ($\epsilon_c = 2$) and dashed lines ($\epsilon_c = 4$) in Fig. 2 define the effect of contraction ratio at the given L^* values. The calculations are for a chamber pressure of 500 psia and a mixture ratio of 5.75.

As shown in Fig. 2, when propellant drop size is small, the effects of chamber geometry are generally attenuated. Conversely, when initial propellant drop sizes are large, chamber geometry effects become more pronounced. For a given initial drop size and chamber L^* , vaporization-limited c^* efficiency can be increased by reduction of the contraction area ratio (corresponding to an increase in physical chamber length). This (contraction ratio) effect is negligible at the high performance level ($\eta_{c^*} \geq 95\%$); however, it becomes significant when $(\eta_{c^*})_{\text{vap}}$ drops below 95 percent.

An important fact should be kept in mind when using Fig. 2 to estimate performance (c^* efficiency). The chamber geometry affects the initial propellant drop size. As was noted during the previous contract (Contract NAS3-11199; Ref. 3), for given injection conditions (orifice diameter, injection velocity, etc.) propellant drop size will be larger in the larger contraction ratio chamber.

Based on the above analytical performance study results, a 2:1 contraction ratio would have been selected for the basic thrust chamber assemblies. Injector design considerations, however, favored use of a higher contraction ratio chamber. A chamber contraction ratio greater than 2:1 is required to permit use of an injector with sufficient elements for good mixing and to allow use of a sufficient number of peripheral elements to control injector-chamber compatibility. Element feeding problems severely limit the number of elements that could be placed in 2:1 contraction ratio chamber injectors. This problem was discussed in the Injector Design section of this report. A nominal, 40-in. L^* , 3:1 contraction ratio chamber was used as the reference chamber assembly.

Chamber L^* could be varied over the 10- to 40-in. range with existing hardware. The 40-in. L^* was chosen as a reference value so that performance losses due to incomplete vaporization would be very small in the reference chamber. (Propellant mean drop sizes \leq 75 microns were expected.) Prime consideration could then be directed toward experiments designed to assess effects of propellant distribution on performance and chamber compatibility. In addition, the reference chamber L^* and contraction ratio are similar to those commonly employed in related programs (e.g., Ref. 17), thus permitting direct comparisons to be made between program results. The L^* range chosen for study permitted definition of chamber L^* effects on performance over a practical range of chamber size.

The cylindrical chamber/nozzle sections consisted of stainless-steel shells (or housing) with ATJ graphite liners. The steel shells were made from pipe and had welded flanges. A liner thickness of \sim 1 in. was sufficient to permit test durations suitable for definition of performance and transient chamber/nozzle heat transfer characteristics. Chamber construction was similar to that successfully used in Contract NAS7-304 (Chamber Technology for Space Storable Propellants; Ref. 17).

A schematic representation of the reference chamber ($L^* = 40$ in.; $\epsilon_c = 3$) assembly is presented in Fig. 21. Direct attachment of the nozzle only to the injector would result in a 10-in. L^* chamber. The L^* of each cylindrical chamber section is 10 in. Consequently, hardware was available for 10-, 20-, 30-, or 40-in. L^* chambers.

The nozzle convergence angle (30 degrees) and exit configuration (15-degree cone) are similar to those commonly used in numerous research program at Rocketdyne (e.g., Ref. 3 and 17). A radius of curvature of the nozzle throat-to-throat radius rates (R_c/R_t) of 2.0 was chosen because the nozzle discharge coefficient for this specific configuration is well defined. A known nozzle discharge coefficient is essential for a valid definition of performance (based on chamber pressure measurement). The chamber liner was bonded into the housing and was retained at the exit end by the retainer plate.

For calculation of a "valid" performance value (based on chamber pressure measurement) care must be taken to ensure measurement of a "valid" static chamber pressure near the start of nozzle convergence. Experience gained on related programs at Rocketdyne (Ref. 3 and 20) indicate that an increase in static chamber pressure can occur near the start of convergence. This increase in pressure appears to be

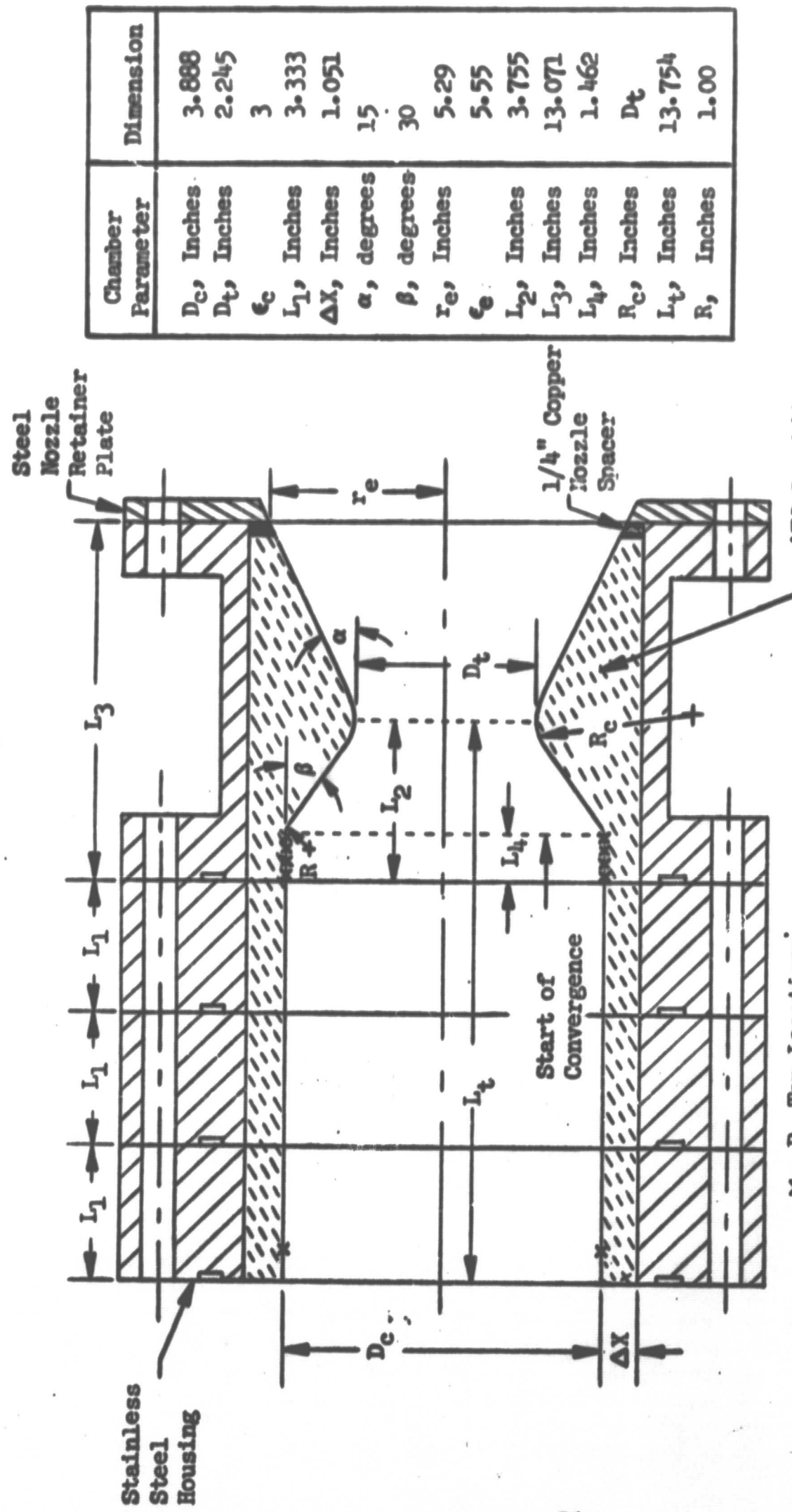


Figure 21. Schematic Representation of Reference (L* = 40 In.; ϵ = 3) Chamber Assembly Showing Segmented Design and Dimensions

caused by the subsonic decelerating effects associated with the turning of the combustion gases prior to acceleration in the nozzle. The magnitude of this increase is dependent on the geometric configuration of the nozzle. Measurement of the static pressure must be taken sufficiently far upstream of the start of convergence so that its value is not affected by the subsonic decelerating effects discussed above. Furthermore, chamber pressure must be measured where combustion is nearly complete.

To ensure that the proper static chamber pressure measurement was employed for calculation of performance, the hot-fire static pressure profile along the wall of the nozzle section was determined. Static pressure taps were located axially along the wall of the initial nozzle assembly so that the pressure profile in the region near the start of convergence was well defined. Location of the chamber pressure taps in the initial nozzle are noted in Fig. 21. Pressure taps were located at four axial positions in the nozzle. Two taps 180 degrees apart were located 1/2, 0.75, 1.00, and 1.25 in. downstream of the nozzle assembly inlet. The start of nozzle convergence is 1.462 in. downstream from the nozzle inlet. Subsequent/backup chamber assemblies employed chamber pressure taps located at only two axial positions: two taps 180 degrees apart, 1/2 in. from the injector face, and three taps 120 degrees apart, 0.712 in. upstream of the start of nozzle convergence. The correct placement for the latter three chamber pressure taps was based on results of tests conducted in the initial nozzle.

The nozzle has an optimum sea level expansion ratio (5.55) at the design operating conditions ($MR = 5.25$; $P_c = 500$ psia). Nozzle exit base pressure was measured by means of pressure taps placed in the nozzle retainer ring to ensure that a valid thrust measurement was used for calculation of performance.

4.2.2 Heat Flux Transducer

Specially designed heat flux transducers were installed in the chamber/nozzle regions to measure heat flux profiles. A schematic representation of the chamber heat flux transducers employed is shown in Fig. 22.

The 1/4-in.-diameter graphite rods were fabricated from a graphite material with relatively well-defined thermal properties (thermal conductivity, specific heat, etc.). These heat flux transducers offer several advantages (e.g., reduced cost and increased data precision) over other potential methods of obtaining heat flux measurements in graphite thrust chambers.

This heat flux meter design is substantially more economical (~\$100 each) than that of other proved heat flux transducers. Their construction also permitted reuse of the tantalum-sheathed, tungsten-rhenium thermocouples in subsequent heat flux transducers, thereby further reducing the overall cost of the heat flux measurements. The rod installation technique offers several advantages over simply embedding thermocouples in the chamber wall. Exact determination of thermocouple depth is possible. This would not be possible if thermocouples were simply embedded in the chamber wall. The quality of the heat flux data is a direct function of the precision of the measurement of the thermocouple depths. The rod technique also provides a resistance interface and permits measurement of one-dimensional heat flux values. A photograph of the hardware on the test stand (Willie stand in the Propulsion Research Area) is shown in Fig. 23.

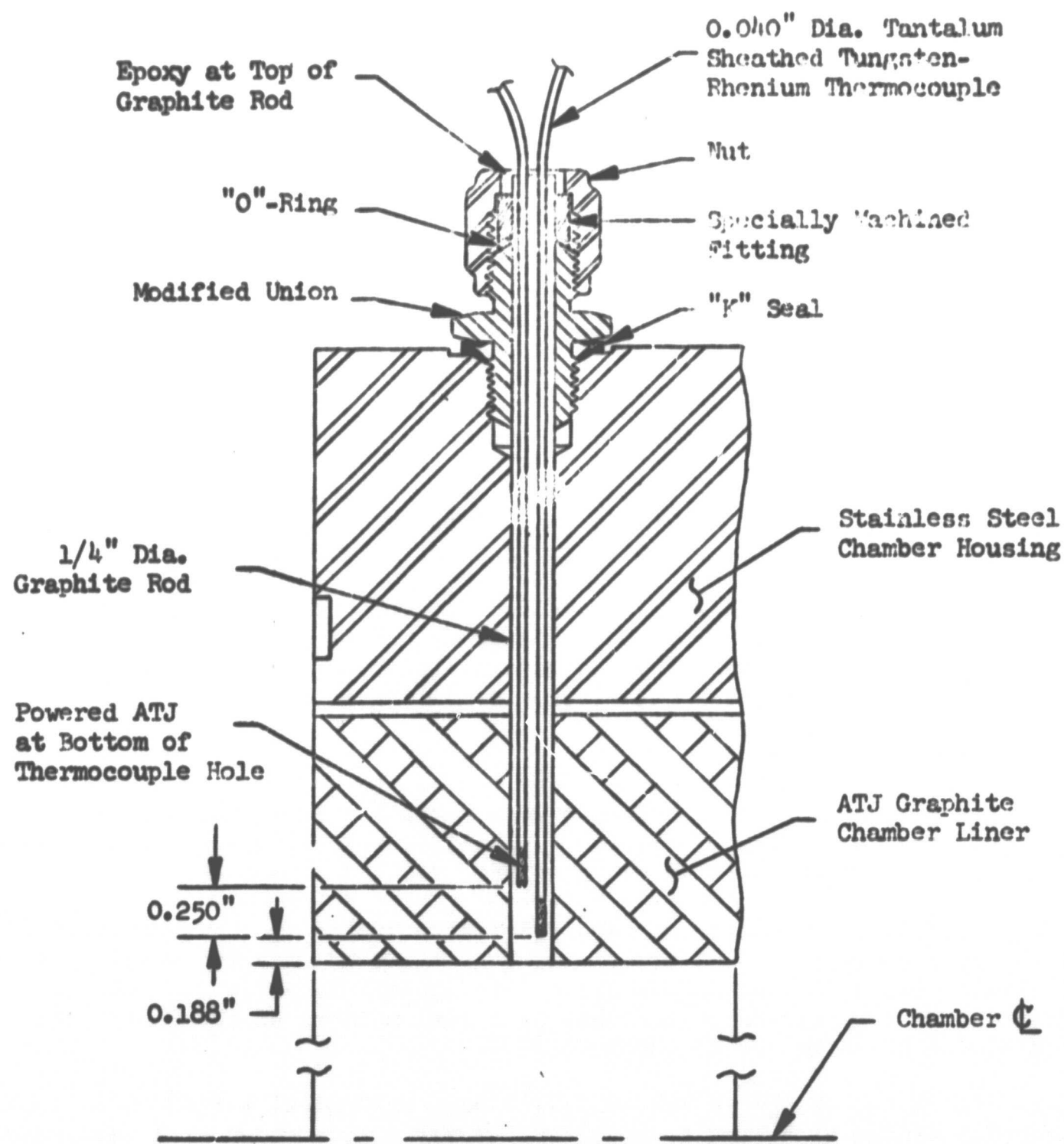
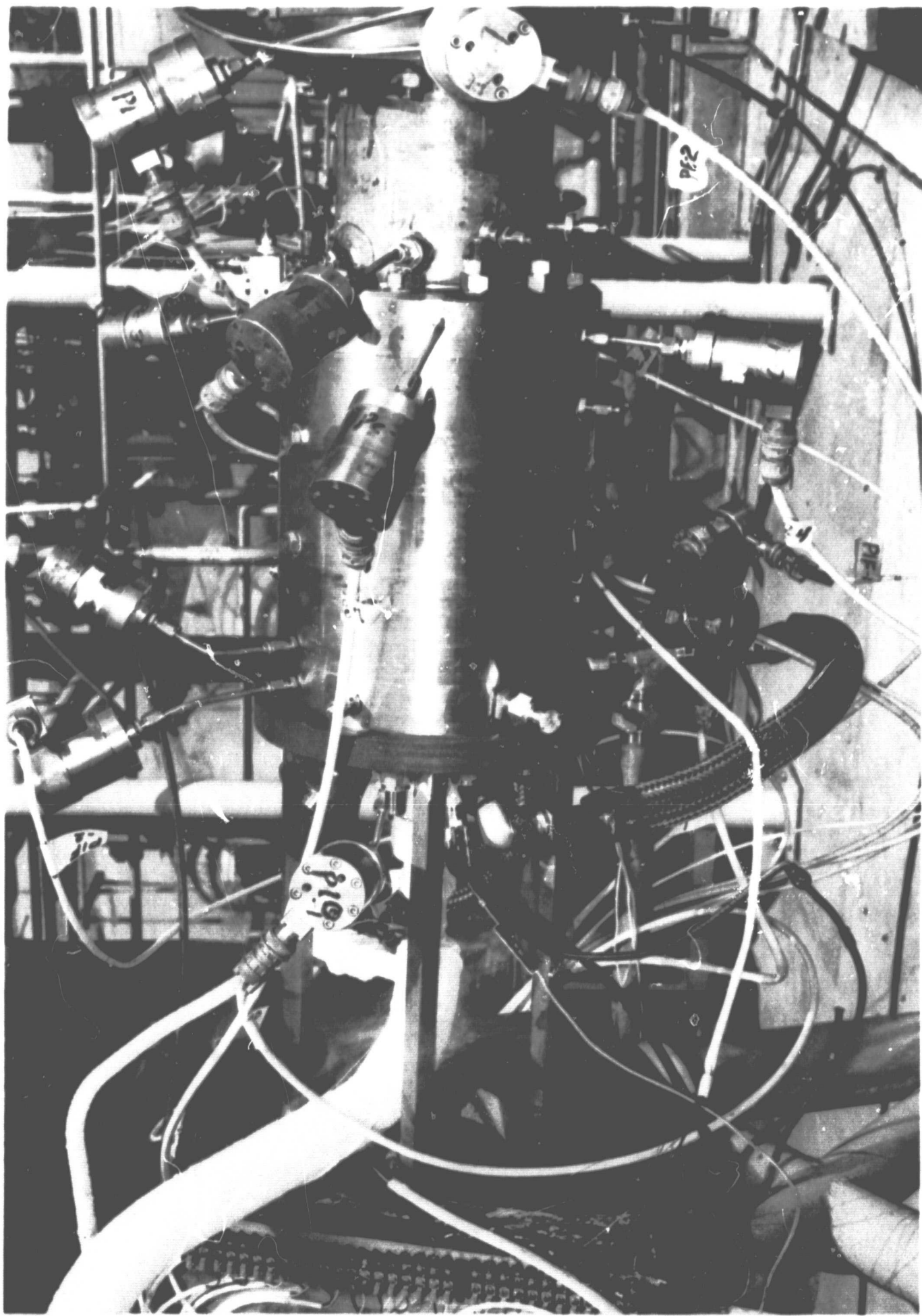


Figure 22. Schematic of Chamber Heat Flux Transducer

5AA24-6/14/71-S1B

Figure 23. Photograph of Hardware on Test Stand Willie at Propulsion Research Area



PRECEDING PAGE BLANK NOT FILMED

5.0 EXPERIMENTAL RESULTS AND DISCUSSION

The program experimental results are presented herein under three separate major topic headings: (1) Injector Models, (2) Full-Scale Performance and Chamber-Compatible Injectors, and (3) Optimized Injector Configuration.

5.1 INJECTOR MODELS

Results from cold-flow distribution and atomization experiments, conducted with injector models, to support design of the full-scale hot-fire hardware are presented herein. All injector model experiments conducted during the like-doublet portion of the subject contract (NAS3-12051) were cold-flow simulation tests. The majority of the experiments were mixing oriented and were conducted primarily using single elements. Mixing tests were conducted to provide element design criteria for both the performance (A) and chamber-compatible (C) injectors using single elements. One mixing test was conducted with a 1/4-segment model of an A injector configuration to provide information on element density/interaction effects on mixing. Atomization experiments also were conducted with performance-type (fan spacing = 0) single elements to define the effects of the gaseous fuel injection and throttling on liquid (oxidizer) atomization.

The primary design and operating variables (parameters) that can influence performance/chamber compatibility for the like-doublet element are fan spacing, propellant momentum ratio, and for inclination angle. Experiments were conducted with the performance-type element (fan spacing = 0) to define (optimize) mixing as function of propellant momentum ratio and fan inclination angle. Element density/interaction effects also can significantly influence performance of a like-doublet injector. Consequently, element density/interaction effects on mixing also were studied with performance-optimized like-doublet elements. Experiments were conducted with the chamber-compatible (i.e., nonzero fan spacing) type element to define mixing levels and chamber wall mixture ratio distribution as a function of fan spacing, for inclination angle, and propellant momentum ratio.

Performance element and chamber-compatible element experimental results are presented under separate headings in subsequent paragraphs.

5.1.1 Performance Element

Initially, single-element performance element experimental results from mixing experiments conducted prior to complete development of the mixing test apparatus/procedures of Appendix B are presented. These results were used as a basis for design of the A injector. Results from mixing experiments conducted later in the program (after development of the facility and procedures described in Appendix B) to confirm these initial results are presented next. This is followed by discussion of the element density effects and single-element atomization characteristics experimental results.

Single-Element Mixing Characteristics. Details of the single-element, cold-flow mixing/distribution experiments conducted to support design of the A (performance) injector are presented herein.

Injector A was designed primarily for high performance in terms of having specific element features that promote efficient propellant mixing/atomization. To attain high performance with FLOX (82.6%)/CH₄(g), careful consideration must be given to injector design variables that influence propellant distribution (mixing). For the like-doublet pattern, propellant mixing depends primarily on the degree of interpenetration of paired fuel and oxidizer spray fans. The geometric factors affecting propellant distribution for a like-doublet element were shown in Fig. 10. For a fixed geometry, mixing is primarily a function of the propellant momentum ratio, defined as the ratio of the injected momentum flux of the oxidizer doublet to that of its paired fuel doublet.

Previous experience with liquid/liquid propellant systems employing like-doublet element injectors and specific injector design constraints for this program were used to help select a practical test matrix to support definition of element design criteria for the A injector. Preselection of a zero fan spacing (S) and impingement angle (β) as optimum was predicated on previous studies with liquid/liquid propellant systems. Design considerations for the full-scale injectors (number of elements required for simultaneous attainment of high performance and control of injector-chamber compatibility, available injector face area, orifice diameters required for good atomization/reasonable injector pressure drops, etc.) limited the range of usable intra-element spacing (~0.15 to 0.30 in.) and orifice diameters (~0.03 to 0.09 in.). An intra-element spacing of 0.20 in. was employed for the initial experiments. Selection of this value was based on previous experience with liquid/liquid propellant systems. Those results indicate that, in general, optimization of the spacing and fan inclination angle are interrelated. However, in the range of practical interest for injector A, intra-element spacing effects have been negligible. Fan inclination angle (α) and propellant momentum ratio were, therefore, selected as the primary test variables. Previous experience with liquid/liquid like-doublet elements indicated that both of these variables influence mixing and lend themselves to optimization.

Six single-element, cold-flow mixing experiments were initially conducted to support definition of element design criteria for the A injector. The fan inclination angle (α) was varied in 15-degree increments from 0 to 45 degrees at a constant momentum ratio (o/f) of 0.25, and momentum ratio was varied from 0.25 to 1.0 at a constant fan inclination angle of 15 degrees. The gas orifice diameter was varied at constant mixture ratio to permit variation of the propellant momentum ratio at fixed flowrates. A liquid orifice diameter of 0.052 in. and gas orifice diameters of 0.055, 0.082 and 0.104 were employed. A summary of the cold-flow mixing test conditions and results are presented in Table I. The tests were conducted at a mixture ratio near that for the planned hot-fire elements (~5).

It should be noted that during these cold-flow experiments, momentum ratio was varied by successive enlargement of the gas orifice diameter at constant mixture ratio and chamber pressure. During the hot-fire tests, momentum ratio was varied by: (1) throttling at constant mixture ratio, (2) varying mixture ratio at constant chamber pressure, and (3) successive enlargement of the fuel/oxidizer orifice diameters.

TABLE I. SUMMARY OF COLD-FLOW TEST CONDITIONS* AND RESULTS
(For Initial Series of Single-Element Mixing Experiments
to Define Element Design Criteria for Injector A)

Test No.	Element Configuration		α , Fan Inclination Angle, Degrees	\dot{m}_g , lbm/sec	\dot{m}_g' , lbm/sec	Mixture Ratio, \dot{m}_g'/\dot{m}_g	Momentum Ratio, Liquid-to-Gas	Σ_m , $\frac{\dot{m}_g}{\dot{m}_g'}$	$(\eta_{c*})_{dist}$
	d_g , inches	d_g' , inches							
1	0.055	0.052	0	0.098	0.0181	4.96	0.25	64.0	80.3
2			15	0.092	0.0182	4.90		63.4	78.9
3			30	0.0871	0.0178	4.90		64.0	82.9
4			45	0.0902	0.0182	4.95		67.0	83.5
5	0.082		15	0.0890	0.0182	4.89	0.56	61.8	77.3
6	0.104		15	0.0890	0.0182	4.89	0.90	60.8	76.2

*Simulated Conditions: $\text{FLOX} (82.6\% \text{F}_2)/\text{CH}_4(\text{g})$

Chamber Pressure: 500 psia

Mixture Ratio: 5.0

Tests conducted with conical diffuser
gas recirculation suppression device

Propellant Simulants: $\text{FLOX} (82.6\% \text{F}_2)$ ---Water
 $\text{CH}_4(\text{g})$ ----- $\text{CH}_4(\text{g})$ ----- $\text{CH}_4(\text{g})$

**Fan Spacing = $S = 0$; Fan Impingement Angle = $\beta = 0$; Intra-Element Spacing = $Y = 0.20$ -inch; as defined in Fig. 10.
Impingement angle of individual doublet streams was 60 degrees.

The distribution experiments described in Table I were conducted in a pressurized environment to model the hot-fire gas/liquid flow fields of interest. Test conditions simulated were: propellants = FLOX (82.6% F_2)/ $CH_4(g)$; chamber pressure = 500 psia; MR = 5.0. Propellant simulants were water (FLOX) and GN_2 (methane). A description of the pressurized gas/liquid cold-flow mixing facility and its operating procedures are presented in Appendix B. However, these experiments were conducted early in the development of the apparatus and procedures and were not conducted according to the later developed methods described in Appendix B. Instead of employing a low-velocity base bleed to suppress flow field recirculation, the elements were cold-flowed into a conical diffuser (Fig. 24). As will be shown later, results of these initial experiments led to selection of element design parameters/operating conditions for the A injector similar to those based on the later experiments. Distribution measurements were made ~ 2 in. from the injector face.

A considerable amount of gas recirculation (~ 4 to 8 times the injected gas flow-rate) was encountered during this first set of single-element distribution experiments. This was indicated by negative dynamic pressure measurements in zones of reversed gas flow as well as by the large flowrates measured in zones of positive dynamic pressure. The gas mass flux profile was normalized for calculation of $E_m/\eta_{c^*}^{mix}$. Liquid collection efficiency was near 100 percent. Mixing-limited c^* efficiency, $(\eta_{c^*})^{mix}$, and mixing efficiency, E_m , are shown in Fig. 25 for these experiments. As seen in Fig. 25A for a fixed liquid-to-gas momentum ratio (0.25), both values appear to be relatively independent of fan inclination angle over the range studied. These same parameters are shown plotted as a function of propellant momentum ratio (liquid-to-gas) for a fan inclination angle of 15 degrees in Fig. 25B. E_m and $(\eta_{c^*})^{mix}$ also appear to be relatively independent of propellant momentum ratio over the range investigated. It should be noted that the levels of $E_m/(\eta_{c^*})^{dist}$ obtained from these gas/liquid single-element experiments are comparable to those obtained with similar single-element liquid/liquid like-doublents. Because of the relative insensitivity of $(\eta_{c^*})^{mix}$ to α and M_o/M_f seen in these results, selection of a specific inclination angle and/or momentum ratio for the A injector required further analysis of the distribution data. As will be described below, examination of local values of the propellant mass flux distribution provided criteria for selection of a specific fan inclination angle and momentum ratio for the A injector elements.

Graphical display of local values of total propellant mass flux for these six single-element experiments are presented in Fig. 26 and 27. These plots are presented to permit further evaluation of fan inclination angle and propellant momentum ratio effects on propellant distribution. The data are presented in the form of crosshatch plots. The density gradation of the crosshatch permits visual determination of the relative concentration or intensity. The circular shape of the plots is that imposed by the conical diffuser (Fig. 24). Table II provides an index to indicate the quantitative value of the crosshatch densities in Fig. 26 and 27.

The effects of fan inclination angle on the local values of total propellant mass flux for a liquid-to-gas momentum ratio of 0.25 are shown in Fig. 26. Examination

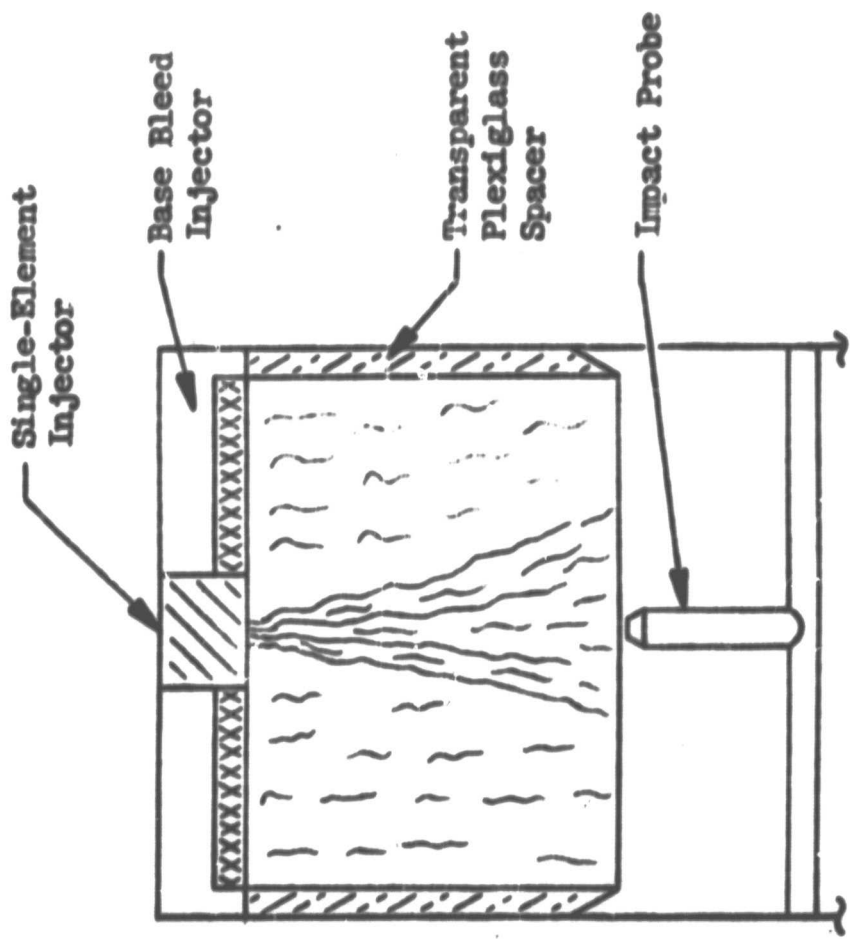
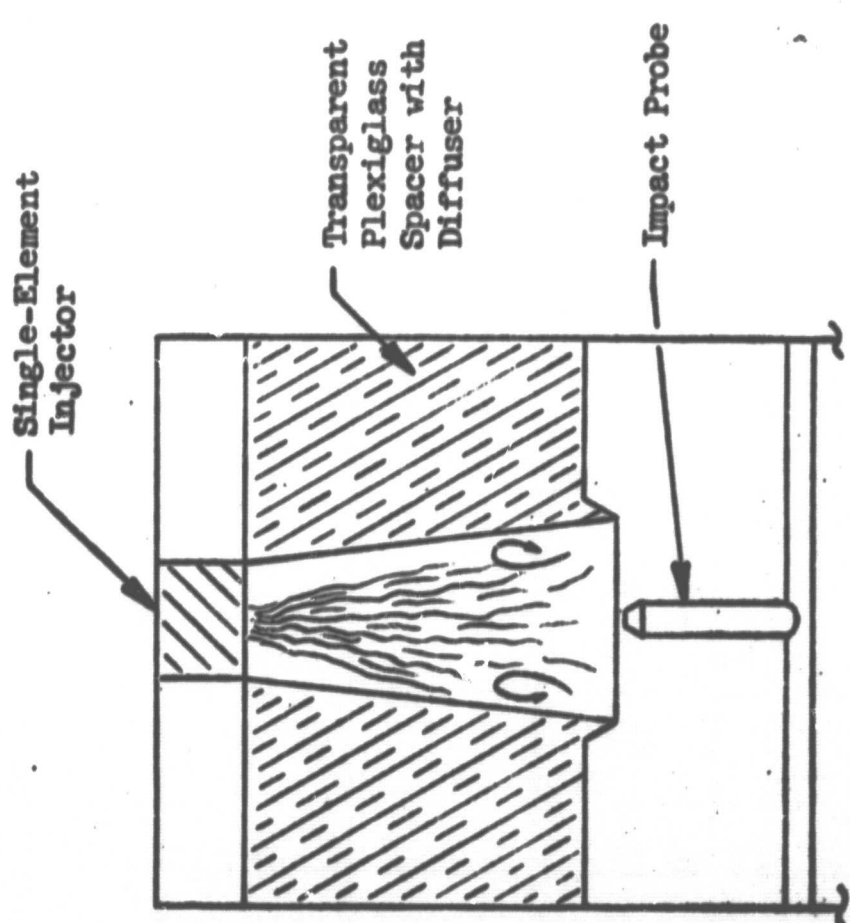


Figure 24. Schematics of Conical Diffuser and Base Bleed Injector Gas Recirculation Suppression Devices Used for Single-Element Cold-Flow Mixing Experiments

SIMULATED CONDITIONS:

Propellants-----FLOX(82.6% F₂)/CH₄(g)
 Chamber Pressure----500 psia
 Mixture Ratio-----5.0

PROPELLANT SIMULANTS:

FLOX-----Water
 CH₄(g)-----GN₂

ELEMENT ORIENTATION

●● -Liquid Doublet ($d_L = 0.052$ -Inches)
 ○○ -Gas Doublet ($0.055'' \leq d_g \leq 0.104''$);
 depending on M
 S = 0 = Fan Spacing
 $\beta = 0$ = Fan Impingement Angle
 Y = 0.20-Inch = Intra-Element Spacing

Tests Conducted Employing Conical Diffuser of Figure 24

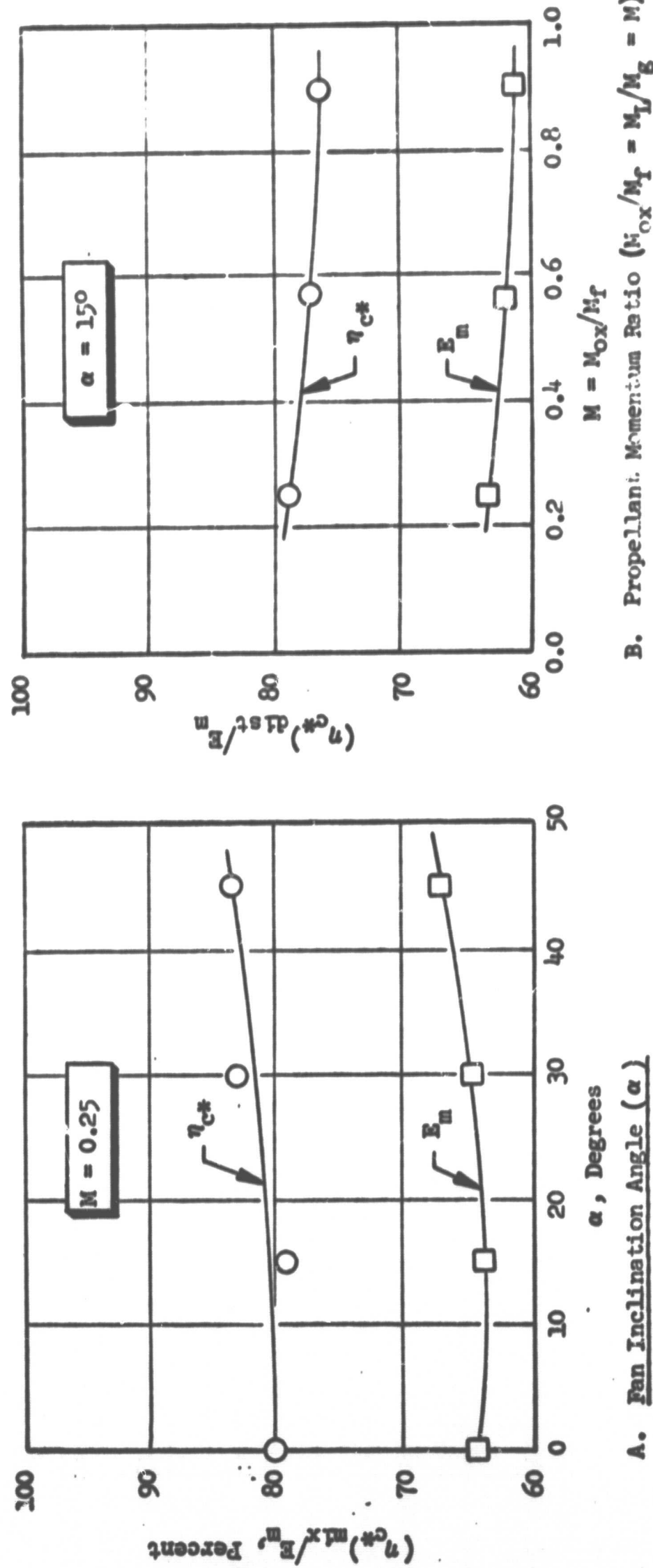
A. Fan Inclination Angle (α)B. Propellant Momentum Ratio ($\eta_{c*} / \eta_f = M_{ox} / M_f = M$)

Figure 25. Distribution c^*/E_m Mixing Efficiency as a Function of Fan Inclination Angle (α) and Propellant Momentum Ratio (M) for Zero Fan Spacing Single-Element Gas/Liquid Like-Doublet Elements

SIMULATED CONDITIONS:

Propellants ----- FLOX(82.6% F₂)/CH₄(g)

Chamber Pressure ----- 500 psia

Mixture Ratio ----- 5.0

Momentum Ratio (o/f) = M = 0.25

PROPELLANT SIMULANTS:

FLOX ----- Water

CH₄(g) ----- GN₂

ELEMENT ORIENTATION:

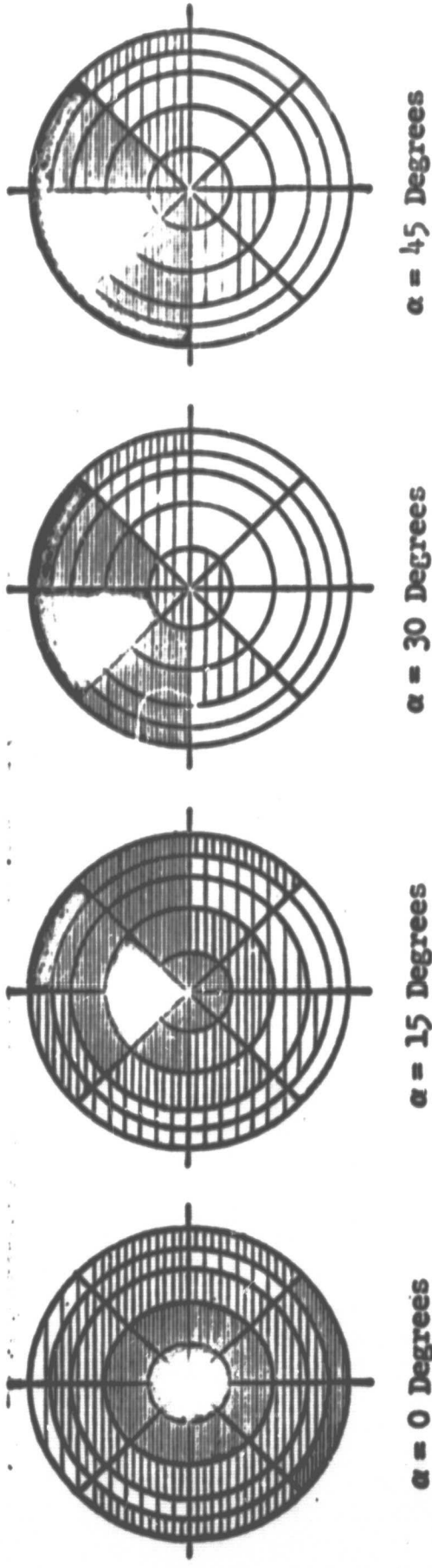
● → Liquid Doublet (d₁ = 0.052-Inch)

○ → Gas Doublet (d_g = 0.055-Inch)

S = Fan Spacing = 0

β = Fan Impingement Angle = 0

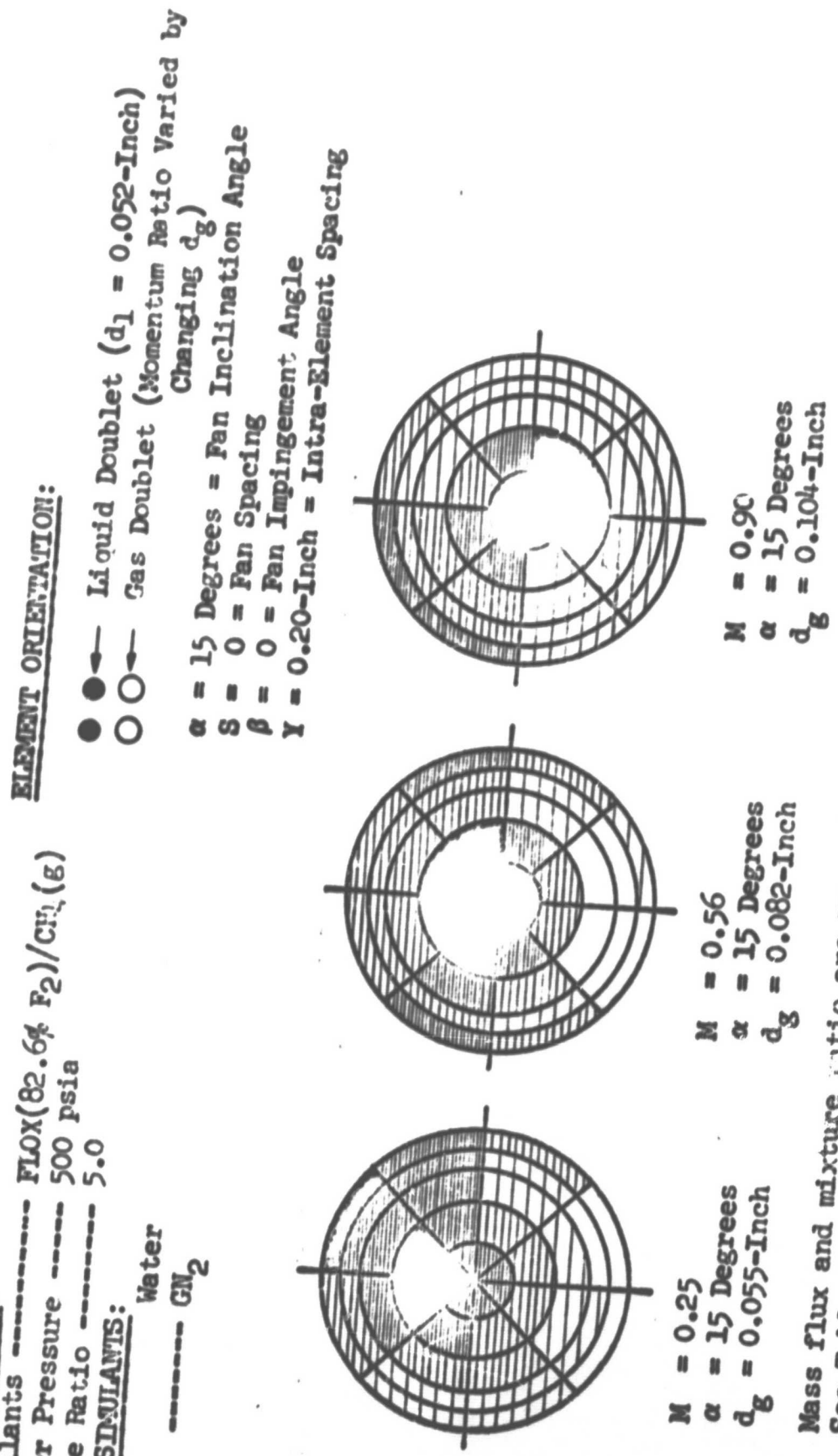
Y = Intra-Element Spacing = 0.20-Inch



Mass flux is proportional to grid density. See Table II for quantitative index to grid density.

Figure 26. Effect of Fan Inclination Angle (α) on Local Propellant Mass Flux Distribution for Zero Fan Spacing Single-Element Gas/Liquid Like-Doublet Element

<u>SIMULATED CONDITIONS:</u>	
Propellants	— FLOX($82.6\% F_2/CH_4(g)$)
Chamber Pressure	— 500 psia
Mixture Ratio	— 5.0
<u>PROPELLANT SIMULANTS:</u>	
FLOX	— Water
$CH_4(g)$	— CH_4



Mass flux and mixture ratio are proportional to grid density.
See Table II for quantitative index to grid density.

Figure 27. Effect of Propellant Momentum Ratio (α/f) on Local Propellant Mass Flux Distribution for Zero Fan Spacing Single-Element Gas/Liquid Like-Doublet Elements

TABLE II. QUANTITATIVE INDEX TO GRID DENSITIES IN FIG. 26 AND 27

Parameter	Figure	Symbol	Range of Parameter	Grid Density, cm/division
Local Total Propellant Mass Flux, $\text{lbm/in.}^2 \cdot \text{sec} \times 10^2$	26/27	X	$X < 0.6$ $0.6 \leq X < 2.4$ $2.4 \leq X < 6.0$ $6.0 \leq X < 12.0$ $12.0 \leq X$	∞ 0.20 0.10 0.05 Solid

of this figure indicates that as the fan inclination angle is increased, the mass flux plots become more nonuniform/unsymmetrical. Since all appear to yield nearly the same mixing-limited c^* efficiency (Fig. 25), a low fan impingement angle would be favored because of the more uniform overall mass flux distribution. The effect of the gas on resultant distribution is quite noticeable at the high fan inclination angles. Propellant distribution is controlled by the gas at high fan inclination angles because of the low liquid-to-gas momentum ratio (i.e., the overall mass is driven in the direction of the net injected gas momentum vector).

From injector design/fabrication considerations, a low fan inclination angle also is favorable. A high fan inclination angle considerably increases the design/drilling complexity of the injector. It also increases the required area per element and decreases the number of elements that can be placed in a fixed area. For these reasons, a low fan inclination angle is desirable.

The effect of momentum ratio on local values of total propellant mass flux for a fan inclination angle of 15 degrees is shown in Fig. 27. Examination of this figure reveals that as the liquid-to-gas momentum ratio is increased (from 0.25 to 0.90) the mass flux plots change considerably. The most uniform/symmetrical mass flux profiles would appear to occur at intermediate liquid-to-gas momentum ratios in the range of 0.56 to 0.90.

A fan inclination angle of 15 degrees in conjunction with an oxidizer-to-fuel momentum ratio of 0.75 at design operating conditions was chosen for the A injector elements. Selection of these values for α and M were based on: (1) the above data, (2) previous experience with liquid/liquid systems that indicate $\alpha = 0$ is not optimum, and (3) design considerations which limit the practical momentum ratio to the 0.25 to 2.0 range. Hot-fire variation of propellant momentum ratio was planned to further optimize this parameter (momentum ratio).

In summary, the following design parameters were incorporated into the initial A injector elements: fan spacing, $S = 0$; fan impingement angle, $\beta = 0$; intra-element spacing, $Y = 0.20$ in.; fan inclination angle, $\alpha = 15$ degrees; momentum ratio (o/f) ≥ 0.75 at design conditions ($P_c = 500$ psia; MR = 5.25).

Shortly after completion of the initial series of single-element, cold-flow mixing experiments, which were conducted to support design of the A (performance) injector, the facilities and procedures described in Appendix B were completed. Consequently, to further ensure that the element design parameters of the D injector core elements (fan spacing = 0) were optimum, and to support future analysis of hot-firing performance data, additional single-element cold-flow mixing tests were conducted with the candidate D injector core elements. The elements considered were 3/4-scale reductions ($S = 0$; $\beta = 0$; $Y = 0.15$ in.; $d_L = 0.037$ in.; $d_g = 0.043$ in.; $\alpha = 0, 15$, and 30 degrees) of those originally employed to define design criteria for the A injector. Mixing experiments were conducted to define the effects of fan inclination angle (α) and momentum ratio on $E_m/\eta_{c^*}^*,_{mix}$. Results from these experiments are presented in Fig. 28 and 29, and are discussed below. A summary of the test conditions and data are presented in Table III.

The effect of fan inclination angle on propellant mixing for the candidate D injector core element is shown in Fig. 28. As expected, $E_m/\eta_{c^*}^*,_{mix}$ were relatively independent of α . The results presented in this figure are for a mixture ratio of 5.25 and a momentum ratio o/f of 0.64. Results for tests conducted with the single elements employing the conical diffuser gas recirculation device are presented in Fig. 28 for comparison. The results for the two series of experiments are similar. Higher mixing levels were achieved in the later series of experiments, primarily due to its operation at a more optimum momentum ratio (0.64 as compared to 0.26; Fig. 29).

The effect of momentum ratio (liquid-to-gas) on mixing for a D injector core element ($\alpha = 15$ degrees) is shown in Fig. 29. Increasing the momentum ratio from 0.3 to 0.6 increases the mixing index E_m by approximately 4.5 percent (64.4 to 68.6). E_m is relatively independent of momentum ratio for momentum ratios ≤ 0.6 over the range investigated (0.3 to 2.0). Results from the earlier tests conducted employing the conical diffuser are again presented for comparative purposes. As indicated, over the range studied, the two sets of data show different trends with increasing momentum ratio. The trend indicated by the tests conducted employing the base bleed gas recirculation suppression technique matches that observed in the hot-fire tests (Fig. 41). This result is attributed to the better simulation of hot-fire conditions by the base bleed gas recirculator suppression technique. In summary, although this later series of tests did not change the element design/operating parameters for the D injector core elements, it did put the design criteria on a higher confidence level.

Element Density/Interaction Effects on Mixing. Since single-element mixing levels were low ($E_m \geq 65$ to 70), it was recognized early in the program that substantial inter-element mixing in the full-scale injectors would be required to achieve high performance. This result was of no great concern since the mixing levels of the gas/liquid single-element were similar to those of liquid/liquid single elements. Element density of the initial (A) injector was based on previous experience with

TABLE III. SUMMARY OF COLD-FLOW MIXING TEST CONDITIONS* AND RESULTS FOR SINGLE-ELEMENT EXPERIMENTS CONDUCTED TO VERIFY INJECTOR D CORE ELEMENT DESIGN

Test No.	Fan Inclination** Angle, α , Degrees	Propellant Momentum Ratio (o/f)	P_c , psia	\dot{W}_q , lbm/sec	\dot{W}_g , lbm/sec	Mixture Ratio \dot{W}_q/\dot{W}_g	E_{III} , %	$\eta_{c^*, \text{mix}}$, %
1	0	0.64	500	0.0892	0.0170	5.25	66.5	85.9
2		0.64	500	0.0892	0.0170	5.25	68.6	86.1
3	30	0.64	500	0.0892	0.0170	5.25	68.5	87.2
4	15	0.32	250	0.0452	0.0086	5.25	64.4	83.5
5	15	1.91	500	0.1050	0.0117	9.0	66.6	86.2

*Simulated conditions: FLOX (82.6% F_2)/ CH_4 (g)

P_c - noted in Table

MR - noted in Table

Tests conducted employing base bleed gas recirculation suppression technique.

Propellant simulants: FLOX-----water
 CH_4 (g)----- gN_2

** $d_q = 0.043"$; $d_{ox} = 0.037"$

$S = 0$; $\beta = 0$; $Y = 0.15"$

Impingement angle of individual doublet streams was 60 degrees.

Simulated Conditions:
 FLOX (82.6% F₂)/CH₄(8)
 P_c = 500 Psia
 MR = 5.25
 Mon. Ratio = 0.64

d_f = 0.043"; d_{ox} = 0.037"
 S = 0; β = 0
 Intra-Element Spacing = 0.15"

- Data from tests conducted employing base bleed gas recirculation suppression technique.
- - - Data from tests conducted employing conical diffuser gas recirculation suppression device.

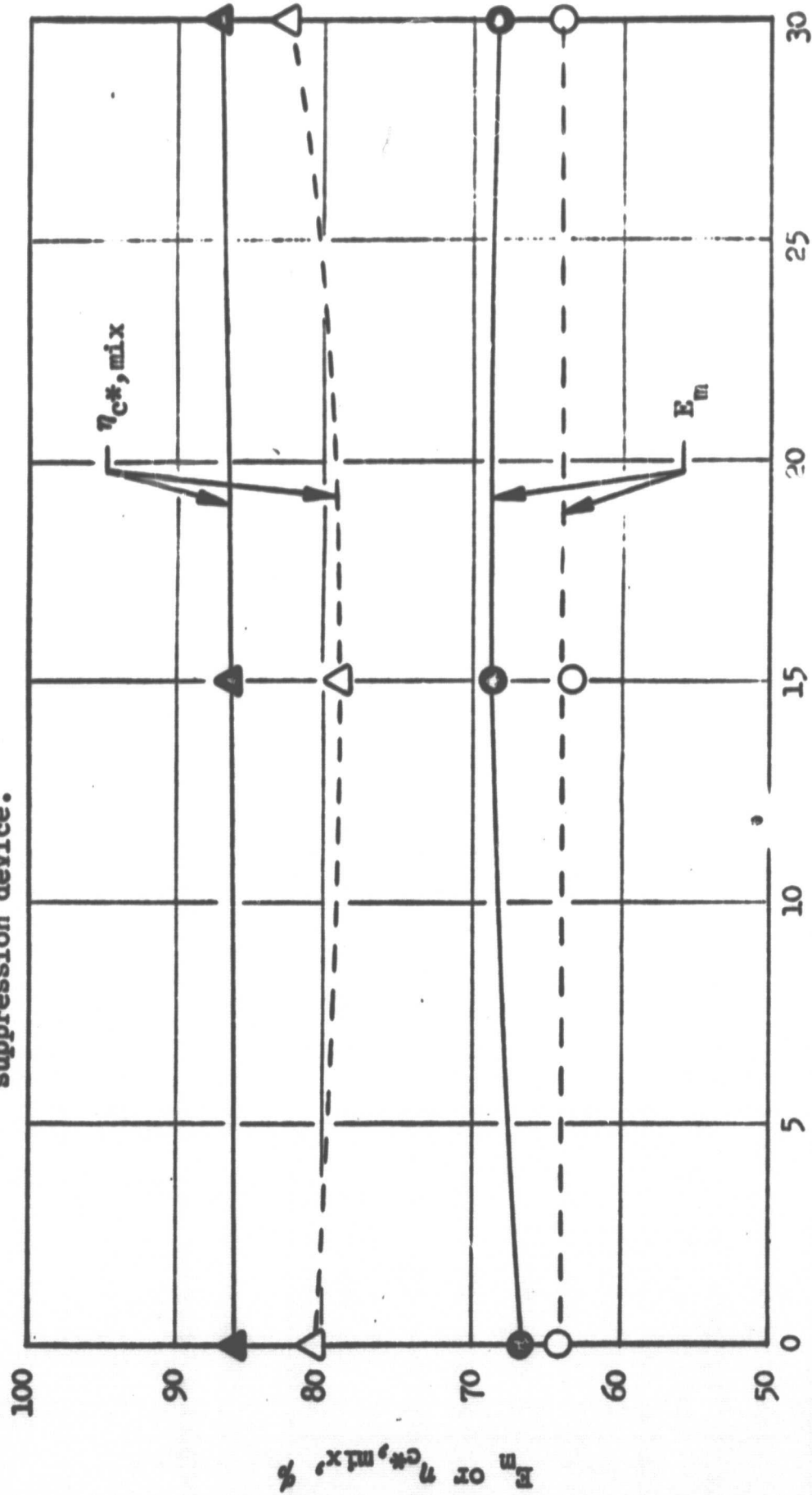


Figure 28. Effect of Fan Inclination Angle (α) on Mixing for Candidate D Injector Core Elements (Fan Spacing = 0)

$d_f = 0.043"$; $d_{ox} = 0.037"$
 $\alpha = 1.5^\circ$; $\beta = 0$
 Intra-Element Spacing = 0.15"
 $S = 0$

Simulated Conditions for
 FLOX (82.6% N_2)/ CH_4 (g)
 are noted

- Data from tests conducted employing base bleed gas recirculation suppression device.
- - - Data from tests conducted employing conical diffuser gas recirculation suppression device.

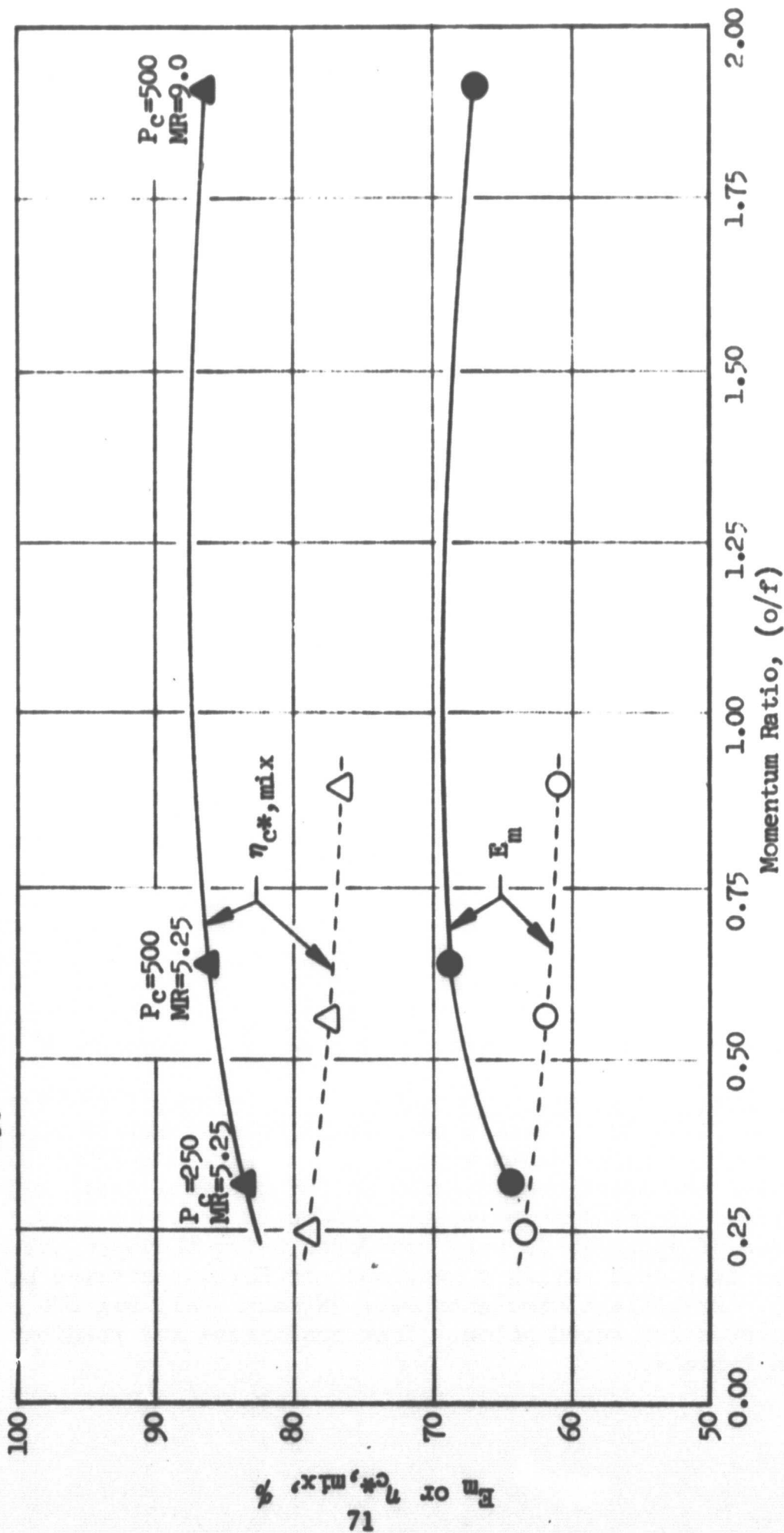


Figure 29. Effect of Momentum Ratio on Mixing for D Injector Core Single-Element
 (Fan Spacing = 0)

liquid/liquid propellant systems. However, a quantitative correlation between element density and mixing level was required to put gas/liquid like-doublet injector design on a firm basis. Consequently, cold-flow mixing experiments were conducted to provide this information.

Data points for definition of element density (interaction) effects on mixing were provided by the single-element and cold-flow evaluation of the A injector. However, to further define element density effects on propellant mixing, a 1/4 segment model of the A injector with an element density $\sim 1\text{-}1/2$ times that of the A injector was fabricated and cold-flow tested. Analysis of these cold-flow mixing data for the mixing optimized zero fan spacing element indicated that to achieve the desired performance goal (99-percent c^* efficiency), an element density (i.e., number of elements per square inch of injector face surface area) in the D injector core about twice that of the initial A design would be required, using previously defined optimized element design (fan inclination angle, fan spacing, etc.) and operating (momentum ratio, etc.) parameters.

Cold-flow c^* mixing efficiency and E_m are shown plotted as a function of element density for the A injector type elements (fan spacing = 0; fan inclination angle = 15 degrees; fan impingement angle = 0) in Fig. 30. Data (Table IV) are presented for: (1) a single-element, (2) the hot-fire A injector, and (3) the 1/4-segment model of the A injector with an element density approximately one-and-one-half times that of the actual A injector. The 1/4-segment of the full-scale injector was a 1/4-segment replica of the full-scale injector with the exception that its design had been photographically reduced to fit into a 3.2-in.-diameter chamber rather than a 3.9-in.-diameter chamber. All testing was conducted in the pressurized propellant mixing test apparatus. Test conditions are noted. These data suggest that if the element density of the initial A injector was doubled, the desired performance goal could be attained.

The element density for the core of the D injector was approximately twice that of the A injector (Fig. 30). This was accomplished by making the elements in the D injector core 3/4-size reductions of the elements in the A injector and by adding another ring of elements in the core region. This element density assured attainment of the desired performance goal for the core of the D injector.

Single-Element Atomization Characteristics. To confirm that the drop sizes calculated from Eq. 8 are indeed upper limits to what may be expected with the A injector, several experiments were conducted with a gas/liquid like-doublet element to evaluate the quantitative influence of the fuel (gas) injection on oxidizer atomization. Initial experiments (conducted prior to completion of the facility/procedures of Appendix C) were conducted using the open-air molten-wax technique which was developed during a previous Air Force-sponsored program at Rocketdyne (Ref. 6). Propellant simulants were GN_2 and Shell Wax 270. Details of the element employed are noted below. Test conditions and resultant wax drop sizes are shown in Table V.

TABLE IV. SUMMARY OF COLD-FLOW DATA USED TO DEFINE ELEMENT DENSITY EFFECTS ON MIXING FOR PERFORMANCE OPTIMIZED LIKE-DOUBLET ELEMENTS

Test No.	Injector*	Element density, elements per square inch of injector fuel area	E_m , %	M_{C^*} , mix, %
1	Single-Element	0.15	65.7	83.0
2	Full-Scale (Injector A)	3.20	93.5	82.5
3	1/4-segment model of A Injector	4.55	97.4	89.0

*All elements are optimized in terms of mixing efficiency

$S = 0$ = For Spacing

$\alpha = 15$ Degrees = For inclination angle

$F = 0$ Degrees = For impingement angle

**Simulated conditions:

$P_c = 5$ psia

$MR \approx 5.0$

Momentum Ratio (l/g) ≈ 0.3

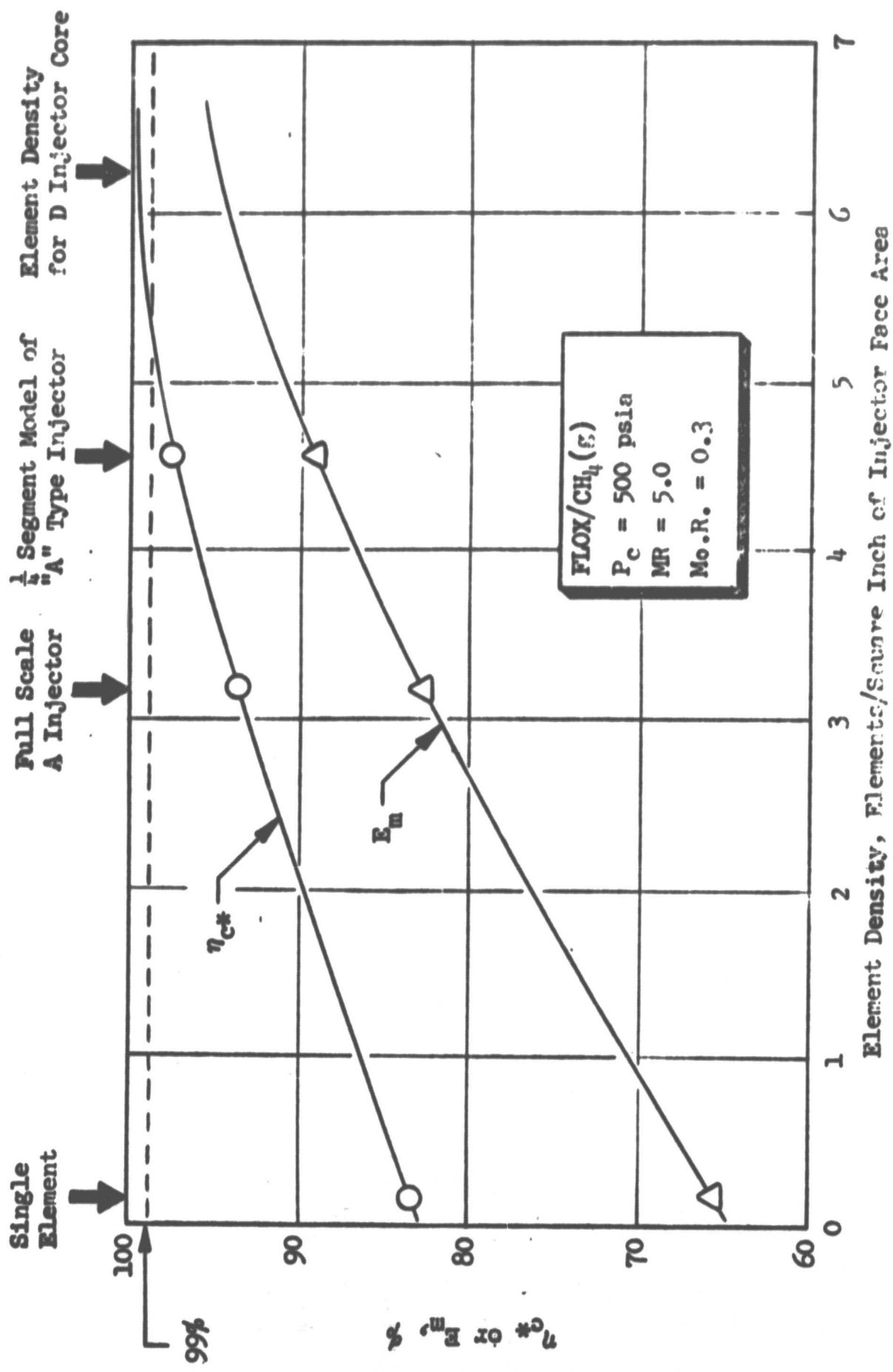


Figure 30. Effect of Element Density on Mixing for Injector A Type (Fan Spacing = 0)
Like-Doublet Elements (Cold Flow Results)

TABLE V. SUMMARY OF DROP SIZE EXPERIMENT TEST CONDITIONS*
AND RESULTS FOR INJECTOR A TYPE SINGLE ELEMENT

Test No.	Element Configuration	\dot{W}_L , lbm/sec	\dot{W}_g , lbm/sec	Mixture Ratio $\dot{W}_L/\dot{W}_g = \frac{W_{ox}}{W_T}$	Injection Velocity ft/sec		Reciprocal Momentum Ratio M_p/M_{ox}	Max Dropsize, D_{30} μ
					Liquid	Gas		
1	1	0.0501	0.0	∞	43.9	---	0.0	252
2	1	0.0500	0.0032	15.6	43.7	753	1.1	198
3	1	0.0501	0.0050	10.0	43.9	1080	2.5	135

*Tests conducted in open air molten wax facility.

Injector Design Details:

A Single-Element Like-Doublet (i.e., a pair of gas and liquid like-doublets) is illustrated in Fig. 10.

$$\begin{aligned}d_1 &= 0.0465 \text{ in.} \\d_g &= 0.0820 \text{ in.}\end{aligned}$$

Impingement Angle of Individual Doublet Streams = 60 degrees

Fan Spacing = 0	}	Parameters Defined in Fig. 10
Fan Impingement Angle = 0		
Intra-Element Spacing = 0.40 in.		
Fan Inclination Angle = 30 degrees		

The liquid orifice diameter was similar to that of the initial A injector elements; however, the gas orifice was larger to simulate hot-fire gas momentum at ambient pressure. Drop size results from these experiments are presented in Fig. 31. The ratio of the measured drop size to that predicted by Eq. 8 is shown plotted as a function of the reciprocal (i.e., fuel-to-oxidizer) momentum ratio in this figure. These results clearly indicate a reduction in propellant drop size as a result of gas injection for the gas/liquid like-doublet element. Propellant drop size was approximately halved when the reciprocal of the momentum ratio was increased from 0 to 2.5. Drop size at a reciprocal momentum ratio of zero (corresponding to liquid injection only) agrees well with that predicted by Eq. 8. Oxidizer drop size at the injector A design operating momentum ratio is approximately 80 percent of the value obtained without the gas injection (Fig. 31).

To support future analysis of hot-fire performance data, atomization tests (Table VI) also were conducted with a D injector core element. Testing was conducted in the pressurized molten wax facility (Appendix C). Facility limitations prevented testing at design condition ($P_c = 500$ psia; MR = 6). Consequently, a series of tests was conducted in which the element was throttled over a 100- to 350-psia simulated chamber pressure range at a constant mixture ratio of 6. These data can be extrapolated to the design chamber pressure. The drop size appears to be relatively independent of simulated chamber pressure over the range investigated. The effect of injected gas (fuel) on the atomization process is apparent upon comparison of the measured drop size at $V_g = 0$ (single point) with the MR = 6 ($V_g \geq 700$ ft/sec) curve in Fig. 32. An approximately 20-percent reduction in drop size is attained as a result of the gas injection.

5.1.2 Chamber Compatible Elements

Cold-flow distribution (mixing) experiments were conducted with single-element models to support design of the full-scale, chamber-compatible (B and C) injectors. The purpose of the B and C injector investigation was to define performance losses and chamber flux reduction for like-doublet injectors in which the fans' major axes were intentionally displaced (i.e., fan spacing 0) to provide a mixture ratio bias. Data from this effort were utilized to support design of the peripheral element configuration for the final (D) injector so that performance losses were minimized while providing a fuel-rich zone near the chamber wall to reduce chamber heat flux.

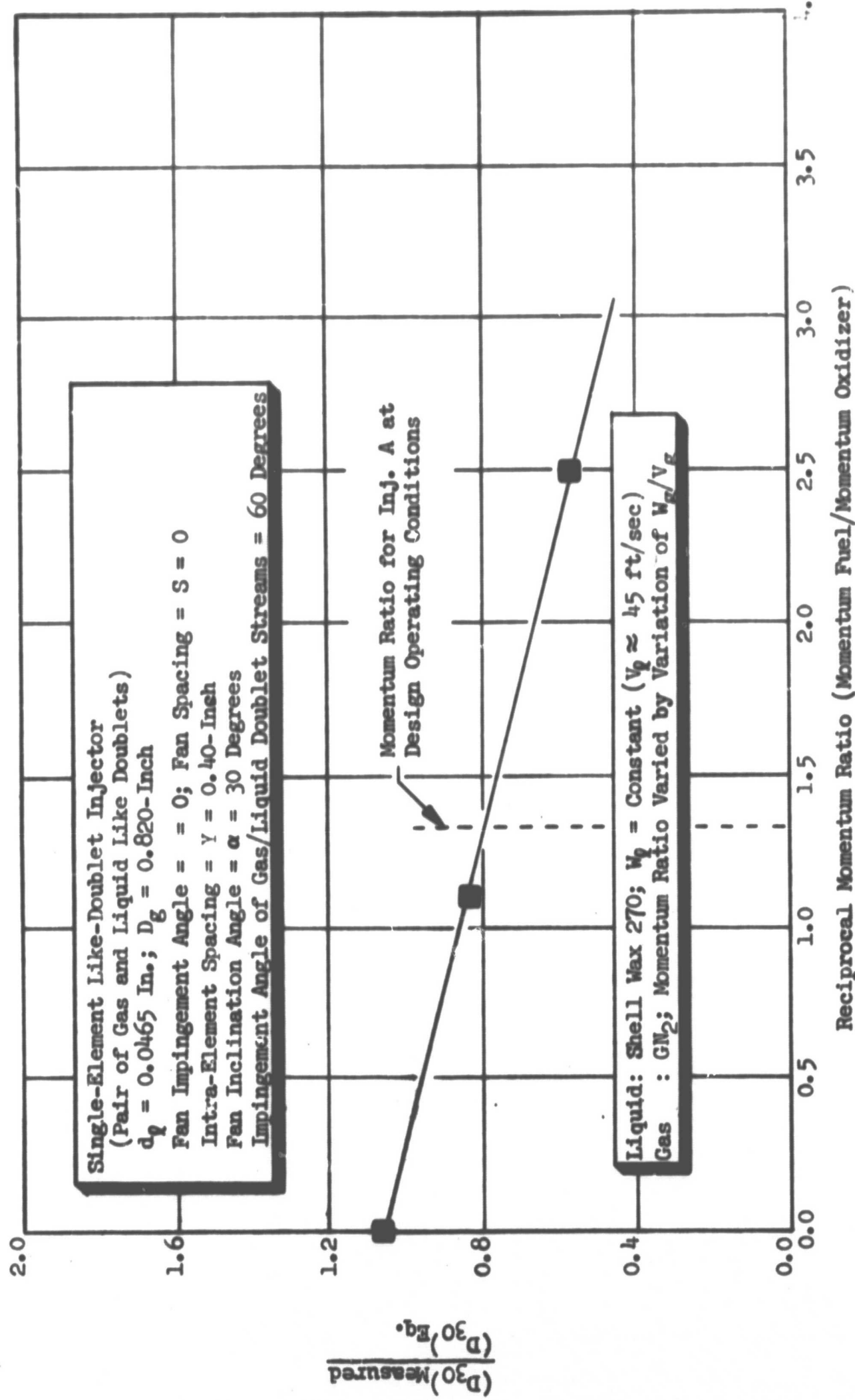


Figure 31. Effect of Gas Injection on Drop Size for Gas/Liquid Like-Doublet Element

TABLE VI. SUMMARY OF ATOMIZATION EXPERIMENT TEST CONDITIONS
AND RESULTS FOR D INJECTOR CORE ELEMENT

Test No.	Simulated Conditions*			$\frac{V_L}{D}$, ft/sec	Max Drop Size, $\frac{D}{D}$, Microns
	P_c , psia	MR	V_g , ft/sec		
1	125	6	~ 700	48	270
2	250	6	~ 700	96	290
3	350	6	~ 700	144	290
4	250	∞	0	96	365

*Element configuration: $d_g = 0.043$ in.

$d_l = 0.037$ in.

Fan Spacing = 0

Fan Inclination Angle = 15 degrees

Intra-Element Spacing = 0.15 in.

Fan Impingement Angle = 0 degrees

Tests conducted in pressurized facility (Appendix C)

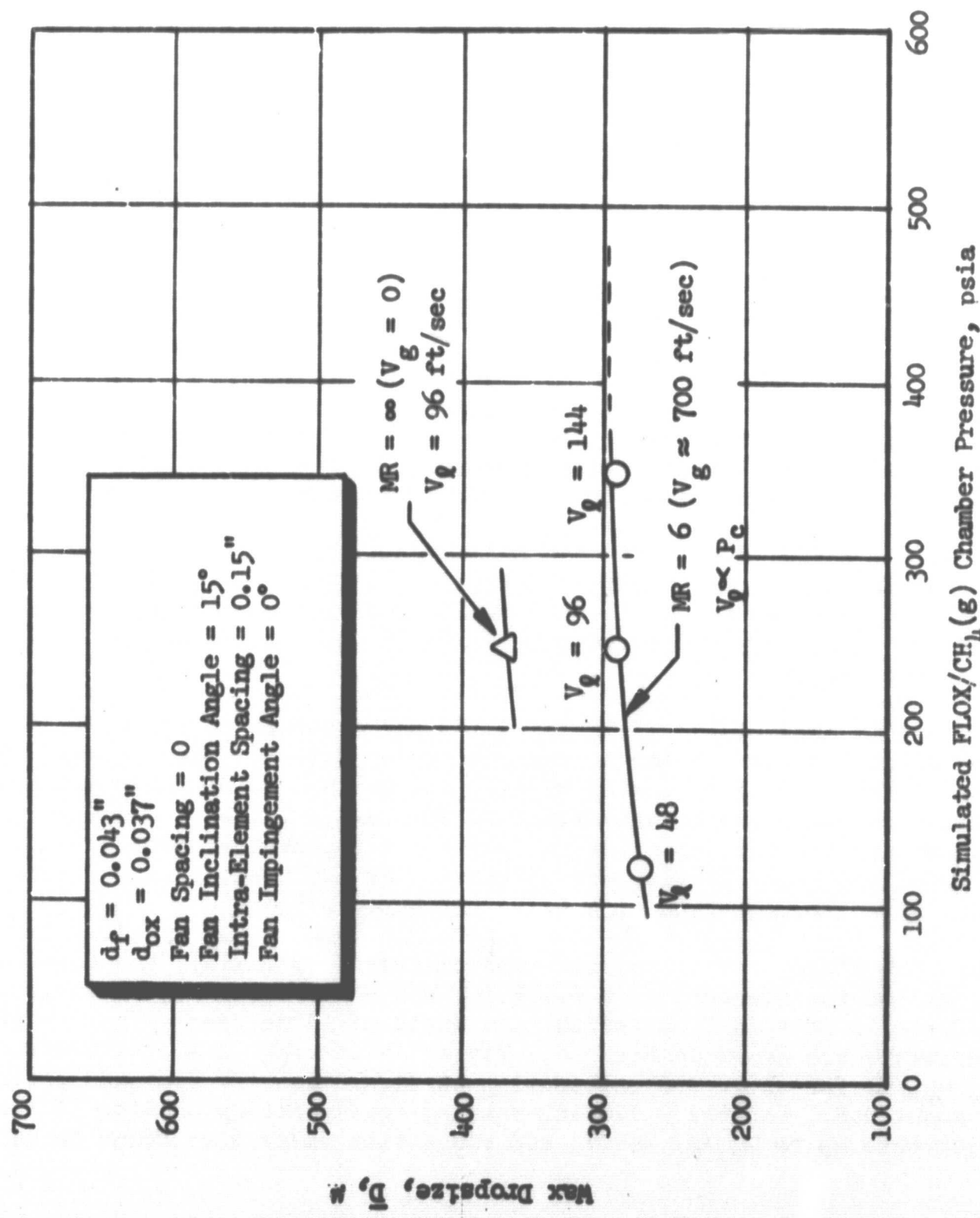


Figure 32. Effect of Chamber Pressure and Gaseous Fuel Injection on Drop Size for D Injector Core Element

The single-element, cold-flow hardware which was previously utilized in the A injector studies was utilized for the B and C injector studies. Test apparatus and procedures described in Appendix B were employed. The primary test variables were fan spacing, fan inclination angle (α), and propellant momentum ratio. Fan spacings of 0.125 and 0.250 in. were employed.

Intra-element spacing was maintained constant at 0.200 in. The fan inclination angle was varied from 0 to 30 degrees at a constant momentum ratio of 0.34 and momentum ratio was varied from ~0.34 to 1.2 at a fan inclination angle of 15 degrees for both fan spacings. Fan inclination angles of 0, 15, and 30 degrees were employed. The gas orifice diameter was varied to permit changing the propellant momentum ratio at constant mixture ratio. The momentum ratio (oxidizer-to-fuel) was varied over a wide range (0.34 to 1.22) by use of a 0.052-in. liquid orifice diameter with gas orifice diameters of 0.055, 0.082, and 0.104 in.

The B and C injector distribution tests were conducted at the following simulated conditions: propellants = FLOX (82.6% F_2)/ $CH_4(g)$; chamber pressure = 500 psia; MR = 5.00. Propellant simulants were water and GN_2 . To simulate operation at a given chamber pressure and mixture ratio and hot-fire injected gas momentum flux, propellant momentum ratio and mixture ratio were matched. These tests were conducted employing the improved (base bleed gas recirculation suppression technique) test procedures. All distribution measurements were made 2 in. from the injector face. A summary of the test condition and data is presented in Table VII.

The first topic considered below is the effect of design/operating parameters on performance as influenced by propellant mixing. The fuel and oxidizer flow distribution of single elements, again as a function of design/operating parameters, are then described and flow patterns that would be most desirable for a peripheral injector element are selected.

Figure 33 presents the results of the experiments to determine the effects of an inclination on mixing for a momentum ratio (o/f) of 0.34 and fan spacings equal to 0.125 and 0.250 in. As indicated by Fig. 33, mixing (E_m) is near optimum for a fan inclination angle (α) of approximately 15 degrees for both spacings. The $\alpha = 30$ degrees and fan spacing 0.125-in. point was repeated to determine data scatter. Excellent repeatability was obtained. As expected, mixing was better with the 0.125-in. spacing than with 0.250 in. between fans.

To determine the effects of propellant momentum ratio on mixing, the momentum ratio (M_{ox}/M_f) of the elements ($S = 0.125$ in. and $S = 0.250$ in.) was varied from 0.34 to 1.22 for a constant fan inclination angle of 15 degrees. The results of these experiments are shown in Fig. 34. Mixing levels show a slight decline with increasing M_{ox}/M_f for the 0.250-in. spacing configuration for momentum ratios in excess of about 0.8. For the 0.125-in. spacing configuration, mixing levels were found to increase up to $M_{ox}/M_f \approx 0.7$, and above that value were found to be nearly constant.

The effect of fan inclination angle on propellant mixing for the performance ($S = 0$) and chamber compatible elements are compared in Fig. 35. The intended core elements produce a higher level of mixing principally because of the zero fan spacing.

TABLE VII. SUMMARY OF COLD-FLOW MIXING TEST CONDITIONS AND
RESULTS FOR SINGLE-ELEMENT EXPERIMENTS CONDUCTED
TO DEFINE ELEMENT DESIGN CRITERIA FOR CHAMBER
COMPATIBLE (FAN SPACING 0) ELEMENTS

Test No.	Momentum Ratio (\dot{q}/g)	Fan Spacing, S , in.	Fan Inclination Angle, α , degrees	Gas Orifice Diameter, in.	E_m , %	$M_{C^*, mix}$, %
1	0.34	0.125	0	0.055	58.4	76.8
2			15		63.6	79.0
3			30		51.7	73.6
4			30		52.0	73.0
5	0.250	0	0		57.5	74.6
6			15		59.2	76.3
7			30		37.2	63.9
8	0.78	0.125	0	0.082	71.1	86.5
9	1.22	0.125	0	0.104	70.9	86.7
10	0.78	0.250	0	0.082	58.6	76.6
11	1.22	0.250	0	0.104	55.1	75.8

*Simulated P_C and MR were 500 psia and 5.75, respectively

$\beta = 0$ degrees = Fan Impingement Angle

$Y = 0.20$ in. = Intra-Element Spacing

$d_L = 0.052$ in. = Liquid orifice diameter

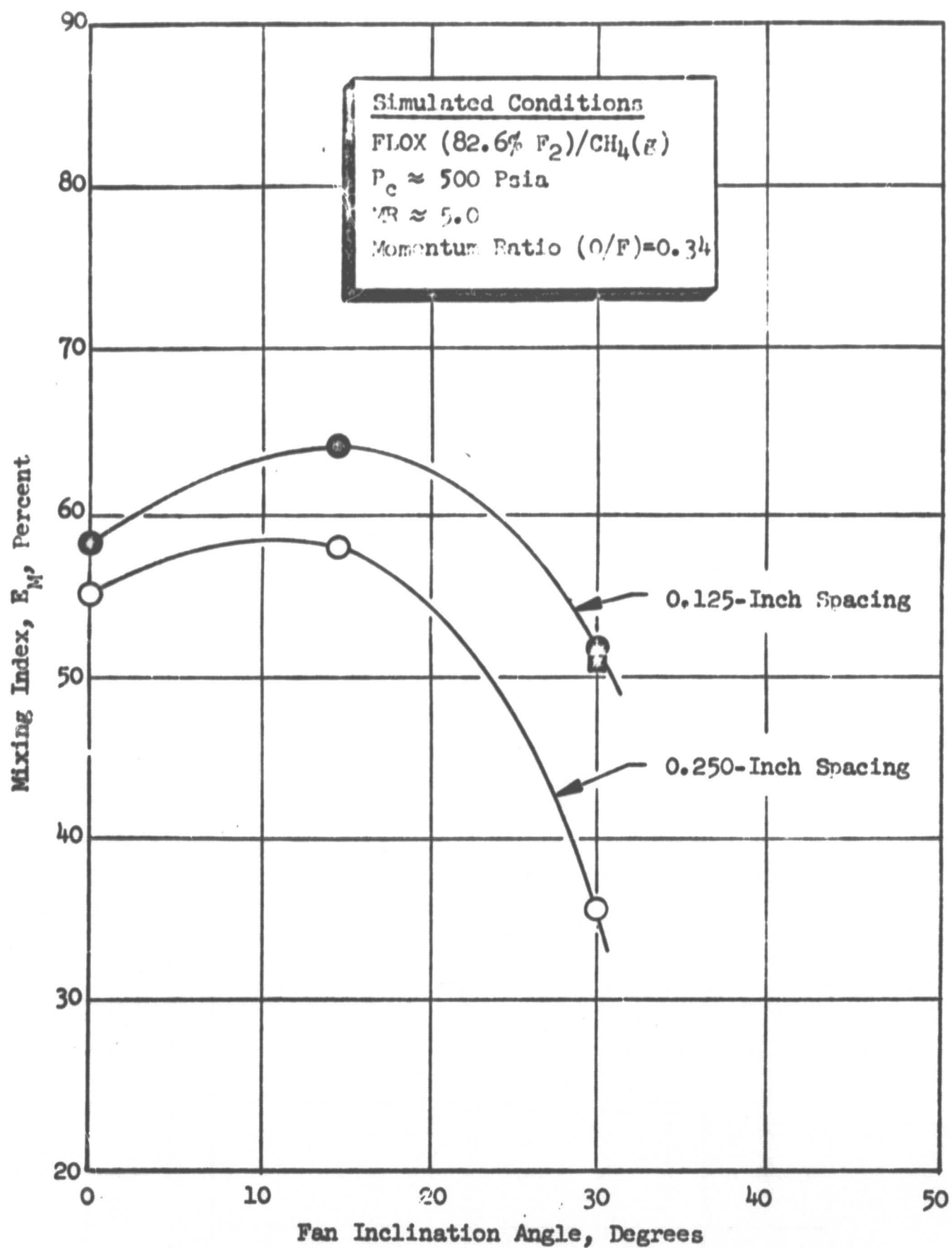


Figure 33. Effect of Fan Spacing and Inclination Angle on the Mixing Index E_M for Chamber Compatible Single-Element Gas/Liquid Like-Doublet Elements

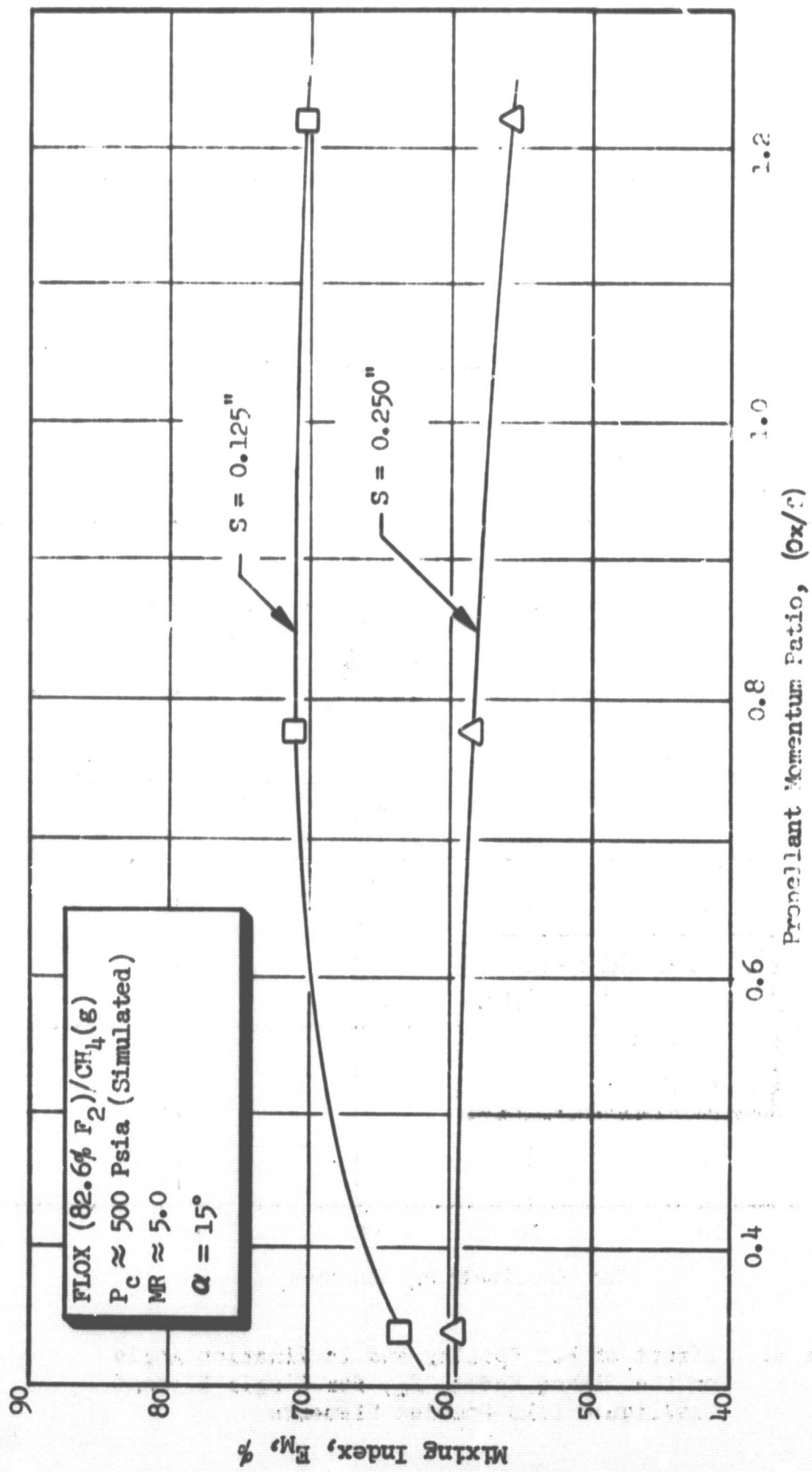


Figure 34. Effect of Oxidizer to Fuel Momentum Ratio on E_M for Single-Element Chamber Compatible Gas/Liquid Like-Doublt Elements (Cold-Flow Results)

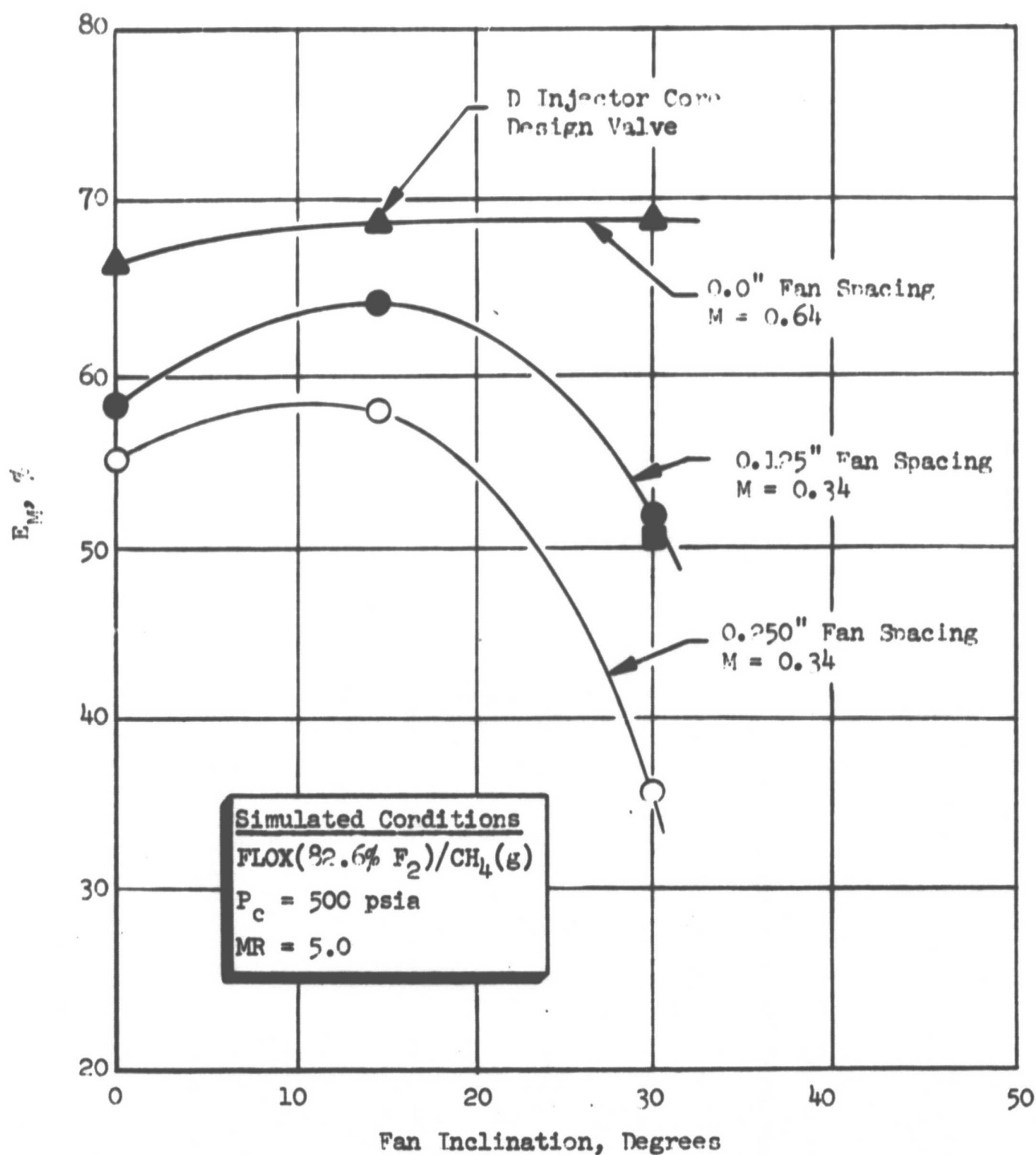


Figure 35. Effect of Fan Spacing and Inclination Angle on the Mixing Index, E_M , for Single-Element Gas/Liquid Like-Doublet Elements

The same cold-flow distribution data from the B and C single-element studies as were used to determine the values of E_m just described were examined to determine potential wall mass and mixture ratio distributions. From a performance standpoint (i.e., maximum E_m), a near-optimum design for both the 0.250-and 0.125-in. fan spacing configurations would incorporate a fan inclination angle of 15 degrees and a momentum ratio of approximately 0.75. However, as will be discussed in subsequent paragraphs, the optimum performance configurations do not necessarily yield optimum wall mass and mixture ratio distributions.

Figures 36 and 37 present fuel and oxidizer mass flux data for both the 0.125- and 0.250-in. spacing configurations, respectively, for a fan inclination angle of 15 degrees and a momentum ratio of approximately 0.75. The scales of the ordinates (liquid and gas mass fluxes) are normalized by a factor of 5; consequently, if the oxidizer value (solid lines) and the fuel values (dashed lines) coincide at a point, then the mixture ratio at that point is equal to 5. If the dashed line (fuel) lies about the solid line (oxidizer), then the local mixture ratio is less than 5 (i.e., "low" mixture ratio) and vice versa. The injected mixture ratio was 5.

Also illustrated on each plot is the angular orientation of that profile with respect to the element orientation.

Examination of Fig. 36 for the 0.125-in. configuration ($S = 0.125$ inch) with $\alpha = 15$ degrees and $M_{Ox}/M_f = 0.775$, shows a relatively low mixture ratio ($MR < 5$) region exists in adjacent sectors 8, 1, and 2 so that this would be the most desirable zone to have near the wall (for this configuration). Examination of Fig. 37, obtained from a 0.250-in. spacing configuration with $\alpha = 15$ degrees, $M_{Ox}/M_f = 0.775$ shows that a low mixture ratio periphery ($MR < 5$) would be possible if the wall were to be placed adjacent to sectors 1 and 2. However, examination of all the data with $M_{Ox}/M_f = 0.34$ ($S = 0.125, 0.250$ in., $\alpha = 0, 15, 30$ degrees) revealed that the configuration of $\alpha = 0$ degrees and $S = 0.250$ in. resulted in the lowest potential wall mixture ratio. These data are shown in Fig. 38. Note that a strong, low mixture ratio bias would be obtained if the chamber wall were placed adjacent to either section 1, 8, or 7. The absolute values of gas mass flux in these sectors are substantially higher than the best sectors shown in Fig. 36 and 37 ($\alpha = 15$ degrees, $M_{Ox}/M_f = 0.775$, $S = 0.250$ in.).

Selection of $\alpha = 0$ degrees, $S = 0.250$ in. instead of $\alpha = 15$ degrees, $S = 0.250$ in. would result in a loss in mixing performance (corresponding to the decrease in E_m) of approximately 3 percent. However, considering the mass and mixture ratio profiles of the $\alpha = 0$ degrees, $S = 0.250$ -in. case as opposed to $\alpha = 15$ degrees, $S = 0.125$ and 0.250 in., the former is clearly superior from the standpoint of providing wall mixture ratio bias.

Examination of the mass and mixture ratio profiles for the tests to define the effects of propellant momentum revealed (E_m data shown in Fig. 34) that the propellant momentum ratio did not have a significant effect on the wall mass and mixture ratio distributions. Thus, a value of 0.75 for the element momentum ratio should provide near-optimum performance (E_m) while providing a "low" mixture ratio wall region.

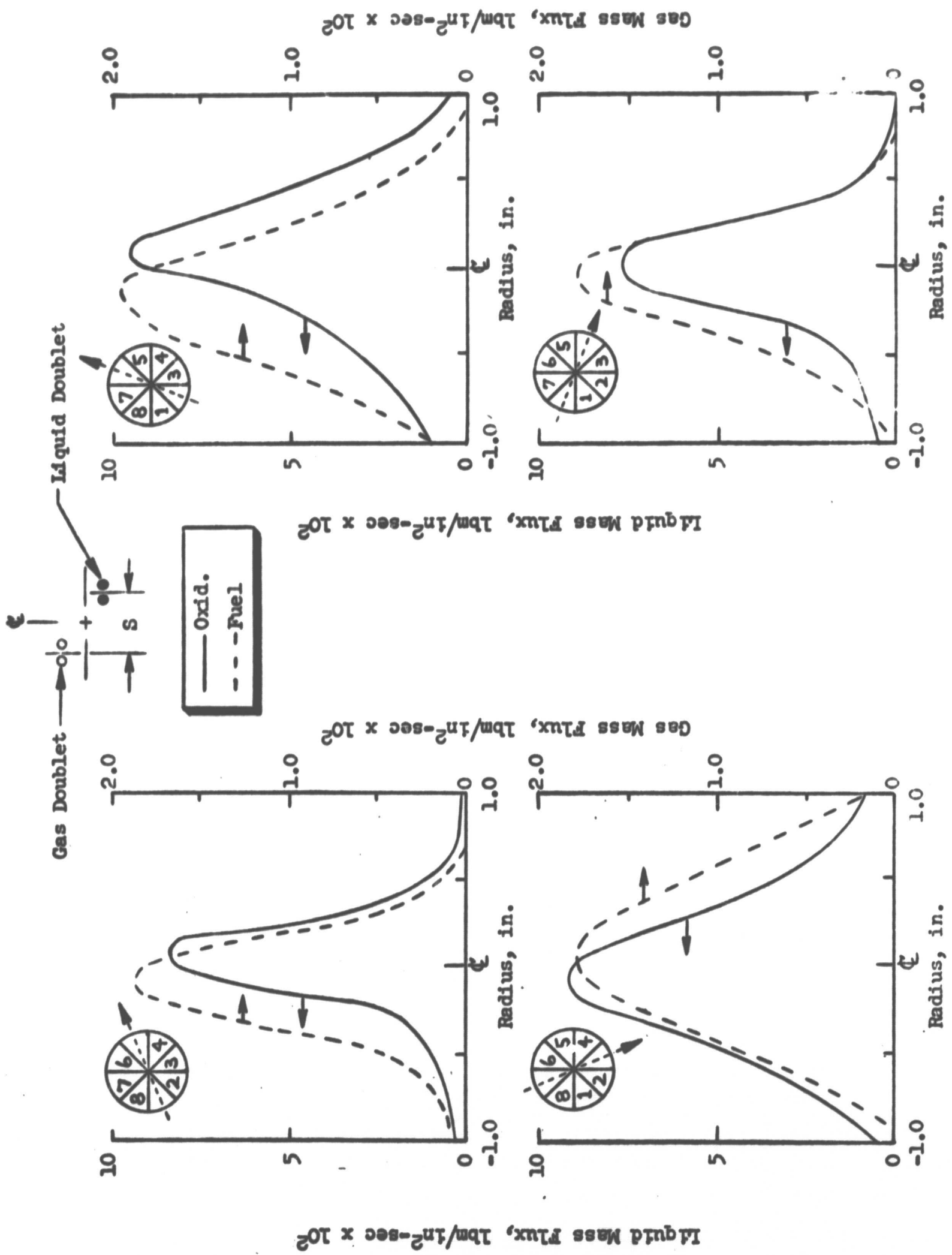


Figure 36. Fuel and Oxidizer Mass Flux Data for Momentum Ratio (α/f) = 0.775,
 $\alpha = 15$ degrees, $S = 0.125$ -Inch Test

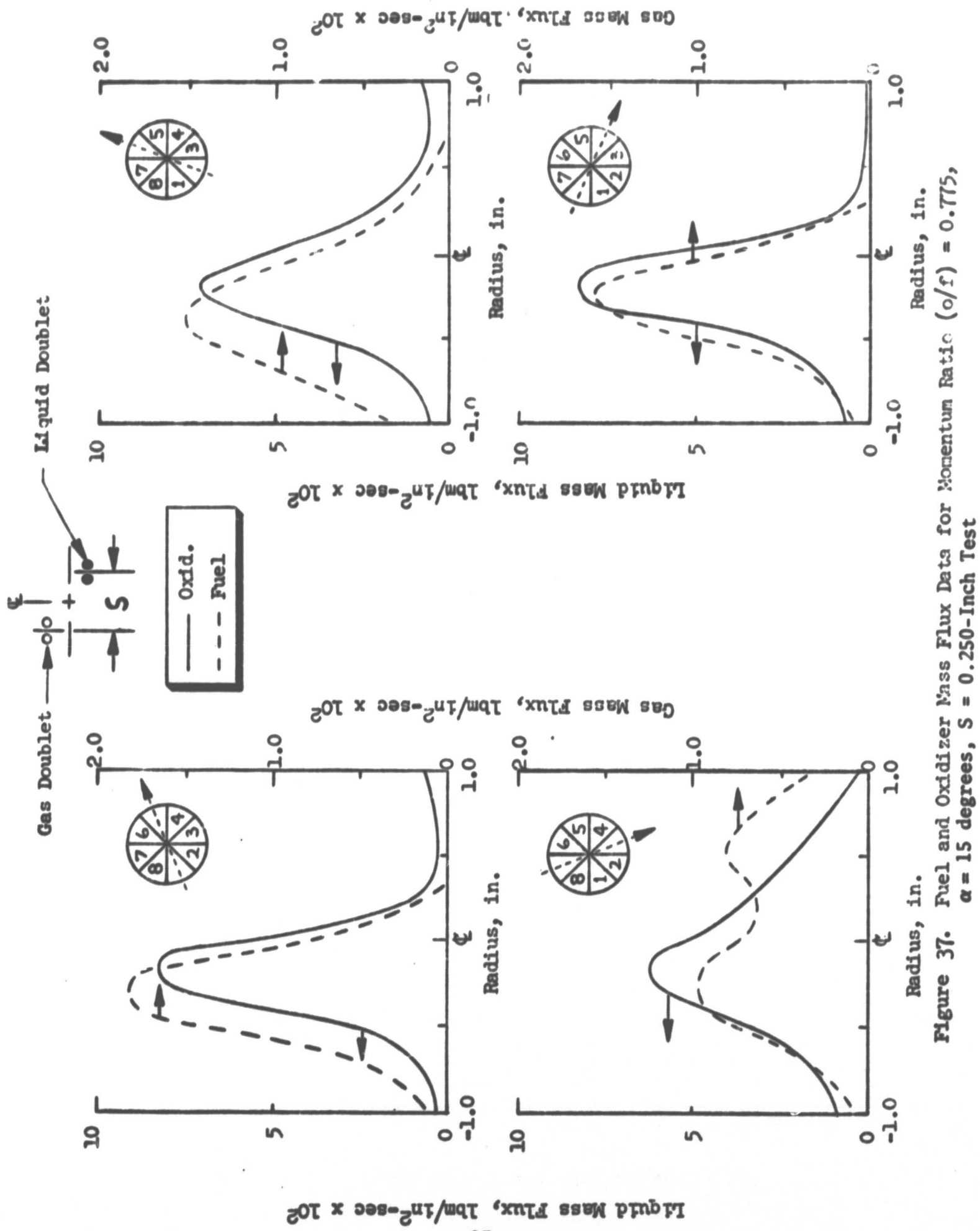


Figure 37. Fuel and Oxidizer Mass Flux Data for Momentum Ratio (σ/f) = 0.775,
 α = 15 degrees, S = 0.250-Inch Test

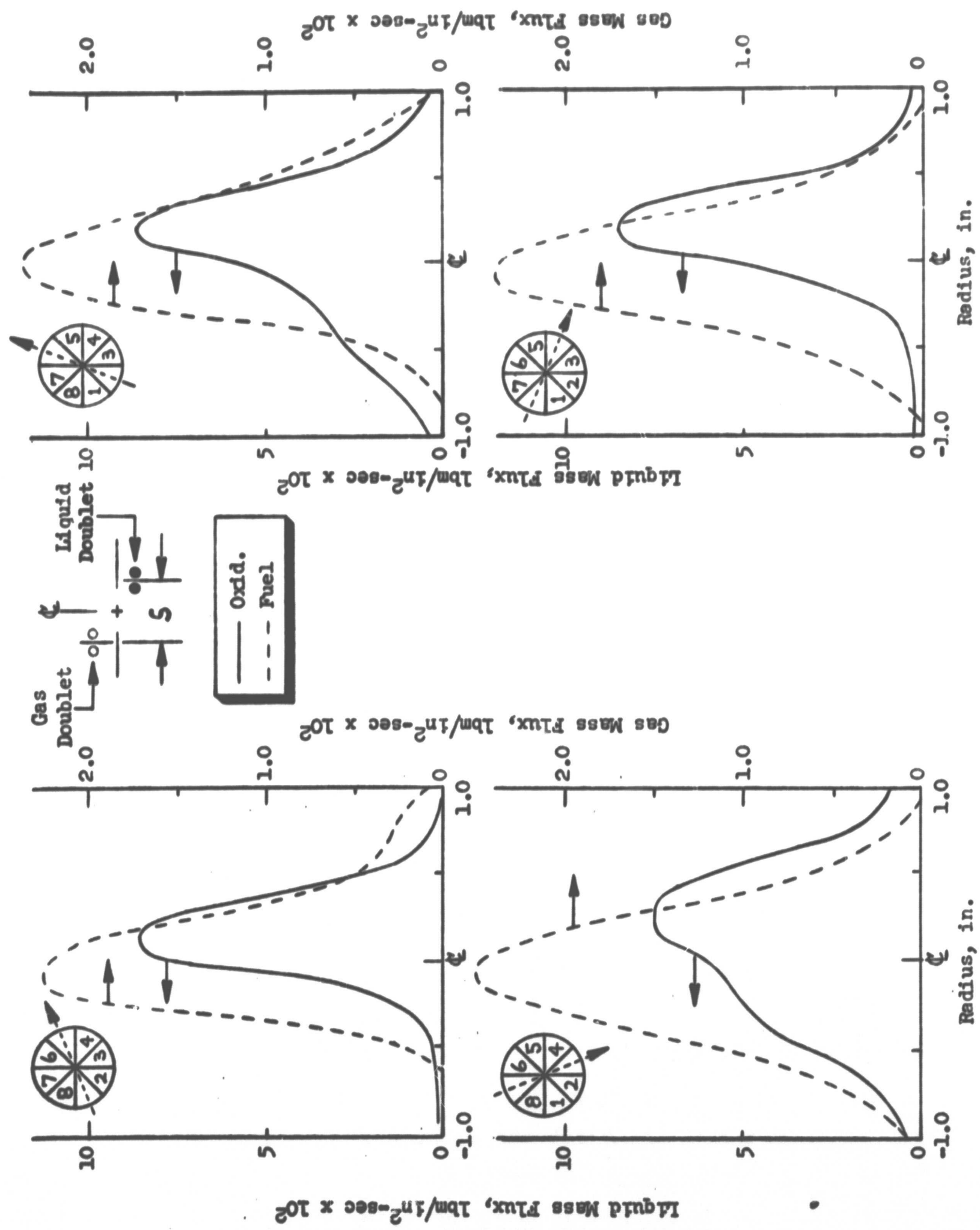


Figure 38. Fuel and Oxidizer Mass Flux Data for Momentum Ratio (α/f) = 0.34,
 $\alpha = 0$ degrees; $S = 0.250$ -Inch Test

Based on these cold-flow data, the following design parameters were recommended for the B configuration injector elements: fan spacing, $S = 0.125$ in.; fan impingement angle, $\beta = 0$ degrees; intra-element spacing, $Y = 0.20$ in.; fan inclination angle, $\alpha = 15$ degrees; momentum ratio (o/f) = 0.75. The following design parameters were recommended for the C injector elements: fan spacing, $S = 0.250$ in.; fan impingement angle, $\beta = 0$ degrees, intra-element spacing, $Y = 0.20$ in.; fan inclination angle, $\alpha = 0$ degrees; momentum ratio (o/f) = 0.75.

Basically, the C design represents the configuration indicated by cold-flow data to offer the best chamber compatibility, though at some cost in performance. The recommended B concept results from a compromise between mixture ratio control and performance potential in which performance should remain relatively high, but wall protection is still provided. Initially, the C injector configuration was designed, fabricated, and hot-fire tested. Experimental evaluation of this injector revealed that its performance in the mixture ratio range of interest (~3 to 4 for the peripheral zone elements) was adequate and it exhibited very favorable heat transfer characteristics. Consequently, the B configuration injector was never designed.

5.2 FULL-SCALE PERFORMANCE AND CHAMBER COMPATIBLE INJECTORS

The effects of injector design/operating parameters on performance and chamber heat transfer characteristics for the A and C injectors are discussed in this section under separate headings.

The purpose of the A injector investigation was to provide injector design criteria for the "high-performance" core of the D injector. The performance goal for the core was 99 percent of the theoretical shifting characteristic exhaust velocity at its design mixture ratio (between 5.25 and 6.5, depending on the peripheral zone mass fraction and mixture ratio). The overall design mixture ratio was 5.25. During the B/C injector studies, experiments were conducted to define design criteria for the "chamber-compatible" peripheral zone of the D injector so that injector chamber compatibility could be achieved with minimal performance losses. Cold-flow distribution and atomization experiments were conducted with single-element injector segment models to support design of full-scale, high-performance, and chamber-compatible injectors.

These full-scale injectors were, in turn, evaluated by cold-flow and hot-firing tests to provide cold-flow mixing-limited c^* efficiencies, hot-fire performance, and chamber heat transfer data to support design of the composite (D) injector.

Full-scale, hot-firing injectors designed, fabricated, and tested included a high-performance type (injector A), and a "chamber-compatible" type (injector C). The injector A elements were modified (fuel/oxidizer orifices enlarged) after initial testing, resulting in additional versions of this injector (A-2 and A-3), which also were tested. Design details of these injectors, and the data upon which their designs were based, were presented in the Experimental Hardware and Injector Models portion of the Experimental Results sections of this report, respectively.

Initially, hot-fire tests were conducted to define chamber L^* effects on performance. Tests were conducted in 20- and 40-in. L^* chambers ($\epsilon_c = 3$). As a result of these tests, a chamber L^* (40 in.) was selected for the remainder of the hot-fire test program. Performance losses due to incomplete propellant vaporization were minimal (~1 percent) in this reference chamber. Hot-fire testing of the A injector configurations (i.e., injectors A-1, A-2, and A-3) was conducted primarily to define performance (propellant mixing) as a function of propellant momentum ratio and orifice diameter ratio. Momentum ratio was varied by: (1) throttling at constant mixture ratio, (2) varying mixture ratio at constant chamber pressure, and (3) successive enlargement of the fuel/oxidizer orifice diameters. Hot-fire tests also were conducted with the C injector to define propellant momentum ratio effects on performance. Momentum ratio was varied with the C injector by throttling at constant mixture ratio and varying mixture ratio at constant chamber pressure. Chamber heat flux data were obtained in the above-described series of tests to define injector design, chamber pressure, and mixture ratio (for the C injector only) effects on chamber heat transfer characteristics.

Cold-flow mixing tests were conducted with the A(A-3) and C injectors to support their evaluation. The A injector was cold-flow evaluated at two simulated hot-firing conditions ($P_c = 250$ psia, MR = 5.7 and $P_c = 500$ psia, MR = 8.9) and the C injector at three conditions ($P_c = 500$ psia, MR = 3.5 and 5.75 and $P_c = 250$ psia, MR = 5.75).

No usable performance/chamber heat transfer data were obtained with the first A injector (injector A; $d_{ox} = 0.0469$ in. and $d_f = 0.055$ in.). Cracking of the ATJ graphite chamber liner in the initial series of checkout tests precluded attainment of usable data. This injector was damaged beyond repair during the next scheduled test. The incident was caused by an internal fire initiated in the oxidizer (FLOX) dome. The site of the initial combustion/erosion was relatively sharp-edged surfaces where adjacent drilled passages intersected within the FLOX dome. Examination of the damaged injector indicated that the incident was not due to, nor did it result in, an interpropellant leak. A thorough examination of the injector indicated that the diffusion bond was in excellent condition. Erosion was confined to the oxidizer dome/feeder passages.

An injector to replace the one damaged in the fluorine (FLOX) incident was fabricated. Precautions were taken to prevent a FLOX incident, similar to that which occurred with the initial injector, prior to continuation of the hot-fire test program. All sharp-edged surfaces such as those that initiated the incident in the first A injector were eliminated by design modification. Oxidizer and fuel orifices in the second A injector (injector A-1) were 0.041 and 0.0469 in., respectively.

5.2.1 Hot-Fire Performance

Chamber L^* Effects. During the initial series of tests with the A-1 injector, it was throttled from a nominal chamber pressure of 500 to 300 psia at a constant mixture ratio of ~6.4 in a 20-in. L^* ($\epsilon_c = 3$) chamber. Theoretical optimum c^* mixture ratio for FLOX (82.6% F_2)/ $CH_4(g)$ is 5.75. The corrected c^* efficiency for these tests was between 92 and 95 percent (Fig. 39). These data, in conjunction

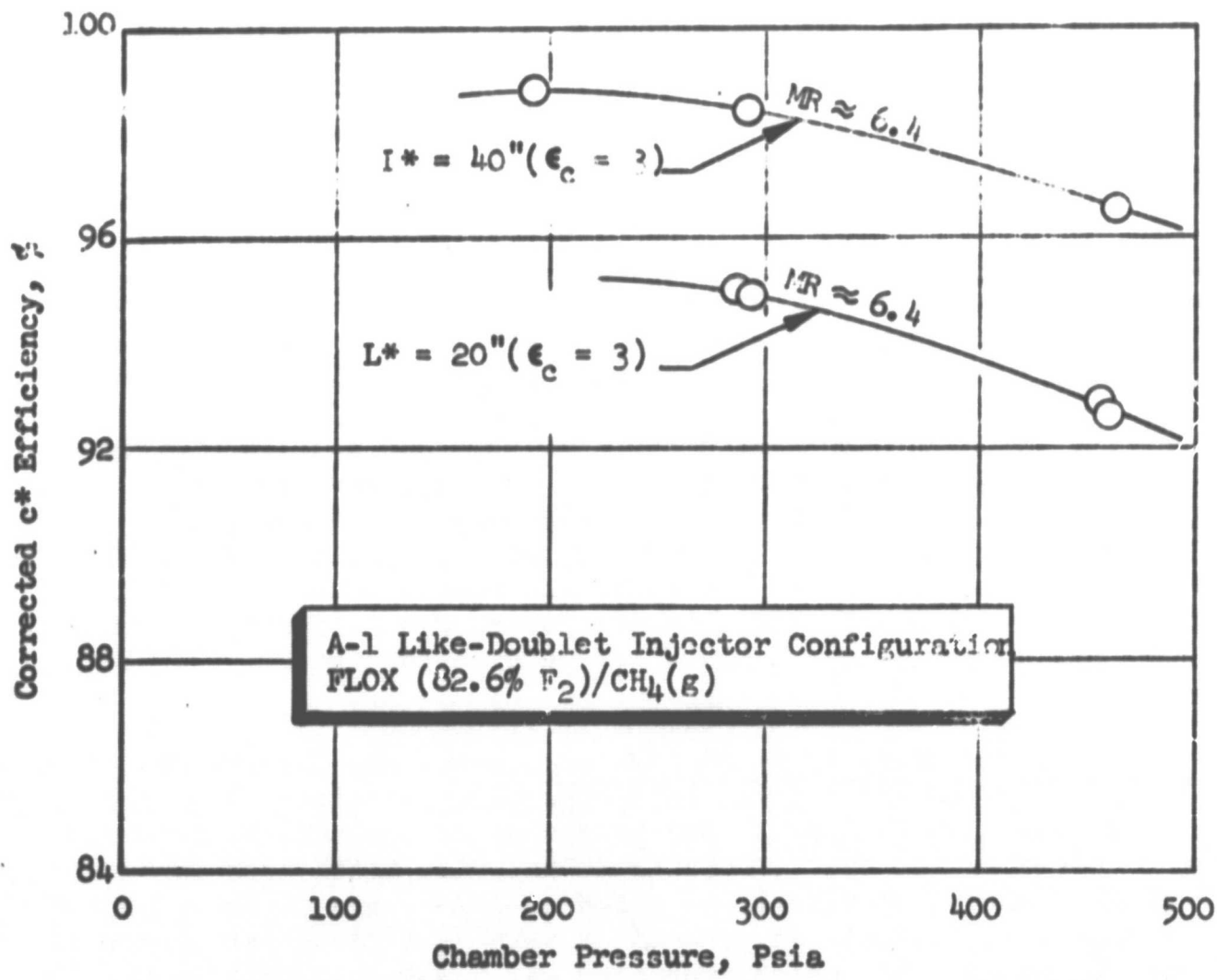


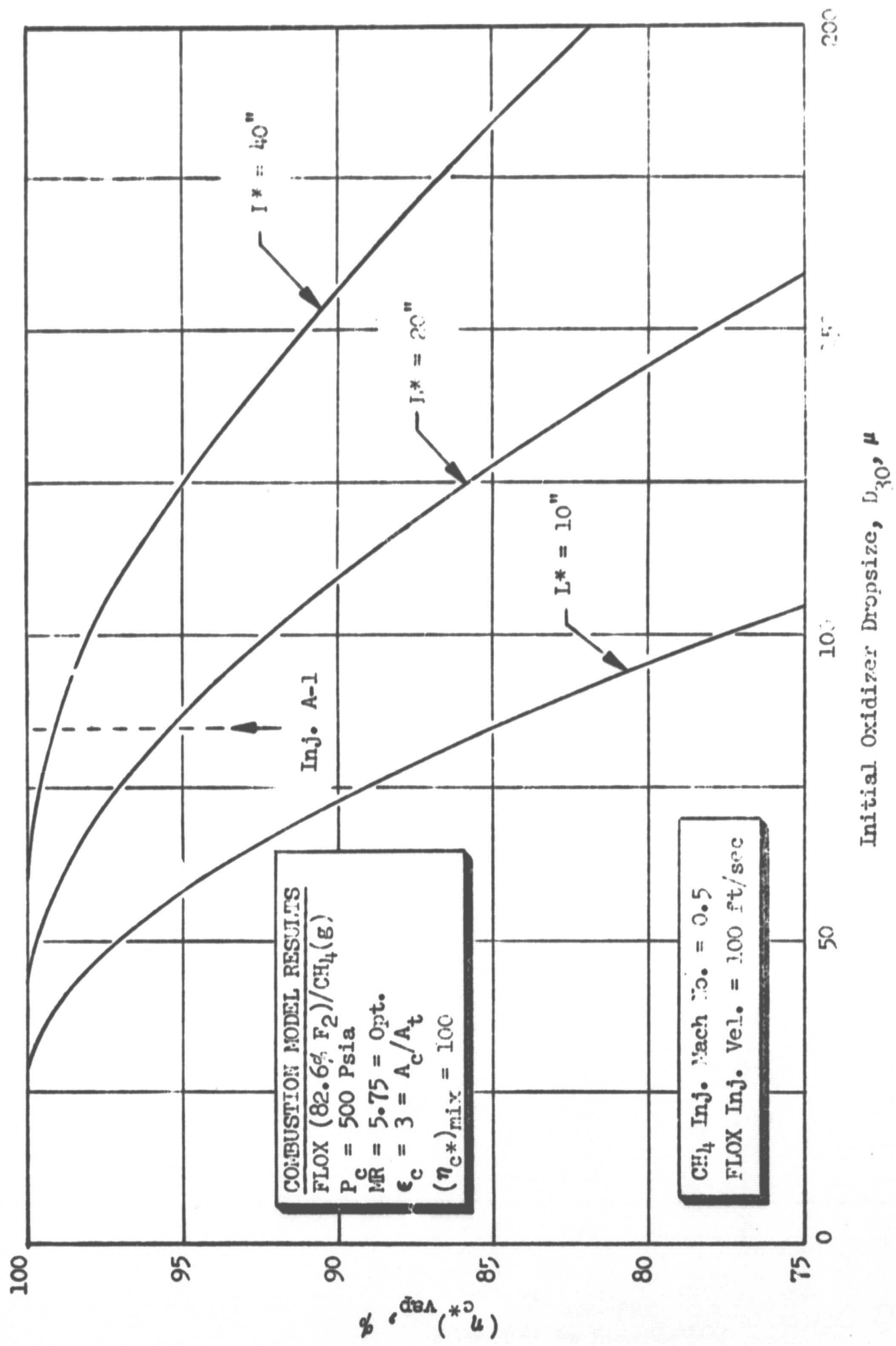
Figure 39. Effect of Chamber L^* and Chamber Pressure on Performance for Like-Doublet Injector A-1

with previous combustion model analyses, suggested that appreciable vaporization losses were being incurred in the 20-in. L^* chamber. To further substantiate this analysis and to increase performance, a series of tests was conducted utilizing the A-1 injector in conjunction with the 40-in. L^* ($\epsilon_c = 3$) reference chamber. This was the longest L^* chamber attainable with available hardware. Results from these tests, in which the injector was throttled at a mixture ratio of ~ 6.4 from 500- to 200-psia chamber pressure, also are presented in Fig. 39 for comparison with the tests conducted in the 20-in. L^* chamber. The data shown in Fig. 39 indicate that approximately 4-percent increase in performance (ϵ_c^* from ~ 92 to 96 percent) is realized at design conditions ($P_c = 500$ psia; MR between 5.25 and 6.5) by use of a 40-in. L^* rather than a 20-in. L^* chamber.

To determine an apparent oxidizer drop size and vaporization c^* efficiency losses in the 20- 40-in. L^* combustion chambers, combustion model results for FLOX (82.5% F_2)/ $CH_4(g)$ were analyzed in conjunction with the above hot-fire data. Pertinent combustion model results are presented in Fig. 40. Vaporization-limited c^* efficiency for FLOX (82.6% F_2)/ $CH_4(g)$ is shown plotted as a function of oxidizer drop size for several characteristic chamber lengths ($\epsilon_c = 3$) in this figure. The calculations are for a chamber pressure of 500 psia and a mixture ratio of 5.75. Based on the change in performance with L^* , the apparent volume mean oxidizer drop size D_{30} for the A-1 injector is on the order of 85 microns at design conditions ($P_c = 500$ psia; MR = 5.75). This drop size suggests an effective combustion gas velocity, calculated from Eq. 8, of 215 ft/sec ($\Delta V = 90$ ft/sec for the A-1 injector at these conditions). Performance losses due to incomplete propellant vaporization are approximately 5.0 and 1.0 percent for the 20- and 40-in. L^* chambers, respectively.

Momentum Ratio and Orifice Diameter Ratio Effects. Since the primary objective of the injector A configuration testing was to define mixing-limited c^* efficiency as a function of the pertinent injector design variables (propellant momentum ratio, orifice diameter ratio, etc.), subsequent hot-fire tests were conducted in the 40-in. L^* chamber where vaporization-limited c^* losses are minimal. D_{30} for the A-2 and A-3 injectors, calculated from Eq. 8 with $V_g = 215$ ft/sec, were in the 75- to 90-micron range. D_{30} calculated from Eq. 8 was ~ 80 microns for the C injector. This value could be somewhat higher (≤ 100 microns) if the fuel momentum does not assist in the atomization process for the nonzero fan spacing element (Fig. 31 and 32). Three A injector configurations (A-1 with $d_f = 0.0469$ in. and $d_{ox} = 0.041$ in.; A-2 with $d_f = 0.0469$ in. and $d_{ox} = 0.052$ in.; A-3 with $d_f = 0.055$ and $d_{ox} = 0.052$ in.) and the C injector were hot-fire evaluated.

Hot-fire performance characteristics of the three A injector configurations are compared in Fig. 41. Corrected c^* efficiency (based on chamber pressure) for all configurations is shown plotted as a function of momentum ratio for mixture ratios ≤ 5.75 (the theoretical optimum) in this figure. All data are for tests conducted in the 40-in. L^* reference chamber. Test conditions (P_c , mixture ratio, etc.) are presented in Table VIII. In general, the performance of all configurations increases slightly with increasing momentum ratio (o/f) over the range investigated

Figure 40. Predicted Effect of Chamber L* on Vaporization c* Efficiency for FLOX/CH₄ (g)

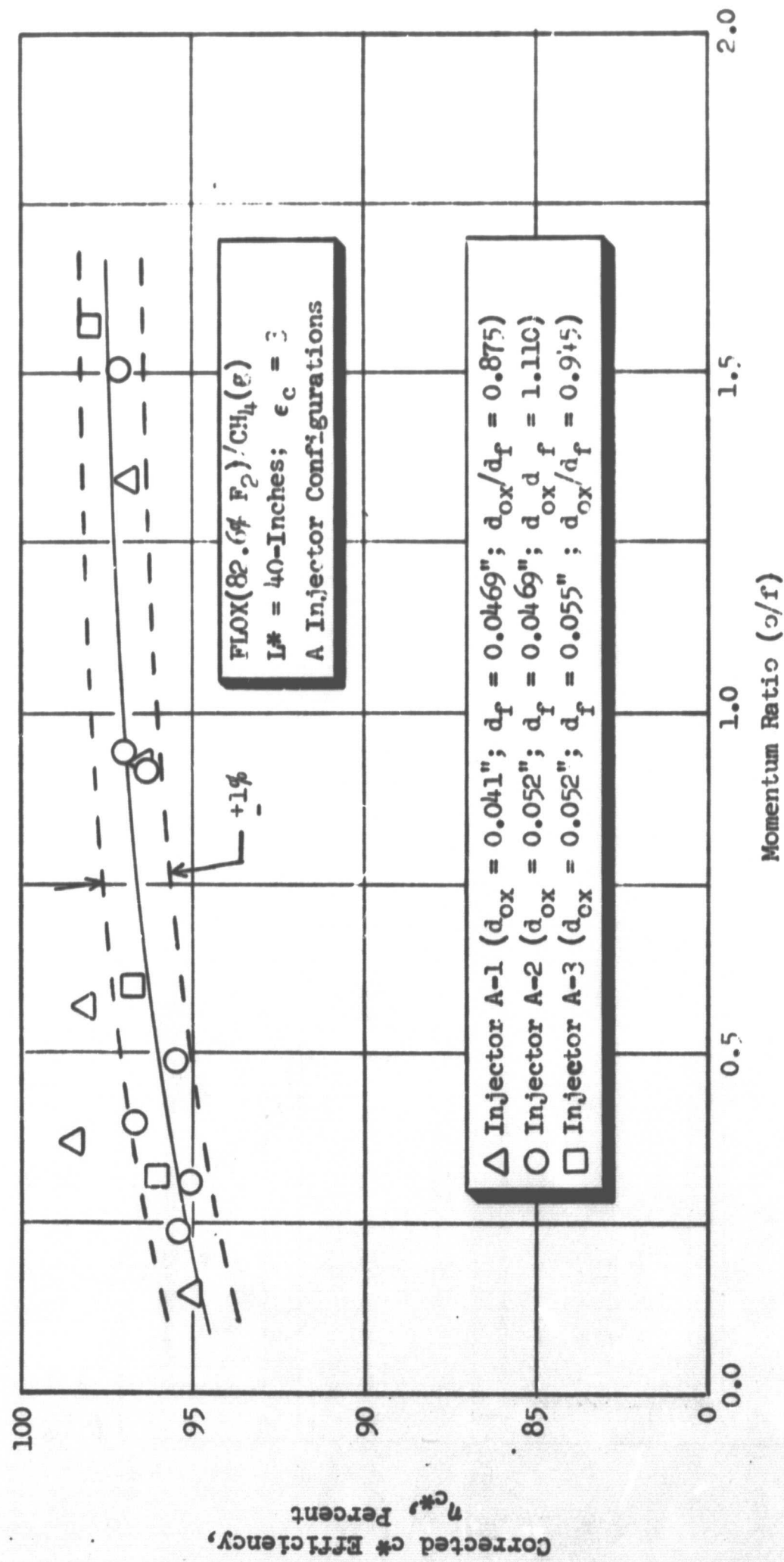


Figure 41. Effect of Momentum Ratio and Orifice Diameter Ratios on Performance for A Injector Configurations

(0.3 to 1.8). This is in agreement with the cold-flow data (Fig. 29). For any given value of momentum ratio, the effect of orifice diameter ratio on c^* efficiency appears to be negligible over the range investigated ($0.875 \leq d_{ox}/d_f \leq 1.1$). The majority of the test points (13 of 15) are within ± 1 percent of the correlation line drawn through the data points.

The excellent agreement between corrected c^* efficiency based on chamber pressure and thrust is illustrated in Fig. 42. Data are presented for every third test in this figure.

Comparison of A and C Injectors. Hot-fire performance characteristics of the A and C configuration full-scale injectors are compared in Fig. 43. Corrected c^* efficiency (based on chamber pressure) for both injector configurations is shown plotted as a function of momentum ratio for mixture ratios ≥ 5.75 (the theoretical optimum) in Fig. 43A, and as a function of mixture ratio ($P_c = 500$ psia) in Fig. 43B. All test data are for the 40-in. L^* ($\epsilon_c = 3$) reference chamber. Test conditions (P_c , mixture ratio, and momentum ratio) are noted. In general, performance of the "high performance" A injector configuration is approximately 4 percent higher than that of the "chamber-compatible" C injector at similar operating conditions (chamber pressure, mixture ratio, and momentum ratio) as predicted by the earlier cold-flow mixing tests. The difference in performance level between the two injectors is attributable primarily to the difference in propellant mixing caused by the difference in fan spacing between injectors. Fan spacing (Fig. 10) for the A and C injectors was 0.0 and 0.25 in., respectively. C^* efficiency increased slightly with increasing momentum ratio (oxidizer-to-fuel) for both injectors (Fig. 43A) over the range investigated (0.3 to 1.8). The range of momentum ratio investigated includes the practical design range for the subject application. Performance at design conditions ($P_c = 500$ psia; $MR \approx 5.5$) is approximately 97 and 92.5 for the A ($S = 0$) and C ($S = 1/4$ in.) injectors, respectively. Performance losses are attributable primarily to nonuniform propellant mixing and, therefore, changes in performance are caused primarily by changes in the propellant mixing uniformity/mixing-limited c^* efficiency. (Previous analyses of hot-fire performance data from tests conducted at several characteristic chamber lengths in conjunction with combustion model results indicate that performance losses due to incomplete propellant vaporization are ~ 1 percent for tests conducted in the 40-in. L^* chamber.)

Performance (η_{c^*}) increased slightly with mixture ratio for mixing ratios greater than the theoretical optimum (5.75) for both injectors (Fig. 43B). Hot-fire c^* efficiency of the C injector increases substantially with decreasing mixture ratio for mixture ratios less than the theoretical optimum. This increase in performance with decreasing mixture ratio is due primarily to the fact that performance losses due to nonuniform mixing are less for a given level of mixing (E_m) for mixture ratios \geq the theoretical optimum than for mixture ratios \leq the theoretical optimum, rather than to changes in the level of propellant mixing (i.e., E_m).

Several important conclusions can be drawn from the performance results presented in Fig. 43. First, the A injector design pattern tested is not adequate for the high-performance core of the D injector ($\eta_{c^*} < 99$ percent in the design mixture ratio range for the core; $5.25 \leq MR \leq 6.5$). Second, performance (η_{c^*}) of the C

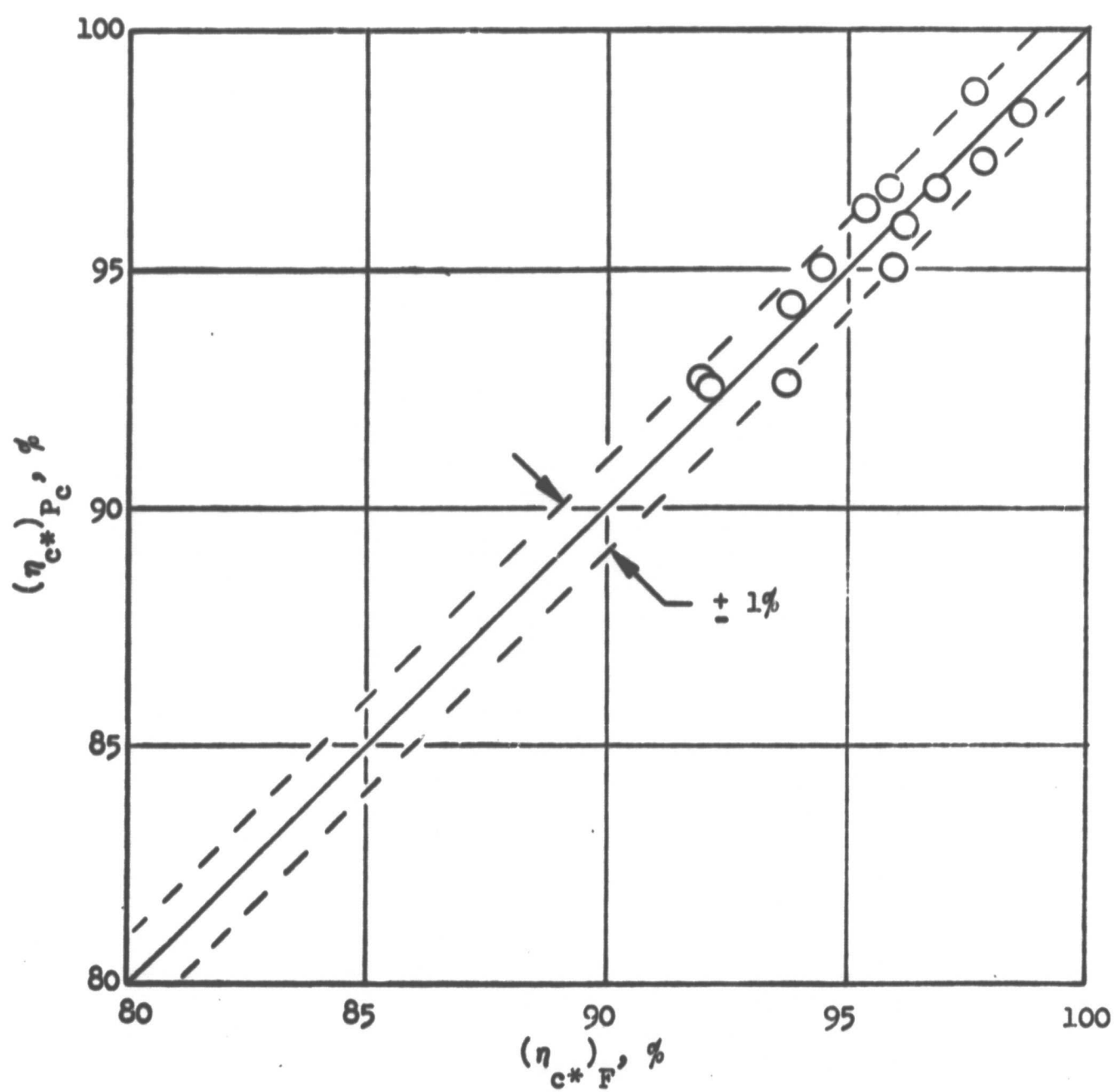
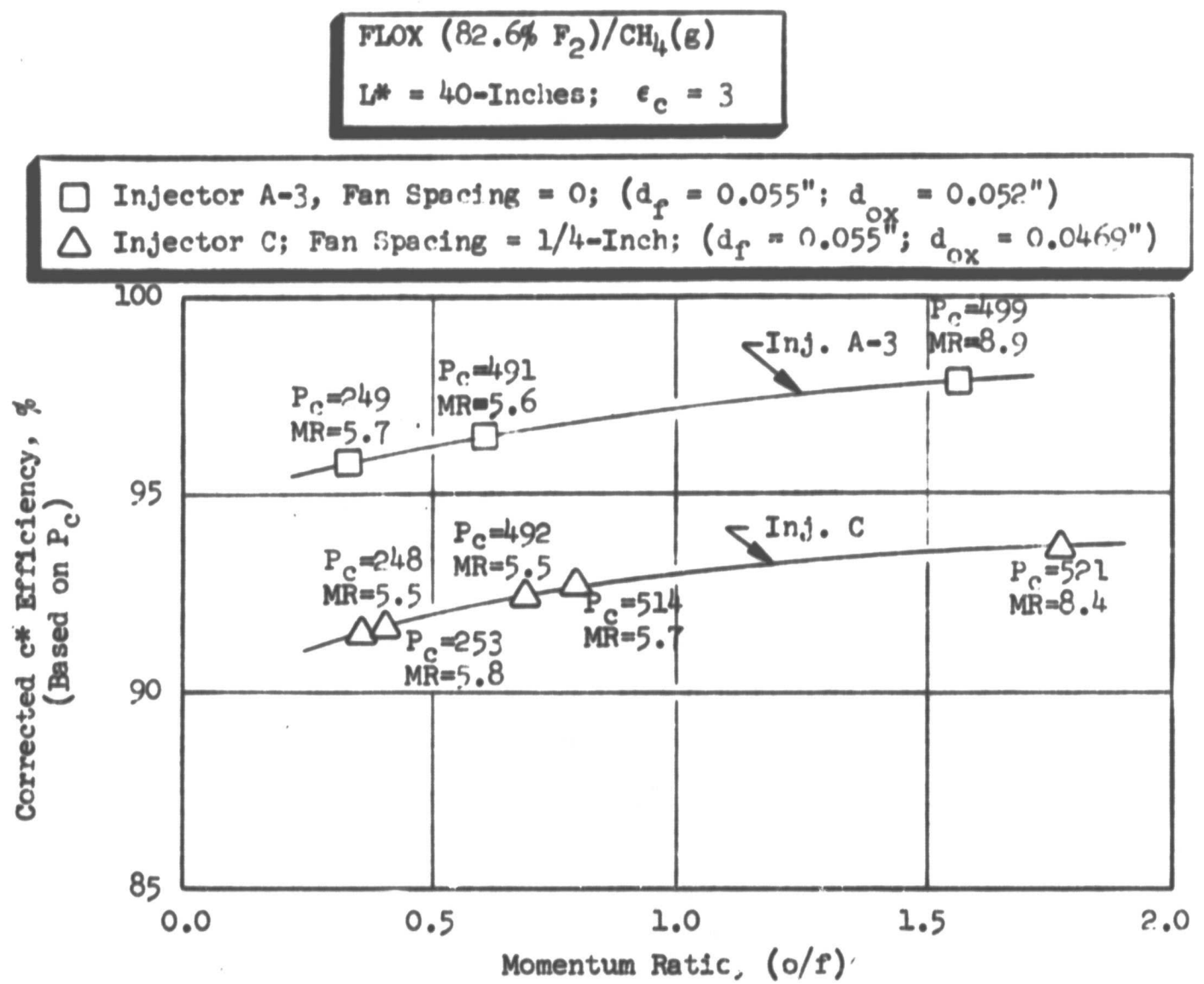
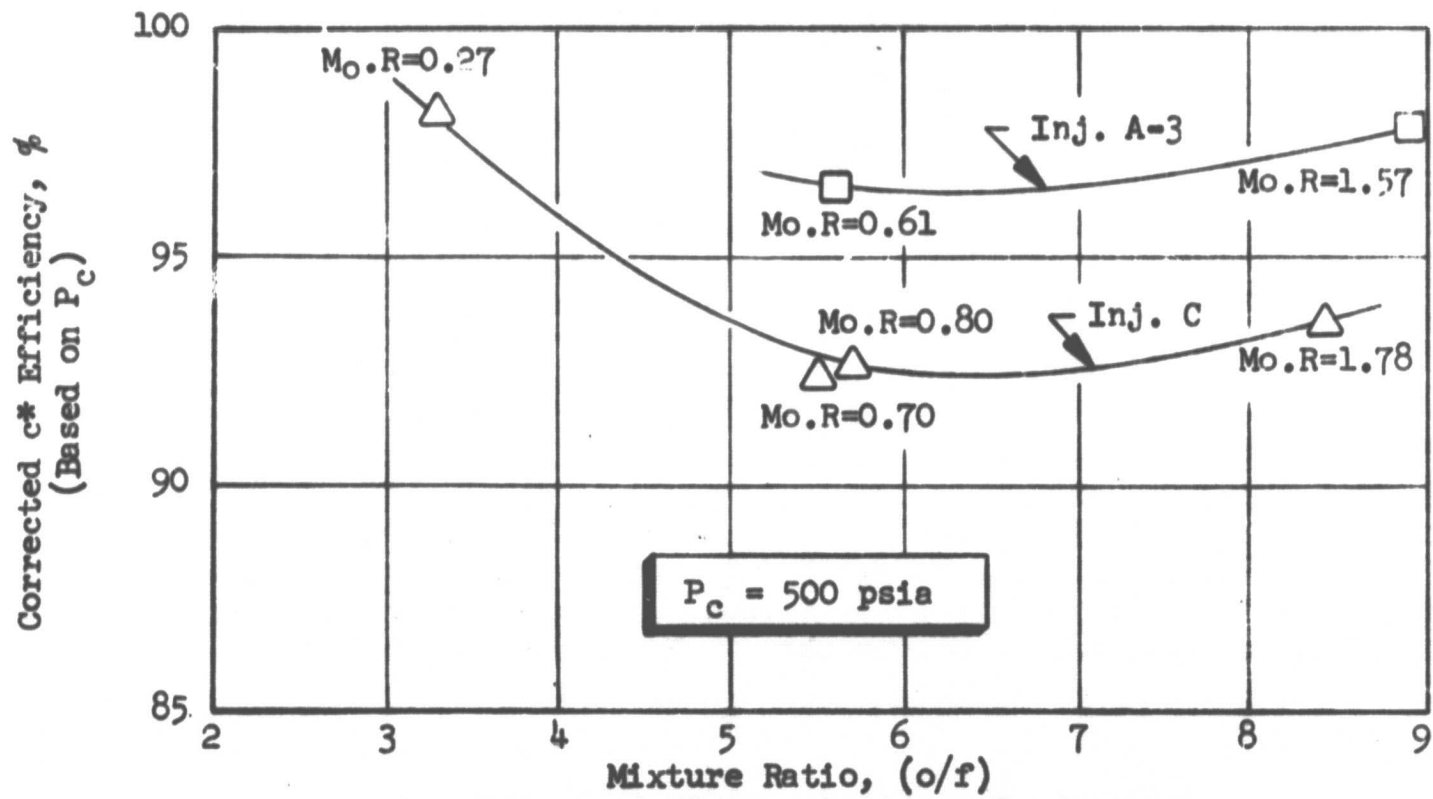


Figure 42. Comparison of Corrected c^* Efficiencies Based on Measurement of Chamber Pressure and Thrust



A. Effect of Momentum Ratio on Performance



B. Effect of Mixture Ratio on Performance

Figure 43. Comparison of Hot-Fire Performance Characteristics of A and C Configuration Like-Doublet Injectors

injector in the mixture ratio range of interest (~ 3 to 4 for the peripheral zone elements) appears to be adequate for its desired application. Performance losses are attributable primarily to nonuniform propellant mixing. Final analysis as to the adequacy of the C injector pattern for use in the periphery of the D injector depended on the chamber heat transfer characteristics associated with the design. As will be shown in the following subsection, the C injector pattern exhibits very favorable chamber heat transfer characteristics.

5.2.2 Chamber Heat Transfer Characteristics

Chamber heat transfer characteristics for the high-performance (A) and chamber-compatible (C) injectors are presented in Fig. 44 and 45. The heat flux values reported are transient values taken approximately 1 second into the tests. The measurements were made using graphite heat flux meters installed in the graphite chambers.

The effect of injector design and chamber pressure on chamber heat flux is presented in Fig. 44. Chamber heat flux is shown plotted as a function of the axial distance from the injector for both injectors. The chamber contour ($L^* = 40$ in.; $\epsilon_c = 3$) also is illustrated. Results are presented for chamber pressures of 500 and 250 psia at a mixture ratio of 5.5. Nominal design operating conditions are a chamber pressure of 500 psia and overall mixture ratio of 5.25. The effect of injector design on chamber heat flux is readily apparent. In general, local heat fluxes for the C injector (fan spacing = 1/4 in.), which was designed for chamber compatibility, are approximately half those of the high-performance A injector (fan spacing = 0) throughout the chamber. Even in the nozzle throat region, heat flux with the C injector is only about 70 percent of that with the A injector at similar operating conditions. Chamber heat fluxes for the two injector configurations appear to increase only slightly with chamber pressure variation between 250 and 500 psia. In the nozzle region, heat flux is proportional to chamber pressure to approximately the 0.8 power for each injector, as would be predicted from standard heat transfer equations.

The effect of mixture ratio on chamber heat transfer characteristics is shown in Fig. 45 for the C injector configuration. Local heat flux is plotted as a function of axial distance from the injector for three tests conducted at a chamber pressure of 500 psia and mixture ratios of 3.3, 5.5, and 8.4. As noted, chamber and nozzle heat flux increases significantly with increasing mixture ratio.

Considering the application of these data, it will be recalled that the D (optimized) injector configuration has separately manifolded high-performance core and chamber-compatible peripheral zones. Design of the high-performance core region was based on the A injector investigation. The chamber-compatible peripheral region design was based on the B/C injector studies. As described later, the chamber heat fluxes for the D (optimized) like-doublet injector were expected to be similar to those of the C injector.

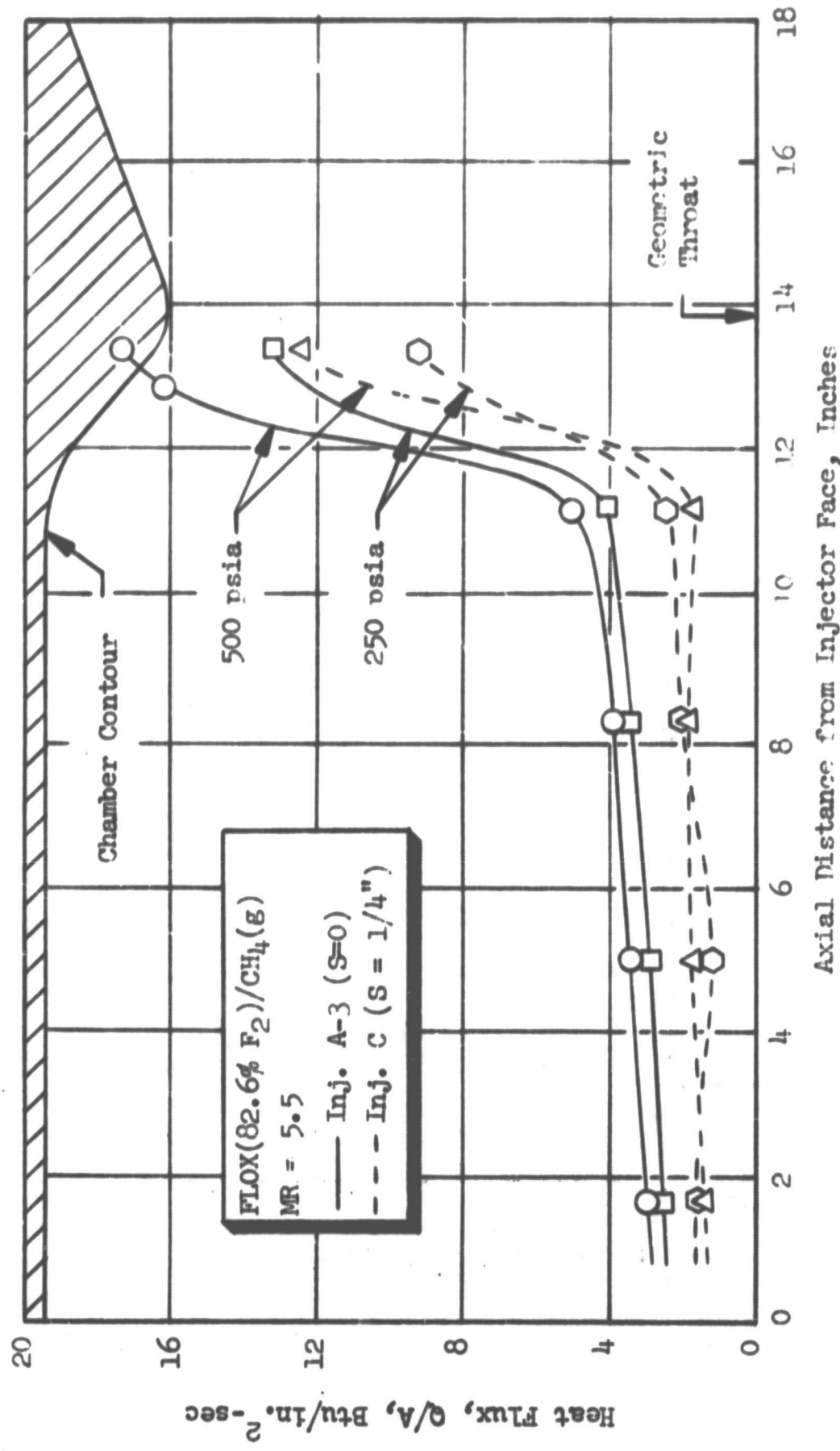


Figure 44. Effect of Injector Design and Chamber Pressure on Thrust Chamber Heat Transfer Characteristics

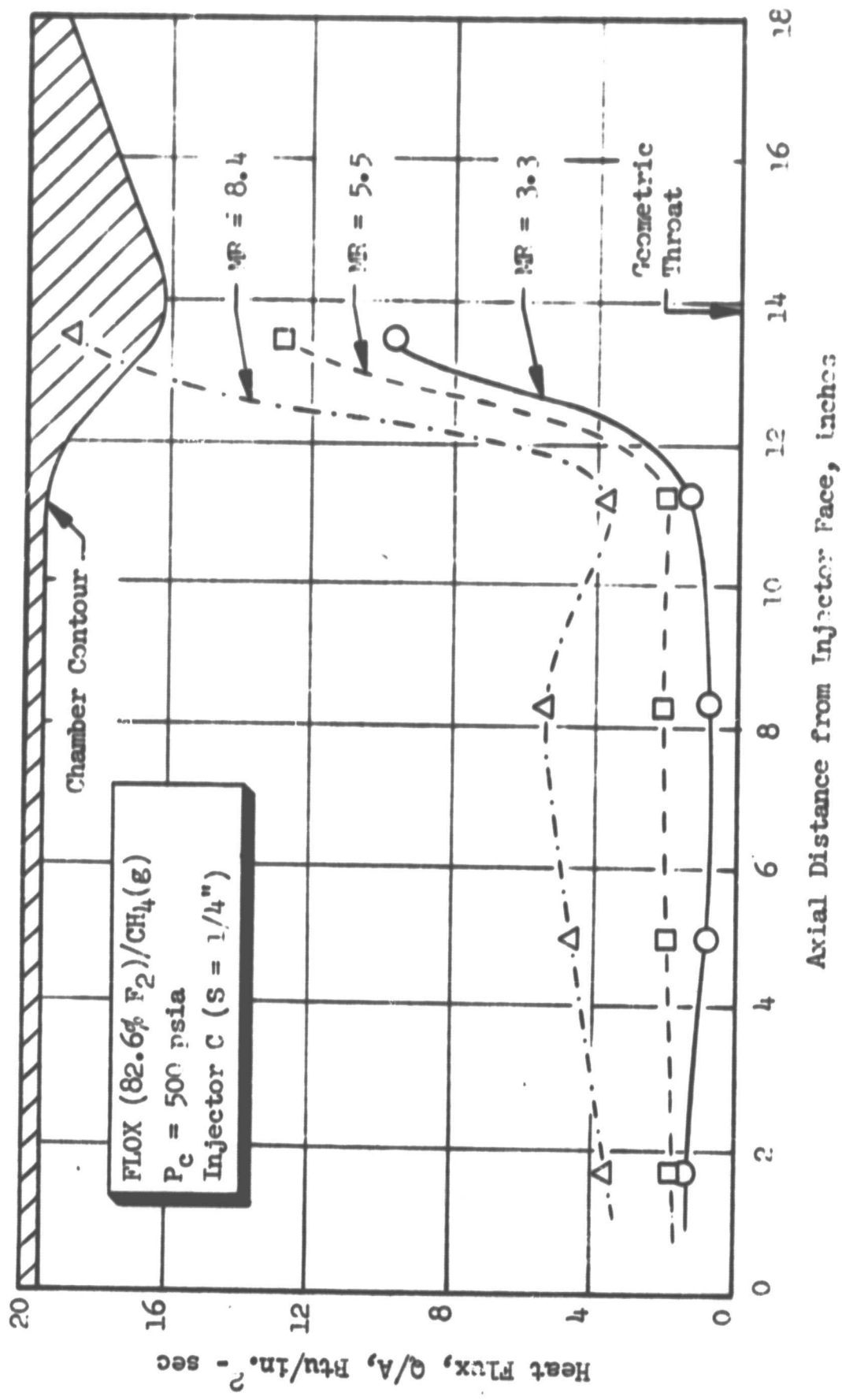


Figure 45. Effect of Mixture Ratio on Thrust Chamber Heat Transfer for Chamber Compatible C Injector

5.2.3 Cold-Flow Mixing

As noted previously, cold-flow mixing tests were conducted with the A (A-3) and C injectors to support their evaluation. The A injector was cold-flow evaluated at two conditions ($P_c = 250$ psia, MR = 5.7 and $P_c = 500$ psia, MR = 8.9) and the C injector at three conditions ($P_c = 500$ psia, MR = 3.5 and 5.75 and $P_c = 250$ psia, MR = 5.75). These data are presented in Table VIII. The resultant mixing-limited c^* efficiencies obtained by analysis of these cold-flow data were used in conjunction with predicted vaporization c^* efficiencies to predict (η_{c^*} ,predicted = η_{c^*} ,mix \times η_{c^*} ,vap) injector performance. Predicted performance is compared with the actual hot-fire performance in Fig. 46. The good agreement between predicted (η_{c^*} ,pred = η_{c^*} ,mix \times η_{c^*} ,vap) and actual performance (η_{c^*} predicted was within $\pm 2\%$ of η_{c^*} actual) lends confidence to the gas/liquid distribution measurement technique employed.

Drop sizes were calculated from Eq. 8 with $V_g = 215$ ft/sec. Since fuel injection momentum effects on D_{30} for the C injector elements were not defined experimentally, drop size from Eq. 8 were assumed to be valid for both the A and C injector configurations.

TABLE VIII. SUMMARY OF COLD-FLOW MIXING TEST CONDITIONS AND
DATA FOR FULL-SCALE INJECTORS A-3 AND C

Test No.	Full-Scale* Injector Configuration	Simulated Conditions		E_m , %	$M_{C^*, mix}$, %
		P_c , psia	MR		
1	A-3	250	5.7	81.5	94.4
2	A-3	500	8.9	84.7	97.7
3	C	500	3.5	83.4	99.9
4	C	500	5.75	86.2	94.8
5	C	250	5.75	79.3	93.1

*Tests were conducted flowing 1/4 segment of the injector

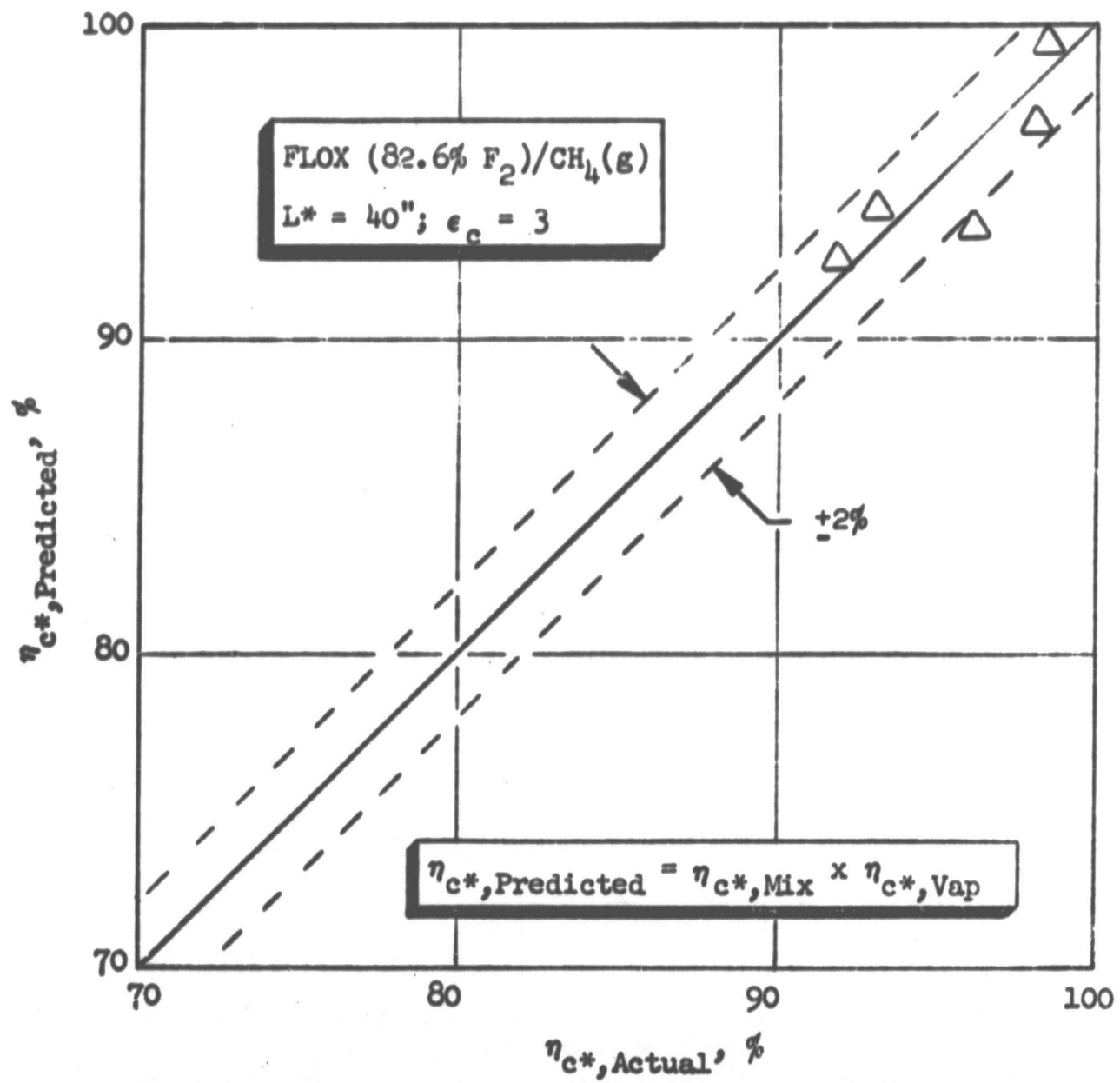


Figure 46. Comparison of Cold-Flow Predicted and Actual Hot-Fire Performance for A and C Like-Doublet Injectors

5.3 OPTIMIZED INJECTOR CONFIGURATION

Hot-fire and cold-flow experiments were conducted with the optimized like-doublet injector configuration to characterize its performance/chamber heat transfer characteristics. Cold-flow testing of the "optimized" injector was completed prior to its hot-fire evaluation.

Initial hot-fire testing of this injector was conducted to define performance characteristics of the core only. A series of tests was conducted in which the core was throttled ($P_c = 250$ to 500 psia) at constant mixture ratio (~ 6) and mixture ratio was varied (5 to 7.5) at constant chamber pressure (~ 500 psia). These experiments were conducted to define injector core performance characteristics and to verify the design criteria upon which the core design was based. During these experiments, the core only was fired in a chamber of the same L^* , length, and contraction ratio as was used for the full injector firings ($L^* = 40$ in.; $\epsilon_c = 3$). The required chamber geometry was obtained by insertion of the proper graphite liner into the existing steel chamber housings.

The second series of hot-fire tests conducted with the D injector was conducted in the reference chamber ($L^* = 40$ in.; $\epsilon_c = 3$) employing the full injector (core and periphery). Experiments were conducted to define the effects of peripheral zone mixture ratio and percent mass flow on performance and chamber heat transfer characteristics. Peripheral mixture ratio was varied from approximately 3 to 5.5 with 30 percent of the mass in the peripheral zone. In addition, the percent mass in the periphery was varied from around 15 to 40 percent at a mixture ratio of about 3.5 to 4.0. The overall mixture ratio and chamber pressure for all tests was 5.25 and 500 psia, respectively. Results from these experiments were used to select an "optimum" operating condition (percent mass flow and mixture ratio in the periphery; $P_c = 500$ psia, overall MR = 5.25). A bomb (stability rating) test was conducted with the optimum injector configuration to conclude the hot-fire experimental effort. Three electrically initiated bombs were sequentially detonated during this test. An extended duration test (~ 30 seconds) similar to that conducted with the coaxial injector (Ref. 5) was not conducted due to funding limitations.

5.3.1 Cold-Flow Mixing

Two cold-flow distribution tests were conducted with the optimized injector configuration. One of these tests was conducted flowing only the "high-performance" core portion of the injector (simulated conditions: $P_c = 500$ psia, MR = 6). The other test was conducted flowing both the "high-performance" core and "chamber-compatible" peripheral portions of the injector (simulated conditions: $P_c = 500$ psia, overall MR = 5.25, core MR = 6, peripheral MR = 4, percent mass flow to core = 70, percent mass flow to periphery = 30). The cold-flow test apparatus chamber diameter employed corresponded to the hot-fire chamber diameters (2.90 in. for the core-only tests; 3.89 in. for the full injector test). Test conditions and results of these tests are summarized in Table IX.

TABLE IX. SUMMARY OF COLD-FLOW TEST CONDITIONS AND DATA FOR OPTIMIZED LIKE-DOUBLE INJECTOR

Test No.	Simulated Conditions			$\eta_{m, mix}$, %	Comments
	P_{CJ} psia	Overall MR	Momentum Ratio(σ/f)		
1	500	6.0	0.85	94.0	<u>Core flow only</u>
2	500	5.25	0.85 (for core)	90.8	Core MR = 6 Peripheral MR = 4 Percent Mass Flow to Core = 70 Percent Mass Flow to Periphery = 30

Initially, the core only was cold-flow tested at its design conditions ($P_c = 500$ psia; MR = 6; momentum ratio (o/f) = 0.85). The mixing efficiency was slightly lower than expected ($E_m = 94.0$; $\eta_{c^*, mix} = 98.6$). An $\eta_{c^*, mix}$ of 99+ percent was expected.

Simulated conditions for the cold-flow test conducted flowing the full injector were:

$P_c = 500$ psia

Overall MR = 5.25

Core MR = 6.0

Peripheral MR = 4.0

Percent Mass Flow to Core = 70

Percent Mass Flow to Periphery = 30

Note that the core flow conditions are the same as for the initial test. The resulting mass and mixture ratio distributions both looked quite favorable (Fig. 47). The majority of the mass (≈ 80 percent) was in the core region and was relatively well mixed. Peripheral zone mass flux and mixture ratio were low as desired. E_m and $\eta_{c^*, mix}$ were 90.8 and 98.2 percent, respectively. This result, in combination with a predicted $\eta_{c^*, vap}$ of ~ 99 percent in the 40-in. L^* chamber, indicated that the "optimized" injector should be capable of attaining simultaneous high-performance and chamber compatibility.

The cold-flow results are compared with hot-fire data in subsequent paragraphs.

5.3.2 Hot-Fire Performance

High-Performance Core. Six hot-fire tests were conducted employing only the core portion of the injector. Test variables were chamber pressure (250 and 500 psia at MR = 6) and mixture ratio (5 to 7.5 at the design P_c of 500 psia). The tests were conducted in a 40-in. L^* ($\epsilon_c = 3$) chamber and were approximately 3 seconds in duration. No chamber heat flux measurements were made during these tests. Test conditions and results are summarized in Table XI.

Performance characteristics of the D injector core are presented in Fig. 48. Hot-fire corrected c^* efficiency and cold-flow mixing c^* efficiency are shown plotted as a function of momentum rates (o/f) in this figure. Hot-fire test conditions (P_c and mixture ratio) are noted. The performance predicted based on the cold-flow data and combustion models ($\eta_{c^*, predicted} = \eta_{c^*, mix} \times \eta_{c^*, vap} \cong 97.6$) is within ~ 1.5 percent of the hot-fire measured value.

Full-Scale D Injector. Nine tests were conducted employing the full injector (both the core and peripheral elements). Test variables were peripheral zone mixture ratio and percent mass flow to the periphery. Peripheral zone mixture ratio was varied from 3.0 to 5.5 with 30-percent mass flow to the periphery. In addition, the peripheral zone mass flow was varied from 15 to 40 percent at a peripheral zone mixture ratio of approximately 3.75. Overall mixture ratio and chamber

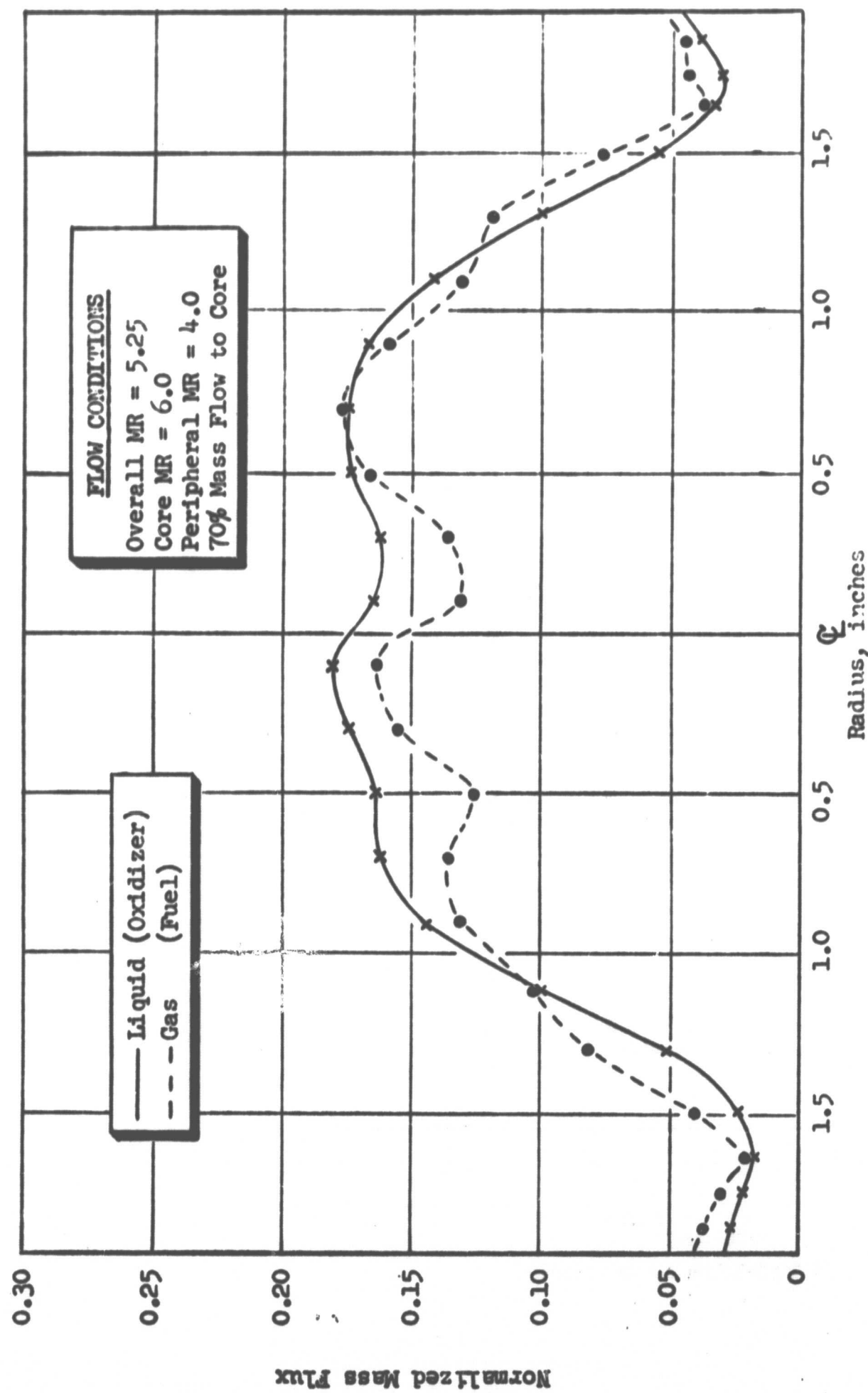


Figure 47. Normalized Mass Flux Profile for Cold-Flow Mixing Test Conducted With Full D Injector

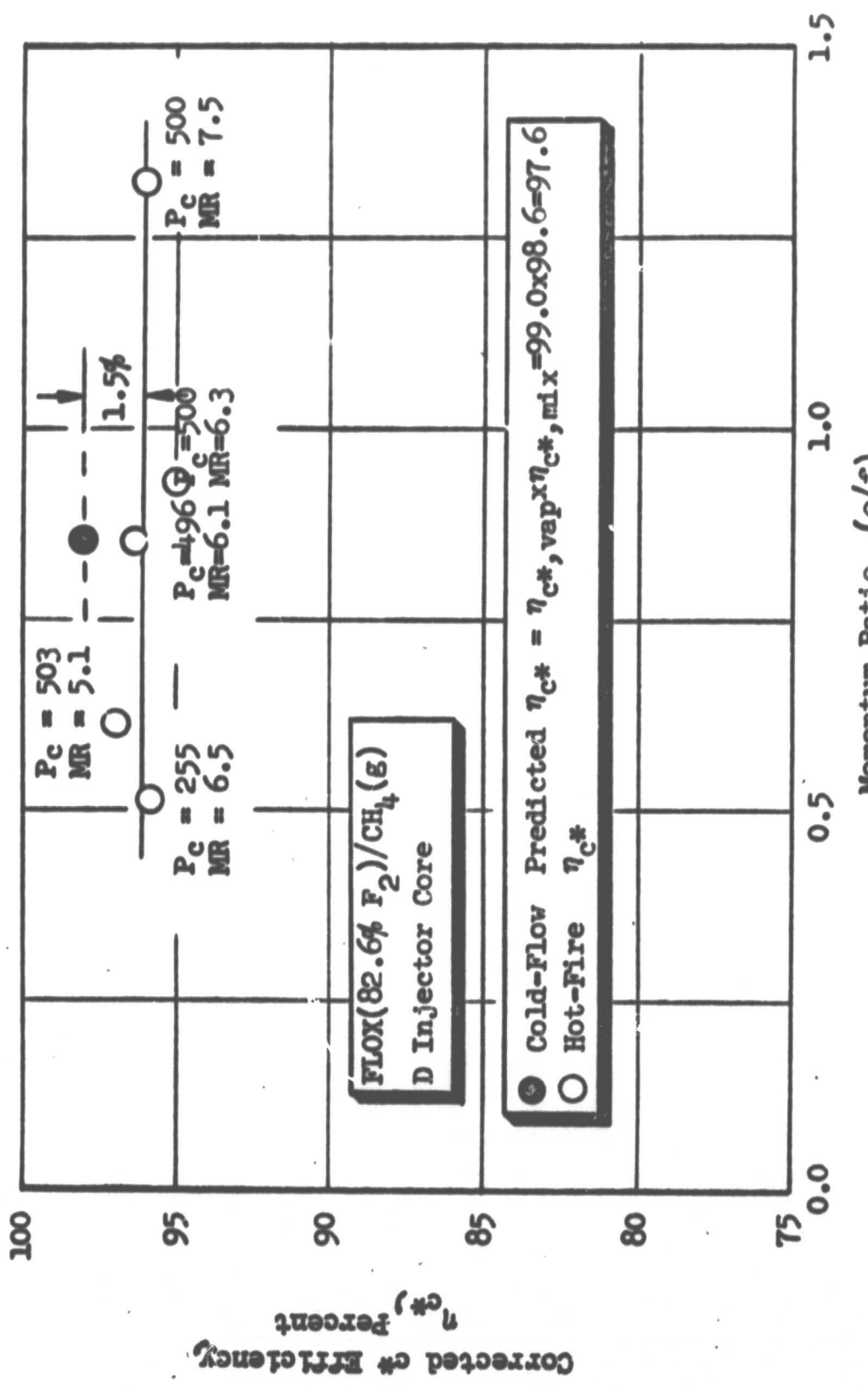


Figure 48. Performance Characteristics of D Injector Core

pressure was held constant at 5.25 and 500 psia for all the full injector tests. All tests were conducted in the 40-in. L* ($\epsilon_c = 3$) chamber and were approximately 3 seconds in duration. Chamber heat flux measurements were made during all but one of these tests (the test conducted with 40 percent more flow to the periphery).

The effects of peripheral zone mixture ratio and percent mass flow to the periphery (at design conditions; $P_c = 500$ psia and overall mixture ratio = 5.25) on performance are presented in Fig. 49. Performance (η_{c*}) is in the 92.5 to 97.5 range. With 30-percent mass flow to the periphery, (η_{c*}) increases substantially with increasing peripheral zone mixture ratio in the 3 to 4 range and is relatively constant for mixture ratios between 4 and 5.5. Decreasing the percent mass flow to the periphery from 30 to 15 percent (at a $MR \geq 4.1$) appears to have little effect on performance. Increasing the percent mass flow to the periphery from 30 to 40 percent (at $MR \geq 3.5$) caused approximately a 2.5-percent loss in performance.

Cold-flow predicted performance (η_{c*} ,predicted = η_{c*} ,mix $\times \eta_{c*}$,vap = 97.2) is within 1 percent of the actual performance (see data point in Fig. 49 for peripheral zone mixture ratio of 4.0 with 30-percent mass flow to the periphery).

5.3.3 Chamber Heat Transfer

The effects of peripheral zone mixture ratio and percent mass flow to the periphery (at design conditions; $P_c = 500$ psia and overall $MR = 5.25$) on chamber heat transfer characteristics is presented in Fig. 50 through 52. These data are for a common inside wall temperature of 1000 F. The hot-fire data show that chamber wall heat flux can be significantly reduced by controlling the peripheral zone mixture ratio or the percentage of mass flow to the peripheral zone.

The effect of peripheral zone mixture ratio on chamber heat flux (average q/A in the cylindrical chamber section) for the "optimized" like-doublet injector is presented in Fig. 50. Chamber heat flux increases with increasing peripheral zone mixture ratio and decreasing percent mass flow to the periphery, as expected. No heat flux data were obtained for the test conducted with 40-percent mass flow to the periphery.

Figures 51 and 52 present chamber heat flux profiles for the tests conducted with the "optimized" like-doublet injector. Heat flux is shown plotted as a function of axial distance from the injector in these figures. The effect of peripheral zone mixture ratio on chamber heat transfer characteristics is shown in Fig. 51 for a constant percent mass flow (30 percent) to the peripheral zone. Note that reducing the peripheral zone mixture ratio reduced the nozzle heat flux as well as the chamber heat flux. Good data repeatability was observed (note the agreement between the two tests conducted with a peripheral zone mixture ratio of 5.5). The effect of percent mass flow to the periphery on chamber heat transfer is shown in Fig. 52 for the 15- and 30-percent mass flow tests ($MR \geq 4$). Reducing the percent mass flow from 30 to 15 percent at a peripheral zone mixture ratio of ~ 4 causes an increase of approximately 30 to 40 percent in the chamber heat load.

FLOX/CH₄(g)
 $P_c = 500$ psia
 $(MR)_o = 5.25$
 Like-Doublet Injector

■ $\eta_{c^*,\text{predicted}} = \eta_{c^*,\text{vap}} \times \eta_{c^*,\text{mix}} = 99.0 \times 98.2 = 97.2$

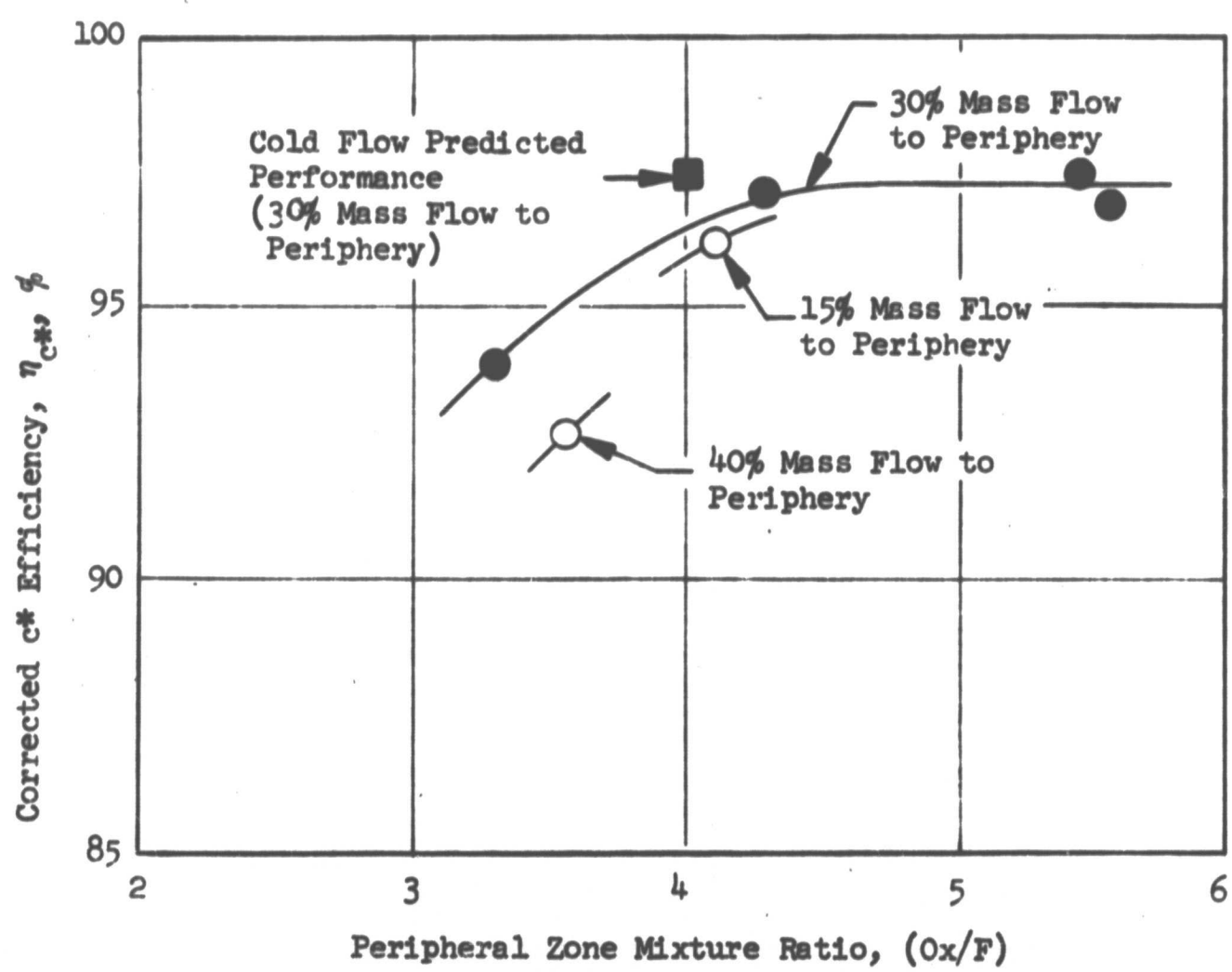


Figure 49. Effect on Peripheral Zone Mixture Ratio on Performance for Optimized Like-Doublet Injector Configuration

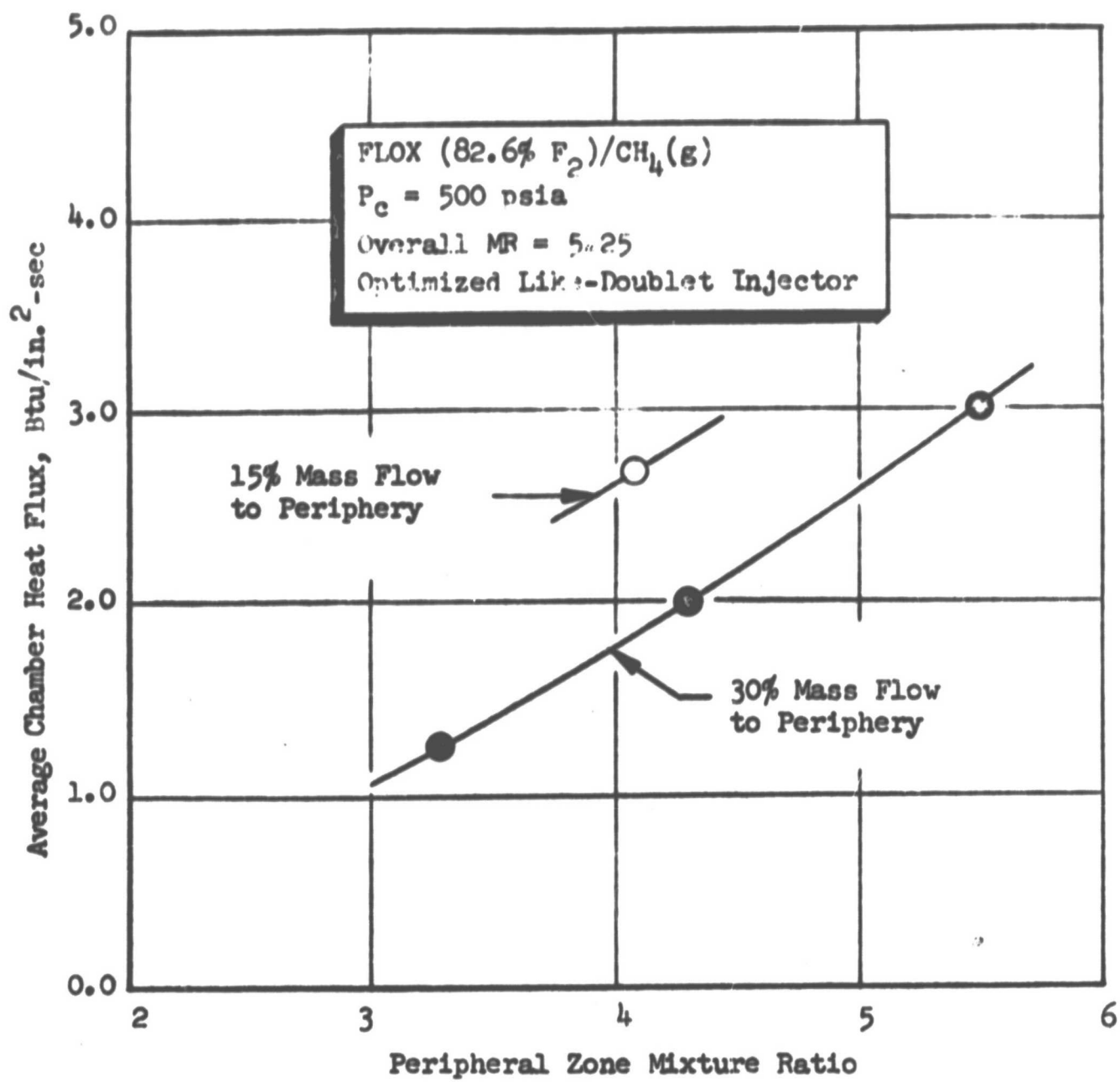


Figure 50. Effect of Peripheral Zone Mixture Ratio on Chamber Heat Flux for Optimized Like-Doublet Injector Configuration

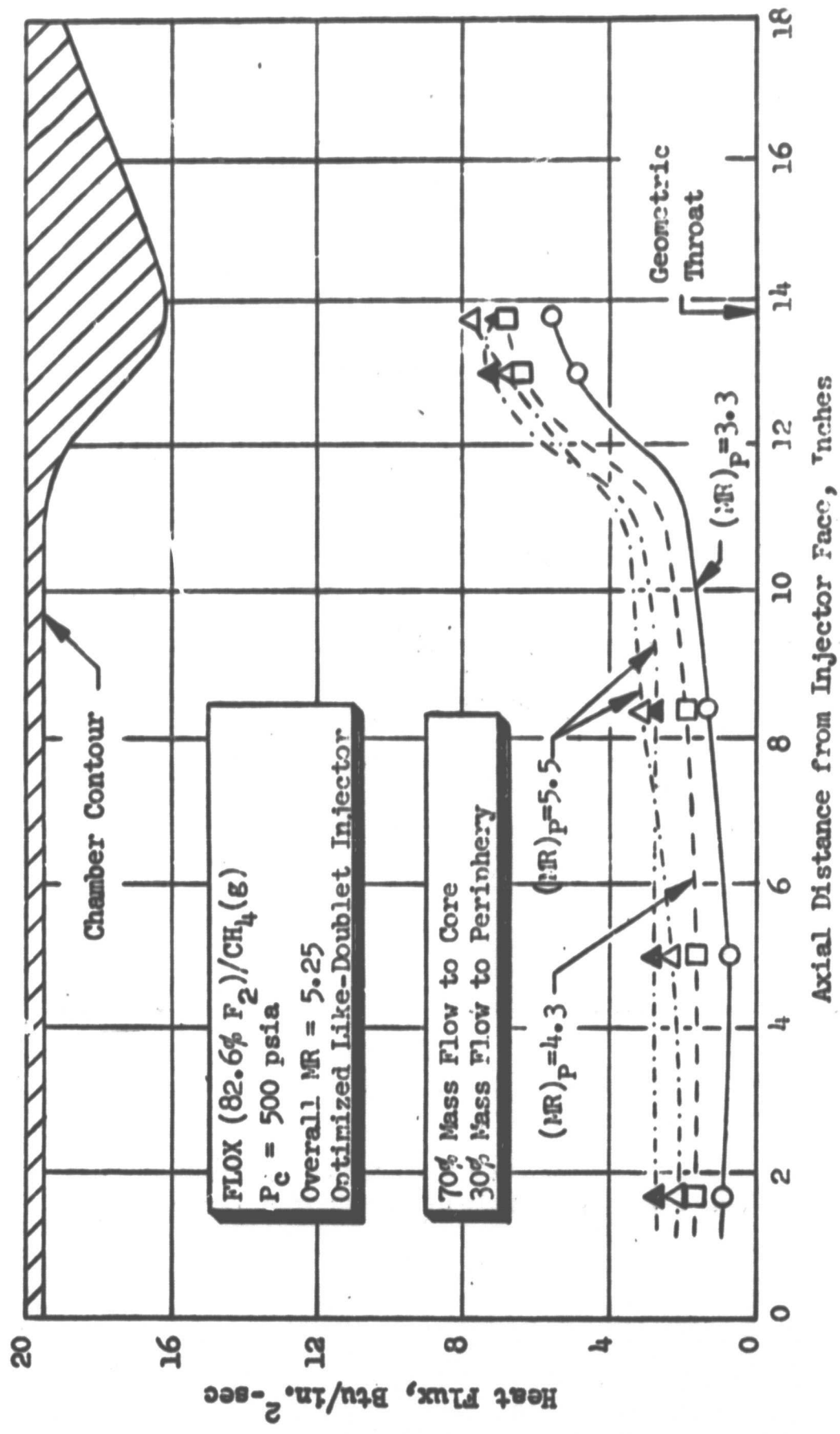


Figure 51. Effect of Peripheral Zone Mixture Ratio on Chamber Heat Transfer Characteristics for Optimized Like-Doublet Injector

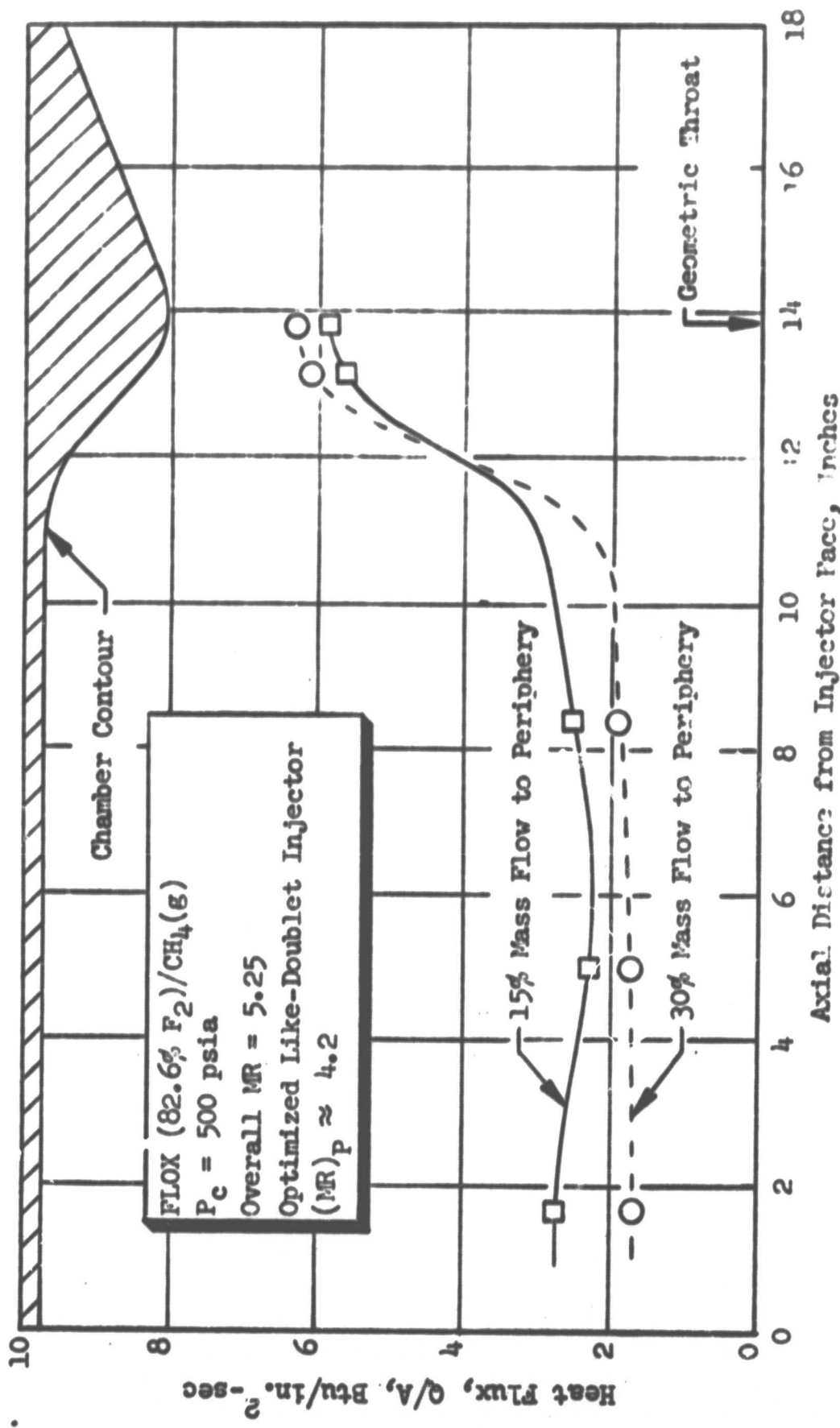


Figure 52. Effect of Percent Mass Flow to Peripheral Zone on Chamber Heat Transfer for Optimized Like-Doublet Injector

5.3.4 Dynamic Stability

An injector stability rating test was conducted with the full D injector at the following test conditions:

$P_c = 500$ psia

Overall MR = 5.25

Core MR = 6

Peripheral MR = 3.5

Percent Mass Flow to Periphery = 40

The test constituted sequential pulsing of the engine with bombs of increasing size (2.5, 4.5, and 6.5 grains).

The bomb rating tests revealed that the like-doublet injector was marginally unstable at the flow conditions tested. Some injector damage (face burning) was encountered during the stability rating test. Damage was minimal and future testing with the injector is feasible.

It should be recognized that stability of this injector is probably a function of the peripheral zone flow conditions (i.e., percent mass flow and mixture ratio) and that further testing to define injector stability characteristics as a function of these parameters is in order. The injector may be completely stable at the selected "optimum" test conditions (i.e., peripheral zone mass flow percentage = 30 percent and mixture ratio ≥ 4). During the test conducted, self-damping of the pressure disturbance did occur, although this took approximately 1 second. It appears that if it is necessary, the injector could be made stable with minimal effort by use of acoustic cavities. The resonant frequency for the first tangential mode (~ 8000 Hz) is within the range where acoustic cavities have been quite successful in stabilizing injectors. In addition, the injector was spontaneously stable and did (eventually) recover by self-damping of the bomb-initiated instability. No instability problems were encountered in any of the other tests conducted during the program. In fact, one test was conducted at identical conditions to those of the bomb test and no combustion instabilities were noted.

5.4 DATA CORRELATIONS

Predicted and actual performance for the A-3, C and D (both core-only and full injector) injectors are compared in Fig. 53. The average deviation of the predicted performance is only 1.3 percent from the actual hot-fire value. This excellent agreement between cold-flow predicted and actual hot-fire performance lends confidence to the use of the prediction techniques employed.

The effect of element density on the mixing level for optimized (fan spacing = 0) like-doublet elements is shown in Fig. 54. The correlating curve in this figure is based on data obtained with: (1) a single element, (2) the A-3 injector, (3) the 1/4-segment model of the A injector, and (4) the core of the D injector. As is noted in the figure, a high-element density is required for high-mixing c^* efficiency. Mixing c^* efficiency appears to asymptotically approach 99 percent as the element density is increased. Figure 54 defines the element density required to achieve any desired level of mixing.

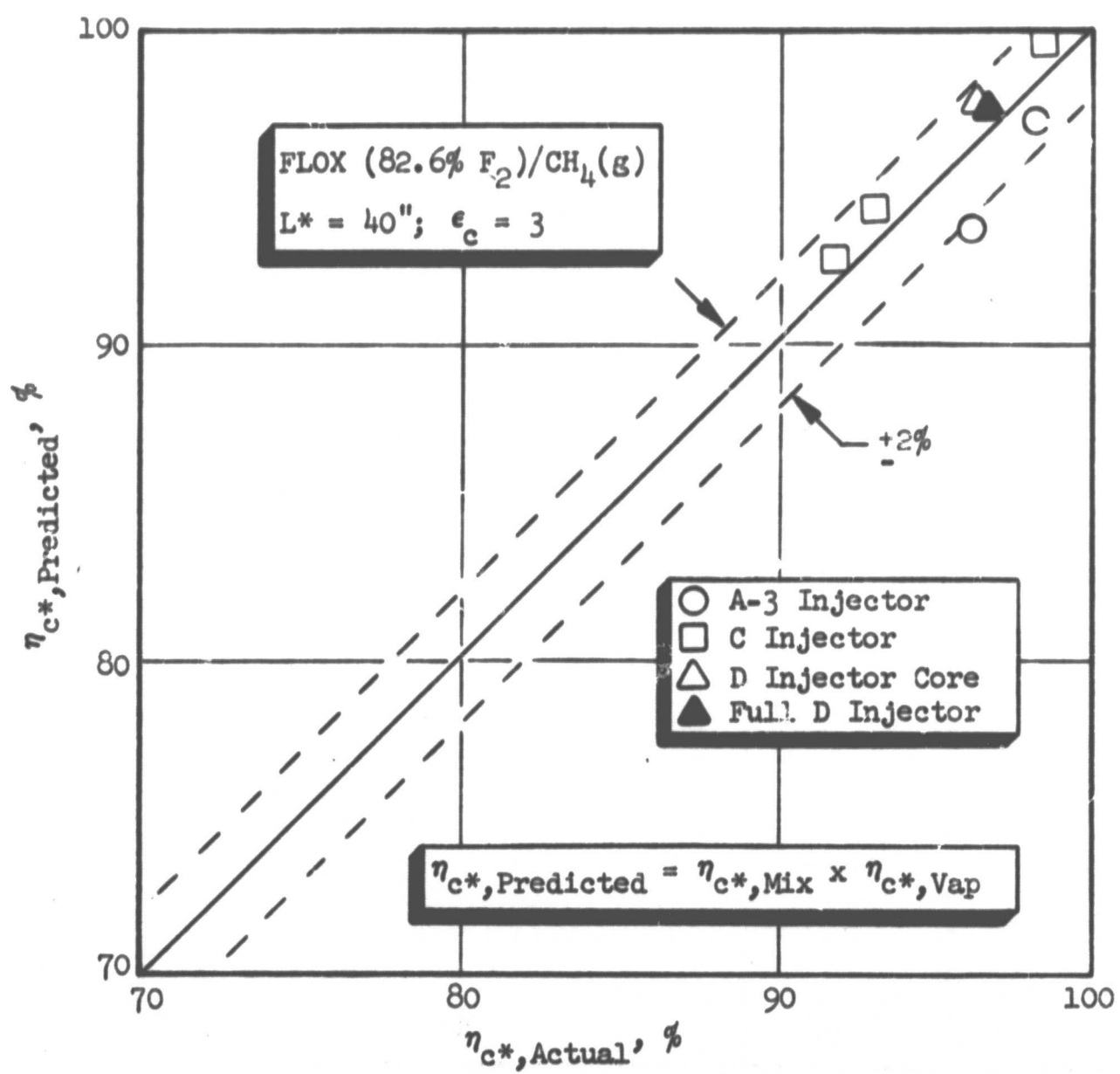


Figure 53. Comparison of Cold-Flow Predicted and Actual Hot-Fire Performance for A, C, and D Like-Doublet Injectors

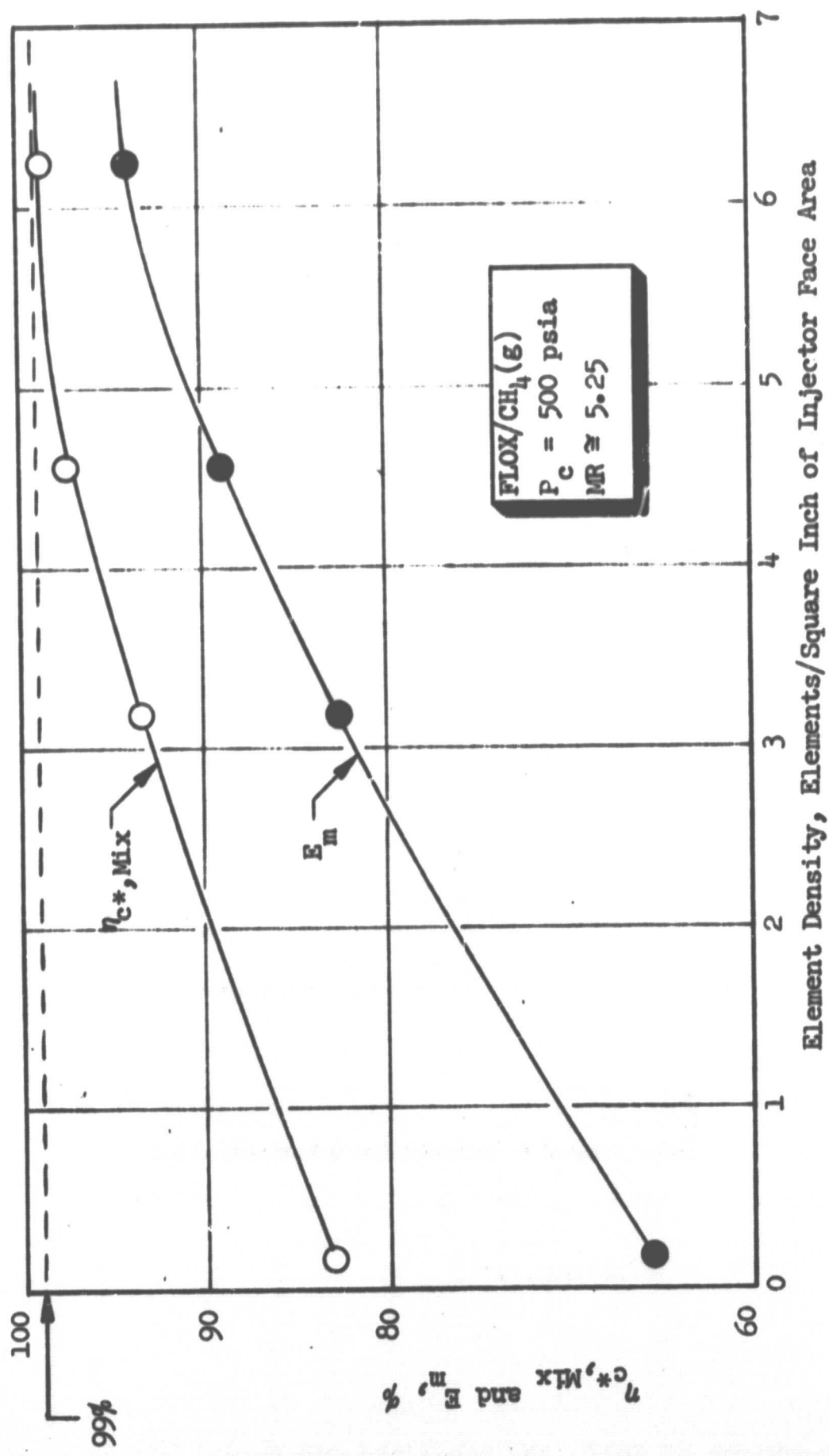


Figure 54. Effect of Element Density on Mixing for Zero Fan Spacing
Optimized Like-Doublet Injector (Cold-Flow Results)

6.0 CONCLUDING REMARKS

This discussion is divided into four sections: (1) performance and chamber heat transfer characteristics of the optimized like-doublet injector configuration, (2) use of cold-flow injector modeling techniques to support injector design, (3) application of data derived in this program to the design of other gas/liquid propellant systems, and (4) recommendations for future work.

6.1 LIKE-DOUBLET PERFORMANCE AND CHAMBER HEAT TRANSFER CHARACTERISTICS

As was shown in Fig. 49, although performance of the optimized like-doublet injector configuration was high at design conditions ($P_c = 500$ psia; $MR = 5.25$), it was slightly below the performance target of the program. Performance was in the 97- to 98-percent range. The program goal was 99 percent of the theoretical shifting characteristic exhaust velocity at the design conditions. Approximately 1-percent loss in performance was due to incomplete propellant vaporization ($\eta_{c^*,\text{vap}} \approx 99$). A 1.5- to 2.0-percent loss in performance was due to nonuniform propellant mixing ($\eta_{c^*,\text{mix}} \approx 98.5$). Element design criteria for both high-performance and chamber compatibility were developed.

It is probable that with warmer methane, the mean drop size could be reduced enough to eliminate the 1-percent vaporization loss. The subject tests were run with approximately 50 F methane in the manifold. Methane from a regenerative-cooling jacket might be on the order of 800 F, leading to a much higher methane injection velocity and, therefore, to improved atomization. Thus, $\eta_{c^*} = 98.5$ percent should be attainable with the present like-doublet injector. On the other hand, the 1.5-percent mixing loss in performance would be difficult to eliminate with the FLOX/methane propellants. The D injector probably represents a practical limit on the number of elements per unit area. Mixing efficiency appears to become asymptotic with the element density greater than about 6.5 elements/square inch of injector face area (the value obtained with the D injector) and, thus, further gains through decreasing the thrust/element do not seem feasible. If the additional 0.5 percent of η_{c^*} were really needed, probably the best approach would be to investigate additional element design parameters such as intra-element spacing, y , or fan impingement angle, β , (this may also result in a lesser number of required elements). These parameters were not specifically evaluated under this program, but could be further optimized using the same cold-flow mixing techniques. It should be noted that for other propellants such as LOX/GH₂ or OF₂/diborane, which are less sensitive to mixing uniformity than FLOX/methane, the same physical degree of mixing achieved with the like-doublet injector would produce essentially 100-percent η_{c^*} and ultrahigh performance should be readily attainable with a like-doublet injector.

Excellent injector/ thrust chamber compatibility was demonstrated in the short-duration tests (~3 seconds). Thrust chamber heat flux profiles for tests conducted with the optimized injector configuration (Fig. 51) result in a state-of-the-art improvement regarding heat flux levels and chamber heat loads for FLOX/CH₄(g) (Ref. 1 and 2). The data show that chamber wall heat flux can be

significantly reduced by controlling peripheral zone element design (fan spacing, fan alignment with respect to the chamber wall, etc.) and/or operating conditions (mixture ratio and percentage of mass flow). The effect of these parameters on average heat flux in the cylindrical chamber is shown in Fig. 55. The results from this program indicate that use of the like-doublet injector with dual-zone design results in a state-of-the-art improvement regarding heat flux levels and thrust chamber thermal management.

No instability was encountered in the 39 performance tests. However, the stability rating tests conducted with the optimized injector configuration indicated that it was marginally unstable when pulsed. This test was conducted with a high mass percentage in the peripheral zone (~40 percent). Further testing of the injector to define its stability characteristics as a function of peripheral zone flow condition is necessary. However, it appears that, if necessary, the injector could be made dynamically stable with incorporation of an acoustic cavity.

6.2 COLD-FLOW INJECTOR MODELING TECHNIQUES

The gas/liquid mixing facility/techniques which were developed on this program and contract NAS3-12001 have been shown to be a powerful tool for the rational design of injectors. In particular, the pressurized single-element experiments provided valuable design criteria not only for mixing levels but also resulting mass flow and mixture ratio distributions (chamber compatibility). Cold-flow data were employed to define element design criteria for both high-performance and control of chamber wall heat flux levels.

Perhaps the most valuable gain from the cold-flow testing is the physical insight into how the gas and liquid flow patterns are influenced by changes in element design and operating conditions. Often very small dimensional changes in the design can substantially alter the mass flux and mixture ratio patterns. An example of the application of this information was the revelation that a slight rotation (~15 degrees) of the C injector elements with respect to the chamber wall results in placement of the lowest mixture ratio (and, therefore, coolest) gas stream along the wall.

The cold-flow results were complemented by full-scale injector hot-fire data which empirically verified results obtained with the cold-flow technique and supporting combustion model analyses. Performance and heat transfer results repeatedly matched parametric trends indicated by the cold-flow and combustion model data. Based on seven tests, the predicted performances showed an average deviation of only 1.3 percent from the hot-firing data.

6.3 APPLICATION OF RESULTS TO OTHER PROPELLANT SYSTEMS

The hot-fire and cold-flow data from this study can be employed as guidelines for design of high-performance, chamber-compatible injectors for other gas/liquid propellant combinations. For like-doublet element injectors, propellant mixing and control of chamber heat flux levels (propellant distribution) has been shown to

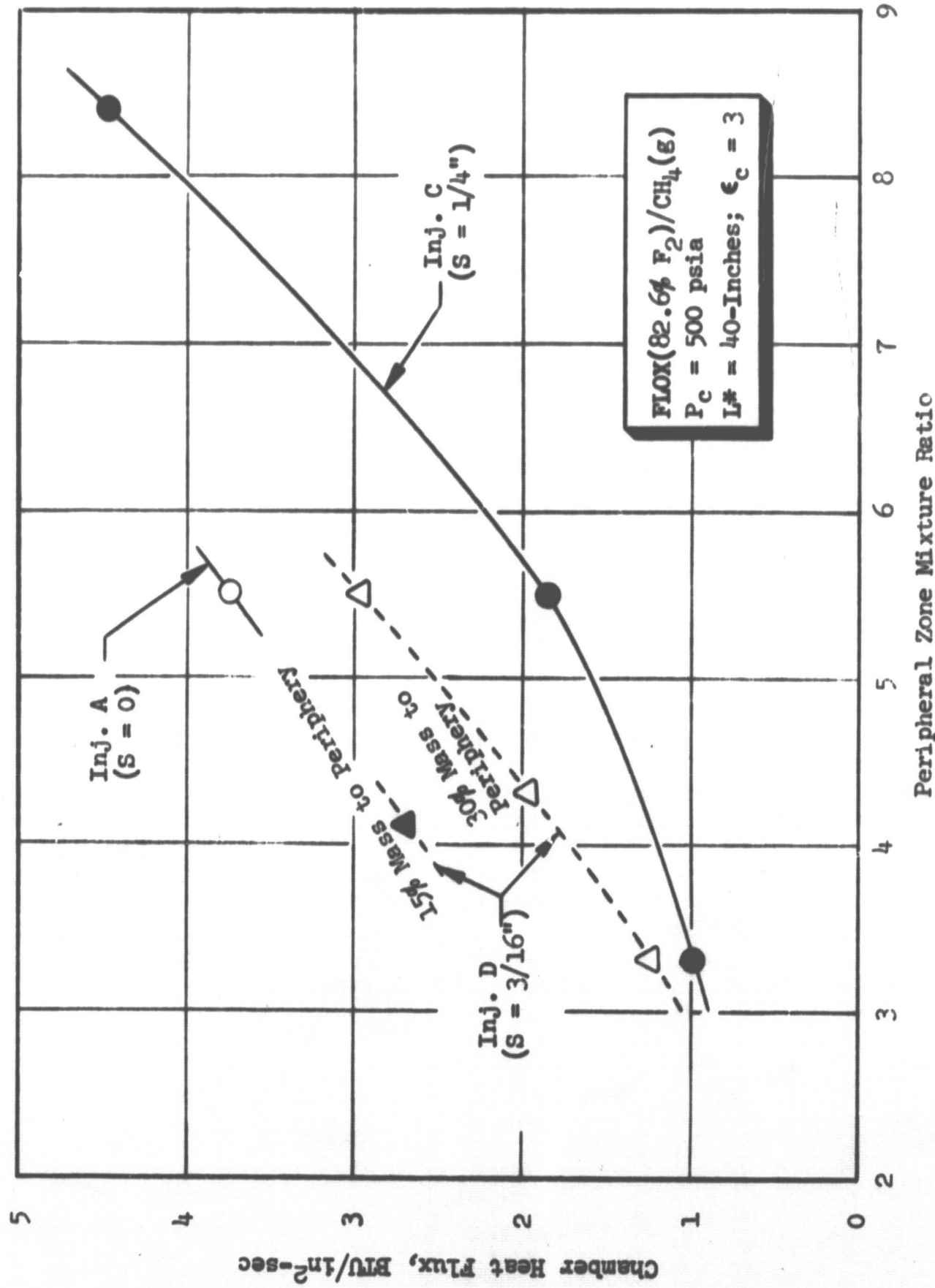


Figure 55. Effect of Peripheral Zone Element Design, Mixture Ratio, and Percent Mass Flow on Average Cylindrical Chamber Heat Flux for FLOX/CH₄(g) Like-Doublet Injector

be primarily a function of geometric element design parameters (fan spacing, fan inclination angle, etc.). The oxidizer/fuel injected momentum ratio influenced performance to a lesser degree over the range investigated (~ 0.25 to 2). However, caution should be exercised when applying these data to propellant combinations whose elements operate in ranges considerably different than those employed in this study. To obtain good quantitative design guidance, the recommended approach would be to apply the cold-flow propellant distribution measurement techniques and combustion models developed and verified under this program directly to the propellant and design requirements of interest.

6.4 RECOMMENDATIONS FOR FUTURE WORK

Recommendations for future work to further substantiate the like-doublet injector design for possible FLOX/methane application which evolved from this study are as follows:

1. An extended-duration test, similar to that conducted with the coaxial injector of Ref. 5, should be conducted to substantiate injector-thrust chamber compatibility.
2. Additional work in the area of combustion stability should be conducted. Experiments to define peripheral zone mass and mixture ratio effects on injector stability characteristics should be conducted. If necessary, an acoustic cavity should be designed, fabricated, and tested to verify dynamic stability.
3. Throttling tests should be performed to verify stability of the injector at throttled conditions.

The ease in control of chamber compatibility with the like-doublet element injector makes it an attractive candidate for other gas/liquid propellant combinations such as LOX/GH₂ and LOX/propane(g). Use of the "two-zone approach," i.e., "high-performance" core and "chamber-compatible" peripheral zone, should permit attainment of excellent chamber heat transfer characteristics with negligible loss in performance. (The reduced sensitivity of O₂/H₂ to imperfect mixing should permit achievement of essentially 100-percent η_c^* mix.) Under development programs, however, it is not advisable to employ injector concepts that have not been subjected to hot-fire evaluation. Therefore, a technology program is recommended to design, fabricate, and test a like-doublet injector for LOX/GH₂ to demonstrate the performance, chamber heat fluxes, and stability of this type.

APPENDIX A

K-PRIME COMBUSTION MODEL

This appendix presents a brief description of the Rocketdyne K-RIME combustion model. More detailed descriptions of the model can be found in Ref. A-1 and A-2.

To determine the degree of propellant vaporization, the combustion model (K-PRIME) takes into consideration:

1. Compressible combustion gas flow with mass and energy addition
2. Droplet drag in the accelerating combustion gas flow field
3. Droplet vaporization with convective heat transfer from the hot combustion gas

These factors result in an analytical description of the "bootstrap" combustion processes typical of rocket engines. The model calculates axial profiles of chamber pressure, combustion gas velocity, vaporization from a range of droplet sizes corresponding to the droplet size distribution produced by the injector, droplet velocities, and the overall percentage of oxidizer which is vaporized.

The combustion model takes into account the compressible flow of combustion gases by the normal gas-dynamic equations; taking into account the effects of mass and energy addition from the vaporizing and reacting propellants.

Droplet drag, for the distribution of droplet sizes produced by the injector, is accounted for by the scalar equation shown below:

$$\frac{dv_D}{dt} = 3/4 \times \frac{C_D \rho_g (v_g - v_D)^2}{\rho_L D} \quad (A-1)$$

where

v_D = droplet velocity, ft/sec
 t = time, seconds
 C_D = drag coefficient (a function of droplet Reynolds number)
 ρ_g = combustion gas density, lbm/ft^3
 ρ_L = droplet liquid density, lbm/ft^3
 v_g = combustion gas velocity, lbm/ft^3
 D = droplet diameter, feet

Droplet vaporization is accounted for by an equation similar to:

$$\frac{d(D^2)}{dt} \cdot k' = \frac{144 \times 8\lambda_g}{\rho_L C_{p_V}} \ln \left[1 + \frac{C_{p_V}}{\Delta H_V} (T_g - T_v) \right] (1 + 0.6 \Pr^{1/3} \text{Re}^{1/2}) \quad (\text{A-2})$$

where

- k' = droplet vaporization constant, in./sec
- D = droplet diameter
- λ_g = combustion gas thermal conductivity
- ρ_L = liquid density
- C_{p_V} = vaporized propellant heat capacity
- ΔH_V = liquid propellant heat of vaporization
- T_g = combustion gas temperature
- T_L = liquid propellant boiling temperature
- \Pr = Prandtl number for the combustion gas
- ρ_g = combustion gas density
- Re = Reynolds number for combustion gas

For computer solution of Eq. A-2, the application is more complex. The simplified expression presented above shows the effects of the various physical parameters on droplet vaporization rate. The last bracketed term on the right-hand side of Eq. A-2 represents the effects of forced convection on droplet vaporization, and the remainder of the terms represent the effects of propellant physical properties and combustion gas properties on droplet vaporization rate (Ref. A-3).

For gas/liquid systems, incomplete oxidizer vaporization degrades c^* performance by reducing the total amount of combustion gas produced which results in the burned gas mixture ratio being different from the injected mixture ratio, thereby affecting the temperature, molecular weight, etc. of the burned gas. This effect has been included by Priem (Ref. A-4) in the following equation which allows the determination of $\eta_{c^*, \text{vap}}$ from parameters calculated by the combustion model computer program:

$$\eta_{c^*, \text{vap}} = \left(\frac{\dot{w}_B}{\dot{w}_I} \right) \left(\frac{c^*_B}{c^*_I} \right) \quad (\text{A-3})$$

where

- \dot{w}_B = flowrate of burned gas at the geometric throat
- \dot{w}_I = injection flowrate of fuel plus oxidizer
- c^*_B = theoretical c^* corresponding to the composition of the burned gas at the geometric throat
- c^*_I = theoretical c^* corresponding to the injection mixture ratio of liquid fuel and oxidizer

This computerized combustion model, the general nature of which is described in very brief form by Eq. A-1 through A-3 was used to parametrically investigate the effects of design and operating variables on $\eta_{c^*,vap}$ for the FLOX/CH₄(g) propellant combination (see Section 3.0).

The two most important variables affecting $\eta_{c^*,vap}$ are propellant drop size and combustion chamber geometry. From Eq. A-2, it is seen that the residence time required to completely vaporize a droplet is proportional to the square of the droplet diameter. Equally important, the geometry of the combustion chamber dictates the total residence time during which the droplets must vaporize. If this residence time is too short, the droplets will not be completely vaporized.

Equation A-2 is an implicit expression showing that propellant vaporization efficiency is governed by droplet acceleration and heating by the high-temperature combustion gas. For thrust chambers having contraction area ratios greater than about 2, combustion gas flow can be considered incompressible; therefore, chamber L^* is a good index of combustion gas residence time. From continuity, combustion gas velocity for the 2-to-1 chamber will always be higher than that for the 4-to-1 chamber. Higher combustion gas velocities will generally be accompanied by an increased velocity lag between combustion gas and propellant droplets. However, the lower contraction area ratio chambers ($L^* = \text{constant}$) will tend to result in longer residence time for the droplets. The higher relative velocity between the combustion gas and propellant droplets will also tend to enhance convective heating and resultant droplet vaporization.

An assumption made in the one-dimensional combustion model program input is the amount of combustion which occurs within the initial injection region. This is required to arrive at a nearly one-dimensional region, and eliminate calculations in the grossly nonuniform injection region (Ref. A-2). It is usually assumed that 10 percent of the propellants have vaporized and reacted within 1 inch of the injector face. This initial condition has proved adequate and permits good correlation with observed experimental results. To assess the effect of variations in this assumption, 5, 10, and 20 percent of the propellants consumed were analytically considered and found to have an insignificant influence on performance. Performance variation due to assumption of 5 to 20 percent initial propellants vaporized instead of 10 percent was $\leq \pm 0.5$ percent in the range of drop size ($D_{30} \leq 150$) and L^* (15 inch $\leq L \leq 60$ inch) considered. Effects of injection velocity and percent of propellants initially reacted were only significant when the propellant drop size is large or when geometric restrictions favored lowered performance.

REFERENCES

- A-1. Lambiris, S. L., L. P. Combs, and R. S. Levine, "Stable Combustion Processes in Liquid Propellant Rocket Engines," Combustion and Propulsion, Fifth AGARD Colloquium: High-Temperature Phenomenon, The MacMillan Co., New York, 1962, pp. 596-636.
- A-2. Combs, L. P., Liquid Rocket Performance Computer Model with Distributed Energy Release, Final Report, NAS7-746, Rocketdyne, a division of North American Rockwell, Canoga Park, California, November 1971.
- A-3. Sutton, R. D. and M. D. Schuman, "Liquid Rocket Combustion Analysis for Coaxial Jet Injection of Gas/Liquid Propellants," CPIA Publication 204, Vol. I, 7th JANNAF Combustion Meeting, February 1971, p 511.
- A-4. Priem, R. J. and Heidmann, M. F., Propellant and Vaporization as a Design Criterion for Rocket Engine Combustion Chambers, NASA TR R-67, 1960.

APPENDIX B

PRESSURIZED COLD-FLOW MIXING FACILITY

INTRODUCTION

Early in the like-doublet portion of the subject program, an analytical investigation was conducted to develop appropriate cold-flow modeling criteria for hot-fire gas/liquid injector systems (Ref. B-1). The analysis considered the flow field of a simple injection system consisting of an axisymmetric gas jet into which a liquid jet is introduced at some arbitrary angle. Cold-flow modeling criteria were derived from consideration of available experimental data and an analysis of the governing conservation equations. In general, it was found that, to satisfy all of the cold-flow modeling criteria for a gas/liquid system, the cold-flow experiments would need to be performed in a pressurized environment. Pressurization was required in order to model the density and dynamic pressure of the hot-fire gas phase (fuel).

MEASUREMENT SYSTEM

To characterize the spray fields generated by gas/liquid rocket motor injectors, a system was developed to determine local values of gas and liquid mass flux under pressurized conditions. Knowing local values of gas and liquid mass flux, the "mixedness" (i.e., E_m) of the two-phase spray field was determined. In addition, examination of local values of mass flux was used to characterize peripheral element/candidates for injector-thrust chamber compatibility (see Section 5.0).

A schematic of the complete measurement system for the characterization of dense gas/liquid spray fields is shown in Fig. B-1. Mixing experiments were performed with both single-element and multi-element gas/liquid injectors. The apparatus consisted essentially of a pressurized test section in which the deceleration probe (described in subsequent paragraphs) was positioned in $r-\theta$ coordinates. The system contained several "water traps" to ensure that water, which can accumulate during extended test periods, does not plug critical pressure lines in the system. A photograph of the system, which is located at the Combustion and Heat Transfer Laboratory, is shown in Fig. B-2.

A problem associated with the characterization of spray fields generated with single-element injectors was the suppression of the flow-field recirculation caused by the injection of high-velocity streams into a finite closed volume. High levels of recirculation within the test section precluded the accurate determination of the gas-phase flow field. To eliminate flow field recirculation, a low-velocity (7 to 12 ft/sec) uniform "base bleed" flow surrounded the single-element injector. These values of base bleed velocity are in accord with the Craya-Curtet criterion for the elimination of recirculation (Ref. B-2).

One additional problem associated with the characterization of spray fields generated with single-element injectors was the determination of the local mass flux of the injectant gas. As the gas/liquid flow field moves through the surrounding environment on its way from the injector to the probe tip, much of the gas in the environment (base bleed) was ingested into the flow field. Therefore, the gas

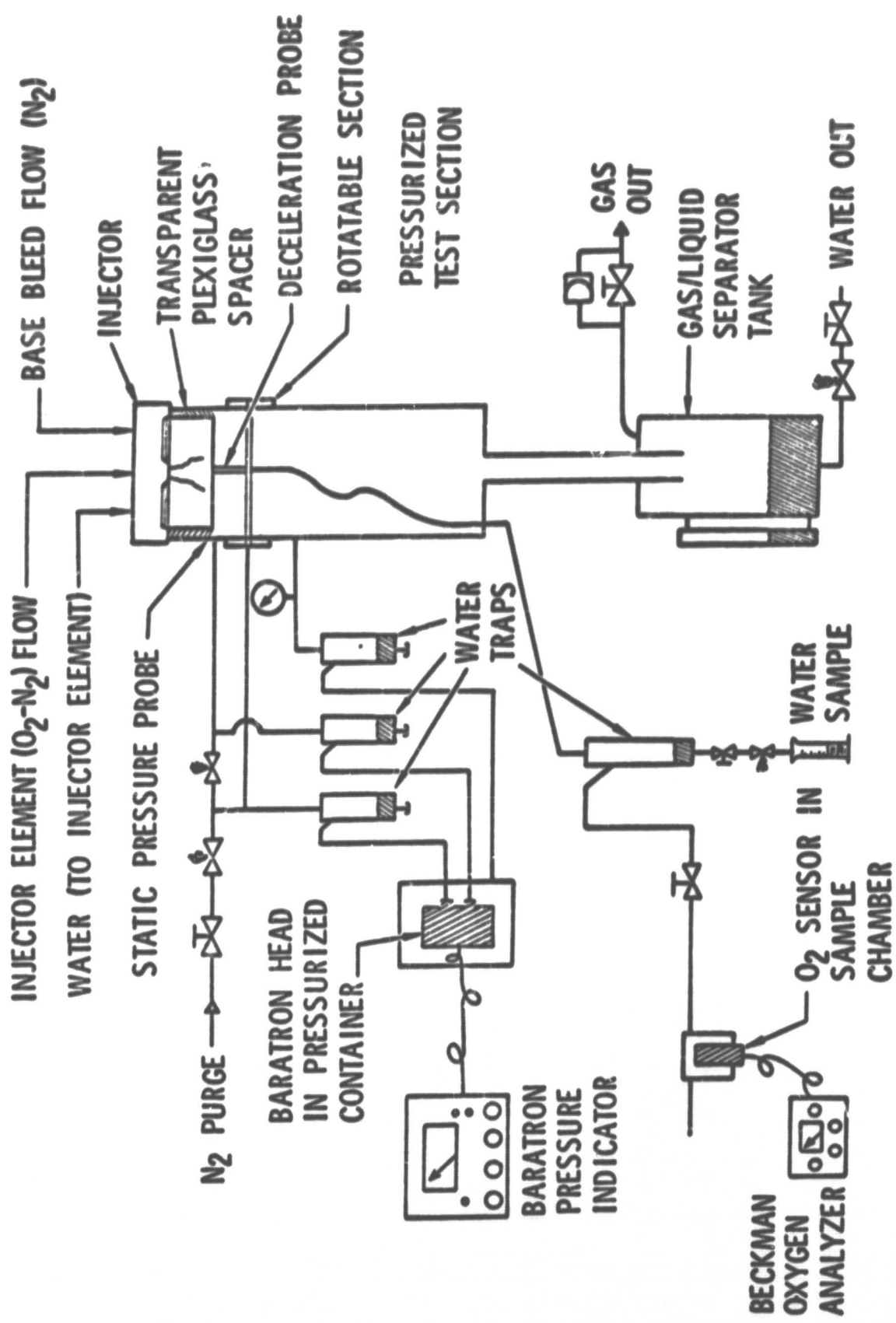


Figure 3-1. Schematic of Pressurized Gas/Liquid Mixing Facility

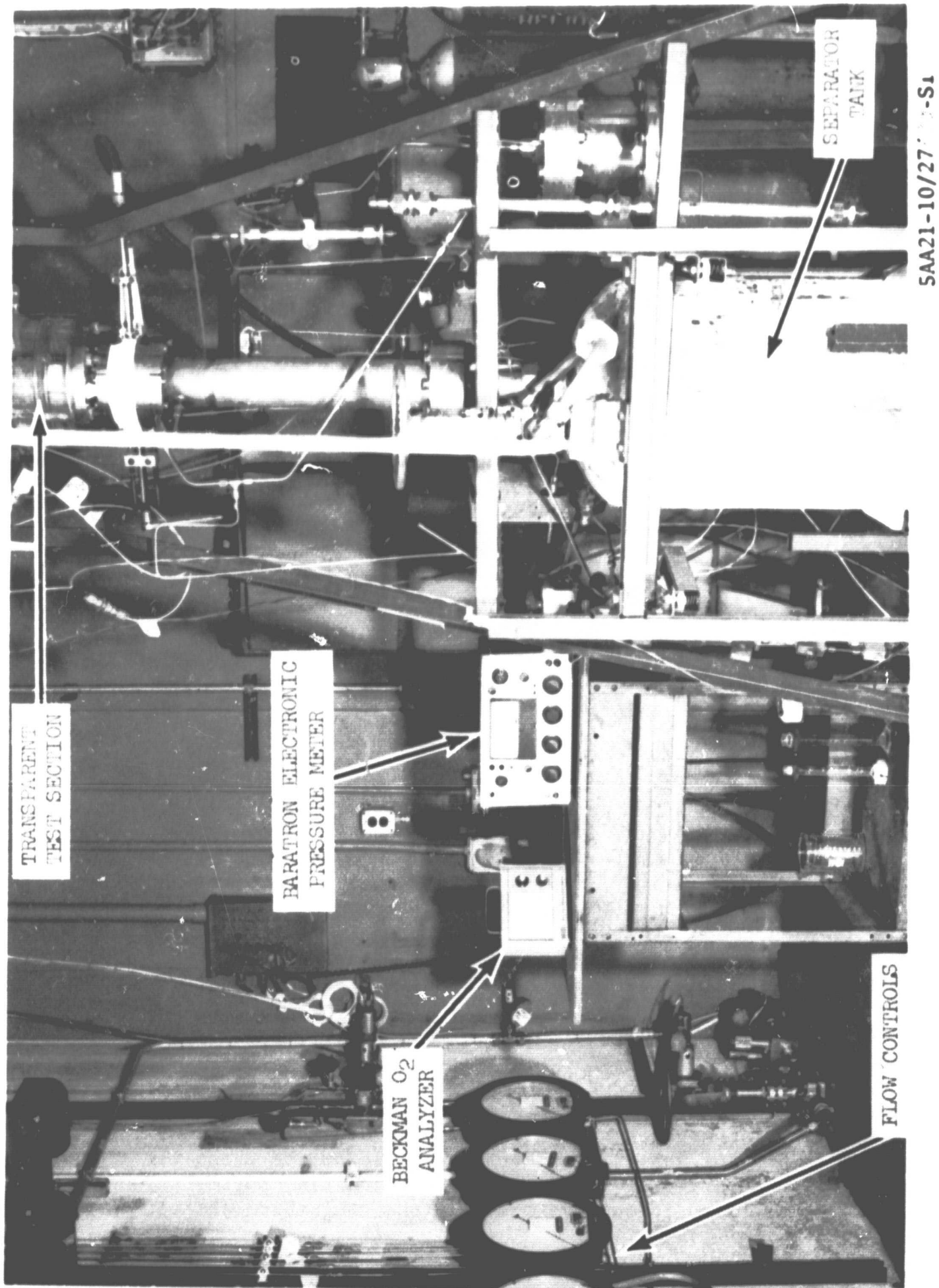


Figure B-2. Pressurized Gas/Liquid Mixing Facility

flowrate measured by the probe was composed both of gas that was injected and gas that was ingested. These two components were segregated to determine the injected portion (for calculation of E_m). To accomplish this, nitrogen and oxygen were mixed in known quantities and injected through the injector element while pure nitrogen was used as a base bleed fluid. The sample which arrived at the probe tip was processed through a Beckman oxygen analyzer (Fig. B-1). The concentration of the oxygen in the sample was then used to determine the concentration of the injected/gas phase.

TWO-PHASE DECELERATION PROBE

The two-phase deceleration probe, which was used for the determination of local values of gas and liquid mass flux, was developed jointly under the subject program and NAS3-12001. Only a brief description of the probe will be presented herein; for a more detailed description see Ref. B-3.

The concept of a deceleration probe for the measurement of gas-phase stagnation pressures, for the determination of gas velocity, in two-phase flow fields was first introduced by Dussourd and Shapiro (Ref. B-4). However, the referenced probe design was operated only in low mass flux ratio (particle flowrate/gas flowrate > 0.2) flow fields. In addition, the probe design of Dussourd and Shapiro was utilized only in ambient-pressure flow fields.

The deceleration probe which was developed was utilized both for the determination of gas-phase stagnation pressures and local liquid mass flux. The probe has been demonstrated to operate successfully in high mass flux ratio (liquid mass flux/gas mass flux 0.2 to 20) two-phase flow fields (Ref. B-5). In addition, measurements have been made in dense gas/liquid flow fields at static pressures up to 500 psia.

A schematic of the deceleration probe, termed the concentric tube two-phase impact probe, is presented in Fig. B-3. The probe was constructed of two concentric tubes (A and B) with a specially designed tip attached to tube B. The tip was designed to prevent the passage of water (termed flooding) into the annulus formed by tubes A and B when the probe is utilized in high mass flux ratio flow fields. The problem of flooding is a serious limitation of the probe design described in Ref. B-4.

The operating principle for the determination of the gas-phase stagnation pressure by the concentric tube two-phase impact probe is illustrated in Fig. B-4. Basically, the intent is to decelerate the gas and measure the gas-phase stagnation pressure in a manner that minimizes momentum exchange from the condensed phase upstream of the measurement location. Particles (or droplets) and gas (each at their own velocity) encounter the probe tip but the gas phase is stagnated at the probe tip where the pressure is approximately equal to the gas-phase stagnation pressure. Deviation from true gas-phase stagnation pressure is due to momentum exchange between the particles and the gas in the near flow field of the probe tip (termed overpressure error). A particle, due to its higher inertia, passes through the probe tip and is decelerated to zero velocity in the stagnation chamber formed by

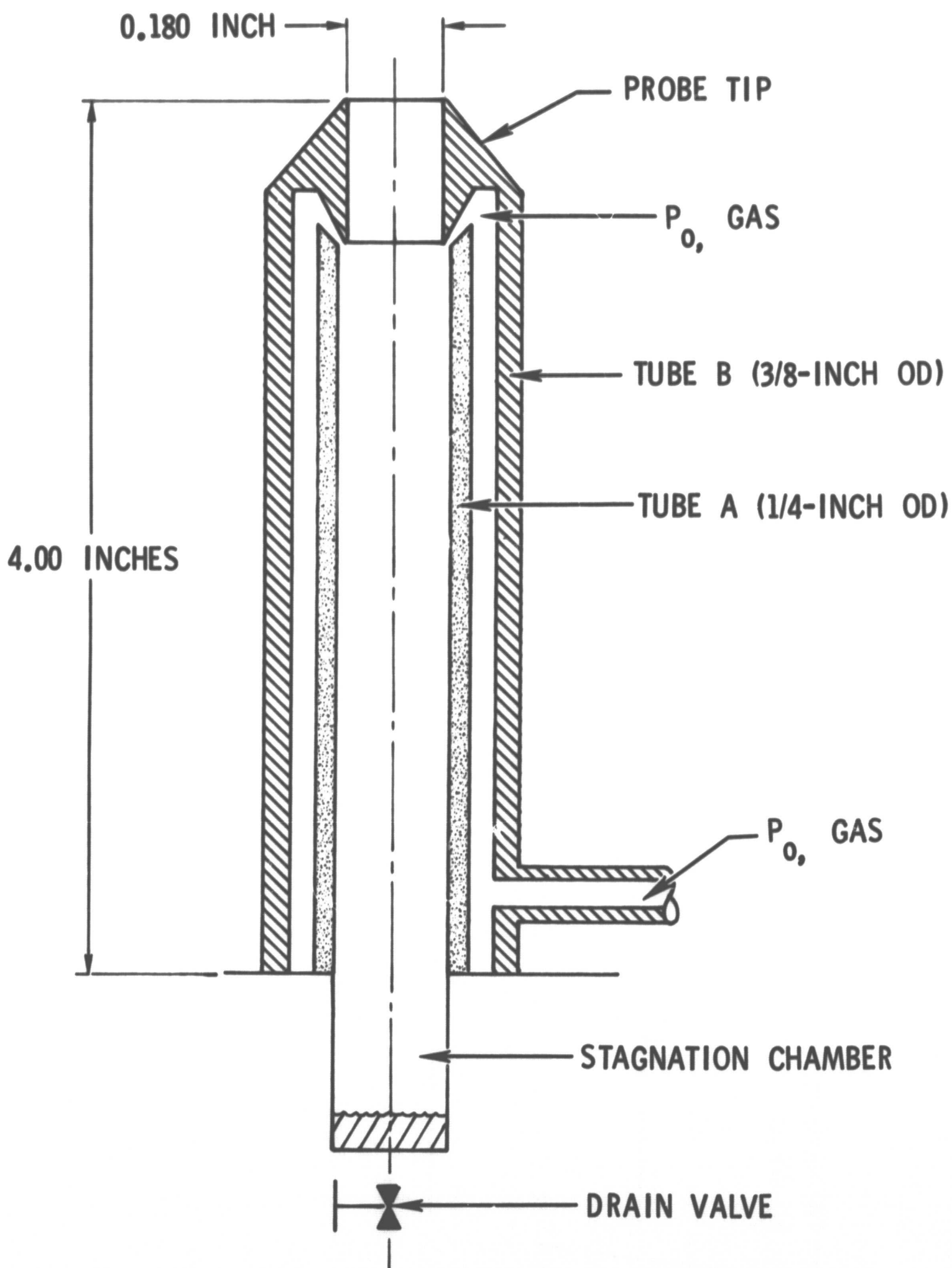


Figure B-3. Schematic of Concentric Tube Two-Phase Impact Probe

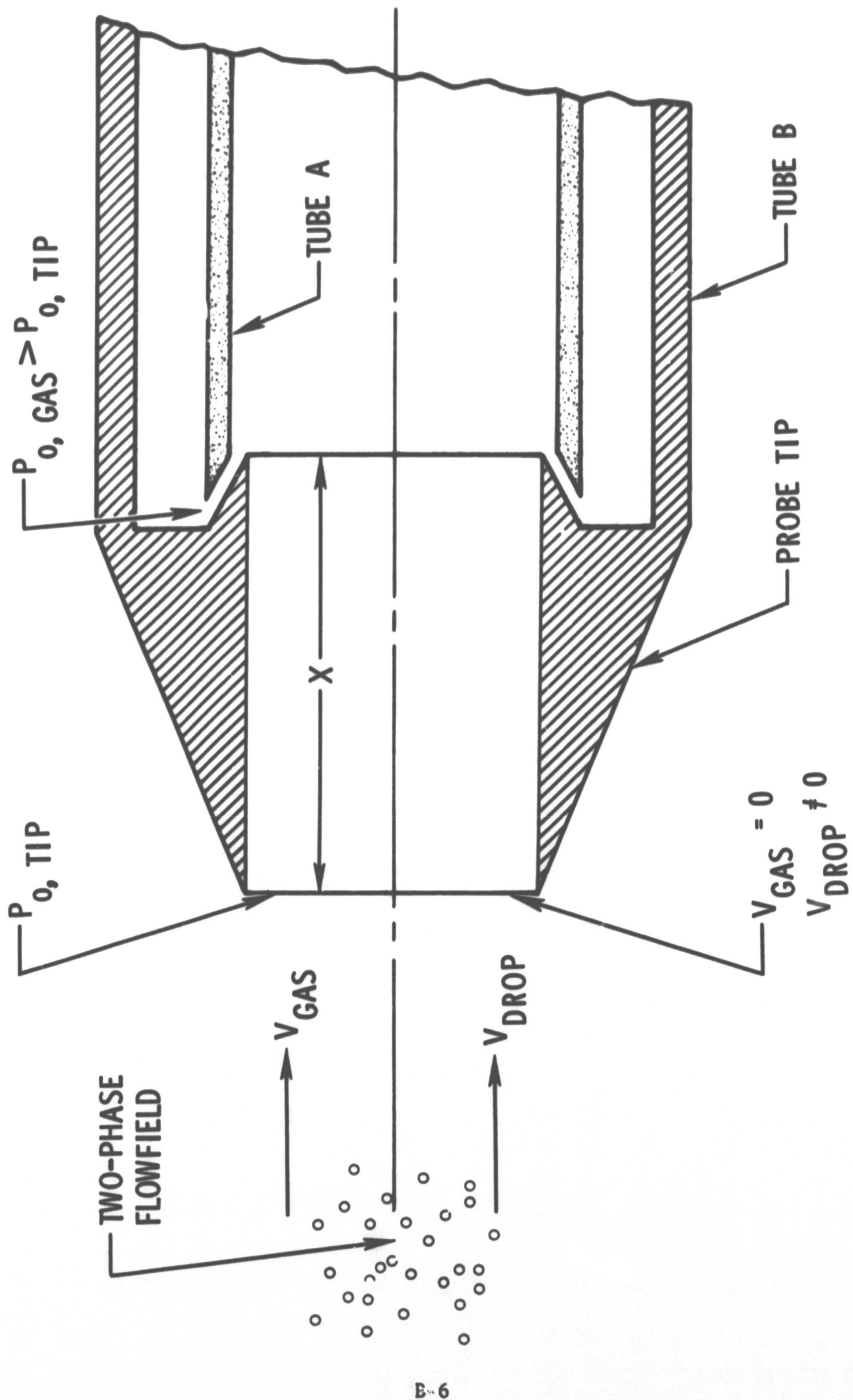


Figure B-4. Principle of Operation

tube A. However, due to momentum exchange between the particles and the stagnated gas, the particles decelerate in the probe tip to some extent over the distance X (see Fig. B-4). The gas-phase stagnation pressure P_0, gas , as measured in the probe annulus, is greater than the gas-phase stagnation pressure, P_0, tip . The difference between the two aforementioned pressures can be made small if the distance X is minimized. However, the total overpressure error (due to particle/gas momentum exchange both near and within the probe tip) can be determined by proper calibration of the probe in known two-phase flow fields (Ref. B-3).

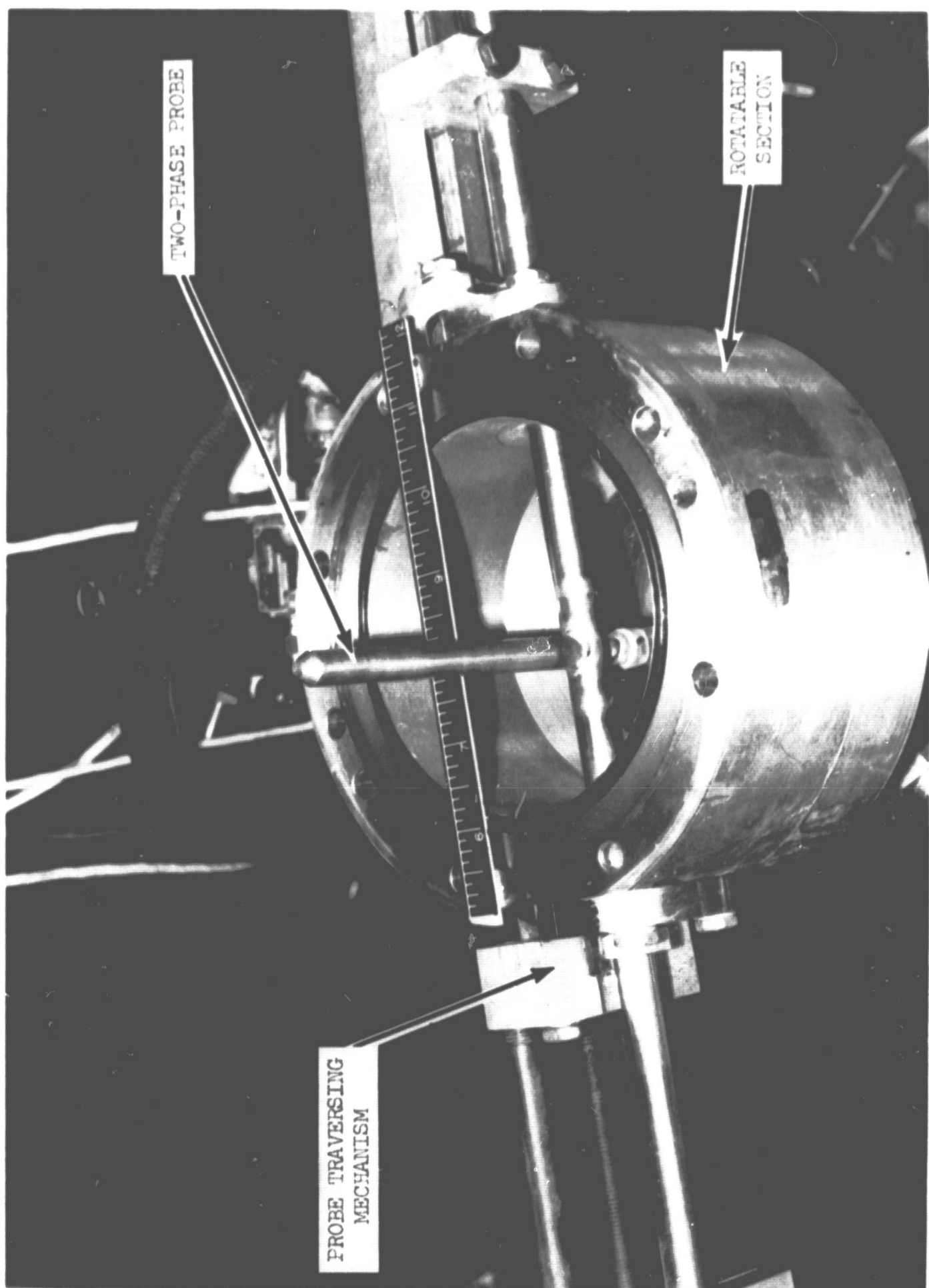
The gas-phase stagnation pressure was measured in the 360-degree annulus at the probe tip rather than at a single point as was done on the probe described in Ref. B-4. Tests conducted with both the subject probe and one of the Ref. B-4 designs in high mass flux ratio (> 3) flow fields demonstrated that the concentric tube probe eliminated the pressure oscillations encountered with a probe of Ref. B-4 design. In addition, the concentric tube probe design avoids the need for an external pressure line at the probe tip that could create flow field disturbances. The gas-phase stagnation pressure in the probe annulus was measured with an MKS Baratron Type 77 electronic pressure meter.

Local values of liquid mass flux were determined by capturing a liquid sample in the probe stagnation chamber (Fig. B-2) for a known time interval. However, since the droplet capture efficiency of the probe design is less than 1 (≈ 0.95) small corrections must be made to the captured liquid mass to determine a value of local liquid mass flux. Values of the probe capture efficiency were determined by calibration of the probe in known two-phase flow fields.

A photograph of the two-phase probe and its traversing mechanism is shown in Fig. B-5. The probe is shown located in the rotatable portion of the test section.

REFERENCES

- B-1. Burick, R. J., "Development of Experimental Cold-Flow Modeling Criteria for Gas/Liquid Injectors," 18 June 1969, IT-69-341-24, Rocketdyne Internal Memo.
- B-2. Becker, H. A., H. C. Hottle, and G. C. Williams, "Mixing and Flow in Ducted Turbulent Jets," Ninth Symposium (International) on Combustion, Academic Press, 1963.
- B-3. Burick, R. J., C. H. Scheuerman, and A. Y. Falk, "Determination of Local Values of Gas and Liquid Mass Flux in Highly Loaded Two-Phase Flow," Paper No. 1-5-21, Symposium on Flow--It's Measurement and Control in Science and Industry, 10-14 May 1971, Pittsburgh, Pa., Paper No. 1-5-21, to be published in Symposium Proceedings.
- B-4. Dussourd, F. L. and A. H. Shapiro, "A Deceleration Probe for Measuring Stagnation Pressure and Velocity of a Particle Laden Gas Stream," Jet Propulsion, pp 24-34, January 1958.
- B-5. Mehegan, P. F., et al., NASA CR-72703, Investigation of Gas-Augmented Injectors, Rocketdyne, a division of North American Rockwell Corporation, Canoga Park, California, September 1970.



SAA36-11/19/70-S1B

Figure B-5. Two-Phase Impact Probe in Rotatable Section

APPENDIX C

PRESSURIZED COLD-FLOW ATOMIZATION FACILITY

INTRODUCTION

The operating conditions and injector dynamics that control the gas/liquid mixing processes also influence the atomization processes. Thus, early in the coaxial characterization program, work was initiated on the construction of a pressurized atomization facility. The facility is located at the Combustion and Heat Transfer Laboratory. The pressurized system was an addition to an existing molten wax facility which has been used successfully to characterize injector spray fields in a number of programs (Ref. C-1 and C-2). The use of a pressurized environment in the investigation of gas/liquid atomization processes was accomplished for the first time during the subject program.

EQUIPMENT TECHNIQUE

To simulate the dynamic injection conditions of hot-fire propellant systems, the atomization experiments were conducted at simulated gas-phase densities. In this case, gaseous nitrogen and molten wax (Shell-270) were used as nonreactive fuel/oxidizer simulants, respectively. In this molten wax technique, the wax droplets freeze prior to collection and are subsequently subjected to sieve analysis after drying.

A series of 23 standard sieves ranging in size from 53 to 2380 microns (53 to 2380×10^{-6} in.) was available for sample sieving. For any particular sample, only 12 of the sieves were used, the particular sieve sizes which were used depended on the anticipated size range. The particular wax sample (≈ 10 grams) was placed on the largest screen of the selected set of 12 sieves. The sieves were shaken on a RO-TAP automatic shaker for 30 minutes. After the sieving operation was completed, the mass of particles on each sieve was weighed on an electric balance. A total recovery of 96 to 98 percent of the mass originally introduced into the sieves was possible. The mass fraction of sample on each sieve was then plotted as a function of sieve size to determine a mass median drop size.

EXPERIMENTAL FACILITY

A schematic of the pressurized atomization facility that was employed in these studies is presented in Fig. C-1. The system consisted of a 600-gallon cylindrical tank in which a single-element injector model was mounted. Molten wax and heated GN_2 were supplied to the injector from a system that was heated with circulating hot oil. All lines and valves in the wax supply system were oil jacketed to prevent wax freezing. Heated GN_2 was supplied to the injector at a temperature above the melting point of the wax (≈ 200 F) so that the resulting wax droplets did not freeze prior to the completion of the liquid jet breakup and atomization processes. A water flush was supplied to the inner tank walls during testing to ensure that molten wax did not adhere to the tank walls. A photograph of the pressurized atomization facility is shown in Fig. C-2.

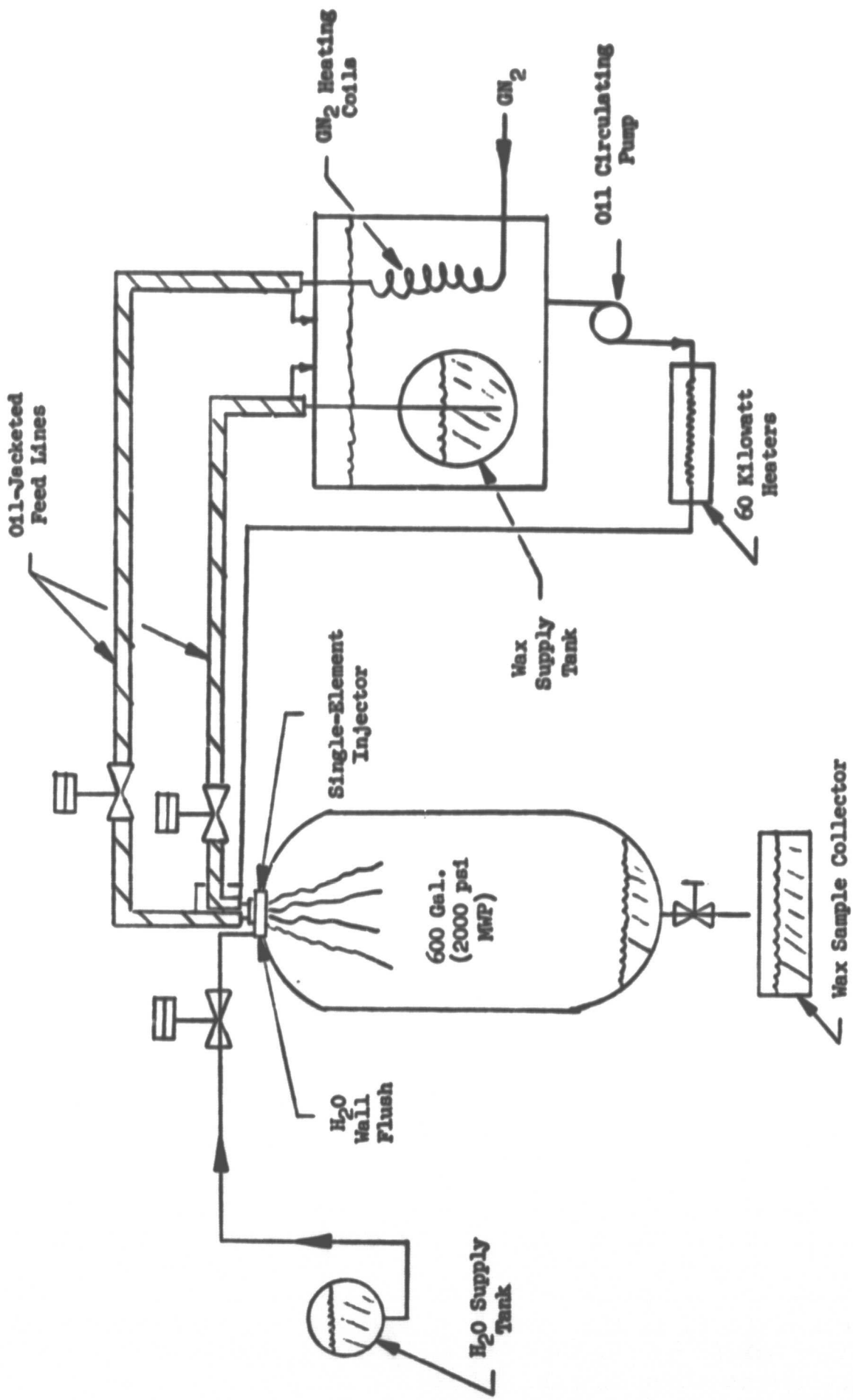
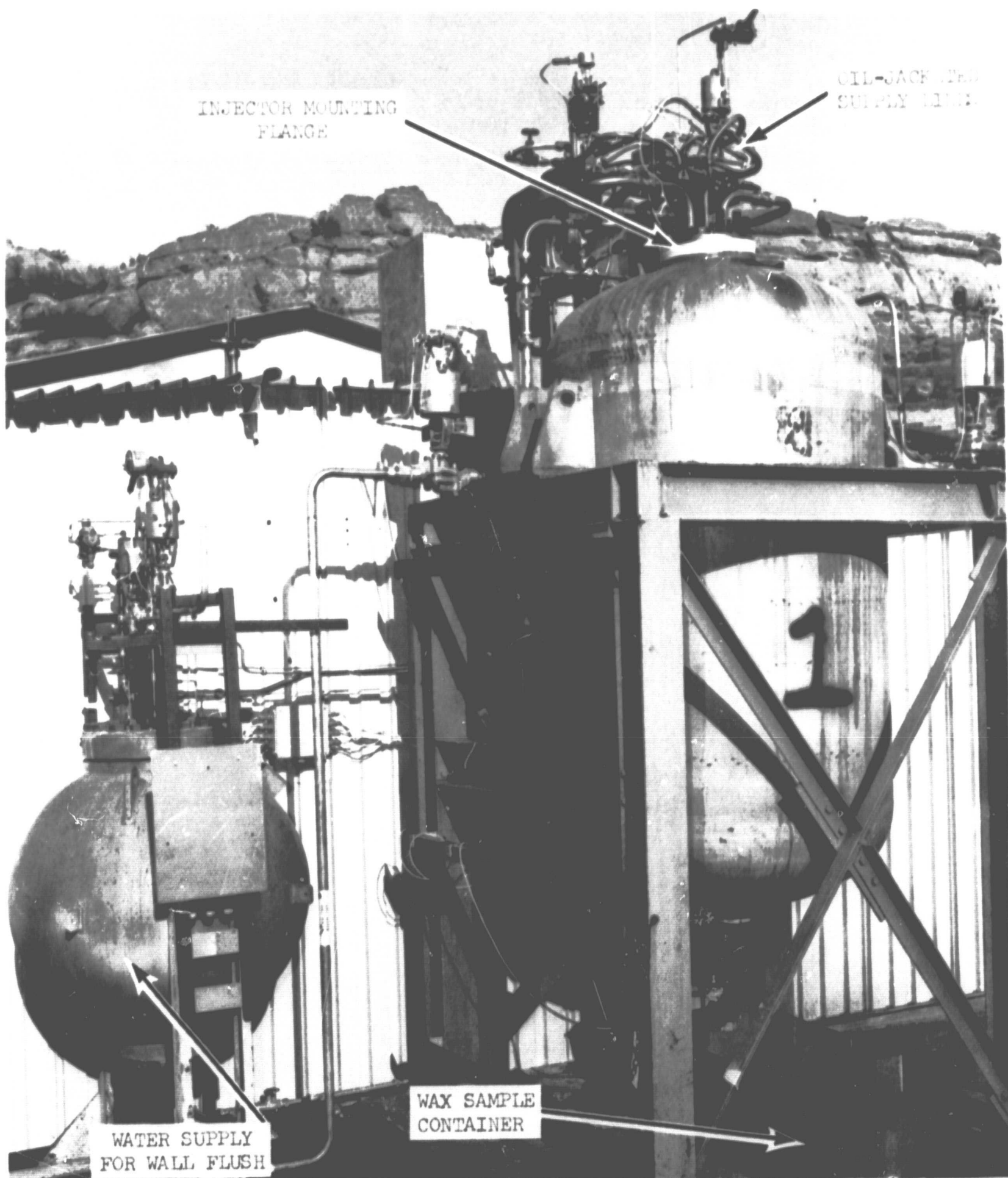


Figure C-1. Schematic of Pressurized Atomization Facility



5AA36-11/20/70-S1B

Figure C-2. Pressurized Atomization Facility

REFERENCES

- C-1. Dickerson, R., et al., Correlation of Spray Injector Parameters with Rocket Engine Performance, Report AFRPL TR-68-147, Rocketdyne, a division of North American Rockwell, Canoga Park, California, June 1968.
- C-2. Mehegan, D. F., et al., NASA CR-72703, Investigation of Gas-Augmented Injectors, Rocketdyne, a division of North American Rockwell, Canoga Park, California, September 1970.

APPENDIX D

HOT-FIRE FACILITIES AND PROCEDURES

INTRODUCTION

Detailed description of the hot-firing test stand instrumentation, data recording (test documentation) procedures, and pertinent experimental procedures, utilized during the program are presented in this appendix. The hot firings were conducted on Willie stand.

HOT-FIRING TEST FACILITY

The full-scale hot-fire experimental portion of the program was conducted on test stand Willie at Rocketdyne's Propulsion Research Area (PRA) test complex. A schematic flow diagram of the test facility (Willie stand) with instrumentation locations is presented in Fig. D-1.

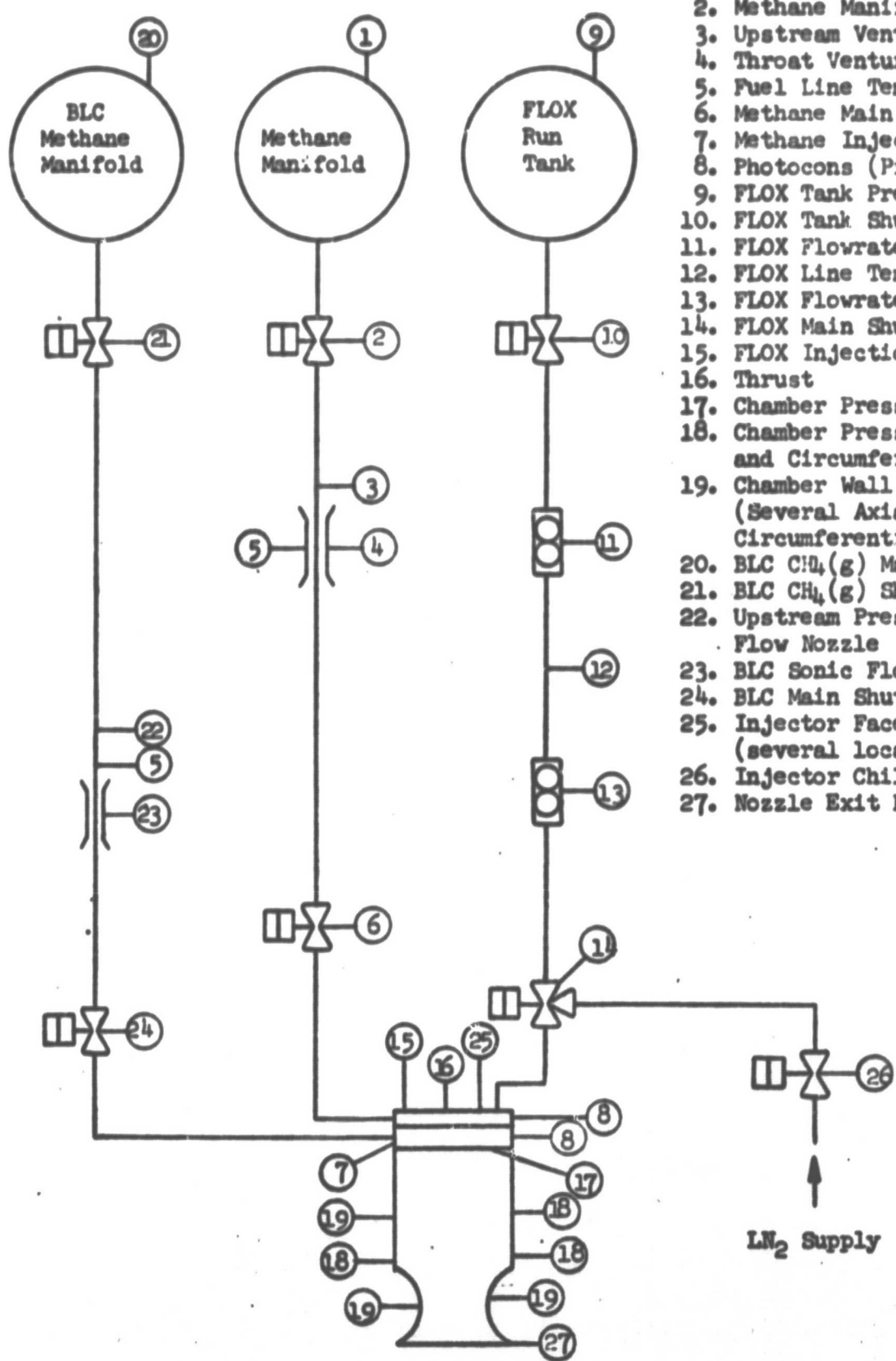
The FLOX system was identical to that employed in numerous fluorine programs at Rocketdyne. FLOX is stored in the 300- and 120-gallon, vacuum-jacketed, tri-wall storage tanks. FLOX was transferred from the storage tank to the run tank (43 gallons, 2000-psi MWP) prior to each day's testing. Procedures for storage, transfer, and handling of the FLOX have been established on previous programs at Rocketdyne. Prior to assembly, all facility and experimental hardware was thoroughly cleaned in accordance with prescribed procedures.

The (jacketed) FLOX system was completely chilled with liquid nitrogen from the storage tank to the engine. In addition, provisions were made to permit prerun chilldown of the oxidizer dome and injector by means of a liquid nitrogen bleed directly through the injector and thrust chamber, thus preventing the propellant from flashing in the initial portion of the firing and minimizing flow transients. Dried, filtered helium was used for FLOX tank pressurization.

The fuel (gaseous methane) was supplied to the engine from a gaseous methane manifold. The methane was stored in industrial cylinders (K-bottles). Approximately 20 cylinders were connected to the supply manifold.

The engine was mounted horizontally. Tank and purge pressures were set by motorized dome loaders in conjunction with electrically operated tank vent and control valves. Dried and filtered gaseous nitrogen purges were used on the propellant lines.

Test operations and data acquisition were conducted through a central control and recording center. The data recording systems, particular transducers to be used for the various types of measurements, and calibration procedures are briefly described below.



1. Methane Manifold Pressure
2. Methane Manifold Shutoff Valve
3. Upstream Venturi Pressure
4. Throat Venturi Pressure
5. Fuel Line Temperatures
6. Methane Main Shutoff Valve
7. Methane Injection Pressure
8. Photocons (Propellant Manifolds)
9. FLOX Tank Pressure
10. FLOX Tank Shutoff Valve
11. FLOX Flowrate #1
12. FLOX Line Temperature
13. FLOX Flowrate #2
14. FLOX Main Shutoff Valve
15. FLOX Injection Pressure
16. Thrust
17. Chamber Pressure (Injector Face)
18. Chamber Pressure (Several Axial and Circumferential Locations)
19. Chamber Wall Temperature (Several Axial and Circumferential Locations)
20. BLC CH₄(g) Manifold Pressure
21. BLC CH₄(g) Shutoff
22. Upstream Pressure, BLC Sonic Flow Nozzle
23. BLC Sonic Flow Nozzle
24. BLC Main Shutoff Valve
25. Injector Face Temperature (several locations)
26. Injector Chill Valve
27. Nozzle Exit Pressure

Figure D-1. Schematic Flow Diagram of Hot-Fire Test Facility
Showing Location of Instrumentation (Full-Scale
Coaxial Injector)

Hot Firing, Test Instrumentation, and Data Recording

Facility instrumentation locations are shown in Fig. D-1. Redundant measurements were made on the important experimental parameters (e.g., chamber pressure, flow-rates, etc.) to increase data reliability. The particular transducers used for the various types of measurements are described below.

Thrust

The thrust chamber mount was supported on flexures, which allowed free movement parallel to the engine axis (horizontally), restrained in the thrust direction by a Baldwin-Lima-Hamilton double-bridge load cell.

Pressures

Pressures were measured with bonded strain-gage transducers (Taber "Teledyne" Series 206 or equivalent). Chamber pressures were measured at several circumferential and axial positions in the chamber. Redundant measurements were made at pertinent axial locations.

Flowrates

Oxidizer flowrate was measured by Fischer-Porter turbine flowmeters that measure the volumetric flowrate. The oxidizer line had two flowmeters in series to increase data reliability. The fuel flowrate to the injector core was measured by calibrated sonic venturi meters.

Temperatures

Reliable measurement of cryogenic propellant flowrates requires accurate determination of liquid density as well as volumetric flowrate. Density of cryogenic propellants is a sensitive function of temperature; therefore, it is important to make careful measurements of propellant temperature as close to the flowmeters as practical. This was accomplished by use of shielded platinum resistance bulbs (Rosemont Model 176) immersed in the liquid stream. These instruments are very sensitive to temperature changes in the cryogenic region and are the preferred method of measurement. Oxidizer temperature was measured between the two flowmeters and in the injector manifolds. Fuel temperature was measured in the venturi plenum and injector manifolds using iron-constantan thermocouples.

Temperature histories of the chamber and/or nozzle were measured by chromel-alumel thermocouples embedded in the graphite chamber wall.

Special Instrumentation

Photocon pressure transducers were used to monitor high-frequency pressure oscillations in the fuel/oxidizer manifolds of the injector.

Calibration Procedures

Transducer calibrations were employed not only to obtain appropriate factors for test data reduction, but to develop statistical histories for each transducer, so that estimates of short- and long-term deviations could be made, and probable error bands calculated. The calibration methods which were employed for the various types of transducers are described below.

The thrust-measuring load cell was calibrated in-place by a permanently mounted, manually operated, hydraulic force cell, which deflects the load cell exactly as does the engine, i.e., through a yoke tension-rod system. Known loads were applied to the force cell through a Morehouse compression-type, temperature-compensated, proving ring calibrated by the National Bureau of Standards (NBS). A thrust calibration was conducted prior to testing on each test day.

Pressure transducers were calibrated end-to-end by mounting them on stand manifolds in which pressures were read with high-precision Heise-Bourdon tube gages. The latter were calibrated periodically on Ruska deadweight testers. Maximum length of pickup line from pressure tap to transducer was less than 1/2 foot.

The turbine flowmeters in the oxidizer line were calibrated prior to the initial test firing and at the conclusion of the test series. The sonic venturi meters were calibrated by the manufacturer to determine the discharge coefficient (C_D).

Resistance of the platinum thermometers to be used in the cryogenic propellant lines was converted to millivolt output by a triple-bridge system. This was calibrated by substituting a decade resistance box for a sensor and setting it at various resistances corresponding to a temperature-resistance calibration for each instrument. These precision platinum resistance sensors have no significant calibration drift. Chamber thermocouples were employed on the basis of the standard NBS millivolt/temperature tables. Thermocouple records were electrically calibrated.

Data Recording Systems

Pertinent pressure, temperature, and flow measurements were recorded on tape during each firing by a Beckman Model 210 Data Acquisition and Recording System. This system acquires analog data from the transducers, which it converts to digital form in binary-coded decimal format. The latter were recorded on tapes, which were then used for computer processing.

The Beckman Data Acquisition Unit sequentially samples the input channel at a range of 5625 samples per second. Programmed computer output consists of tables of time versus parameter value (in engineering units) printed out at approximately 10-millisecond intervals during the firing, together with calibration factors, prerun and postrun zero readings, and related data. The same computed results are machine plotted and displayed as CRT outputs on approximately scaled and labeled grids for simple determination of gradients, establishment of steady state, etc.

Primary data recording for the firings, and subsequent calculation of performance, were on the Beckman 210 system. In addition, the following auxiliary recording systems were employed:

1. An 8-channel, Brush, Mark 200 recorder was employed in conjunction with the Beckman unit, primarily to establish time intervals for computer data reduction and, additionally, for "quick-look" information on the most important parameters. This is a direct-inking system, with display on high-gloss, graduated paper moving at 20 mm/sec.
2. A CEC, 36-channel, direct-reading oscillograph was used as backup for the Beckman 210 system and for indication of any oscillatory combustion.
3. Direct-inking graphic recorders (DIGR's), either Dynalog rotary chart or Esterline-Angus strip chart, were used to set prerun propellant supply pressures, to provide quick-look information, and as secondary backup to the Beckman and oscillograph recorders.

PRECEDING PAGE BLANK NOT FILMED

APPENDIX E

CALCULATION OF CORRECTED C* EFFICIENCY

INTRODUCTION

The index of injector performance used in this experimental program was corrected c^* efficiency. This parameter was calculated by two independent methods for the full-scale injector tests, one based on measurement of chamber pressure and the other on measurement of thrust. Performance data for the single-element hot-firing were based on chamber pressure due to the difficulty of accurately measuring small thrust levels (≈ 70 pounds) on a 5000-pound-thrust stand. Details of the computational procedures and of the corrections applied are given in this appendix. A numerical example is included.

CALCULATIONS BASED ON CHAMBER PRESSURE

Characteristic velocity efficiency based on chamber pressure is defined by the following equation

$$\left(\eta_{c^*} \right)_{p_c} = \frac{(P_{c^*})_o (A_t)_{\text{eff}} g_c}{(\dot{w}_T) (c^*)_{\text{theo}}} \quad (E-1)$$

where

$(P_{c^*})_o$ = stagnation pressure at the throat, psia
 $(A_t)_{\text{eff}}$ = effective thermodynamic throat area, in.²
 g_c = conversion factor (32.174 lbm-ft/lbf-sec²)
 \dot{w}_T = total propellant weight flowrate, lbm/sec
 $(c^*)_{\text{theo}}$ = theoretical characteristic velocity based on shifting equilibrium, ft/sec

Values calculated from Eq. E-1 are referred to as "corrected" c^* efficiencies, because the factors involved are not measured directly, but are obtained by application of suitable corrections to measured parameters. Thus, stagnation pressure at the throat was obtained from measured static pressure near the start of nozzle convergence by assumption of isentropic expansion; effective throat area was estimated from measured geometric area by allowing for radius changes during firing and for nonunity discharge coefficient; and chamber pressure was corrected to allow for energy losses from the combustion gases to the chamber wall by friction and measured heat transfer rates. Equation E-1 may therefore be written as follows:

$$\left(\eta_{c^*} \right)_{p_c} = \frac{P_c A_t g_c f_p f_{TR} f_{DIS} f_{FR} f_{HL}}{(\dot{w}_o + \dot{w}_f) (c^*)_{\text{theo}}} \quad (E-2)$$

where

P_c = measured static pressure near the start of nozzle convergence, psia

A_t = measured geometric throat area, in.²

\dot{w}_o = oxidizer weight flowrate, lbm/sec

\dot{w}_f = fuel weight flowrate, lbm/sec

f_p = factor correcting observed static pressure to throat stagnation pressure

f_{TR} = factor correcting for change in throat radius during firing

f_{DIS} = factor correcting throat area for effective discharge coefficient

f_{FR} = factor correcting measured chamber pressure for frictional drag of combustion gases at chamber wall

f_{HL} = factor correcting measured chamber pressure for heat losses from combustion gases to chamber wall

Methods of estimation of the various correction factors are described in the following paragraphs.

Pressure Correction (f_p)

Measured static pressure near the start of convergence was converted to stagnation pressure at the throat by assumption of no combustion in the nozzle and application of the isentropic flow equations.

For calculations of a "valid" performance value, care must be taken to ensure measurement of a "valid" static chamber pressure near the start of nozzle convergence. Experience gained on this and related programs (Ref. E-1) at Rocketdyne indicates that a definite increase in static pressure can occur near the start of convergence. This increase in pressure appears to be caused by subsonic deceleration effects associated with the turning of the combustion gases by the converging walls prior to acceleration in the nozzle. The magnitude of this increase is dependent upon the geometric configuration of the nozzle. Measurement of the static chamber pressure must be taken sufficiently upstream of the start of convergence so that its value is not affected by the subsonic decelerating effects discussed above. Furthermore, chamber pressure must be measured where combustion is nearly complete.

During this program, chamber pressure taps were located 0.50, 0.75, 1.00, and 1.25 inches upstream of the start of nozzle convergence. Measured pressures at these four locations were found to be essentially identical for all runs. Consequently, the four pressure readings were averaged to determine a mean static chamber pressure.

The values of f_p , the stagnation-to static pressure ratio, was estimated to be 1.026, for the 3:1 contraction ratio chamber. Variations in the shifting equilibrium specific heat ratio were minor over the range of test conditions (chamber pressure, mixture ratio) employed. This same correction factor ($f_p = 1.026$ for $\epsilon_c = 3$) was, therefore, considered applicable over the entire test matrix.

Throat Radius Correction (f_{TR})

Temperature gradients produced in an uncooled nozzle wall by radiative and convective heat transfer from the hot combustion gases result in thermal stresses which can affect the throat radius. Consequently, the geometric throat diameter measured in an ambient-temperature nozzle is not necessarily the same as that which exists during firing. Furthermore, throat diameter during firing will be a function of time, as well as of the physical properties of the throat material, the temperature and pressure of the combustion gases, and the nozzle geometry (i.e., wall thickness, etc.).

A throat radius correction factor, f_{TR} , was used for all tests and is defined as:

$$f_{TR} = \frac{A_{t \text{ hot}}}{A_{t \text{ cold}}} \quad (\text{E-3})$$

During the hot-firing tests, the thrust chamber throat diameter and area would increase (compared to the ambient dimensions) as a function of the wall temperature. The "hot" throat area was computed for each test as follows:

$$A_{t \text{ hot}} = \left[(\alpha \Delta T_{\text{avg}} + 1) D_{t, \text{ cold}} \right]^2 \pi/4 \quad (\text{E-4})$$

where

α = thermal expansion coefficient (ATJ graphite)

ΔT_{avg} = change in average throat wall temperature during the test

$D_{t, \text{ cold}}$ = cold throat diameter (pretest)

The average change in throat wall temperature was based on measured throat heat flux data. For the short-duration tests, average wall temperature was calculated (based on nozzle thermocouple measurements) to be approximately 965 F. Thus, ΔT_{avg} was taken as 885 F for all short-duration tests. A value of $\alpha = 1.16 \times 10^{-6}$ in./in.-F was employed for the thermal expansion coefficient for the ATJ graphite throat. Based on the aforementioned data, Eq. E-3 yields a throat radius correction factor, f_{TR} , equal to 1.002.

Throat Discharge Coefficient (f_{DIS})

The discharge coefficient is defined as the ratio of actual flowrate through the throat to the theoretical maximum based on geometric throat area and ideal, uniform, one-dimensional flow with no boundary layer. Values of the discharge coefficient may be estimated either analytically or from correlations of the results of experimental studies of gas flow through nozzles.

Experimental conical nozzle discharge coefficients obtained with air by various investigators are plotted in Fig. E-1 against the indicated geometric parameters. Data sources also are listed in Fig. E-1.

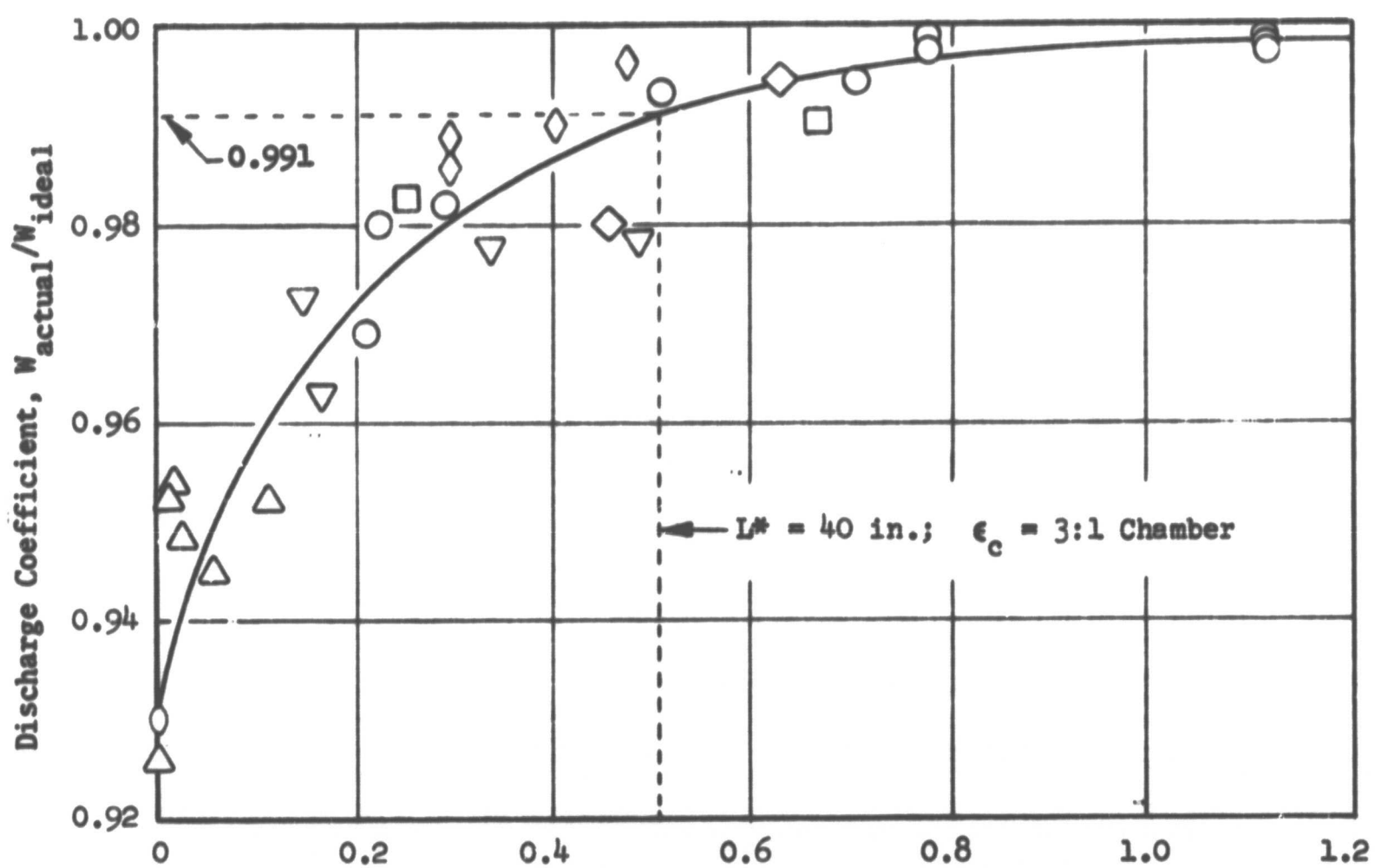
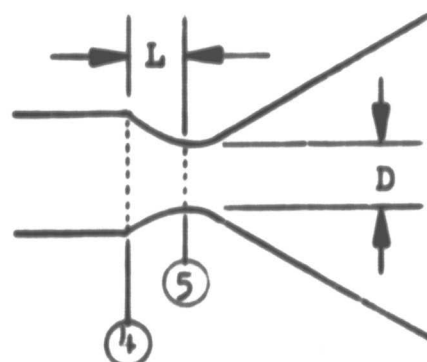
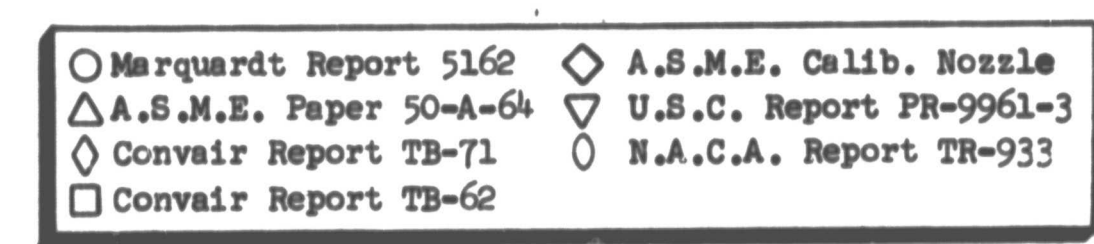
Based on the correlating curve shown and the nozzle geometry of the thrust chamber, the throat discharge correction factor is $f_{DIS} = 0.991$.

Frictional Drag Correction (f_{FR})

Calculation of c^* efficiency based on chamber pressure is concerned with chamber phenomena up to the nozzle throat. Drag forces to this point are generally small. For the present application, measured chamber pressure should be (and was) corrected for frictional losses only from the injector to the point where the chamber pressure was measured. Details of the method of estimation of f_{FR} are presented below. This discussion is general and applies to frictional losses for performance based on thrust as well as chamber pressure. Differences between the values of frictional losses for thrust and chamber pressure calculated performance are associated with the different regions over which the frictional losses are integrated.

This factor (f_{FR}) corrects for the energy losses caused by drag forces resulting from the viscous action of the combustion gases on the thrust chamber walls. Its magnitude, which is the integral of the local friction forces over the chamber inside wall, has been estimated by a boundary layer analysis utilizing the integral momentum equation for turbulent flow (Ref. E-2). The analysis accounted for boundary layer effects from the injector to the nozzle exit by suitable description of the boundary layer profile and local skin friction coefficient. A computer program was used to carry out a numerical integration of the equation, including effects of pressure gradient, heat transfer, and surface roughness. The program required a potential core solution of the nozzle flow which was obtained from the variable-property, axisymmetric method of characteristics calculation of the flow field outside the boundary layer; corresponding properties for the subsonic combustion chamber flow field were also calculated.

The above-mentioned program was not run specifically for the thrust chamber which was utilized in this program. However, parametric data generated in NAS3-11199 (FLOX/LPG) was sufficient to interpolate a value of the frictional drag losses for the chamber which was utilized in this study. The value employed for f_{FR} was 1.0036 which is similar to that reported in a recent FLOX/CH₄ program which utilized a similar thrust chamber configuration ($f_{FR} = 1.0025$, Ref. E-3).



$$\left(\frac{L}{D} \right) \left(\frac{A_5}{A_4 - A_5} \right) = \frac{L}{D} \left(\frac{1}{\epsilon_c - 1} \right)$$

Figure E-1. Discharge Coefficient as Function of Nozzle Dimensions; A_4 = Cross-Sectional Area of Chamber, A_5 = Cross-Sectional Area of Throat (Data Taken From Indicated References for Cold Flows With Air.)

Heat Loss Correction (f_{HL})

Heat transfer from the combustion gases to the walls of an uncooled thrust chamber results in loss of enthalpy and thus decreases chamber pressure and thrust. This enthalpy loss is substantially reduced in a graphite chamber and is effectively recovered in a chamber cooled regeneratively by one of the propellants, whose initial enthalpy is raised by the heat absorbed. To obtain a true indication of performance efficiency in an uncooled chamber, measured chamber pressure must be corrected by a factor which accounts for heat loss to the walls. Heat transfer to the injector was neglected in this correction because a major portion of injector heat flux is absorbed by the injected propellants.

Using the following equation, f_{HL} was estimated:

$$f_{HL} = \left\{ \left[1 + \frac{c^*_{\text{theo}}}{c^*_{\text{meas}}}^2 \frac{\sum (\dot{q}/A)A}{\dot{w}_T \cdot c_{p_m} \cdot T_c} \right] \right\}^{1/2} \quad (E-5)$$

where

- c^*_{theo} = theoretical characteristic velocity at test conditions, based on full shifting equilibrium
- c^*_{meas} = measured characteristic velocity, corrected for the previously discussed losses
- $(\dot{q}/A)A$ = measured heat loss to chamber walls
- \dot{w}_T = total propellant flowrate
- c_{p_m} = mean specific heat of combustion chamber gases at test conditions
- T_c = theoretical combustion gas temperature at test conditions

The basis for use of this equation is presented in Ref. E-4 and E-5.

Only heat losses to the chamber wall between the injector and the chamber pressure taps employed for calculation of performance based on chamber pressure are included in Eq. E-5.

Due to the low chamber heat flux levels which were measured in this program, f_{HL} was not large amounting to approximately 1.007 at the design point.

CALCULATIONS BASED ON THRUST

An alternate determination of corrected c^* efficiency is based upon the following defining equation:

$$(\eta_{c^*})_F = \frac{F_{vac} g_c}{(C_F)_{vac} \dot{w}_T (c^*)_{theo}} \quad (E-6)$$

where

- F_{vac} = measured thrust corrected to vacuum conditions by the equation: $F_{vac} = F + P_a A_e$, lbf
- F = measured thrust, lbf
- P_a = ambient pressure, psia
- A_e = area of nozzle exit, in.²
- g_c = conversion factor (32.174 lbm-ft/lbf-sec²)
- $(C_F)_{vac}$ = theoretical shifting thrust coefficient (vacuum)
- \dot{w}_T = total propellant flowrate, lbm/sec
- $(c^*)_{theo}$ = theoretical shifting-equilibrium characteristic velocity, ft/sec

Corrected values of vacuum thrust may be obtained by application of suitable corrections to measurements of thrust made at sea level. With these values, which include allowances for all important departures from ideality, theoretical thrust coefficients may be used for calculation of c^* . That is, C_F coefficient is 100 percent if there is no combustion in the nozzle, if chemical equilibrium is maintained in the nozzle expansion process, and if energy losses from the combustion gases are taken into account.

Applicable corrections to measured thrust are specified in the following equation:

$$(\eta_{c^*})_F = \frac{(F + P_a A_e) g_c \phi_{FR} \phi_{DIV} \phi_{HL}}{(C_F)_{vac} (\dot{w}_o + \dot{w}_f) (c^*)_{theo}} \quad (E-7)$$

where

- $(C_F)_{vac}$ = theoretical shifting thrust coefficient (vacuum)
- \dot{w}_o = oxidizer weight flowrate, lbm/sec

\dot{w}_f = fuel weight flowrate, lbm/sec
 ϕ_{FR} = correction for frictional losses
 ϕ_{DIV} = correction for nozzle divergence
 ϕ_{HL} = correction for heat losses to chamber and nozzle walls

The correction factors in Eq. E-7 were applied to vacuum thrust ($F + P_a A_e$) instead of to measured site thrust (F) because, for convenience, the correction factors were calculated as changes in efficiency based on theoretical vacuum parameters, so that the total correction was of the form $\Delta F/F_{vac}$.

Although they do not appear explicitly in Eq. E-7, corrections to geometric throat area and to measured static chamber pressure at start of nozzle convergence are implicit in the use of theoretical C_F values. Thus, calculation of corrected c^* efficiency from thrust measurement includes all the corrections described above for calculations from chamber pressure measurement plus an additional one to account for nonparallel nozzle exit flow. However, because $(C_F)_{vac}$ is essentially independent of the very small changes in chamber pressure and contraction ratio which are involved in corrections to P_c and A_t , these corrections are of no practical significance in calculation of c^* from thrust measurements.

Corrections for Frictional Drag (ϕ_{FR})

The basis for and method of calculation of this factor were discussed under calculation of performance based on chamber pressure.

The value of ϕ_{FR} which was used for the 40-in. L^* chamber was 1.015 at the design operating condition. This value is similar to that reported in a similar FLOX/CH₄ program (Ref. E-3; $\phi_{FR} = 1.018$, $L^* = 40$ in., $\epsilon_c = 4:1$).

Correction for Nozzle Divergence (ϕ_{DIV})

The one-dimensional theoretical performance calculations assume that flow at the nozzle exit is uniform and parallel to the nozzle axis. The correction factor, ϕ_{DIV} , allows for nozzle divergence (i.e., for nonaxial flow) and for nonuniformity across the nozzle exit plane. It has been calculated by a computer program which utilized the axisymmetric method of characteristics for a variable-property gas (Ref. E-6).

The geometric efficiency was essentially independent of chamber pressure and mixture ratio for the entire test matrix. A value of $\phi_{DIV} = 1.018$ was employed to correct for nozzle divergence losses.

Correction for Heat Losses (ϕ_{HL})

Heat loss correction factors for performance calculated from measured thrust are similar to those for performance calculated from chamber pressure, except that heat fluxes in the nozzle are included in the calculations. Thus, Eq. E-5 was employed with the measured heat flux summed from the injector to nozzle exit (Fig. 33).

A computer program was used to calculate ϕ_{HL} from the measured heat flux values. In the 40-in. L^* chamber, at design operating conditions, the value of ϕ_{HL} was approximately 1.008.

NUMERICAL EXAMPLE

The method of performance data reduction and correction are illustrated by the following numerical example. This example is typical of all tests. Data from test No. 17 (full-scale injector) are analyzed in this example. The subject test was conducted in the graphite lined chamber ($L^* = 40$ in., $\epsilon_c = 3$) at nominal design operating conditions ($P_c = 500$ psia, $MR = 5.38$, 0% BLC). Pertinent steady-state raw data (static chamber pressure, propellant flowrates, measured thrust, etc.) from this test are presented in Table E-1. Figure 60 presents the chamber heat flux characteristics for the subject test. CRT printouts of the pertinent parameters (as a function of Beckman time) were used to determine when steady-state had been achieved. Analog Beckman traces of static chamber pressure, measured thrust, oxidizer flowrate, and fuel venturi pressures for test No. 17 are shown in Fig. E-2 through E-7. The data slice interval for calculation of performance is noted. Steady-state performance was determined at approximately 2.0 seconds into the 2.5-second test. These traces are representative of the hot-fire tests conducted during the program. Digital Beckman data were used for calculation of all performance values.

Performance Based on Chamber Pressure

Corrected c^* efficiency based on chamber pressure measurement was calculated using Eq. E-2. Values of the measured parameters (\dot{w}_{ox} , \dot{w}_f , and A_t) and the theoretical C^* used in Eq. A-2 are shown in Table E-1. The average static chamber pressure measured upstream from the start of nozzle convergence was used for calculation of performance.

Methods of estimation of the various correction factors in Eq. E-2 were outlined previously. Estimation of these correction factors for test No. 17 is described in the following paragraphs.

Pressure Correction (f_p). Measured static pressure was converged to stagnation pressure at the throat by assumption of no combustion in the nozzle and application of the isentropic flow equations. The value of f_p , the stagnation-to-static pressure ratio, was estimated to be 1.026 for the 3:1 contraction ratio chamber.

Throat Radius Connection (f_{TR}). Throat area changes were minor over the time interval of interest. For the subject configuration/operating conditions, f_{TR} was estimated to be 1.002.

Throat Discharge Coefficient (f_{DIS}). For all experiments, the throat discharge coefficient was estimated to be 0.991.

Frictional Drag Correction (f_{FR}). For the subject test conditions, f_{FR} was estimated to be 1.0036.

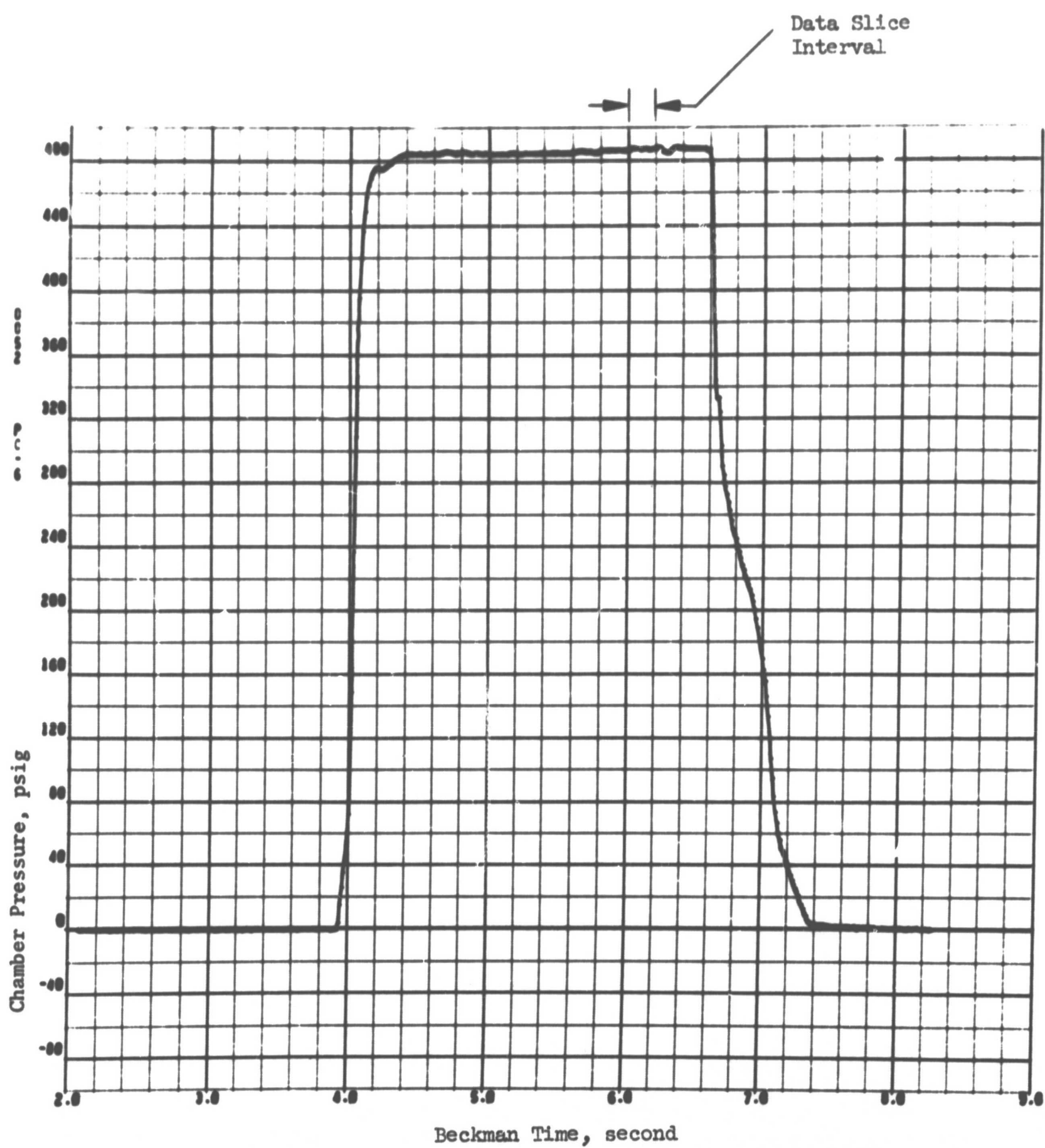


Figure E-2. Static Chamber Pressure (at Position No. 6) as a Function of Beckman Time for Test No. 17

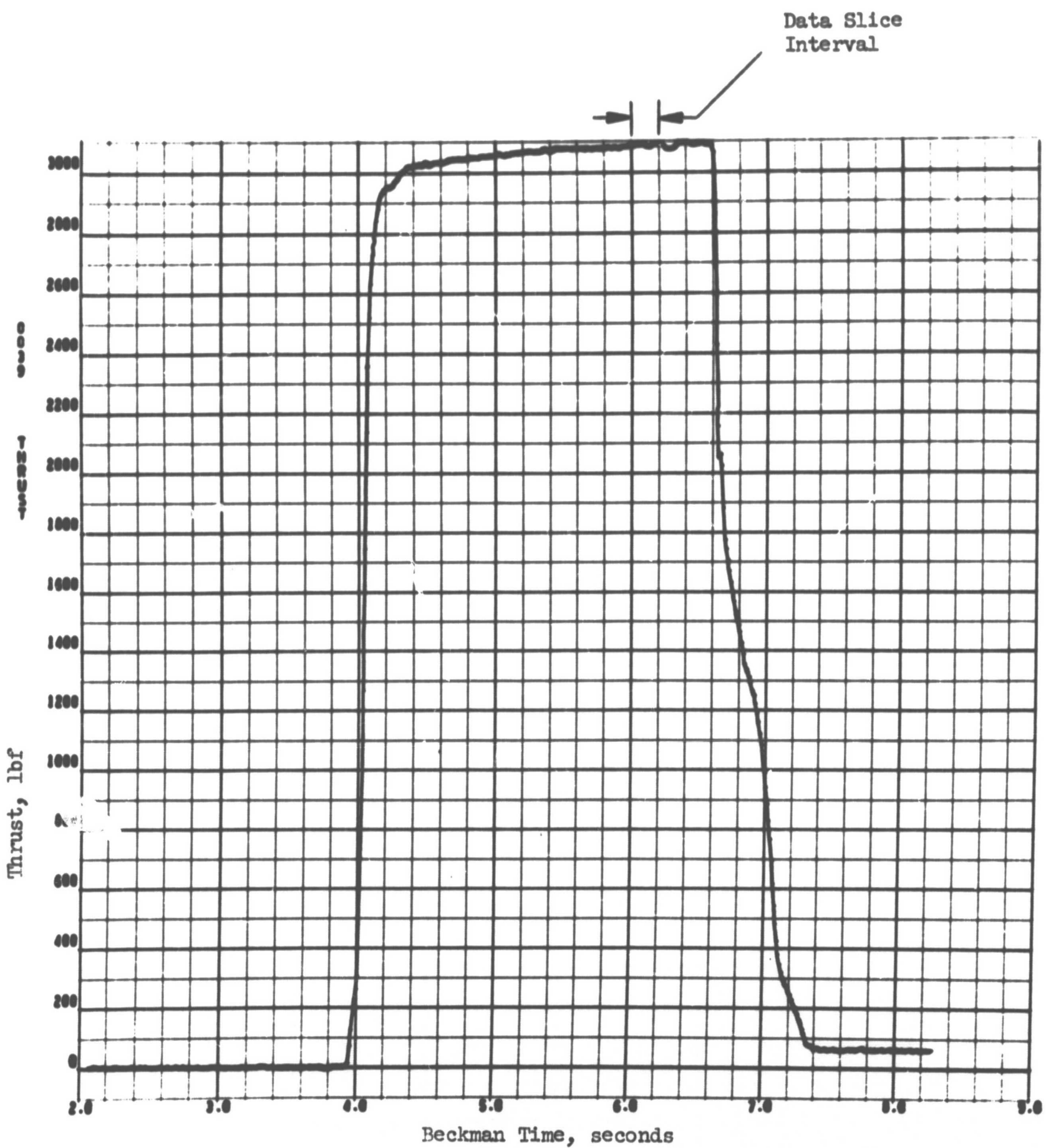


Figure E-3. Measured Site Thrust as a Function of Beckman Time for Test No. 17

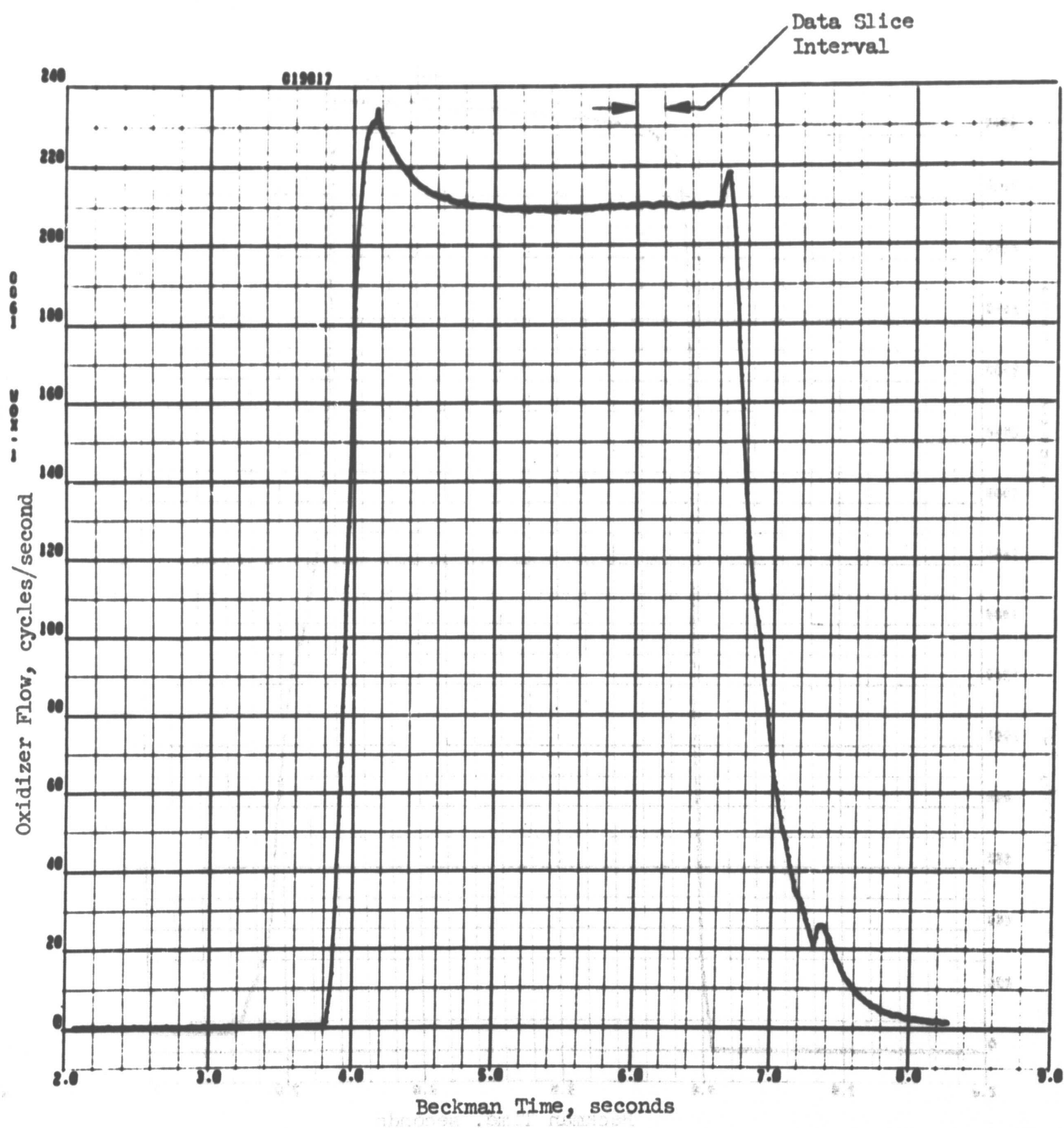


Figure E-4. Oxidizer Flowrate (No. 1 Meter, Cycles/Second) as a Function of Beckman Time for Test No. 17

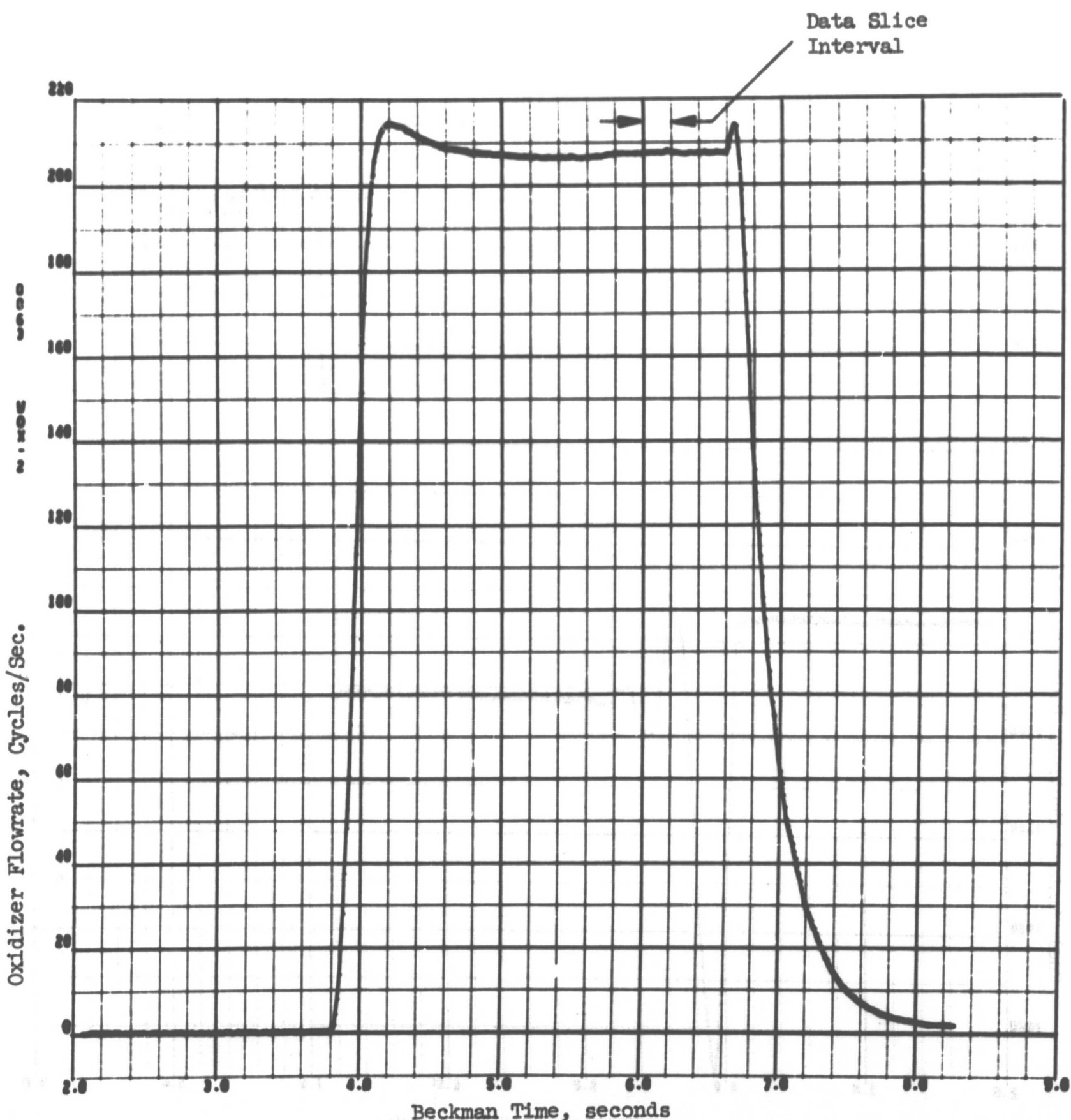


Figure E-5. Oxidizer Flowrate (No. 2 Meter, Cycles/Second) as a Function of Time for Test No. 17

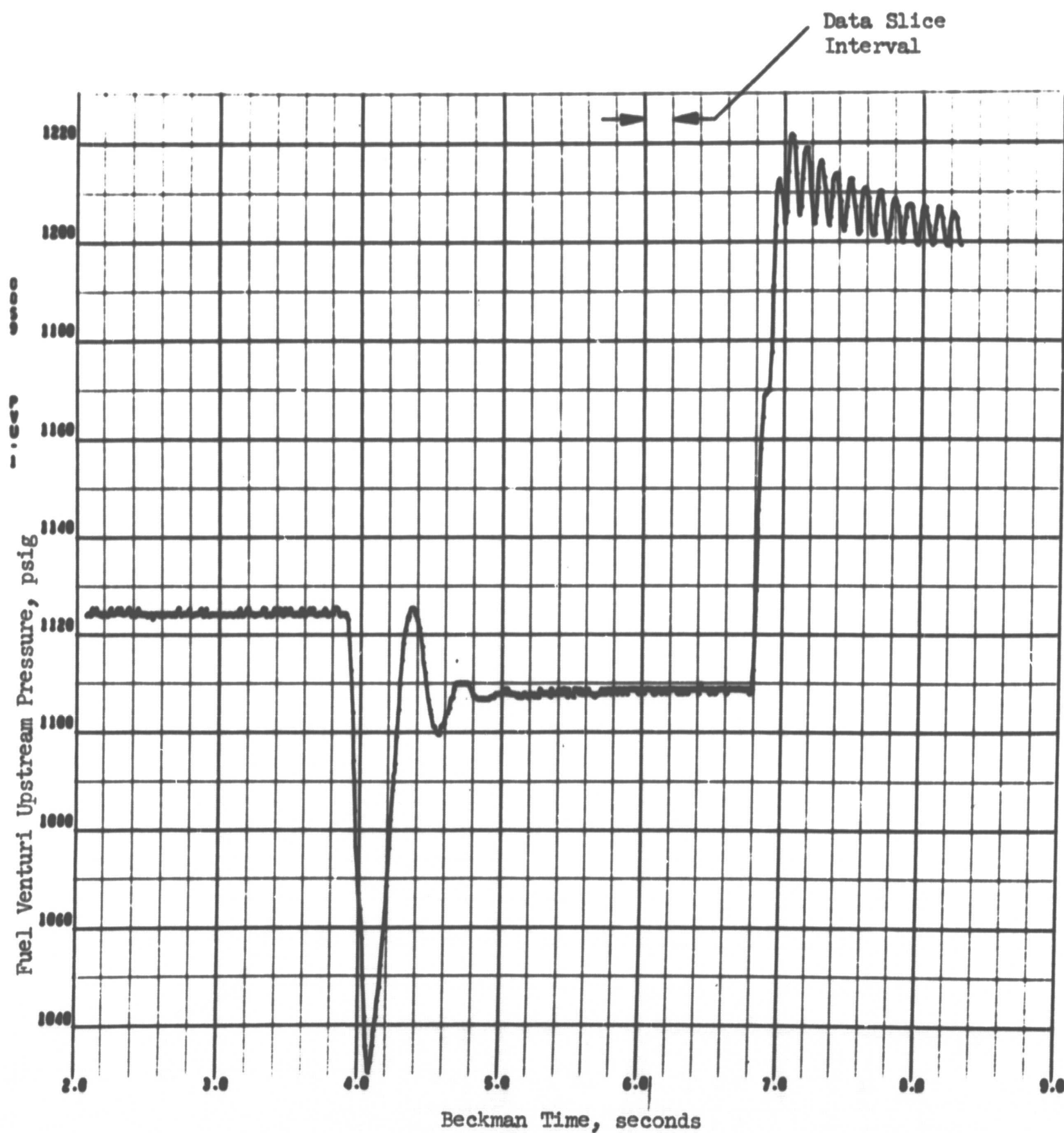


Figure E-6. Upstream Venturi Pressure (Fuel) as a Function of Beckman Time for Test No. 17

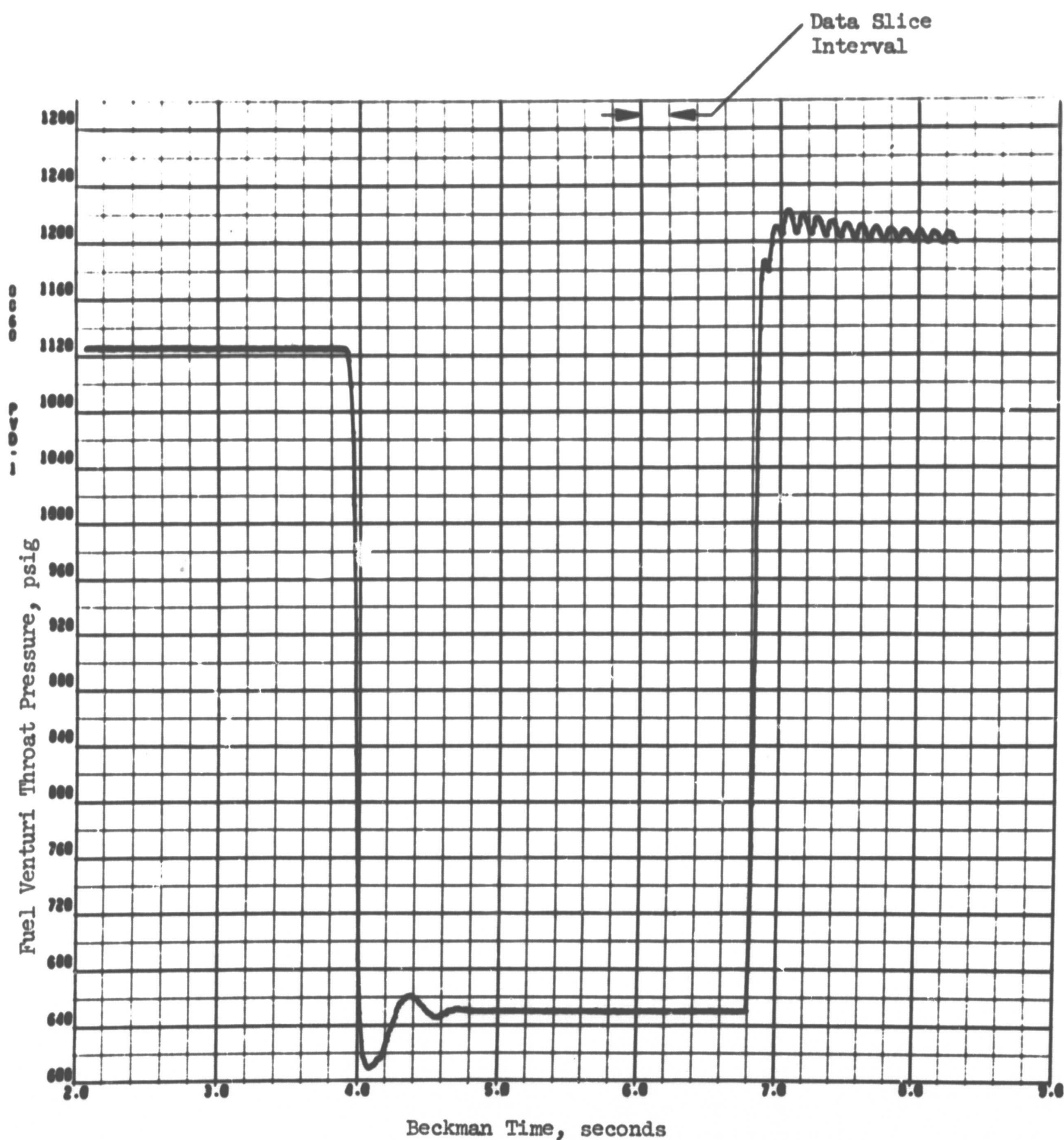


Figure E-7. Venturi Throat Pressure (Fuel) as a Function of Beckman Time for Test No. 17

TABLE E-1. DATA FROM TEST NO. 17

Static Chamber Pressure ^①	$(484.57 + 480.63 + 491.88 + 485.46)/4 =$ 485.6 psig = 509.4 psia
Oxidizer Flowrate ^②	$(7.926 + 7.895)/2 = 7.911 \text{ lbm/sec}$
Fuel Flowrate ^③	1.471 lbm/sec
Throat Area ^④	3.960 in.
Mixture Ratio	5.38
c* Theoretical	7139 ft/sec
$(C_V)_{VAC}$	1.6746

① Average value of two rows of pressure taps 180 degrees apart

② Value is average of two turbine flowmeters in series

③ Calculated from calibrated sonic venturi pressure measurements

④ Measured with hardware at ambient temperatures (≈ 75 F)

Heat Loss Correction (f_{HL}). The heat loss correction was estimated from the measured performance and observed chamber heat flux values by use of Eq. E-5. Terms in Eq. E-5 were calculated and defined as follows:

c^*_{theo} = theoretical characteristic velocity at test conditions (based on full shifting equilibrium) = 7139 ft/sec

c^*_{meas} = measured characteristic velocity (corrected for the previously determined losses)

$$= \frac{P_c A_t f_p g_c f_{TR} f_{DIS} f_{FR}}{\dot{w}_T}$$

$$= 6958 \text{ ft/sec}$$

$$T_c = 8142 \text{ R}$$

$$c_{p_m} = 0.431 \text{ Btu/lbm R}$$

$$\dot{w}_T = 9.382 \text{ lbm/sec}$$

$\Sigma(\dot{q}/A)(A)$ = heat losses to the chamber wall

$$= 399.2 \text{ Btu/sec (see Fig. 63 for } \dot{q}/A \text{ profile)}$$

The heat loss correction factor, f_{HL} , for this test is calculated below:

$$f_{HL} = \left\{ 1 + \left[\frac{c^*_{\text{theo}}}{c^*_{\text{meas}}} \right]^2 \left[\frac{\Sigma(\dot{q}/A) \cdot (A)}{\dot{w}_T \cdot c_{p_m} \cdot T_c} \right] \right\}^{1/2}$$

$$f_{HL} = \left\{ 1 + \left[\frac{7139.0}{6958.0} \right]^2 \left[\frac{399.2}{9.382 \times 0.431 \times 8142} \right] \right\}^{1/2}$$

$$f_{HL} = [1.0128]^{1/2} \approx 1.007$$

Equation E-2 with the appropriate numerical values shown is presented below for test No. 17:

$$(\eta_{c^*})_{p_c} = \frac{p_c A_t g_c f_p f_{TR} f_{DIS} f_{FR} f_{HL}}{(\dot{w}_o + \dot{w}_f) (c^*)_{\text{theo}}}$$

$$(\eta_{c^*})_{p_c} = \frac{(509.39)(3.960)(32.174)(1.026)(1.002)(0.991)(1.0036)(1.007)}{(7.911 + 1.471)(7139.0)}$$

$$(\eta_{c^*})_{p_c} = 97.8\%$$

Thus, for test No. 17, corrected c^* efficiency based on chamber pressure was 97.8 percent.

Performance Based on Thrust

Corrected c^* efficiency based on thrust measurement was calculated using Eq. E-7. Initially, vacuum thrust was calculated from the measured thrust, ambient pressure, and nozzle exit area as follows:

$$F_{\text{vac}} = F_{\text{meas}} + P_a A_e = 3024.6 + (13.7)(20.99) = 3312.0 \text{ lbf}$$

This was necessary because the corrections to be applied were calculated as changes in efficiency based on theoretical vacuum parameters.

Methods of estimation for the correction factors to be applied to the vacuum thrust in the calculation of c^* efficiency were presented previously. Estimation of the values used for test No. 17 are described below in the following paragraphs.

Corrections for Fractional Drag (ϕ_{FR}). For the subject test conditions ϕ_{FR} was estimated to be 1.015.

Nozzle Divergence Correction (ϕ_{DIV}). For all experiments, the nozzle divergence losses were estimated to be 1.8 percent (i.e., $\phi_{DIV} = 1.018$).

Heat Loss Correction (ϕ_{HL}). As was the case for the heat loss correction factor for performance based on chamber pressure, (f_{HL}), the heat loss correction factor was estimated using Eq. E-5. For this case, however, the measured c^* is based on thrust and total chamber heat losses are employed (i.e., heat losses are summed from injector face to nozzle exit). Terms in Eq. E-5 were calculated and defined as follows:

$$c^*_{\text{theo}} = 7139.0$$

$$T_c = 8142 \text{ R}$$

$$c_{p_m} = 0.431 \text{ Btu/lbm-R}$$

$$\dot{w}_T = 9.382 \text{ lbm/sec}$$

$$(C_F)_{vac} = 1.6746$$

$$c^*_{meas} = \frac{F_{vac} g_c \phi_{FR} \phi_{DIV}}{(C_F)_{vac} \dot{w}_T}$$

$$= \frac{(3312) (32.174) (1.015) (1.018)}{(1.6746) (9.382)}$$

$$= 7008.1 \text{ ft/sec}$$

$\Sigma(\dot{q}/A)(A)$ = heat losses to the chamber wall between the injector face and nozzle exit

$$= 504.6 \text{ Btu/sec (see Fig. 63 for } \dot{q}/A \text{ profile)}$$

The heat loss correction factor, ϕ_{HL} , was calculated as follows:

$$\begin{aligned} \phi_{HL} &= \left\{ 1 + \left[\frac{c^*_{theo}}{c^*_{meas}} \right]^2 \left[\frac{\Sigma(\dot{q}/A)(A)}{\dot{w}_T \cdot c_p \cdot T_c} \right] \right\}^{1/2} \\ &= \left\{ 1 + \left[\frac{7139}{7008.1} \right]^2 \left[\frac{504.6}{9.382 \times 0.431 \times 8142} \right] \right\}^{1/2} \\ &= [1.015]^{1/2} \approx 1.008 \end{aligned}$$

Equation, E-7 with the appropriate numerical values shown, is presented below for test No. 17:

$$(\eta_{c^*})_F = \frac{(F + P_a A_e) g_c \phi_{FR} \phi_{DIV} \phi_{HL}}{(C_F)_{vac} (\dot{w}_o + \dot{w}_f) (c^*)_{theo}}$$

$$(\eta_{c^*})_F = \frac{(3312) (32.174) (1.015) (1.018) (1.008)}{(1.6746) (9.382) (7139)}$$

$$(\eta_{c^*})_F = 98.9\%$$

Thus, corrected c^* efficiency (based on thrust) for this test was 98.9 percent as compared to 97.8 percent based on chamber pressure measurements.

REFERENCES

- E-1. LAP 68-411 (RC), Static Pressure Measurement for Contract NASw-1229 Combustion Chamber, Rocketdyne, a Division of North American Rockwell Corporation, 19 August 1968.
- E-2. Falk, A. Y., et al., NASA CR-72487, Space Storable Propellant Performance Study, Final Report, Rocketdyne, a Division of North American Rockwell, Canoga Park, California, November 1968.
- E-3. Carter, W. A., NASA CR-72708, Gas-Liquid Space Storable Propellant Performance, TRW Systems Group, Redondo Beach, California, June 1970.
- E-4. Arbit, H. A., and S. D. Clapp, Fluorine-Hydrogen Performance Evaluation. Part I: Analysis, Design, and Demonstration of High-Performance Injectors for the Liquid Fluorine-Gaseous Hydrogen Propellant Combination, Research Report No. 66-10, Rocketdyne, a Division of North American Rockwell Corporation, Canoga Park, California, April 1966.
- E-5. Chamber Technology for Space Storable Propellants - Task II, Prepared for National Aeronautics and Space Administration, Contract NAS7-304, Report No. R-6028-2, Rocketdyne, a Division of North American Rockwell Corporation, Canoga Park, California, 13 October 1965.
- E-6. Hauenstein, C. A., Alternate Throat Development Program for the Apollo Command Module Reaction Control Engines, Report No. R-5941, Rocketdyne, a Division of North American Aviation, Inc., Canoga Park, California, 16 November 1964.

APPENDIX F

HEAT TRANSFER DATA REDUCTION TECHNIQUE

Local values of chamber wall and injector face heat flux were determined by analysis of transient thermocouple data acquired during short duration firings (~3 seconds). The transient thermocouple data were reduced to equivalent heat flux values by assuming that the graphite chamber wall was a semi-infinite slab initially at a uniform temperature which is suddenly exposed to a constant heat flux. The expression for the resulting temperature distribution in the slab is given as (Ref. F-1):

$$T - T_0 = 2 \frac{q}{A} \left[\frac{\sqrt{\alpha \theta}}{k} \operatorname{erfc} \frac{x}{2\sqrt{\alpha \theta}} \right] \quad (F-1)$$

where

T_0 = initial temperature of the slab

q/A = the local heat flux

α = the thermal diffusivity

k = the thermal conductivity

x = the distance from the surface, and

θ = the time

Rewriting Eq. F-1 yields

$$T - T_0 = 2 \left(\frac{q}{A} \right) \frac{\sqrt{\alpha \theta}}{k} \left[\frac{1}{\sqrt{\pi}} e^{-\frac{x^2}{4\alpha\theta}} - \frac{x}{2\sqrt{\alpha\theta}} + \left(\frac{x}{\sqrt{\alpha\theta}} \operatorname{erf} \frac{x}{\sqrt{\alpha\theta}} \right) \right] \quad (F-2)$$

The error function was expressed in terms of its infinite series, and the expression differentiated with respect to time. The resulting expression is closely approximated by the following:

$$\frac{\partial T}{\partial \theta} = \frac{q}{A} \left[\frac{1}{k} \sqrt{\frac{\alpha}{\pi\theta}} e^{-\frac{x^2}{4\alpha\theta}} \right] \quad (F-3)$$

or

$$\frac{q}{A} = \frac{\partial T / \partial \theta}{K_1}$$

where K_1 is a function of the physical properties of the wall, the location of the thermocouple, and the time.

By knowing the location of the thermocouple from the chamber wall and its thermal properties, the local value of heat flux was computed employing Eq. F-3 by utilizing the slope of the temperature-time output trace of the thermocouple.

As an example, Fig. F-1 shows the temperature-time history for one thermocouple located 5 inches from the face. For the data slice at 6.2 seconds (Beckman time), Eq. F-3 yields a local heat flux value of 1.89 Btu/in.²-sec.

Figure F-2 presents values for the thermal diffusivity and conductivity of ATJ graphite (Ref. F-2) as a function of temperature which were employed for calculation of local values of chamber wall heat flux.

REFERENCES

- F-1. Carslaw, H. S., and J. C. Jaeger, Conduction of Heat in Solids, The Clarendon Press, Oxford, England, 1959, pp 75-77.
- F-2. Lowrie, R., Research on Physical and Chemical Principals Affecting High Temperature Materials for Rocket Nozzles, National Carbon Co., Contract No. DA-30-069-ORD-2787, December 1963.

At Slice Point:

$$\frac{\partial T}{\partial x} = 210 \text{ }^{\circ}\text{F/sec}$$

$$\alpha = 0.048 \text{ in.}^2/\text{sec}$$

$$k = 0.00094 \text{ BTU/in.-sec-}^{\circ}\text{R}$$

$$x = 0.018 \text{ in.}$$

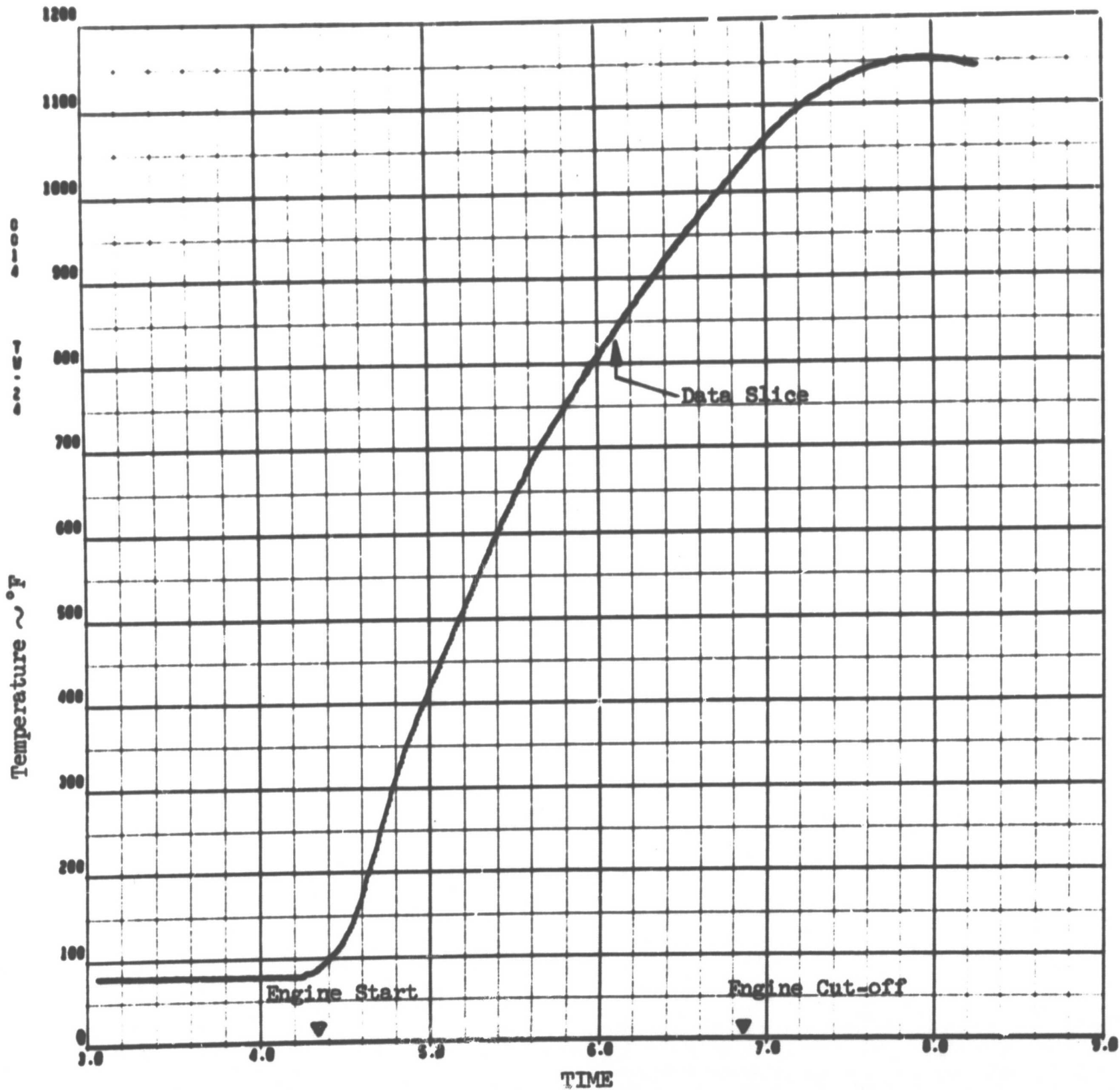


Figure F-1. Typical Temperature-Time History for Chamber Thermocouple

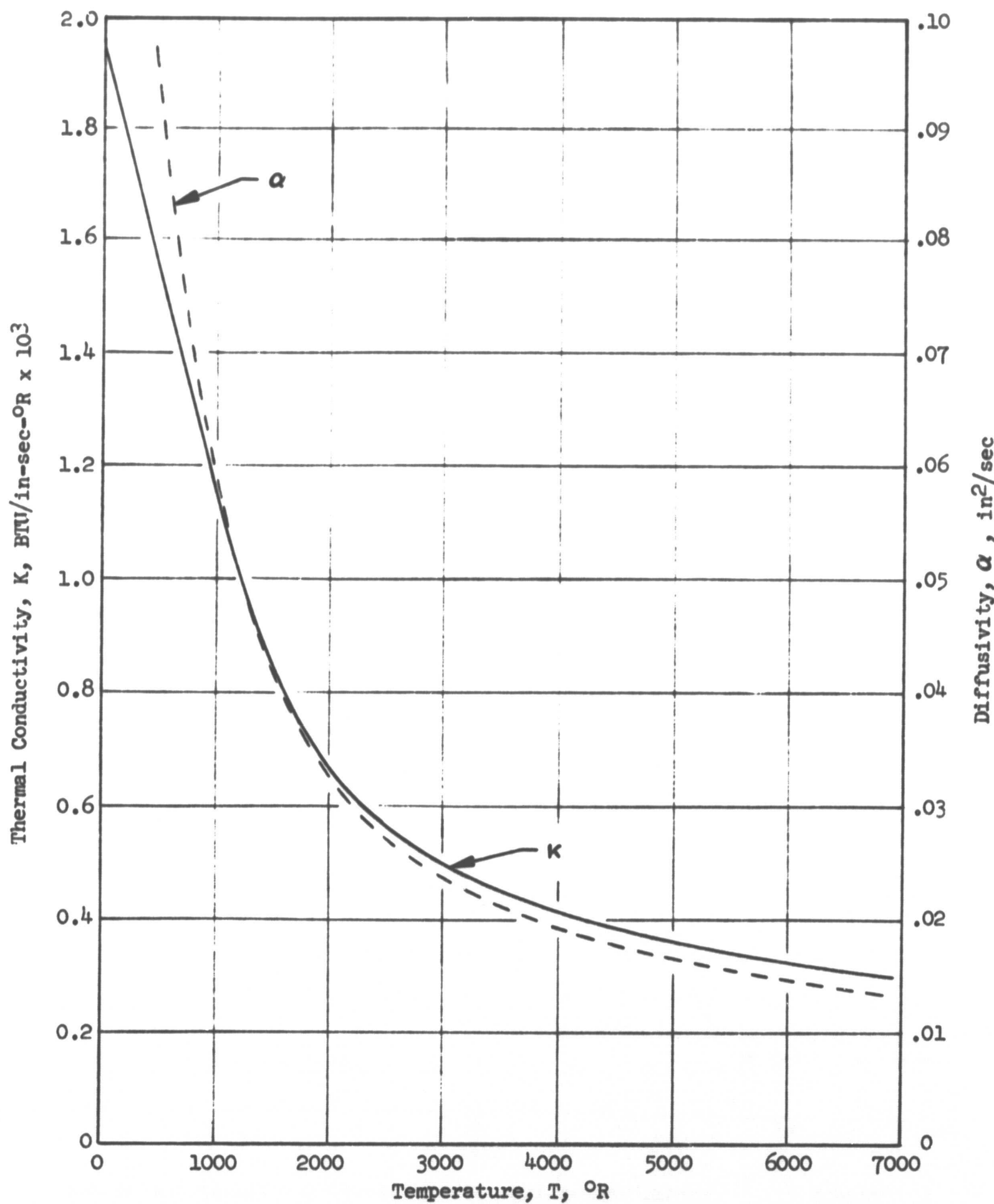


Figure F-2. Thermal Conductivity and Diffusivity as a Function of Temperature for ATJ Graphite

APPENDIX G

PHYSICAL PROPERTY AND THEORETICAL PERFORMANCE SUMMARY

The theoretical performance, combustion temperature, and physical properties of the propellants used for this program are presented in this appendix.

THEORETICAL PERFORMANCE

Theoretical performance of the liquid FLOX (82.6% F_2)/gaseous methane combination is presented in this section. Theoretical shifting equilibrium characteristic velocity (c^*) is shown in Fig. G-1 as a function of mixture ratio and chamber pressure. The theoretical combustion temperature as a function of mixture ratio and chamber pressure are presented in Fig. G-2. These data were generated employing Rocketdyne's Propellant Performance Program.

PROPELLANT PROPERTY DATA

The physical properties of the propellants used for this program are tabulated in Tables G-1 and G-2. The density and vapor pressure of FLOX (82.6% F_2) are presented in Fig. G-3 and G-4, respectively. Figures G-5 and G-6 present values for methane for the specific heat ratio, γ , and the compressibility factor, Z , respectively. These property data, in conjunction with the venturi manufacturer's C_D calibration factors, were employed for the determination of methane fuel flowrates.

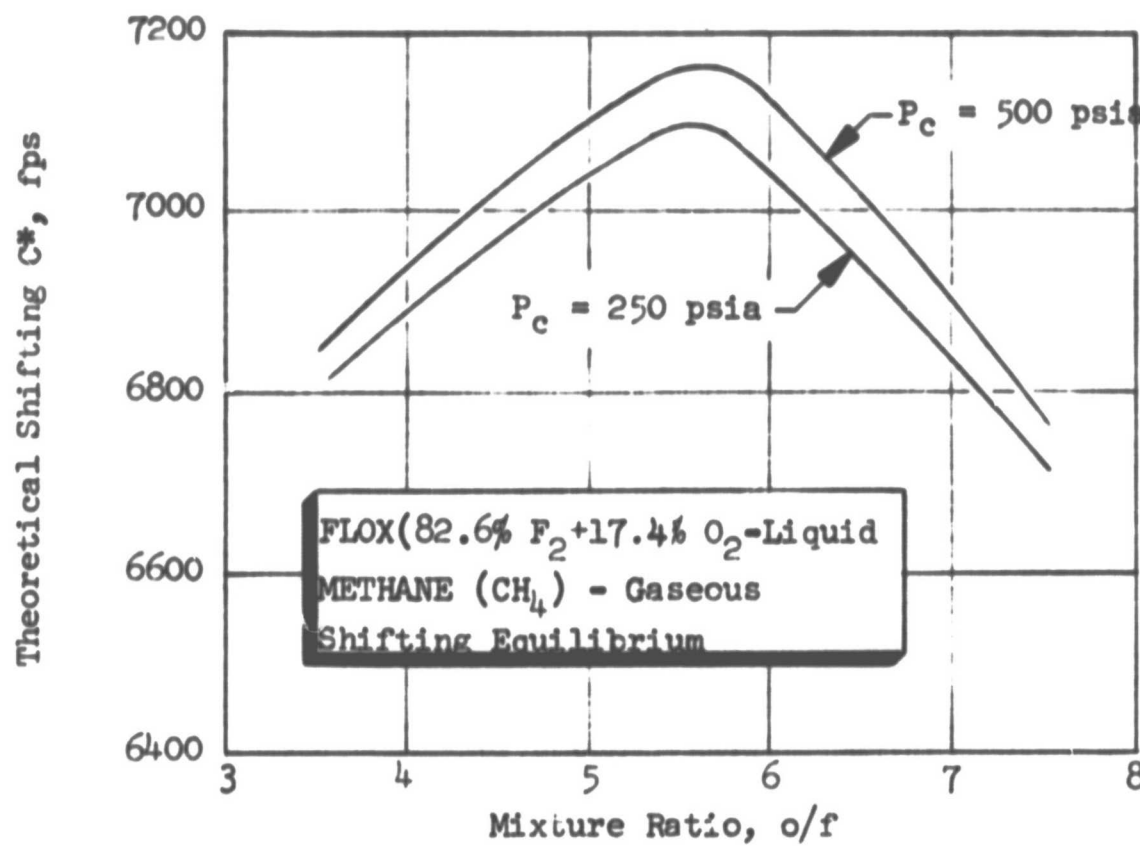


Figure G-1. Theoretical Combustion Temperature as a Function of Mixture Ratio and Chamber Pressure

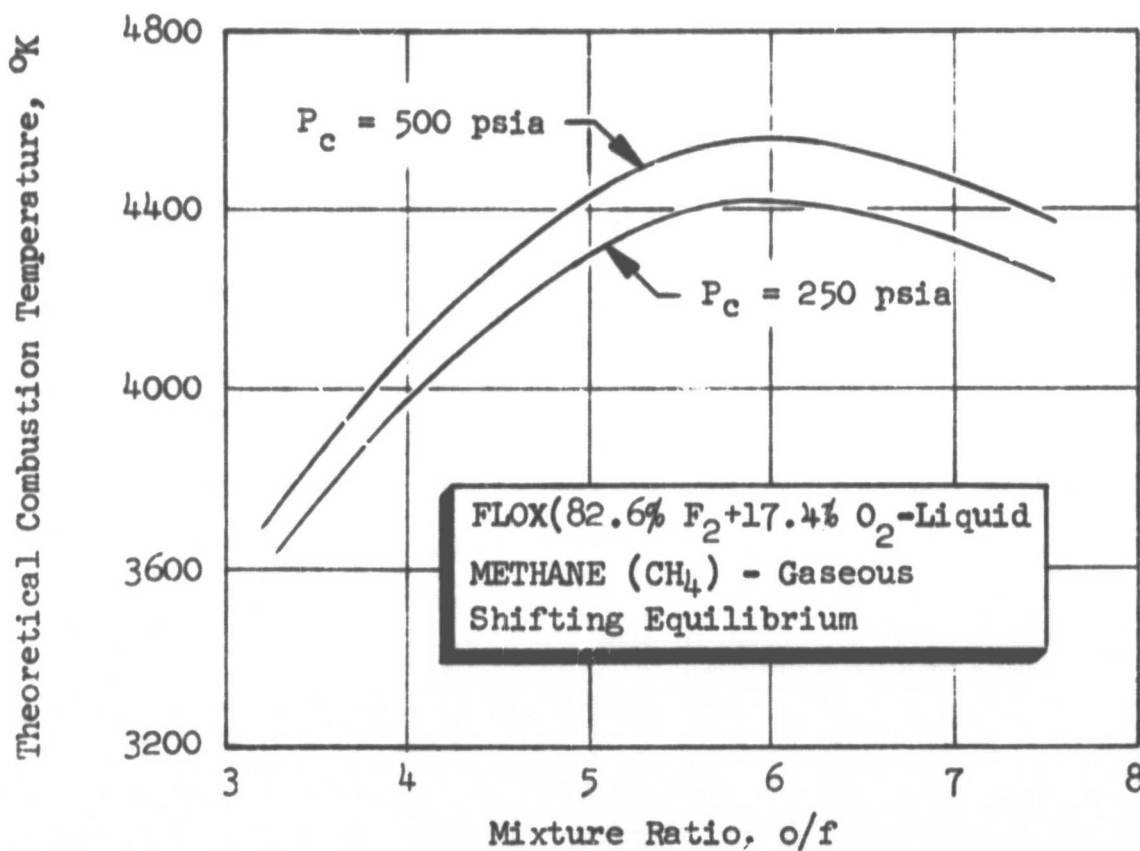


Figure G-2. Theoretical Combustion Temperature as a Function of Mixture Ratio and Chamber Pressure

TABLE G-1. FLOX PROPERTY SUMMARY

(Ref.: NASA SP-3037)

Chemical Formula	82.6%F ₂ + 17.4 O ₂
Normal Freezing Point, °R	--
Normal Boiling Point, °R	154°R
Liquid Density at NBP, lb/ft ³	91
Critical Temperature, °R	--
Critical Temperature, °R	--
Critical Pressure, psia	--
Critical Volume, ft ³ /lb	--
ΔH (vaporization) at NBP, Btu/lb	74.5
ΔH (fusion), Btu/lb	--
Viscosity at NBP, lb/(sec)(ft ²)	5.0
Thermal Conductivity at NBP, Btu/ft-hr-°R	0.090
Specific Heat at NBP, Btu/lb-°R	0.372
Specific Heat, Gas at 60°F	
C _p , Btu/lb-°R	0.200
C _v , Btu/lb-°R	
Ratio, C _p /C _v	
Viscosity at 60°F, centipoise	0.0216
Viscosity, gas, 32°F, 1 atm, centipoise	0.0203
Gas Constant, R, ft-lb _f /lb _m °R	49.8

TABLE G-2 METHANE PROPERTY SUMMARY
(Ref.: Pratt & Whitney Aircraft, PWA FR-1443)

Chemical Formula	CH ₄
Molecular Weight	16.042
Normal Freezing Point, °R	163.2
Normal Boiling Point, °F	200.8
Liquid Density at NBP, lb/ft ³	26.48
Critical Temperature, °R	43.3
Critical Pressure, psia	673
Critical Volume, ft ³ /lb	0.0989
ΔH (vaporization) at NBP, Btu/lb	219.22
ΔH (fusion), Btu/lb	25.25
Viscosity at NBP, lb/ft-sec	7.0 × 10 ⁻⁵
Thermal Conductivity at NBP, Btu/ft-hr-°R	0.1075
Specific Heat at NBP, Btu/lb-°R	0.80
Specific Heat, Gas at 60°F	
C _p , Btu/lb-°R	0.5271
C _v , Btu/lb-°R	0.4032
Ratio, C _p /C _v	1.307
Viscosity at 60°F, centipoise	0.012
Viscosity, Gas, 32°F, 1 atm, centipoise	0.009
Gas Constant, R, ft-lbf/lbm-°R	96.31
Gas Density at 32°F, 1 atm	0.045 lb/ft ³
70°F, 1 atm	0.041
70°F, 100 psia	0.285
70°F, 500 psia	1.495
70°F, 1000 psia	3.17
70°F, 2000 psia	6.80*
70°F, 4000 psia	11.77*
70°F, 6000 psia	14.80*

* Calculated from theoretical compressibility curve.

(1) Thermodynamic Properties
of Fluorine: Allied Chemical
Corp., Jan. 1965

(2) Thermodynamic Data on Oxygen
and Nitrogen ASD-TR-61-625
Wright-Patterson AFB, Sept. 1961

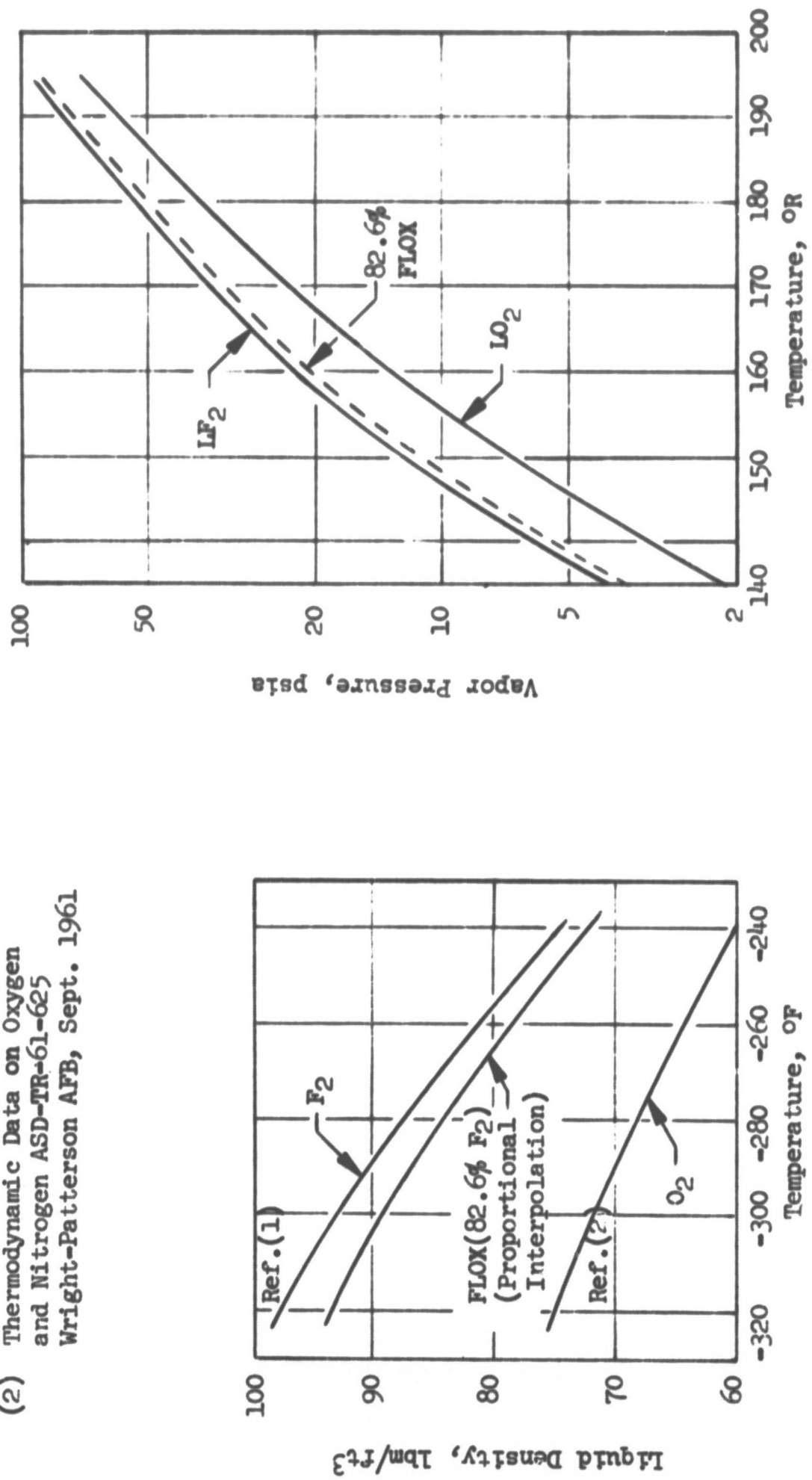


Figure G-3. Liquid Fluorine, Oxygen and
FLOX Density as a Function
of Temperature

Figure G-4. Vapor Pressure of Liquid Fluorine,
Oxygen and FLOX as a Function of
Temperature

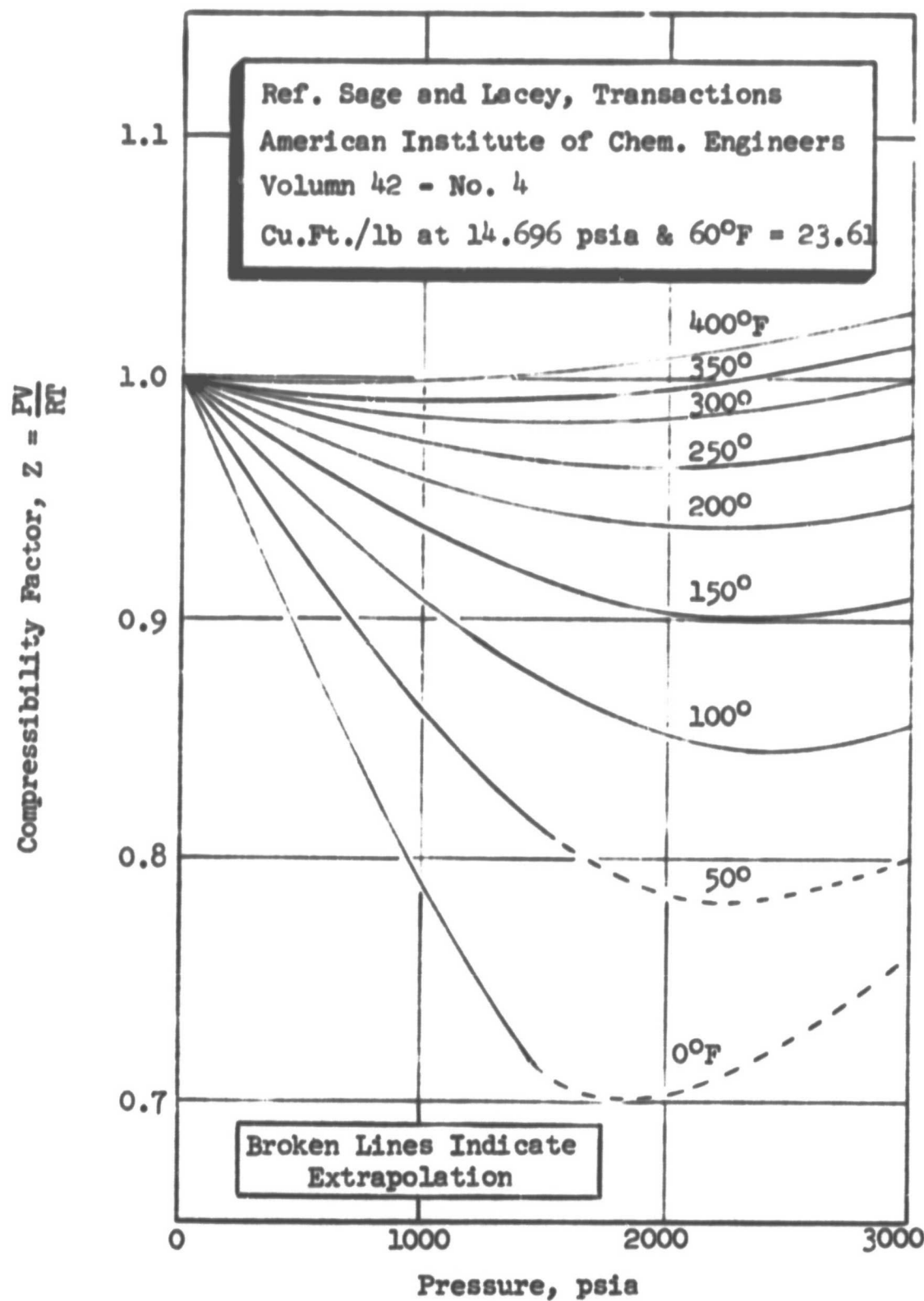


Figure G-5. Compressibility of Methane Gas as a Function of Temperature and Pressure

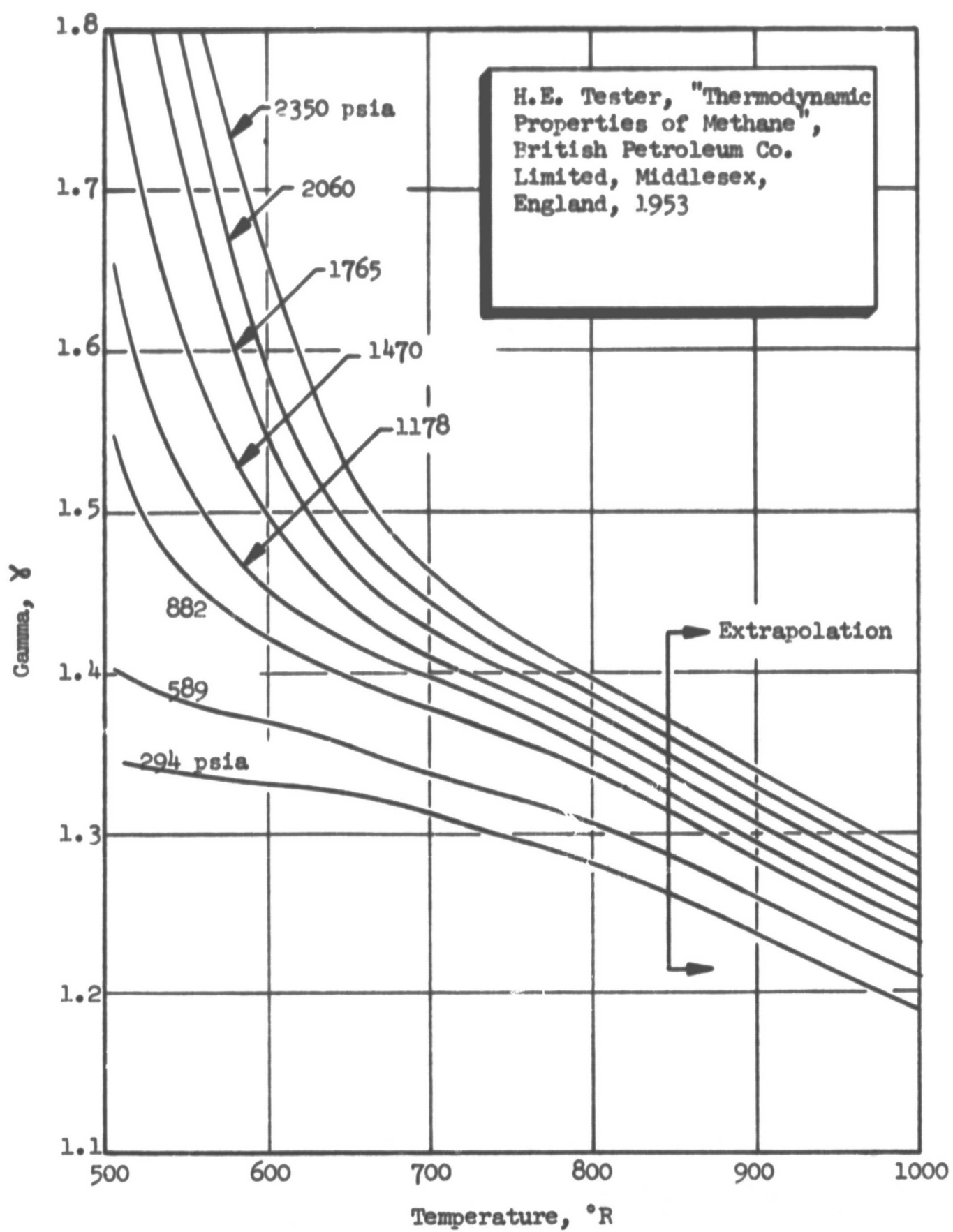


Figure G-6. Specific Heat Ratio of Methane Gas as a Function of Pressure and Temperature

PRECEDING PAGE BLANK NOT FILMED

APPENDIX H

PERFORMANCE DATA MEASUREMENT ERROR ANALYSIS

INTRODUCTION

Because it is not possible to measure the true value of any physical property or parameter, the error limits, or uncertainty interval associated with any experimental measurement should be specified. It is the purpose of this appendix to indicate the reliability of the experimental results of this program by estimation of the errors inherent in the data acquisition processes and/or in the calculation procedures. This will permit determination of the range within which, at a given confidence level, the true values of the measured or calculated parameters may be expected to fall.

If error is defined as departure of an experimental measurement from the "true" value, its magnitude can never be completely known; if it were known, it would become a correction which could be systematically applied. Hence, error limits can only be stated within probability limits. Performance data (c^* efficiency) precision was estimated by two separate methods, one based on static calibration of the individual transducers, and the other on analysis of repeated firings of the rocket engine.

In the present application, the data precision analysis based on static calibration of the individual transducers was made by an error analysis procedure which consisted of the following steps:

1. Estimation of the uncertainty intervals of the individual transducers, including the measuring systems in which they were used.
2. Combination of the uncertainty intervals of duplicate or redundant sensors into an uncertainty interval for the measurement.
3. Combination of the uncertainty intervals of several measurements (e.g., flowmeter frequency and propellant density) into an uncertainty interval for the parameter they determine (e.g., flowrate).
4. Combination of the uncertainty intervals of the parameters (e.g., chamber pressure, flowrate, and throat area) entering into calculation of the value of the desired variable (e.g., characteristic velocity efficiency) to estimate the uncertainty interval of the calculated result.

As noted above, the second method used to estimate the uncertainty (confidence) interval associated with the experimental determination of characteristic velocity efficiency was by analysis of data from repeated firings of the rocket motor. For this case, the test data were analyzed as a completely randomized design, by use of the analysis-of-variance technique.

Two types of errors are possible in any measurement:

1. Systematic Errors. These are associated with the particular system, with the experimental techniques employed, or with the calibration procedures. They cannot be estimated by statistical methods, and are minimized primarily by careful calibration with the best available standards, by requirements for consistency and traceability of the experimental and calibration techniques, and by critical examination of experimental data.
2. Random Errors. These arise from unpredictable and unknown variations in the experimental situation and are generally assumed to follow a normal distribution to permit simple statistical analysis. Error analysis is concerned only with random errors and implicitly assumes that systematic errors can be eliminated in a carefully conducted experimental program.

SENSOR PRECISION

A measurement analysis program (Random Walk measurement analysis program) is employed at Rocketdyne which uses transducer calibrations to provide appropriate factors for test data reduction. In addition, statistical histories for each transducer are developed so that estimates of short- and long-term deviations can be made and probably error bands calculated. This program is discussed in detail in Appendix I.

The precision of a measurement obtained as the output of a physical instrument or sensor is a quantitative estimate of the uncertainty associated with that measurement. (The word sensor means not only the transducer itself, but the complete system which converts the transducer signal to a numerical value of its physical parameter analog.) This estimate is made by statistical analysis of the outputs of the sensor when repeatedly acted upon by known inputs. The known inputs, of course, have uncertainty limits of their own but, for practical purposes, it is assumed that they are accurate (i.e., identical to true values) within the limits required by the experimental situation. Ultimately, these inputs must be directly traceable to established standards, such as those of the National Bureau of Standards.

When a sensor is calibrated against known inputs, precision may be considered as the certification of an error and within the calibrated interval and within a given confidence level. Thus, it provides a measure of "closeness to truth" of the reduced data. Precision may be numerically expressed as the standard deviation of a measurement, which has the same units as the measurement itself, or as the coefficient of variation (C_v), which permits valid comparisons between measurements in different units. It also permits valid comparisons to be made between large and small things. Coefficient of variation (C_v) is the standard deviation (σ) expressed as a percentage of the mean, thus making it dimensionless:

$$C_v = \frac{\sigma}{\mu} \cdot 100 \quad (H-1)$$

where

- σ = the standard deviation
- μ = sample mean value
- C_v = coefficient of variation

Pressure

The coefficients of variations of the pressure transducers were obtained by application of the Random Walk measurement analysis program to the calibration data. Chamber pressure values ranged from 0.25 to 0.53 percent for static calibrations made on a pressure manifold mounted on the thrust stand.

For all tests, redundant sensors were used to measure the chamber pressure. Two or three independent transducers were used to measure this important parameter in order to increase the measurement reliability.

Other errors in pressure measurement may arise in addition to the random statistical uncertainty limits. In measurement of chamber pressure through a drilled wall tap, as herein, erroneous values of stream pressure may be indicated because of the effect of the hole itself upon the flow. Estimated magnitudes of this error, which is a function of stream velocity, were based on experimental data obtained with water and gas (Ref. H-1). For the experimental situation herein, these errors are insignificant. Coupling errors, arising from effects of the tubing joining the pressure taps to the transducers were also insignificant in the present series of experiments (Ref. H-2). The locations of the pressure taps from which combustion chamber throat stagnation pressure (or performance) is calculated is quite critical. Procedures were followed to ensure that the proper static pressure measurement was employed. Thus, this source of error is assumed to be insignificant.

Thrust

Values of coefficient of variation obtained by application of the Random Walk measurement analysis program to thrust calibrations were in the 0.23- to 0.35-percent range. A possible source of error in thrust measurement arose from the necessity of taking system prerun zeros with the same degree of propellant line chill as existed during the firings. On the basis of thrust calibrations made with chilled and unchilled propellant lines, the above C_v values should be applicable. The coefficient of variation increase due to line chill variations between tests should (and is assumed to) be negligible.

Throat Area

Geometric throat diameter was measured with an expansion micrometer prior to, and following, each firing. The maximum coefficient of variation of the calculated areas was 0.42 percent. Throat area variation during firing was observed to be small.

Volumetric Flowrate

The coefficients of variation of the turbine flowmeters used to measure the propellant flowrates were determined from flow-bench calibration data. Each meter was calibrated prior to the start, and at the end, of the program. The meters were calibrated with water. Redundant (two) flowmeters, in series, were placed

in the oxidizer line. A C_V value for the oxidizer flowmeter was 0.02. In addition, however, there are predictable water-to-cryogenic calibration shifts (Ref. H-3) which introduce additional sources of error. The coefficient of variation arising from this course is approximately 0.5 percent (Ref. H-4).

Temperature

The platinum resistance thermometers (Rosemount bulbs) were precision calibrated by the manufacturer. These calibrations were checked by taking several emf readings with the sensors immersed in LN₂ and in LO₂ at atmospheric pressure; they were correct within the limits of readability. Root-sum-square (RSS) error limits of these sensors based on specifications of repeatability, insulation, time lag, friction heating, and interchangeability are approximately 0.1 percent (Ref. H-5). Voltage readout of the transducers was adjusted to calibration values by a standard decade resistance box with error limits of 0.2 percent.

COMBINED ERROR ESTIMATION

Redundant Measurements

Redundant transducers were used to measure the most important parameters in order to increase the measurement reliability. The most probable value of a redundant measurement is the weighted average. The variance of the weighted mean value, σ_m^2 , is given by the following equation:

$$\frac{1}{\sigma_m^2} = \frac{1}{\sigma_1^2} + \frac{1}{\sigma_2^2} + \dots + \frac{1}{\sigma_n^2} = \sum_{i=1}^n \frac{1}{\sigma_i^2} \quad (H-2)$$

where

σ_m^2 = the variance of the weighted mean

σ_i^2 = the variance of the i^{th} measurement

Clearly, the variance of a weighted mean is less than any of the individual variances.

Combined Measurements

When several measured variables are combined algebraically to yield an experimental result, the standard deviation of the result, which takes into account the propagation of the individual error, is given by the following equation (Ref. H-6):

$$\sigma_R = \sqrt{\left[\frac{\partial R}{\partial x_1} \sigma_1 \right]^2 + \left[\frac{\partial R}{\partial x_2} \sigma_2 \right]^2 + \dots + \left[\frac{\partial R}{\partial x_n} \sigma_n \right]^2} \quad (H-3)$$

where

σ_R = the standard deviation of the calculated result

x_1, x_2, \dots, x_n = measured variables

$R = f(x_1, x_2, \dots, x_n)$

$\sigma_1, \sigma_2, \dots, \sigma_n$ = standard deviations of x_1, x_2, \dots, x_n , respectively

When the individual measurements are combined by addition, and are independent, the standard deviation is given by Ref. H-6:

$$\sigma_R = \sqrt{\sigma_1^2 + \sigma_2^2 + \dots + \sigma_n^2} \quad (H-4)$$

DATA PRECISION

Static Calibration Precision Analysis

Characteristic velocity can be calculated by two methods, one based on chamber pressure (P_c) measurement and one on thrust (F) measurement, as given below:

$$c^* = \frac{(P_c)_o A_t g_c}{\dot{w}_t} \quad (H-5)$$

or

$$c^* = \frac{F_{vac} g_c}{(C_F)_{vac} \dot{w}_t} \quad (H-6)$$

where

c^* = characteristic velocity (calculated), ft/sec

$(P_c)_o$ = stagnation pressure at the throat, psia

A_t = measured geometric throat area, in.²

g_c = conversion factor (32.174 lbm-ft/lbf-sec²)

\dot{w}_t = total propellant mass flowrate, lbm/sec

$(C_F)_{vac}$ = theoretical shifting thrust coefficient (vacuum)

F_{vac} = measured thrust corrected to vacuum conditions by the equation:
 $F_{vac} = F + P_a A_e$, lbf

F = measured thrust, lbf

P_a = ambient pressure, psia

A_e = area of nozzle exit, in.²

It should be noted that these expressions yield uncorrected characteristic velocity.

The standard deviation of the characteristic velocity based on both methods of calculation can be determined by application of Eq. H-3 to Eq. H-5 and H-6. The standard deviation of the uncorrected characteristic velocity (based on chamber pressure) is calculated as follows:

$$(\sigma_{c^*})_{p_c} = \sqrt{\left[\left(\frac{A_t g_c}{\dot{w}_t}\right) \sigma_{p_c}\right]^2 + \left[\left(\frac{(p_c)_o g_c}{\dot{w}_t}\right) \sigma_{A_t}\right]^2 + \left[\left(\frac{(p_c)_o g_c}{\dot{w}_t^2}\right) \sigma_{\dot{w}_t}\right]^2} \quad (H-7)$$

The resulting expression for the standard deviation of the characteristic velocity, based on thrust, is:

$$(\sigma_{c^*})_F = \sqrt{\left[\left(\frac{g_c}{C_F \text{vac}} \dot{w}_t\right) \sigma_{F \text{vac}}\right]^2 + \left[\left(\frac{F_{\text{vac}} g_c}{C_F \dot{w}_t^2}\right) \sigma_{\dot{w}_t}\right]^2} \quad (H-8)$$

Substitution of numerical values into these expressions yield the resulting standard deviations. As far as random errors only are concerned, there was no significant difference in the estimated standard deviations based on chamber pressure or thrust. The standard deviation of the uncorrected characteristic velocity was approximately 35 ft/sec. This corresponds to a coefficient of variation of approximately 0.5 percent for the uncorrected c^* efficiency. Therefore, the uncorrected c^* efficiencies determined in the present program are estimated to have an error band of approximately ± 1.0 percent at the 95-percent (2 σ) confidence level).

Application of the corrections to measured uncorrected characteristic velocities could cause an increase in the error associated with corrected characteristic velocities. Assuming proper application of these corrections, however, the resulting characteristic velocity efficiencies reported herein are estimated to be within ± 1.0 percent of the true value.

Calculation of approximate values for σ_{p_c} , σ_{A_t} , and $\sigma_{F \text{vac}}$ for use in Eq. H-7 and H-8 are straightforward. Estimation of $\sigma_{\dot{w}_t}$ is more complicated and, therefore, is discussed briefly herein.

For the turbine flowmeter, the propellant mass flowrate (\dot{w}_i) is a function of the flowmeter frequency (f_i) and the propellant density (ρ_i):

$$\dot{w}_i = \dot{w}_i (f_i, \rho_i) \quad (H-9)$$

In particular,

$$\dot{w}_i = (f_i) (\rho_i) (\text{flowmeter constant})_i \quad (K) \quad (H-10)$$

where

f_i = flowmeter output frequency, cps $\equiv x_i$
 ρ_i = propellant density, lbm/ft³
 $(\text{flowmeter constant})_i$ = flowmeter constant, gal/cycle
 K = conversion factor = $(1/7.48) \text{ ft}^3/\text{gal}$

Therefore, the standard deviation of each meter's flowrate is given by

$$\sigma_{\dot{w}_i} = \sqrt{\left(\frac{\partial \dot{w}_i}{\partial f_i} \sigma_{f_i} \right)^2 + \left(\frac{\partial \dot{w}_i}{\partial \rho_i} \sigma_{\rho_i} \right)^2} \quad (\text{H-11})$$

or

$$\sigma_{\dot{w}_i} = \left[K(\rho_i) (x_i) (\sigma_{f_i}) \right]^2 + \left[f_i (x_i) (\sigma_{\rho_i}) K \right]^2$$

Actually, flowrate is a function of flowmeter frequency and propellant temperature (assuming no significant error in conversion of propellant temperature to equivalent density). Thus, Eq. H-11 may be written as follows:

$$\sigma_{\dot{w}_i} = \left[K(\rho_i) (x_i) (\sigma_{f_i}) \right]^2 + \left[(f_i) (x_i) (\sigma_T)_i K \right]^2 \quad (\text{H-12})$$

Standard deviation is converted to coefficient of variation by use of Eq. H-1. The standard deviation of each propellant flowrate is then determined by application of Eq. H-2 to the redundant measurements. The coefficient of variation of the total propellant flowrate may be obtained from the coefficients of variation of its component parts by use of the following equation:

$$(C_V)_{\dot{w}_t} = \sqrt{\frac{r^2 (C_V)_{\dot{w}_o}^2 + (C_V)_{\dot{w}_f}^2}{(r + 1)^2}} \quad (\text{H-13})$$

where

$$r = \text{mixture ratio} = \dot{w}_o / \dot{w}_f$$

The standard deviation of the total propellant flowrate can then be obtained from Eq. H-1.

Dynamic Precision Analysis

The estimates of expected standard deviations in characteristic velocity calculated above are based on static calibrations of pressure/thrust sensors and, hence, may not be strictly applicable to the dynamic system represented by a firing

rocket motor. It is generally assumed, however, that such calibration data may be extended without significant change to dynamic systems oscillating at very low frequencies and amplitudes and that steady-state stable combustion is such a system.

An indication of the possible magnitude of the uncertainty interval associated with the experimental determination of characteristic velocity efficiency may be obtained by analysis of repeated firings of a rocket motor with the same set of transducers. If systematic errors are assumed to be insignificant, variations from indicated "correct" values (i.e., those which are on the best curve through the experimental points) may be ascribed to random errors and hence are subject to statistical analysis. The usefulness of such an analysis is a direct function of the number of data points used to obtain the correct or average values. With only three or four data points available for determination of efficiency at a given condition, statistical calculation of measurement reliability has no great absolute value but may be used for comparisons with those estimated from transducer calibrations.

During this program, several different test conditions were duplicated. These test data were analyzed as a completely randomized design (Ref. H-7) by use of the analysis of variance technique. (This is, perhaps, the most powerful and widely used statistical technique.) On the basis of this analysis, the experimental c^* efficiencies determined in the present program are estimated to have an error band of approximately ± 1.0 percent at the 95-percent confidence level.

SUMMARY

Both methods of estimation of the performance data precision indicates that the experimental c^* efficiencies determined in the present program have an error band of approximately ± 1.0 percent at the 95-percent (2σ) confidence level. Of course, both of these estimates are based on the assumption that the corrections applied to the uncorrected c^* efficiencies (Appendix E) are valid.

REFERENCES

- H-1. Dean, R. C., Jr., Aerodynamic Measurements, Gas Turbine Laboratory Massachusetts Institute of Technology, Cambridge, Massachusetts, 1953.
- H-2. Thomson, D. B., The Effect of Tubing on Dynamic Pressure Recording, TN-61-3, Rocketdyne, a division of North American Rockwell, Canoga Park, California, 28 February 1961.
- H-3. Bucknell, R. L., "Calibration Systems and Turbine-Type Flow Transducers for Cryogenic Flow Measurements," Advances in Cryogenic Engineering, Vol. 8, Plenum Press, New York, 1963, pp 360-369.
- H-4. Alspach, W. J., and T. M. Flynn, "Considerations When Using Turbine-Type Flowmeters in Cryogenic Service," Advances in Cryogenic Engineering, Vol. 10, Plenum Press, New York, 1965, pp 246-252.
- H-5. Research Report No. 66-10, Fluorine-Hydrogen Performance Evaluation. Part I: Analysis, Design, and Demonstration of High-Performance Injectors for the Liquid Fluorine-Gaseous Hydrogen Propellant Combination, Arbit, H. A. and Clapp, S. D., Rocketdyne, a division of North American Rockwell, Canoga Park, California, April 1966.
- H-6. Arkin, H. and Colton, R.R., Statistical Methods, Barnes and Nobel, Inc., N.Y.
- H-7. Ostle, B., Statistics in Research, The Iowa State College Press, Ames, Iowa.

APPENDIX I

RANDOM WALK MEASUREMENT ANALYSIS PROGRAM

INTRODUCTION

The primary purpose of a sensor measurement analysis program is to provide a function which relates observed sensor outputs to estimates of corresponding system inputs, together with quantitative indications of the precision of this conversion. The function and the precision estimates are established on the basis of sensor calibration history, that is, upon a sequence of periodic calibrations of the sensor and its associated measuring and recording system against known inputs.

Because calibrations must of necessity be made at a time differing from the actual firing time by several hours to several days, the changes in random sensor error with time must be established. In the Random Walk measurement analysis program (Ref. I-1) this is accomplished by assuming that the input-to-output ratio at a particular input level performs a random walk in time which has normal distribution and variance. It assumes also that there is a random measurement error in the observed datum which is independent of the random walk and which is also normally distributed. Mathematical foundations and development of the program are given in Ref. I-2 and I-3.

On the basis of a sequence of periodic calibrations, the Random Walk program provides the following:

1. A function, either linear or cubic, which converts observed system outputs into estimates of true system inputs;
2. Coefficients of short-term and random walk variations, as well as a combined value valid at specified times; and
3. A decision, based upon the calculated coefficient of variation and a pre-specified imprecision limit, as to whether the sensor should be used as is, recalibrated immediately, or discarded, and the maximum allowable interval to next calibration.

MEASUREMENT PROGRAM OUTPUT

A typical Random Walk computer program output is shown in Fig. I-1. The first line of output gives the test stand name and number (Willie, 0019), recording system (Beckman), transducer serial number (651705), ID number for data cards (019050), and the physical parameter being calibrated (P_c -4).

The next set of numbers ("Latest Output") is the most recent raw calibration data. On the left are the readings (in Beckman counts) for the listed calibration input steps ("Input"); on the right are the precalibrate throw zero (Z1), the calibrate throw reading (CT), the postthrow zero (Z2), the precalibration zero (Z3), the postcalibration zero (Z4), and the date of calibration ("Time").

WILLIE		BKH		651705		900		019050		PC4	
LATEST OUTPUT		498		1246		1998		2740		3484	
Y(1)	X(1)	Y(2)	X(2)	Y(3)	X(3)	Y(4)	X(4)	Y(5)	X(5)	Y(6)	X(6)
100.0	0.1266	300.0	0.3798	500.0	0.6344	700.0	0.8856	900.0	1.1374		
100.0	0.1255	300.0	0.3789	500.0	0.6329	700.0	0.8850	900.0	1.1367		
100.0	0.1259	300.0	0.3790	500.0	0.6335	700.0	0.8846	900.0	1.1360		
100.0	0.1269	300.0	0.3794	500.0	0.6345	700.0	0.8853	900.0	1.1371		
100.0	0.1266	300.0	0.3794	500.0	0.6332	700.0	0.8846	900.0	1.1371		

SHORT TERM COEFFICIENT OF VARIATION (PRECISION)											
RANDOM COEFFICIENT OF VARIATION											
OFFSET COEFFICIENT OF VARIATION											
COEFFICIENT OF VARIATION REQUIRED FOR SYSTEM											
COEFFICIENT OF VARIATION REQUIRED FOR DATA REDUCTION MODEL											

DATA REDUCTION MODEL(1) IS											
COEFFICIENT OF VARIATION OF MODEL(1) = 1.5834E-01 PERCENT											
STANDARD DEVIATION OF MODEL(1) = 7.9171D-01											
DEGREES OF FREEDOM OF MODEL(1) = 23											

DATA REDUCTION MODEL(2) IS											
COEFFICIENT OF VARIATION OF MODEL(2) = 1.5611E-01 PERCENT											
STANDARD DEVIATION OF MODEL(2) = 7.8054D-01											
DEGREES OF FREEDOM OF MODEL(2) = 22											

SYSTEM SHOULD BE CALIBRATED ON OR BEFORE 1-22-70											

Figure I-1. Typical Random Walk Computer Output

The first two zeros (Z1 and Z2) are averaged and subtracted from the throw to obtain a reduced throw. For each calibration step, a linear interpolation is made between the last two zeros (Z3 and Z4) and the interpolated result is subtracted from the reading to obtain a reduced reading. Each reduced reading is then divided by the reduced throw to obtain a scaled output. All scaled output values from all calibrations in the system history are then listed ("Scaled Output") under the appropriate input pressures, with one calibration per line and its date ("Time") listed at the right of each line.

The first three lines following the scaled output table are estimates of the measurement variance (σ_m^2) in the input-to-scaled output ratio, the random walk variance (σ^2) in the input-to-scaled output ratio, and the ratio (k) of the former (short-term) variance to the latter (long-term) variance. The variances (σ_m^2 and σ^2) are used in computing the data reduction imprecision, which is defined as the standard deviation of an estimated input about the true input.

The next line of output gives the coefficient of short-term variation, which is the standard deviation (σ_m) expressed as a percentage of the average input-to-scaled output ratio. This quantity is generally the largest component of data reduction imprecision. The following entry gives the coefficient of random walk (long-term) variation, which is the standard deviation (σ) also expressed as a percentage of the average input-to-scaled output ratio. This item is meaningful only after calibrations are obtained over a period of time. The final listing in this block is the prespecified maximum limit of data reduction imprecision expressed as coefficient of variation.

The program now calculates revised scaled output values corresponding to the state of the system at the time of the most recent calibration. These values are then fit by least squares with either a linear or cubic function by the following procedure. The null hypothesis is that the function is linear, and the specified error (the probability that a truly linear function is mistakenly concluded to be nonlinear) is printed out. If the linearity hypothesis is rejected, a cubic fit is made. In either case, the formula for converting scaled outputs to estimated inputs is then given, and, if the relationship is cubic, an input-output table is printed out for convenience in data reduction.

The next line gives the result of the second test, which checks whether or not the input-output model is consistent with the estimate of σ_m (the root-mean-square estimate for the calibration curve fit and σ_m should be approximately equal). If it is, then the model is labeled "SATISFACTORY"; if not, the model is labeled "UNSATISFACTORY," indicating a significant intercept or an error in the input data.

The following item indicates the ability of the system to meet the specified imprecision requirement. On the basis of the calibration data, three situations are recognized:

1. The system can never meet required precision, and should be replaced
2. The system will fail the requirement within the next two days and should be recalibrated immediately

3. The system will meet the requirement up to a certain date (30 days maximum), on or before which it should be recalibrated. In this case, the estimated data reduction imprecision is given for test data taken two days after the most recent calibration and on the specified recalibration date.

In the present program, the system transducers were calibrated weekly, regardless of the leeway allowed by reason of little or no random walk variation and consequent minimum degradation in precision.

The final item is a 2 by 2 matrix, denoted by R, which is used to estimate data reduction imprecision at any other time of interest and for any scaled output by the following expression:

$$P = \left[V + s^2 (h\sigma^2 + \sigma_m^2) \right]^{1/2}$$

where

P = estimated standard deviation for a reduced datum

s = scaled output

h = number of days after most recent calibration

V = matrix product: $(s, s^3) R \left(\begin{matrix} s^3 \\ s \end{matrix} \right)$

Application of the results of this sensor measurement analysis program to estimation of random experimental errors and to measurement reliability is given in Appendix G.

REFERENCES

- I-1. Rothman, D.: Random Walk Program for Measurements Analysis of Static Systems, RM-1119-351, Rocketdyne, a division of North American Rockwell, Canoga Park, California, 25 January 1965.
- I-2. Rothman, D.: A Random Walk Model for Non-Uniform, One-Parameter, Static, Linear Measurement Systems, RR-59-47, Rocketdyne, a division of North American Rockwell, Canoga Park, California, 15 December 1959.
- I-3. Rothman, D.: Gaussian Random Walk with Gaussian Measurement Errors, SORUM-63-9, Rocketdyne, a division of North American Rockwell, Canoga Park, California, 24 September 1963.

APPENDIX J

REFERENCES

1. Pauckert, R. P., Space Storable Regenerative Cooling Investigation, R-8266 (NASA CR-72705), Rocketdyne, a Division of North American Rockwell Corporation, Canoga Park, California, June 1970.
2. Space Storable Regenerative Cooling Investigation -- Interim Report, Pratt and Whitney Aircraft, FR-2552, NASA CR72341, Contract NAS3-11190, July 1968.
3. Falk, A. Y., et al., Space Storable Propellant Performance Study, Final Report, R-7677 (NASA CR-72487), Rocketdyne, a Division of North American Rockwell Corporation, Canoga Park, California, November 1968.
4. Mageean, J. V., Space Storable Propellant Performance, Final Report, NASA CR-72489, 1969.
5. Burick, R. J., Space Storable Propellant Performance Study -- Coaxial Injector Characterization, NASA CR-120936, Final Report, R-8973-2, Rocketdyne, a Division of North American Rockwell Corporation, Canoga Park, California, October 1972.
6. AFRPL-TR-68-147, Correlation of Spray Injector Parameters with Rocket Engine Performance, R. Dickerson, et al., Rocketdyne, a Division of North American Rockwell Corporation, Canoga Park, California, June 1968.
7. Mehegan, D. F., et al., Investigation of Gas-Augmented Injectors, NASA CR-72703, Rocketdyne, a Division of North American Rockwell Corporation, Canoga Park, California, September 1970.
8. Lambiris, S., L. P. Combs, and R. S. Levine, "Stable Combustion Processes in Liquid Propellant Rocket Engines," Combustion and Propulsion, Fifth AGARD Colloquium: High Temperature Phenomena, The MacMillan Company, New York, N. Y., 1962, 596-636.
9. Priem, R. J., and Heidmann, M. F., Propellant Vaporization as a Design Criteria for Rocket Engine Combustion Chambers, NASA TR-R-67, 1960.
10. Pieper, J. L., L. E. Dean, and R. S. Valentine, "Mixture Ratio Distribution- Its Impact on Rocket Thrust Chamber Performance," J. Spacecraft Rockets, Vol. 4, No. 6, pp 786-789, June 1967.
11. Rupe, J. H., A Correlation Between the Dynamic Properties of a Pair of Impinging Streams and the Uniformity of Mixture-Ratio Distribution in the Resulting Spray, Progress Report No. 20-209, Jet Propulsion Laboratory, Pasadena, California, 28 March 1956.
12. Rupe, J. H., An Experimental Correlation of the Nonreactive Properties of Injection Schemes and Combustion Effects in a Liquid-Propellant Rocket Engine, Technical Report No. 32-255, Jet Propulsion Laboratory, Pasadena, California, 15 July 1965.

13. Riebling, R. W., "Criteria for Optimum Propellant Mixing in Impinging Jet Injection Elements," J. Spacecraft Rockets, Vol. 4, No. 6, pp 817-819, June 1967.
14. Wrubel, J. R., "Some Effects of Gas Stratification on Choked Nozzle Flows," AIAA Paper 64-266, 1964.
15. Rupe, J. H., The Liquid Phase Mixing of a Pair of Impinging Streams, Progress Report No. 20-195, Jet Propulsion Laboratory, Pasadena, California, 6 August 1953.
16. R-7796-1, Space Storable Propellant Performance, Technical Proposal, Rocketdyne, a Division of North American Rockwell Corporation, Canoga Park, California, 26 March 1969.
17. Contract NAS7-304, Chamber Technology for Space Storable Propellants, Third Interim Report, Rocketdyne, a Division of North American Rockwell Corporation, Canoga Park, California, May 1967.
18. Technical Documentary Report No. TR-65-107, "Performance Characteristics of Compound "A"/Hydrazine Propellant Combinations," Rocketdyne, a Division of North American Rockwell, Canoga Park, California, May 1965.
19. Rocketdyne General Order No. 9222, "Space Storable Propellant Studies,-- Statement of Work for General Order 9222," 30 June 1969.
20. LAP 68-411 (RC): Static Pressure Measurement for Contract NASw-1229 Combustion Chamber, Rocketdyne, a Division of North American Rockwell Corporation, 19 August 1968.